Study of the $\mathbf{H \rightarrow ZZ^{(*)} \rightarrow 4\ell}$ Decay Channel and Contribution to the Forward Muon Detection with the ATLAS Experiment

by

KALLIOPI IORDANIDOU

A Dissertation Submitted in Fulfillment of the Requirements for the Degree of
Doctor of Philosophy in Physics

Nuclear and Particle Physics Section
Physics Department
National and Kapodistrian University of Athens

Advisor: D. Fassouliotis

Athens, January 2015

To all those who inspired me in any way

Contents

Acknowledgments

I would like to express my gratitude to my advisor D. Fassouliotis who guided me through my studies in particle physics, from the undergraduate level to the Ph.D. His constant support, patience and encouragement were crucial for my academic progress and helped to keep things in perspective.

I would like to deeply thank M. Schernau, who willingly accepted to share his detector and DAQ knowledge with me and devoted significant time for our scientific discussions.

I am honestly grateful to C. Kourkoumelis and V. Polychronakos who gave me the chance to collaborate and be financially supported by the University of Athens and the Brookhaven National Laboratory respectively. Looking further back in time, I would like to thank P. Ioannou who first introduced me to the Athens ATLAS particle physics group.

I would like to thank the SLAC team for the opportunity to be part of the NRC group, specifically M. Huffer, D. Su, R. Bartoldus, R. Claus, N. Garelli, L. Ruckman, C. Young. Also, I would like to thank R. Murillo (ex-UCI) for his inadequate help, not only with the NRC.

I would like to thank my colleagues and especially A. Antonaki, S. Angelidakis, N. Tsirintanis, A. Kourkoumeli, E. Tiouchichine for the professional interaction and friendship.

I would like to thank my family and friends (all around the world) for their long-term support.

Last but not least, I do not forget all those who inspired me in any way ...

Εκτενής Ελληνική Περίληψη

Ένα από τα πρωταρχικά αναπάντητα ερωτήματα της σύγχρονης σωματιδιακής φυσικής αφορά στην προέλευση της μάζας. Στα πλαίσια του Καθιερωμένου Πρότυπου των στοιχειωδών σωματιδίων, το σπάσιμο της ηλεκτρασθενούς συμμετρίας και κατ' επέκταση οι παρατηρούμενες μάζες των φορέων της ασθενούς αλληλεπίδρασης και των σωματιδίων της ύλης, οφείλεται στο μηχανισμό *Higgs*. Άμεση συνέπεια του μηχανισμού *Higgs* είναι η ύπαρξη του μποζονίου *Higgs*, το οποίο αποτελούσε το μοναδικό σωματίδιο του Καθιερωμένου Πρότυπου που δεν είχε ακόμη παρατηρηθεί κατά την έναρξη της εκπόνησης της παρούσας διδακτορικής διατριβής.

Ως εκ τούτου, ένας από τους σημαντικούς στόχους του ερευνητικού προγράμματος του *LHC* (*Large Hadron Collider*) και του ανιχνευτή *ATLAS* στο *CERN* ήταν η ανακάλυψη του μποζονίου *Higgs*. Μια από τις υπογραφές που συνεισέφερε σημαντικά στην ανακάλυψη του μποζονίου *Higgs* ήταν η $H \rightarrow ZZ^{(*)} \rightarrow 4\ell$, όπου $\ell = e, \mu$. Η παρούσα διδακτορική διατριβή αφορά στη βελτιστοποίηση και πιστοποίηση με πραγματικά δεδομένα των κριτηρίων επιλογής για την εν λόγω υπογραφή, ενώ ακόμη μελετούνται διεξοδικά οι συνεισφορές υποβάθρου και αναπτύσσονται μέθοδοί για τον υπολογισμό τους από τα πραγματικά δεδομένα. Εν συνεχεία, μελετώνται τα επιπλέον χαρακτηριστικά των υποψήφιων γεγονότων που φωτίζουν τους μηχανισμούς παραγωγής του. Δεδομένου ότι περισσότερα υποψήφια γεγονότα απαιτούνται για να ενταχθεί το *Higgs* σε κάποιο θεωρητικό πρότυπο, η ευαισθησία του καναλιού στα επόμενα χρόνια της λήψης δεδομένων του *LHC* μελετάτε.

Δεδομένης της ύπαρξης τεσσάρων λεπτονίων στην τελική κατάσταση, προϋπόθεση για την επιτυχή έκβαση της συγκεκριμένης έρευνας αποτέλεσε η μεγιστοποίηση της αποδοχής και απόδοσης στην ανακατασκευή και αναγνώριση των ηλεκτρονίων και των μιονίων. Κατά συνέπεια, ένα σημαντικό ερευνητικό μέρος της διατριβής εστιάζεται στην ανίχνευση των λεπτονίων, και συγκεκριμένα των μιονίων στην εμπρόσθια περιοχή του πειράματος *ATLAS*. Συγκεκριμένα, βελτιώθηκε το λογισμό ανακατασκευής, διεξάχθηκαν μελέτες απόδοσης και υπήρξε μεγάλη συνεισφορά στον τομέα λήψης δεδομένων για τη λειτουργία του ανιχνευτή τόσο στο $Run - I$ όσο και από το 2015 και μετέπειτα.

Τα πειραματικά δεδομένα που αναλύθηκαν είναι 4.5 fb^{-1} σε ενέργεια κέντρου μάζας $\sqrt{s} = 7\ TeV$ και 20.3 fb^{-1} σε $\sqrt{s} = 8\ TeV$. Τα δεδομένα αυτά καταγράφηκαν τα έτη 2011 και 2012 αντίστοιχά.

0.1 Θάλαμοι Καθοδικών Λωρίδων (CSC)

Οι θάλαμοι καθοδικών λωρίδων είναι εγκατεστημένοι στην πολύ εμπρόσθια περιοχή του πειράματος $ATLAS$ ($2.0 \leq \eta \leq 2.7$) και συμβάλλουν στην ανίχνευση μιονίων. Η λειτουργία τους βασίζεται στο προσδιορισμό σήματος από τα πολλαπλά καλώδια που απαρτίζουν τους θαλάμους, όπως παρουσιάζει η Εικόνα 1. Υπάρχουν 16 θάλαμοι σε κάθε πλευρά του ανιχνευτή, διαδοχικά μικροί και μεγάλοι σε μέγεθος, που μερικώς αλληλοκαλύπτονται. Η πληροφορία τους διαβάζεται από μια διαδοχή δυο ηλεκτρικών συστημάτων, όπου τα μεν πρώτα προσάπτονται στους θαλάμους με σκοπό να μεταδώσουν τα δεδομένα στα επόμενα ηλεκτρονικά και τα δε δεύτερα είναι απομακρυσμένα από την περιοχή των θαλάμων και αφαιρούν τη μη χρήσιμη πληροφορία από τα δεδομένα. Τα 'απομακρυσμένα' ηλεκτρονικά αντικαταστάθηκαν πριν το $Run-II$ λόγο της περιορισμένης ικανότητας τους να επεξεργαστούν μεγάλο όγκο δεδομένων. Συγκεκριμένα στο $Run-I$, προκειμένου να τρέξει το σύστημα στον όλο και αυξανόμενο ρυθμό σκανδαλισμού χρειάστηκε να μειωθεί ο αριθμός δειγματοληψίας από 4 σε 2 δείγματα και να προσαρμοστούν τα υπόβαθρα δειγματοληψίας.

Σχήμα 1: Αρχή λειτουργίας των Θαλάμων Καθοδικών Λωρίδων (CSC).

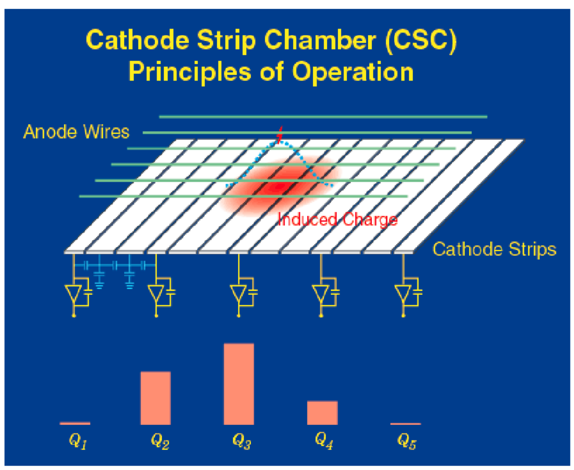

Η αναλυτική ανακατασκευή της πληροφορίας για τον προσδιορισμό τροχιών μιονίων στα CSC βασίζεται στο προσδιορισμό του φορτίου που εναποτέθηκε σε κάθε λωρίδα, στο σχηματισμό συμπλεγμάτων φορτίου και στο συσχετισμό αυτών στις διάφορες λωρίδες. Μια καινούργια μέθοδος αναπτύχθηκε για την βαθμονόμηση του φορτίου και κατέληξε σε βελτιωμένη ποιότητα τροχιάς με χωρική διακριτική ικανότητα που υπολογίζεται στα $78.6 \pm 0.5\ \mu m$.

Η απόδοση της λειτουργίας μελετήθηκε για ολόκληρο το $Run-I$, ξεχωριστά για κάθε περίοδο λήψης δεδομένων με διαφορετικά κριτήρια (Πίνακας 1) και ξεχωριστά για θαλάμους που εμφάνισαν λειτουργικά προβλήματά (Πίνακας 2). Σε κάθε περίπτωση η απόδοση παρέμενε υψηλή.

Πίνακας 1: Πίνακας απόδοσης Θαλάμων Καθοδικών Λωρίδων για κάθε περίοδο λήψης δεδομένων με διαφορετικά κριτήρια.

Επιλογή	Απόδοση (%)			
	4−δείγματα	2−δείγματα	*Wrong Latency*, $\eta > 50,\ \phi > 60$ *ADCcounts*	*Correct Latency*, $\eta > 40,\ \phi > 60$ *ADCcounts*
> 1 η/τροχιά	98.947 ± 0.014	98.956 ± 0.014	~ 94	98.744 ± 0.008
> 1 ϕ/τροχιά	97.746 ± 0.017	97.729 ± 0.020	~ 87	97.699 ± 0.012
> 1 ποιοτικά η/τροχιά	91.77 ± 0.04	91.92 ± 0.04	~ 85	90.870 ± 0.023
Z Tag&Probe	98.915 ± 0.014	98.873 ± 0.016	~ 98	98.764 ± 0.019

Πίνακας 2: Πίνακας απόδοσης Θαλάμων Καθοδικών Λωρίδων για θαλάμους που εμφάνισαν λειτουργικά προβλήματά.

Επιλογή	Απόδοση (%)		
	$C03,\ A05,\ A09$ 1 μη λειτουργικό στρώμα	$C01$ 2 μη λειτουργικά στρώματα	$C05$ Μειωμένη Λειτουργία
> 1 η/τροχιά	98.671 ± 0.025	$85.30 \pm 0.0.14$	89.70 ± 0.04
> 1 ϕ/τροχιά	96.96 ± 0.04	91.67 ± 0.14	97.20 ± 0.06
> 1 ποιοτικά η/τροχιά	89.75 ± 0.08	59.4 ± 0.19	86.40 ± 0.12
Z Tag&Probe	98.52 ± 0.04	97.52 ± 0.04	98.71 ± 0.04

0.2 Μελέτη των Διασπάσεων $H \rightarrow ZZ^{(*)} \rightarrow 4\ell$

Το $H \rightarrow ZZ^{(*)} \rightarrow 4\ell$ είναι η καθαρότερη υπογραφή του μποζονίου *Higgs*. Οι διασπάσεις των υποψήφιων γεγονότων ξεκινά με την επιλογή καλής ποιότητας λεπτονίων πού σκανδάλισαν το καταγεγραμμένο γεγονός. Ειδικότερα, τα λεπτόνια απαιτείται να δημιουργούν ανά δύο ζεύγη ίδιας γεύσης και αντίθετου φορτίου που να πληρούν περιορισμούς ορίων μαζών, να είναι απομονωμένα και να προέρχονται από τον πρωτεύουσα κορυφή του γεγονότος. Οι πιθανές τελικές καταστάσεις είναι $4e,\ 2\mu 2e,\ 2e2\mu,\ 4\mu$.

Το υπόβαθρο καθορίζεται από την διάσπαση του δυνητικού Z μποζονίου και ανάλογα χωρίζεται σε υπόβαθρο ηλεκτρονίων ή μιονίων. Συνολικά στο υπόβαθρο συγκαταλέγονται οι εξής διαδικασίες:

- $ZZ^{(*)}/\gamma \rightarrow 4\ell$: Ονομάζεται και αμείωτο υπόβαθρο γιατί έχει την ίδια τοπολογία με το σήμα.

- Μειώσιμο υπόβαθρο: περιλαμβάνει διαδικασίες $Z+$πίδακες και $t\bar{t}$ και μπορεί να περιοριστεί με κατάλληλη επιλογή κριτηρίων απομόνωσης λεπτονίων ή περιορισμών που αφορούν την καρυφή από την οποία προέρχονται τα λεπτόνια.

Το λεγόμενο μειώσιμο υπόβαθρο υπολογίζεται απευθείας από τα πραγματικά δεδομένα ενώ το αμείωτο εκτιμάται από την προσομοίωση. Η διατριβή εστιάστηκε στη μέτρηση του μειώσιμου υποβάθρου μιονίων με χρήση ταυτόχρονης προσαρμογής σε τέσσερις περιοχές ελέγχου. Αυτές οι περιοχές δημιουργούνται από χαλάρωση ή αντιστροφή κριτηρίων στα μιόνια προερχόμενα από το δυνητικό μποζόνιο Z (το επονομαζόμενο δευτερεύον ζεύγος):

- Περιοχή ελέγχου Zbb: σχηματίζεται αντιστρέφοντας το κριτήριο προέλευσης από τον πρωτεύοντα άξονα στο δευτερεύον ζεύγος
- Περιοχή ελέγχου $Zlight$: σχηματίζεται αντιστρέφοντας το κριτήριο απομόνωσης και επιβάλλοντας το κριτήριο προέλευσης από τον πρωτεύοντα άξονα στο δευτερεύον ζεύγος
- Γενική Περιοχή ελέγχου: σχηματίζεται από δευτερεύον ζεύγος ίδιου φορτίου
- Περιοχή ελέγχου $t\bar{t}$: σχηματίζεται από γεγονότα eμ+μμ.

Η ταυτόχρονη προσαρμογή στη μάζα του πρώτου ζεύγους (παρουσιάζεται στο Σχήμα 2) υπολογίζει ξεχωριστά τις πηγές υποβάθρου Zbb, $Zlight$ και $t\bar{t}$ σε μια άλλη περιοχή ελέγχου που φτιάχνεται από γεγονότα αντίθετου φορτίου στο δευτερεύον ζεύγος αλλά χωρίς επιβολή κριτηρίων απομόνωσης και προέλευσης από τον πρωτεύοντα άξονα. Η περιοχή αυτή δε συγκαταλέγεται άμεσα στην ταυτόχρονη προσαρμογή λόγο του ότι η περιοχή σήματος είναι μέρος αυτής.

Η συνεισφορά των εκτιμώμενων υποβάθρων στην περιοχή σήματος υπολογίζεται λαμβάνοντας υπόψη την πιθανότητα κάθε τύπου υποβάθρου να πληρεί τα κριτήρια απομόνωσης και προέλευσης από τον πρωτεύοντα άξονα, όπως προβλέπεται από την προσομοίωση. Συγκεντρωτικά τα αποτελέσματα για το $Run - I$ παρουσιάζονται στον Πίνακα 3 και οι μάζες δείχνονται στην Εικόνα 3.

0.3 Μελέτη των Μηχανισμών Παραγωγής του Μποζονίου *Higgs*

Μετά την ανακάλυψη του $Higgs$ το ενδιαφέρον στράφηκε στη μελέτη των ιδιοτήτων του, μια εκ των οποίων είναι ο μηχανισμός παραγωγής. Αναπτύχθηκαν και εφαρμόστηκαν μέθοδοι για την εύρεση του μηχανισμού παραγωγής του μποζονίου $Higgs$. Θεωρητικά το $Higgs$ θα μπορούσε να παραχθεί από τις παρακάτω διαδικασίες:

- Αλληλεπίδραση διανυσματικών Μποζονίων (VBF): χαρακτηρίζεται από την ύπαρξη δύο πιδάκων ενέργειας που παράγονται σε αντίθετο ημισφαίριο

Σχήμα 2: Η ταυτόχρονη προσαρμογή στις τέσσερις περιοχές ελέγχου για τον υπολογισμό των Zbb, $Zlight$ και $t\bar{t}$ υποβάθρων. Οι περιοχές ελέγχου σχηματίζονται ως: (α′) αντιστρέφοντας το κριτήριο προέλευσης από τον πρωτεύον άξονα στο δευτερεύον ζεύγος, (β′) αντιστρέφοντας το κριτήριο απομόνωσης και επιβάλλοντας το κριτήριο προέλευσης από τον πρωτεύον άξονα στο δευτερεύον ζεύγος, (γ′) από δευτερεύον ζεύγος ίδιου φορτίου και (δ′) από γεγονότα eμ+μμ.

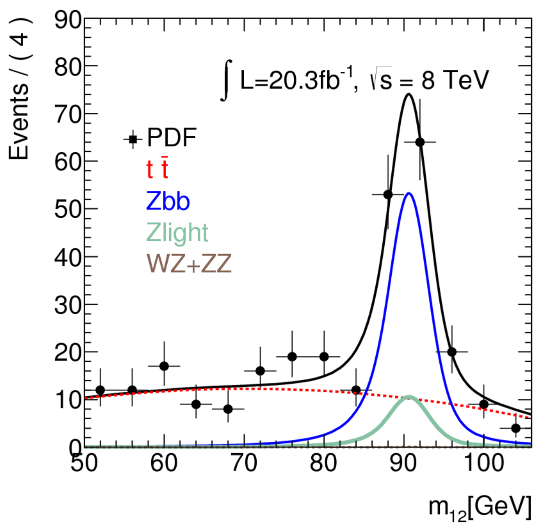

(α′)

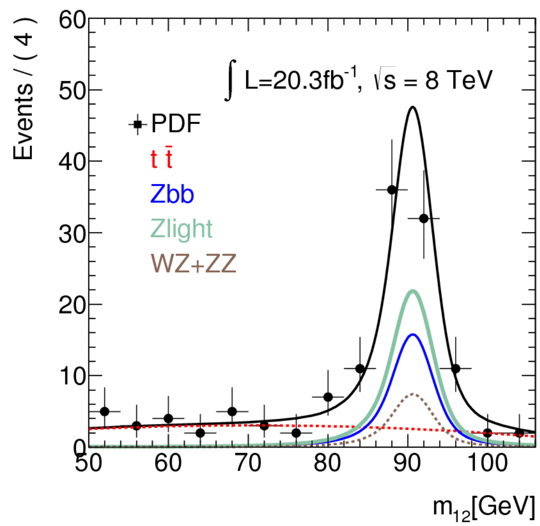

(β′)

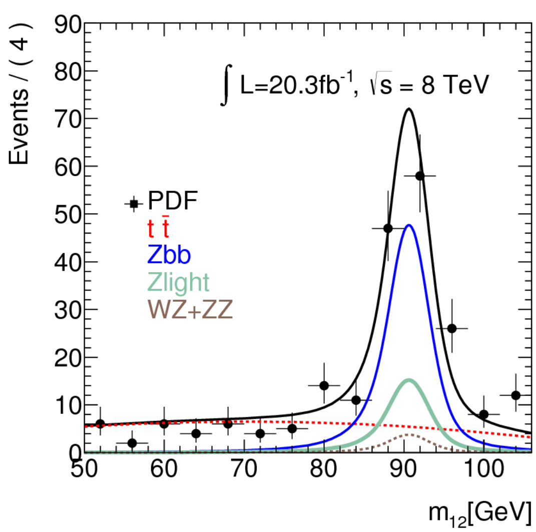

(γ′)

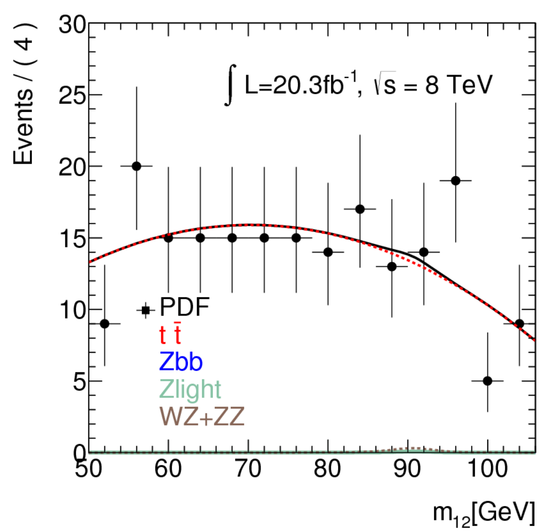

(δ′)

Πίνακας 3: Αποτελέσματα υπολογιζόμενου σήματος και υπόβαθρου για το κανάλι $H \rightarrow ZZ^{(*)} \rightarrow 4\ell$. Οι θεωρητικές προβλέψεις επίσης παρουσιάζονται.

	Σήμα	Σήμα $\sim 125\ GeV$	ZZ	Z+πίδακες, $t\bar{t}$	S/B	Αναμενόμενα	Παρατηρούμενα
			$\sqrt{s} = 7\ TeV$				
4μ	1.00 ± 0.10	0.91 ± 0.09	0.46 ± 0.02	0.10 ± 0.04	1.7	1.47 ± 0.10	2
$2e2\mu$	0.66 ± 0.06	0.58 ± 0.06	0.32 ± 0.02	0.09 ± 0.03	1.5	0.99 ± 0.07	2
$2\mu 2e$	0.50 ± 0.05	0.44 ± 0.04	0.21 ± 0.01	0.36 ± 0.08	0.8	1.01 ± 0.09	1
$4e$	0.46 ± 0.05	0.39 ± 0.04	0.19 ± 0.01	0.40 ± 0.09	0.7	0.98 ± 0.10	1
Σύνολο	2.62 ± 0.26	2.32 ± 0.23	1.17 ± 0.06	0.96 ± 0.18	1.1	4.45 ± 0.30	6
			$\sqrt{s} = 8\ TeV$				
4μ	5.80 ± 0.57	5.28 ± 0.52	2.36 ± 0.12	0.69 ± 0.13	1.7	8.33 ± 0.6	12
$2e2\mu$	3.92 ± 0.39	3.45 ± 0.34	1.67 ± 0.08	0.60 ± 0.10	1.5	5.72 ± 0.37	7
$2\mu 2e$	3.06 ± 0.31	2.71 ± 0.28	1.17 ± 0.07	0.36 ± 0.08	1.8	4.23 ± 0.30	5
$4e$	2.79 ± 0.29	2.38 ± 0.25	1.03 ± 0.07	0.35 ± 0.07	1.7	3.77 ± 0.27	7
Σύνολο	15.6 ± 1.6	13.8 ± 1.4	6.24 ± 0.34	2.00 ± 0.28	1.7	22.1 ± 1.5	31
			$\sqrt{s} = 7\ TeV$ και $\sqrt{s} = 8\ TeV$				
4μ	6.80 ± 0.67	6.20 ± 0.61	2.82 ± 0.14	0.79 ± 0.13	1.7	9.81 ± 0.64	14
$2e2\mu$	4.58 ± 0.45	4.04 ± 0.40	1.99 ± 0.10	0.69 ± 0.11	1.5	6.72 ± 0.42	9
$2\mu 2e$	3.56 ± 0.36	3.15 ± 0.32	1.38 ± 0.08	0.72 ± 0.12	1.5	5.24 ± 0.35	6
$4e$	3.25 ± 0.34	2.77 ± 0.29	1.22 ± 0.08	0.76 ± 0.11	1.4	4.75 ± 0.32	8
Σύνολο	18.2 ± 1.8	16.2 ± 1.6	7.41 ± 0.40	2.95 ± 0.33	1.6	26.5 ± 1.7	37

Σχήμα 3: Μάζες $m_{4\ell}$ για τα υποψήφια $Higgs$ γεγονότα για $\sqrt{s} = 7$ και $8\ TeV$, όπου η θεωρητική πρόβλεψη του σήματος είναι αυξημένη κατά 1.51. Οι μάζες αφορούν τα διάφορα λεπτονικα κανάλια (α′) 4μ, (β′) $2\mu 2e$, (γ′) $2e2\mu$, (δ′) $4e$.

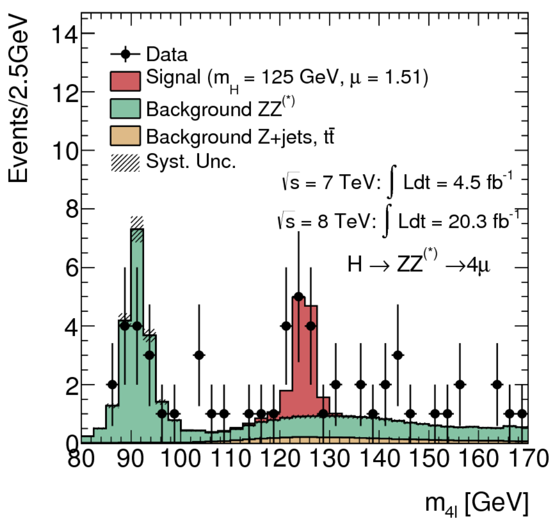

(α′)

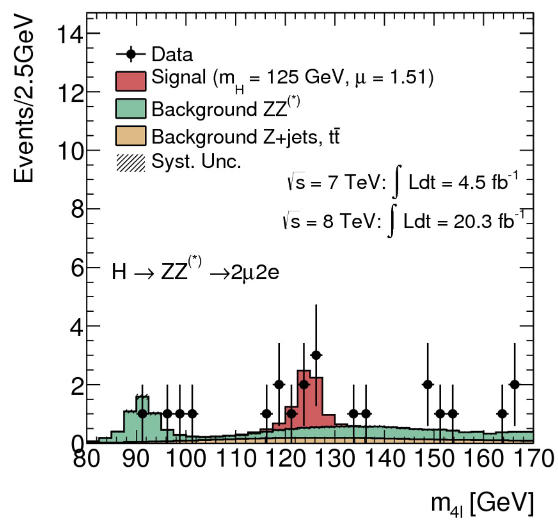

(β′)

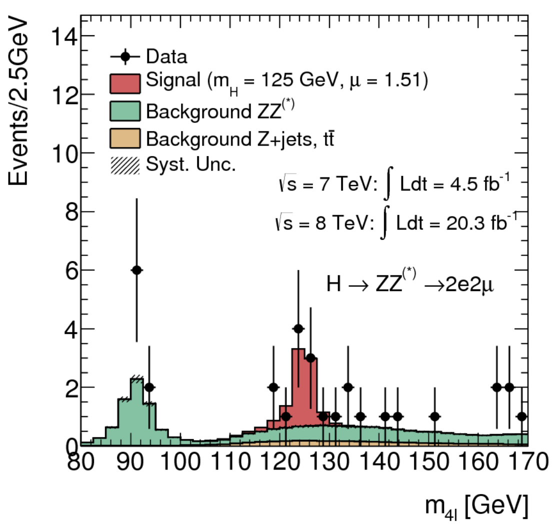

(γ′)

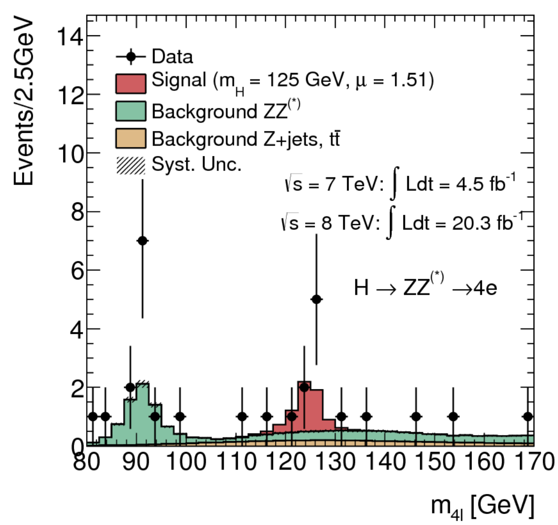

(δ′)

Πίνακας 4: Θεωρητικές ενεργές διατομές των διαφόρων μηχανισμών παραγωγής για $\sqrt{s} = 7\ TeV$ και $\sqrt{s} = 8\ TeV$.

	$\sqrt{s} = 7\ TeV$		$\sqrt{s} = 8\ TeV$	
Παραγωγή	Ενεργός Διατομή $[pb]$	Ποσοστό $[\%]$	Ενεργός Διατομή $[pb]$	Ποσοστό $[\%]$
$gg \to H$	15.1	86.4	19.3	86.4
$qq' \to Hqq'$	1.22	7.0	1.58	7.1
$q\bar{q} \to WH$	0.579	3.3	0.705	3.2
$q\bar{q} \to ZH$	0.335	1.9	0.415	1.9
$q\bar{q}/gg \to t\bar{t}H$	0.086	0.5	0.13	0.6

- Παραγωγή συσχετισμένη με μποζόνια W ή Z (WH, ZH): ανίχνευση μέσω της διάσπασης των W ή Z, που μπορεί να είναι είτε αδρονική είτε λεπτονική. Στη μεν πρώτη ανιχνεύονται πίδακες ενέργειας συμβατοί με τη μάζα των W ή Z, ενώ στη δε δεύτερη λεπτόνια συμβατά με διασπάσεις W ή Z.

- Παραγωγή συσχετισμένη με ζεύγη $t\bar{t}$ ή $b\bar{b}$ (ttH, bbH): ανιχνεύονται μέσω των ζευγών $t\bar{t}$ ή $b\bar{b}$

- Αλληλεπίδραση γλυονίων (ggH): όταν καμία από τις παραπάνω παραγωγές δεν ανιχνεύεται.

Λόγω της χαμηλής ενεργού διατομής, όπως φαίνεται από τον Πίνακα 4, για το $Run-I$ οι παραγωγές συσχετισμένες με ζεύγη $t\bar{t}$ ή $b\bar{b}$ δε λαμβάνονται υπόψη στην κατάταξη των υποψήφιων $Higgs$ γεγονότων.

Η κατηγοριοποίηση των γεγονότων ξεκινά με την περίπτωση αλληλεπίδρασης διανυσματικών μποζονίων, όπου πίδακες αναλλοίωτης μάζας μεγαλύτερης των 130 GeV διαχωρίζονται με μέθοδο ανάλυσης πολλών μεταβλητών. Αυτές οι μεταβλητές είναι η μάζα των πιδάκων ενέργειας, ο διαχωρισμός τους σε επίπεδο ψευδοωκύτητας, οι εγκάρσιες ορμές και των δύο και η ψευδοωκύτητα του πίδακα με τη μεγαλύτερη ορμή.

Αν το γεγονός δεν είναι συμβατό με αλληλεπίδραση διανυσματικών μποζονίων, τότε μελετάτε η πιθανότητα να προέρχεται από παραγωγή συσχετισμένη με μποζόνια W ή Z που διασπώνται αδρονικά. Σε αυτή την περίπτωση οι πίδακες ενέργειας απαιτείται να έχουν μάζα μικρότερη από 130 GeV ώστε να είναι συμβατοί με τις μάζες των W ή Z. Εν συνεχεία, μια μέθοδος ανάλυσης πολλών μεταβλητών, με τις ίδιες μεταβλητές όπως στην προηγούμενη κατηγορία, εφαρμόζεται.

Αν το γεγονός δεν πέρασε καμία από τις παραπάνω κατηγοριοποιήσεις τότε ερευνάται η πιθανότητα να προέρχεται από παραγωγή συσχετισμένη με μποζόνια W ή Z που διασπώνται λεπτονικά. Το γεγονός πρέπει να έχει τουλάχιστον ένα επιπλέον λεπτόνιο των τεσσάρων

Πίνακας 5: Αποτελέσματα της μελέτης των μηχανισμών παραγωγής.

	Σήμα				Υπόβαθρο		Συνολικά	Παρατηρούμενα
Κατηγορία	$ggF + b\bar{b}H + t\bar{t}H$	VBF	$VH-$αδρονική	$VH-$λεπτονική	$ZZ^{(*)}$	$Z+$πίδακες, $t\bar{t}$	Αναμενόμενα	Γεγονότα
$120 < \mathbf{m_{4\ell}} < 130$ GeV								
VBF	1.18 ± 0.37	0.75 ± 0.04	0.083 ± 0.006	0.013 ± 0.001	0.17 ± 0.03	0.25 ± 0.14	2.4 ± 0.4	3
$VH-$***αδρονική***	0.40 ± 0.12	0.034 ± 0.004	0.20 ± 0.01	0.009 ± 0.001	0.09 ± 0.01	0.09 ± 0.04	0.80 ± 0.12	0
$VH-$***λεπτονική***	0.013 ± 0.002	< 0.001	< 0.001	0.069 ± 0.004	0.015 ± 0.002	0.016 ± 0.019	0.11 ± 0.02	0
ggF	12.8 ± 1.3	0.57 ± 0.02	0.24 ± 0.01	0.11 ± 0.01	7.1 ± 0.2	2.7 ± 0.4	23.5 ± 1.4	34
$110 < \mathbf{m_{4\ell}}$ GeV								
VBF	1.4 ± 0.4	0.82 ± 0.05	0.092 ± 0.007	0.022 ± 0.002	$20. \pm 4.$	1.6 ± 0.9	$24. \pm 4.$	32
$VH-$***αδρονική***	0.46 ± 0.14	0.038 ± 0.004	0.23 ± 0.01	0.015 ± 0.001	9.0 ± 1.2	0.6 ± 0.2	10.3 ± 1.2	13
$VH-$***λεπτονική***	0.026 ± 0.004	< 0.002	< 0.002	0.15 ± 0.01	0.63 ± 0.04	0.11 ± 0.14	0.92 ± 0.16	1
ggF	14.1 ± 1.5	0.63 ± 0.02	0.27 ± 0.01	0.17 ± 0.01	$351. \pm 12.$	16.6 ± 2.2	$383. \pm 12.$	420

λεπτονίων που πληρεί τις προϋποθέσεις απομόνωσης και προέλευσης από τον πρωτεύον άξονα.

Σε περίπτωση που δεν πληρείται καμία από τις παραπάνω προϋποθέσεις το γεγονός θεωρείται ότι είναι προϊόν αλληλεπίδρασης γλυονίων.

Από την ανάλυση των δεδομένων του $Run - I$ 3 υποψήφια γεγονότα βρέθηκαν για παραγωγή μέσο αλληλεπίδρασης διανυσματικών μποζονίων και η θεωρητική πρόβλεψη είναι 2.4. Όλα τα υπόλοιπα γεγονότα ανήκουν στη παραγωγή μέσω αλληλεπίδρασης γλουονίων, ενώ καμία από τις υπόλοιπες κατηγορίες δεν παρατηρήθηκε. Συνοπτικά τα αποτελέσματα παρουσιάζονται στον Πίνακα 5.

0.4 Πρόβλεψη Μελλοντικής Ευαισθησίας του $H \to ZZ^{(*)} \to 4\ell$

Λόγω της μικρής παραγωγής γεγονότων με μποζόνια $Higgs$ στην τελική κατάσταση απαιτείται η συλλογή μεγάλου όγκου δεδομένων ώστε να κατανοηθεί πλήρως η φύση του σωματιδίου, συμπεριλαμβανομένων των μηχανισμών παραγωγής. Επομένως, ενδιαφέρον παρουσιάζει η μελέτη της ευαισθησίας του καναλιού στο μελλοντικό πρόγραμμα του LHC. Συγκεκριμένα θεωρείται ότι λήψη δεδομένων θα πραγματοποιηθεί σε $\sqrt{s} = 14\ TeV$ και συνολικά θα συγκεντρωθούν $3000\ fb^{-1}$ δεδομένων.

Η κατηγοριοποίηση ξεκινά από του μηχανισμούς με χαμηλότερη ενεργό διατομή ώστε να αυξηθεί η ευαισθησία τους. Δηλαδή, η σειρά που ακολουθείται είναι ttH, ZH, WH, VBF και ggF αν δεν ανήκει σε καμία από τις προηγούμενες διαδικασίες. Σε αυτή την περίπτωση η πιθανότητα παραγωγής συσχετισμένη με ttH δεν είναι αμελητέα και δεν μπορεί να αγνοηθεί. Η επιλογή γίνεται μέσω κριτηρίων που αποσκοπούν στην ανάδειξη του εκάστοτε μηχανισμού αποφεύγοντας επικάλυψη με άλλους μηχανισμούς.

Τα αποτελέσματα της μελέτης που βασίστηκε σε προσομοίωση συνοψίζονται στον Πίνακα 6. Είναι εμφανές ότι η ανίχνευση του μηχανισμού θα μπορέσει να καθοριστεί με αυτό τον όγκο δεδομένων.

Πίνακας 6: Πρόβλεψη των γεγονότων από τους πιθανούς μηχανισμούς παραγωγής υποθέτοντας μάζα $Higgs$ $m_H = 125\ GeV$ και $3000\ fb^{-1}$ δεδομένων.

Κατηγορία	ggF	VBF	WH	ZH	ttH	Υπόβαθρο
ttH	3.1 $\pm$1.0	0.6 $\pm$0.1	0.6 $\pm$0.1	1.1 $\pm$0.2	30 $\pm$6	0.6 $\pm$0.2
ZH	0.0	0.0	0.01 $\pm$0.02	4.4 $\pm$0.3	1.3 $\pm$0.3	0.06 $\pm$0.06
WH	22 $\pm$7	6.6 $\pm$0.4	25 $\pm$2	4.4 $\pm$0.3	8.8 $\pm$1.8	13 $\pm$0.8
VBF	41 $\pm$14	54 $\pm$6	0.7 $\pm$0.1	0.4 $\pm$0.1	1.0 $\pm$0.2	4.2 $\pm$1.5
ggF	3380 $\pm$650	274 $\pm$17	77 $\pm$5	53 $\pm$3	25 $\pm$4	2110 $\pm$ 50

Επιπλέον με τα παραπάνω μελετήθηκε η περίπτωση αύξησης της κάλυψης μιονικών θαλάμων, εσωτερικού ανιχνευτή και μαγνητών, ώστε τα μιόνια να μπορούν να ανιχνευτούν μέχρι την περιοχή ψευδοωκύτητας $\eta \leq 4.0$. Το σενάριο αυτό δεν περιλαμβάνει καμία αλλαγή στην ανίχνευση ηλεκτρονίων και επομένως επηρεάζει κυρίως το 4μ κανάλι. Τα πιθανά οφέλη παρουσιάζονται στον Πίνακα 7. Είναι εμφανές ότι θα βελτιωθεί σημαντικά η ακρίβεια μέτρησης των ρυθμών παραγωγής του μποζονίου $Higgs$ με τους υπο μελέτη μηχανισμούς, σε αυτό το σενάριο, αλλά η μελέτη των ιδιοτήτων του $Higgs$ δεν επωφελείται σημαντικά λόγω της μεγάλης αύξησης του υποβάθρου.

Πίνακας 7: Πρόβλεψη των 4μ γεγονότων από τους πιθανούς μηχανισμούς παραγωγής υποθέτοντας μάζα $Higgs$ $m_H = 125\ GeV$, $3000\ fb^{-1}$ δεδομένων και επέκταση την περιοχής ανίχνευσης μιονίων.

	Προσομοιομένα Σήματα					
	ggF	VBF	WH	ZH	ttH	Υπόβαθρο
$\eta < 2.7$	3439	335	104	64	66	2126
$\eta < 4.0$	3765	361	116	72	68	2493
Σταθμισμένο Όφελος	9.49%	7.88%	11.92%	11.88%	3.81%	17.30%
Πραγματικό Όφελος	12.04%	9.85%	15.97%	15.46%	4.31%	26.86%

1

Theory Introduction

1.1 Introduction

The Standard Model, the theory attempting to describe the particle physics, is briefly introduced in this chapter, mainly focused on the Higgs mechanism. Starting from the electroweak theory, the spontaneous symmetry breaking mechanism and the Goldstone bosons are explained. After the short theoretical introduction, the production phenomenology of the Higgs boson at hadron colliders and the sensitivity of observing it are explored. Both theoretical and experimental constraints on the Higgs boson mass are also presented.

The theory decomposes the complexity of the elementary particles of the ordinary matter and the interactions taking place between them to two group of particles, the quarks and the leptons, and a set of four force carriers [1], schematically shown in Figure 1.1.

Leptons are spin-$\frac{1}{2}$ particles which do not take part in the strong interactions. They compose three generations formed by the integer charged lepton and the relevant neutrino [2]. Besides the charge, leptons have also different masses. Individually, they are denoted as $\mathrm{e}, \mu, \tau, \nu_\mathrm{e}, \nu_\mu, \nu_\tau$ or collectively by ℓ [3]. Their basic properties are summarized in table 1.1.

The quarks (q) are fractionally charged spin-$\frac{1}{2}$ strongly interacting particles which are known to form the composites collectively called hadrons. Two categories of hadrons are known, the mesons and the baryons. Mesons are made up from a quark and an

Figure 1.1: Schematic view of the building blocks of the ordinary matter, the quarks and the leptons, along with the force carriers [1].

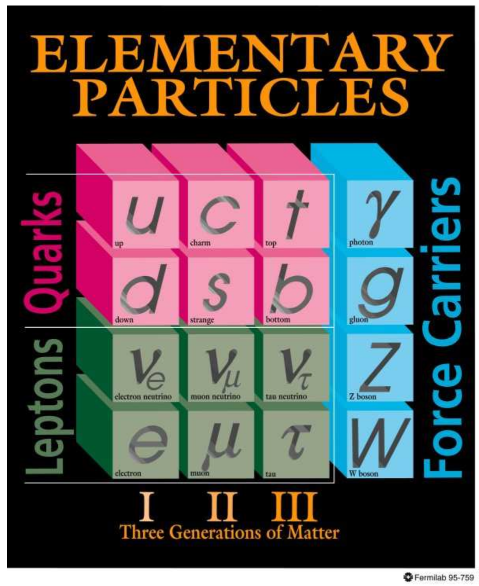

Table 1.1: Summary of the lepton types along with their basic properties, charge, mass and mean life time [2].

Lepton	Charge	Mass	Mean Life
e	-1	$0.510998928 \pm 0.000000011$ MeV	$> 4.6 \times 10^{26}$ years
μ	-1	$105.6583715 \pm 0.0000035$ MeV	$(2.1969811 \pm 0.0000022) \times 10^{-6} s$
τ	-1	1776.82 ± 0.16 MeV	$(290.6 \pm 1.0) \times 10^{15} s$
ν_e	0	< 225 eV (95% CL)	$> 15.4\times$mass s (90% CL)
ν_μ	0	< 0.19 MeV (90% CL)	$> 15.4\times$mass s (90% CL)
ν_τ	0	< 18.2 MeV (95% CL)	$> 15.4\times$mass s (90% CL)

Table 1.2: Quark quantum numbers: charge Q, baryon number B, strangeness S, charm c, bottomness b, and topness t [4].

name	symbol	Q	B	S	c	b	t
up	u	$\frac{2}{3}$	$\frac{1}{3}$	0	0	0	0
down	d	$-\frac{1}{3}$	$\frac{1}{3}$	0	0	0	0
strange	s	$-\frac{1}{3}$	$\frac{1}{3}$	-1	0	0	0
charm	c	$\frac{2}{3}$	$\frac{1}{3}$	0	1	0	0
bottom	b	$-\frac{1}{3}$	$\frac{1}{3}$	0	0	-1	0
top	t	$-\frac{1}{3}$	$\frac{1}{3}$	0	0	0	1

antiquark ($q\bar{q}$), consequently have integer spin, and are described by the Bose Statistics. Baryons are a combination of three quarks (qqq), have half-integer spin and obey the Fermi statistics. There are six different types of quarks, known as flavors: up (u), down (d), strange (s), charm (c), bottom (b), and top (t); their properties are given in Table 1.2. The antiquarks have opposite signs of electric charge, baryon number, strangeness, charm, bottomness, and topness. The quarks carry "color" which enables them to interact strongly with one another [4]. Each quark flavor can have three colors usually designated red, green and blue and the antiquarks are colored antired, antigreen and antiblue respectively. The composites the quarks create, are made up of three quarks one of each color (baryons) or consist of a quark-antiquark pair of a particular color and its anticolor (mesons). Both baryons and mesons are thus colorless or white. Because the color is different for each quark, it serves to distinguish them and allows the exclusion principle to hold.

Quarks and leptons are called fermions and interact via the four known basic forces – gravitational, electromagnetic, strong, and weak – that can be characterized on the basis of the following four criteria [4]: the types of particles that experience the force, the relative strength of the force, the range over which the force is effective, and the nature of the particles that mediate the force. The force carriers are the gauge bosons: the electromagnetic force is carried by the spin–1 photon, the strong force is mediated with the eight massles spin–1 gluons, the $W^{\pm}$ and Z^0 spin–1 bosons transmit the weak force, while no gravitational mediator has been observed yet. A comparison of the approximate relative force strengths is given in Table 1.3. Gravity, on a nuclear scale, is the weakest of the four forces and its effect at the particle level can nearly always be ignored [4].

The electromagnetic and the weak interactions are unified after identifying them as two different manifestations of a more fundamental (single) interaction, the electroweak interaction. The so called "Glashow–Weinberg–Salam electroweak theory" [5, 6, 7] has had many notable successes [8], culminating in the discovery of the predicted $W^{\pm}$ and Z^0

Table 1.3: Relative strength of the four forces for two protons inside a nucleus [4].

Type	Relative Strength	Field Particle
Strong	1	gluons (g)
Electromagnetic	10^{-2}	photon (γ)
Weak	10^{-6}	$W^{\pm}$, Z^0 bosons
Gravitational	10^{-38}	graviton

bosons ($m_W = (80.385 \pm 0.015)$ GeV and $m_Z = (91.1876 \pm 0.0021)$ GeV) [2]. However, the favored electroweak symmetry breaking mechanism indicated broken symmetries and generated questions about the nature of the symmetry breaking.

1.2 The Standard Model Theory

The Standard Model is the theory that provides a unified framework to describe the electromagnetic, weak and strong interactions between quarks and leptons [9, 10]. These interactions are understood as due to the exchange of spin–1 bosons between the spin–$\frac{1}{2}$ particles that make up matter [3]. In the Standard Model, the electroweak theory, which is a Yang–Mills theory based on the symmetry group $\mathrm{SU(2)_L} \times \mathrm{U(1)_Y}$ [3, 10], is combined with the strong interactions, an $\mathrm{SU(3)_C}$ group based on a QCD gauge theory [10].

The $\mathrm{SU(3)_C}$ symmetry [11] is associated with the eight gluons ($8\mathrm{G}^{\alpha}_{\mu\nu}$), the $\mathrm{SU(2)_L}$ is associated with the $\mathrm{W}^{\pm}$ and Z^0 bosons ($3\mathrm{W}^{\alpha}_{\mu\nu}$) and the factor $\mathrm{U(1)_Y}$ with the photon ($\mathrm{B}_{\mu\nu}$) [3]. The conserved quantities, indicated as subscripts in the $\mathrm{SU(2)_L} \times \mathrm{U(1)_Y} \times \mathrm{SU(3)_C}$ symmetry, are the isospin, hypercharge and color respectively. The model, before introducing the electroweak symmetry breaking mechanism, has two kinds of fields:

- The matter fields for the three generations of left–handed and right–handed chiral quarks and leptons [10, 8].

- The gauge fields corresponding to the spin–1 bosons that mediate the interactions

In the next sections the theoretical prerequisites and framework are briefly developed in several steps. It has to be noted that the Gravity is not included in the SM theory.

1.2.1 Motion of Scalar and Pseudoscalar Fields

From the classical mechanics, it is known that the dynamics of a system can be summarized by the Lagrangian:

$$\mathcal{L} = \frac{1}{2}\partial_\mu\phi\partial^\mu\phi - \frac{1}{2}m^2\phi^2 \tag{1.1}$$

and the relevant motion is described by the Euler-Lagrange equation:

$$\partial_\mu(\partial_{\partial_\mu\phi}\mathcal{L}) - \partial_\phi\mathcal{L} = 0. \tag{1.2}$$

By substituting the Lagrangian 1.1 into the Euler-Lagrange equation 1.2:

$$\partial_\mu\partial^\mu\phi + m^2\phi \equiv (\Box^2 + m^2)\phi = 0 \tag{1.3}$$

the result is the so called Klein-Gordon equation which describes the motion of scalar and Pseudoscalar fields.

1.2.2 Relativistic Wave Equation

The Hamiltonian of a system has the general form of:

$$H\psi = (\alpha \cdot \mathbf{P} + \beta m)\psi \tag{1.4}$$

where the α and β are determined by energy and momentum relations that a free particle must fulfill.

By multiplying the equation 1.4 by H, it transforms to:

$$\begin{aligned} H^2\psi &= (\alpha_i P_i + \beta m)(\alpha_j P_j + \beta m)\psi \\ &= (\alpha_i^2 P_i^2 + (\alpha_i\alpha_j + \alpha_j\alpha_i)P_iP_j + (\alpha_i\beta + \beta\alpha_i)P_i m + \beta^2 m^2)\psi. \end{aligned} \tag{1.5}$$

Taking into account that α and β all anti-commute with each other and $\alpha_1^2 = \alpha_2^2 = \alpha_3^2 = \beta^2 = 1$ [8], equation 1.5 transforms to:

$$H^2\psi = (\mathbf{P}^2 + m^2)\psi. \tag{1.6}$$

The lowest dimensionality matrices satisfying the above requirements are the 4×4 Dirac-Pauli matrices [8]:

$$\alpha = \begin{pmatrix} 0 & \boldsymbol{\sigma} \\ \boldsymbol{\sigma} & 0 \end{pmatrix} \quad \text{and} \quad \beta = \begin{pmatrix} \mathrm{I} & 0 \\ 0 & \mathrm{I} \end{pmatrix} \tag{1.7}$$

where the I matrix denotes the unit 2×2 matrix and $\boldsymbol{\sigma}$ the Pauli matrices:

$$\sigma_1 = \begin{pmatrix} 0 & 1 \\ 1 & 0 \end{pmatrix},\ \sigma_2 = \begin{pmatrix} 0 & \text{-i} \\ \text{i} & 0 \end{pmatrix},\ \sigma_3 = \begin{pmatrix} 1 & 0 \\ 0 & \text{-1} \end{pmatrix}. \tag{1.8}$$

By replacing terms in equation 1.4 and multiplying by β, the equation transforms to the covariant form of the Dirac's equation:

$$\begin{aligned} i\,\beta\,\partial_t\psi = -i\,\beta\,\boldsymbol{\alpha}\,.\,\vec{\nabla}\,\psi + m\psi \Leftrightarrow \\ \Leftrightarrow (i\gamma^\mu\partial_\mu - m)\,\psi = 0. \end{aligned} \tag{1.9}$$

In the above equation the Dirac γ-matrices have been introduced ($\gamma^\mu \equiv (\beta, \beta\boldsymbol{\alpha})$).

The Dirac's Lagrangian should be reproduced by the Euler-Lagrange equation 1.2 for independent fields such as the ψ and $\bar{\psi}$. A Lagrangian describing the behavior of spin-$\frac{1}{2}$ relativistic particle of mass m can be written as [4]:

$$\mathcal{L}_{\text{Dirac}} = \bar{\psi}(i\gamma^\mu\partial_\mu - m)\psi. \tag{1.10}$$

1.2.3 Symmetries

The symmetries in physical systems are described by Noether's theorem [12] and are associated with conserved quantities equal in number with the number of symmetries. For example, the invariance under rotations is related to the angular momentum conservation. Mathematically, a conserved quantity, also called current, follows the equation:

$$\partial_\mu J^\mu = 0. \tag{1.11}$$

The existence of a current implies that there must be a "charge" which acts as the generator of the symmetry group.

The interpretation of Noether's theorem in the particle physics case relates the gluons ($8\mathrm{G}^\alpha_{\mu\nu}$), the $\mathrm{W}^\pm$ and Z^0 bosons and the photon (γ) to the fundamental interactions described by the symmetry groups of $\mathrm{SU(3)_C}$, $\mathrm{SU(2)_L}$, and $\mathrm{U(1)_Y}$ respectively.

The unitary Abelian group U(1) is the simplest example of a local symmetry. The term local or internal stands for space-time invariant symmetries and it describes transformations such as the ensemble of wave function phase

$$\Psi \rightarrow e^{i\alpha}\Psi \tag{1.12}$$

$$\bar{\Psi} \rightarrow e^{-i\alpha}\bar{\Psi} \tag{1.13}$$

where α can run continuously over real numbers.

To find the conserved current, the invariance of the Lagrangian $\mathcal{L}$ under the infinitesimal $U(1)$ transformations $\Psi \rightarrow (1+i\alpha)\Psi$ needs to be studied [4]:

$$\begin{aligned}
\delta\mathcal{L} &= \partial_{\psi}\mathcal{L}\ \delta\psi + \partial_{\partial_\mu\psi}\mathcal{L}\ \delta(\partial_\mu\psi) + \delta\bar{\psi}\ \partial_{\bar{\psi}}\mathcal{L} + \delta(\partial_\mu\bar{\psi})\ \partial_{\partial_\mu\bar{\psi}}\mathcal{L} \\
&= \partial_{\psi}\mathcal{L}\ (i\alpha\psi) + \partial_{\partial_\mu\psi}\mathcal{L}\ (i\alpha\partial_\mu\psi) + \ldots \\
&= i\alpha\left[\partial_{\psi}\mathcal{L} - \partial_\mu(\partial_{\partial_\mu\psi}\mathcal{L})\right]\psi + i\alpha\partial_\mu(\partial_{\partial_\mu\psi}\mathcal{L}\ \psi) + \ldots \\
&= 0. \qquad (1.14)
\end{aligned}$$

The term in the square brackets corresponds to the Euler-Lagrange equation and vanishes and the equation 1.14 reduced to the form of:

$$\partial_\mu\left[-\frac{i}{2}\left(\partial_{\partial_\mu\psi}\mathcal{L}\ \psi - \bar{\psi}\ \partial_{\partial_\mu\bar{\psi}}\mathcal{L}\right)\right] = 0. \qquad (1.15)$$

The Lagrangian of a relativistic particle with spin-$\frac{1}{2}$ can be described by Dirac's Lagrangian 1.10 and thus, by replacing in the equation 1.15:

$$\partial_\mu\left[\bar{\psi}\gamma^\mu\psi\ \right] = 0. \qquad (1.16)$$

It follows that the charge $Q \equiv \int d^3xJ^0$ must be a conserved quantity.

1.2.4 Quantum Electrodynamics (QED)

A generalization of the previous section phase transformation 1.12 that includes also the local phase transformations is [4]:

$$\psi \rightarrow \psi' \equiv e^{i\alpha(x)}\ \psi. \qquad (1.17)$$

Possible ψ replacement in the Dirac's Lagrangian will break the invariance due to the derivative of $\partial_\mu\alpha(x)$, with an additional phase change that corresponds to:

$$\delta\mathcal{L}_{\rm Dirac} = \bar{\psi}i\gamma^\mu\left[i\partial_\mu\alpha(x)\right]\psi. \qquad (1.18)$$

The invariance can be restored only if a modified derivative is inserted $\partial_\mu \rightarrow D_\mu \equiv \partial_\mu + ieA_\mu$ and $D_\mu\psi \rightarrow e^{i\alpha(x)}D_\mu\psi$, then:

$$\begin{aligned}
\mathcal{L}_{Dirac} &= \bar{\psi}(i\not{D} - m)\psi \\
&= \bar{\psi}(i\not{D} - m)\psi - e\bar{\psi}\not{A}(x)\psi. \qquad (1.19)
\end{aligned}$$

The Lagrangian under the transformations, given that $\psi \rightarrow \psi'$ and $A \rightarrow A'$, is:

$$\begin{aligned}
\mathcal{L}'_{Dirac} &= \bar{\psi}'(i\not{\partial} - m)\psi' - e\bar{\psi}'\not{A}'\psi' \\
&= \bar{\psi}(i\not{\partial} - m)\psi - \bar{\psi}[\not{\partial}\alpha(x)]\psi - e\ \bar{\psi}\not{A}'\psi. \qquad (1.20)
\end{aligned}$$

The condition $\mathcal{L} = \mathcal{L}'$ is achieved $A(x)$ is a vector potential:

$$A'_\mu(x) = A_\mu(x) - \frac{1}{e}\partial_\mu \alpha(x)\,. \tag{1.21}$$

In other words a gauge field introduced A_μ, which does not change the electromagnetic field strength $F_{\mu\nu}$, that couples to fermions of charge e in exactly the same way as the photon field [4].

The complete Lagrangian that describes the QED should also contain the kinematic term (known from the Maxwell equations):

$$\mathcal{L} = -\frac{1}{4}F_{\mu\nu}F^{\mu\nu} + \bar{\psi}(i\partial\!\!\!/ - m)\psi - e\bar{\psi}A\!\!\!/\psi\,. \tag{1.22}$$

Local phase changes described by the equation 1.17 forms an Abelian $U(1)$ group of transformations and consequently the QED is an Abelian gauge theory [11].

1.2.5 Gauge Fields Lagrangian

A field composed of two complex scalar fields $\Phi_A = \phi_1 + i\phi_2$ and $\Phi_B = \phi_3 + i\phi_4$ can be expressed as [13]:

$$\Phi = \begin{pmatrix} \Phi_A \\ \Phi_B \end{pmatrix}. \tag{1.23}$$

If the Lagrangian density of this field, which is a set of four real fields, is required to be invariant under the a $U(1) \times SU(2)$ transformation, this would be:

$$\Phi \rightarrow \Phi' = e^{-i\theta}\mathbf{U}\Phi \tag{1.24}$$

where $e^{-i\theta}$ is an element of the group $U(1)$ as seen in section 1.2.4 and $\mathbf{U}$ is an element of the group $SU(2)$, so that $\mathbf{U}\mathbf{U}^\dagger = \mathbf{U}^\dagger\mathbf{U} = 1$.

The simplest Lagrangian that could obey such symmetry is :

$$\mathcal{L} = \partial_\mu \Phi^\dagger \partial^\mu \Phi - m^2 \Phi^\dagger \Phi \tag{1.25}$$

where the terms

$$\begin{aligned} \Phi^\dagger\Phi &= \Phi_A^*\Phi_A + \Phi_B^*\Phi_B = \phi_1^2 + \phi_2^2 + \phi_3^2 + \phi_4^2 \\ \partial_\mu\Phi^\dagger\partial^\mu\Phi &= \partial_\mu\phi_1\partial^\mu\phi_1 + \partial_\mu\phi_2\partial^\mu\phi_2 + \partial_\mu\phi_3\partial^\mu\phi_3 + \partial_\mu\phi_4\partial^\mu\phi_4 \end{aligned} \tag{1.26}$$

and the fields describes a set of four independent fields with the same mass m.

The fields must be invariant under the $U(1)$ transformation which can be written as:

$$\Phi \to \Phi' = e^{-i\theta}\Phi = e^{-i\theta I}\Phi \tag{1.27}$$

where I is the unit matrix $\begin{pmatrix} 1 & 0 \\ 0 & 1 \end{pmatrix}$. In order for this symmetry to become a local symmetry we must introduce a vector field $B_\mu(x)I$, with the transformation law:

$$B_\mu(x) \to B'_\mu(x) = B_\mu(x) + (2/g_i)\partial_\mu\theta \tag{1.28}$$

and make the replacement:

$$i\partial_\mu \to i\partial_\mu - (g_i/2)B_\mu \tag{1.29}$$

where g_i is a dimensionless parameter of the theory and the factor 2 follows convention.

An element of $SU(2)$ can be written in the form of:

$$\mathbf{U} = e^{i\alpha^k\sigma^k} \tag{1.30}$$

where α^k are three real numbers and σ^k are the Pauli matrices 1.7, generators of the $SU(2)$ group. A global $SU(2)$ symmetry can be made into a local $SU(2)$ symmetry by making the group element dependent on space and time coordinates $\mathbf{U} = \mathbf{U}(x)$ and introducing a vector gauge field:

$$\mathbf{W}_\mu(x) = W^k_\mu(x)\sigma^k$$

$$\mathbf{W}_\mu(x) \to \mathbf{W}'_\mu(x) = \mathbf{U}(x)\mathbf{W}_\mu(x)\mathbf{U}^\dagger(x) + (2i/g_2)(\partial_\mu\mathbf{U}(x))\mathbf{U}^\dagger(x) \tag{1.31}$$

which is a generalization of equation 1.28.

By defining:

$$D_\mu\Phi = \left[\partial_\mu + (ig_1/2)B_\mu + (ig_2/2)\mathbf{W}_\mu\right]\Phi \tag{1.32}$$

and thus given equation 1.27:

$$D'_\mu\Phi' = \left[\partial_\mu + (ig_1/2)B'_\mu + (ig_2/2)\mathbf{W}'_\mu\right]\Phi' = e^{-i\theta}\mathbf{U}D_\mu\Phi \tag{1.33}$$

the Lagrangian 1.25 can be written as:

$$\mathcal{L} = (D_\mu\Phi)^\dagger D_\mu\Phi - V\Phi^\dagger\Phi. \tag{1.34}$$

The field strength tensors can be expressed as:

$$B_{\mu\nu} = \partial_\mu B_\nu - \partial_\nu B_\mu$$

$$\mathbf{W}_{\mu\nu} = \left[\partial_\mu + (ig_2/2)\mathbf{W}_\mu\right]\mathbf{W}_\nu - \left[\partial_\nu + (ig_2/2)\mathbf{W}_\nu\right]\mathbf{W}_\mu \tag{1.35}$$

and the total contribution to the Lagrangian density associated with these gauge fields is:

$$\mathcal{L} = -\frac{1}{4}B_{\mu\nu}B^{\mu\nu} - \frac{1}{8}Tr\left(\mathbf{W}_{\mu\nu}\mathbf{W}^{\mu\nu}\right). \tag{1.36}$$

1.2.6 The Strong Interactions Lagrangian

Similarly to the electromagnetic and weak interactions, the strong interactions can be described by a gauge theory known as Quantum Chromodynamics (QCD) [13]. Each quark can be described by three fields named after the colors red, green, blue that quarks carry and associated to the triplet:

$$\mathbf{u} = \begin{pmatrix} u_r \\ u_g \\ u_b \end{pmatrix} \tag{1.37}$$

where u_r, u_g, u_b are the Dirac spinors. The theory is invariant under a local $SU(3)$ transformation of the form $\mathbf{q} \to \mathbf{q}' = \mathbf{U}\mathbf{q}$, where $\mathbf{q}$ is any quark triplet and $\mathbf{U}$ is any space and time element of the $SU(3)$ group. A 3×3 matrix gauge field G_μ is introduced (as an analogue of the matrix field $\mathbf{W}_\mu$ of the electroweak theory):

$$\mathbf{G}_\mu \to \mathbf{G}'_\mu = \mathbf{U}\mathbf{G}_\mu\mathbf{U}^\dagger + \frac{i}{g}(\partial_\mu\mathbf{U})\mathbf{U}^\dagger. \tag{1.38}$$

Where $(\partial_\mu + ig\mathbf{G}_\mu)\mathbf{q} \equiv D_\mu\mathbf{q}$ and under a local $SU(3)$ transformation:

$$D'_\mu\mathbf{q}' = (\partial_\mu + ig\mathbf{G}'_\mu)\mathbf{q}' = \mathbf{U}D_\mu\mathbf{q}. \tag{1.39}$$

The parameter g that appears in these equations is the strong coupling constant.

$\mathbf{G}_\mu$ is taken to be Hermitian and traceless, just like $\mathbf{W}_\mu$ in the electroweak theory, and it is expressed as:

$$\mathbf{G}_\mu = \frac{1}{2}\sum_{\alpha=1}^{8} G^\alpha_\mu \lambda_\alpha \tag{1.40}$$

where the fraction $\frac{1}{2}$ is conventional and the $G^\alpha_\mu(x)$ are eight real independent gluon gauge fields. The Yang-Mills constructor, similarly to the electroweak case, is:

$$\mathbf{G}_{\mu\nu} = \partial_\mu\mathbf{G}_\nu - \partial_\nu\mathbf{G}_\mu + ig(\mathbf{G}_\mu\mathbf{G}_\nu - \mathbf{G}_\nu\mathbf{G}_\mu). \tag{1.41}$$

The gluon Lagrangian density is taken to be:

$$\mathcal{L}_{gluon} = \frac{1}{2}Tr\left[\mathbf{G}_{\mu\nu}\mathbf{G}^{\mu\nu}\right]. \tag{1.42}$$

By expanding the $\mathbf{G}_{\mu\nu}$ in terms of each components, using Equation 1.40:

$$\mathbf{G}_{\mu\nu} = \frac{1}{2}\sum_{\alpha=1}^{8} G^\alpha_{\mu\nu}\lambda_\alpha. \tag{1.43}$$

Hence the trace is $Tr\left[\lambda_\alpha\lambda_\beta\right] = 2\delta_{\alpha\beta}$ and the Equation 1.42 becomes:

$$\mathcal{L}_{gluon} = \frac{1}{4}\sum_{\alpha=1}^{8} G^{\alpha}_{\mu\nu}G^{\mu\nu}_{\alpha}. \tag{1.44}$$

The total strong Lagrangian density is:

$$\mathcal{L}_{strong} = \mathcal{L}_{gluon} + \mathcal{L}_{quark} \tag{1.45}$$

where the $\mathcal{L}_{quark}$ is taken from the QED and specifically from the Equation 1.20:

$$\mathcal{L}_{quark} = \sum_{f=1}^{6}\left[\bar{\mathbf{q}}_f i\gamma^\mu(\partial_\mu + ig\mathbf{G}_\mu)\mathbf{q}_f - m_f\bar{\mathbf{q}}_f\mathbf{q}_f\right]. \tag{1.46}$$

1.2.7 Spontaneous Symmetry Breaking and Goldstone Bosons

The simplest Lagrangian 1.25, considered for the estimation of the gauge fields Lagrangian, contributes to the energy only with the term $m^2\Phi^\dagger\Phi$ if Φ is independent of time and space [13]. Given that m^2 is positive, the minimum is achieved when $\phi_1 = \phi_2 = 0$. The Lagrangian density, obtained by changing the sign in front of the m^2, is thus unstable and specifically the potential energy density is unbounded below.

The stability can be restored by introducing a term $(m^2/2\phi_0^2)(\Phi^\dagger\Phi)^2$, where ϕ_0 is a real parameter. The new minimum, given a constant Φ, is obtained on the circle defined by $|\Phi| = \phi_0$ and therefore the vacuum states are infinite. Under the $U(1)$ symmetry 1.17:

$$\phi_1' = \phi_1 cos\theta + \phi_2 sin\theta \tag{1.47}$$

$$\phi_2' = -\phi_1 sin\theta + \phi_2 cos\theta. \tag{1.48}$$

If the vacuum state is taken to be $(\phi_0, 0)$, the $SU(1)$ symmetry breaks. This is an example of *Spontaneous Symmetry Breaking* .

Expanding around this ground state $(\phi_0, 0)$, $\Phi = \phi_0 + (1/\sqrt{2}))x + i\psi)$, the Lagrangian density becomes:

$$\mathcal{L} = \frac{1}{2}\partial_\mu x\partial^\mu x + \frac{1}{2}\partial_\mu\psi\partial^\mu\psi - \frac{m^2}{2\phi_0^2}\left[\sqrt{2}\phi_0 x + \frac{x^2}{2} + \frac{\psi^2}{2}\right]^2 \tag{1.49}$$

where

$$\frac{1}{2}\partial_\mu x\partial^\mu x + \frac{1}{2}\partial_\mu\psi\partial^\mu\psi - m^2x^2 \equiv \mathcal{L}_{free}. \tag{1.50}$$

After breaking the $U(1)$ symmetry, the $\mathcal{L}_{free}$ term is interpreted as the free particle field, which is dominant for classical fields and small oscillations, and the rest corresponds to interactions between the free particles and higher order corrections to their motion.

The term $-m^2x^2$ in 1.50, represents a scalar spin-zero particle of mass $\sqrt{2}m$, which in the case of the ψ field there is no such term, consequently the particle is massless. These massless particles, arise from the global symmetry breaking and are called *Goldstone bosons* [14].

1.2.8 Local Symmetry Breaking and the Higgs Boson

To generalize, the $U(1)$ transformation is considered to be of the form $\Phi \rightarrow \Phi' = e^{-iq\theta}\Phi$, where $\theta = \theta(x)$ is space-time dependent [13]. This requires the introduction of a massless gauge field A_μ, such that:

$$\mathcal{L} = \left[(\partial_\mu - iqA_\mu)\Phi^\dagger\right]\left[(\partial^\mu + iqA^\mu)\Phi\right] - \frac{1}{4}F_{\mu\nu}F^{\mu\nu} - V(\Phi^\dagger\Phi) \tag{1.51}$$

where $F_{\mu\nu} = \partial_\mu A_\nu - \partial_\nu A_\mu$ and $V(\Phi^\dagger\Phi) = \frac{m^2}{2\phi_0^2}\left[\Phi^\dagger\Phi - \phi_0^2\right]^2$.

$\mathcal{L}$ is invariant under the local gauge transformation:

$$\Phi(x) \rightarrow \Phi'(x) = e^{-iq\theta}\Phi(x), \quad A_\mu(x) \rightarrow A'_\mu(x) = A_\mu(x) + \partial_\mu\theta(x). \tag{1.52}$$

The minimum energy is obtained when the fields A_μ vanishes and Φ is constant, defined by the circle $|\Phi| = \phi_0$. If the $\Phi'(x)$ is real, the symmetry breaks, since we are no longer free to make further gauge transformations. Substituting $\Phi'(x) = \phi_0 + h(x)/\sqrt{2}$, where $h(x)$ is real, gives:

$$\begin{aligned}\mathcal{L} = &\left[(\partial_\mu - iqA'_\mu)(\phi_0 + h(x)/\sqrt{2})\right]\left[(\partial^\mu + iqA'^\mu)(\phi_0 + h(x)/\sqrt{2})\right] \\ &- \frac{1}{4}{F'}_{\mu\nu}F'^{\mu\nu} - \frac{m^2}{2\phi_0^2}\left[\sqrt{2}\phi_0 h + \frac{h^2}{2}\right]^2.\end{aligned} \tag{1.53}$$

The Lagrangian is again separated to two term $\mathcal{L} = \mathcal{L}_{free} + \mathcal{L}_{int}$:

$$\mathcal{L}_{free} = \frac{1}{2}\partial_\mu h\partial^\mu h - m^2h^2 - \frac{1}{4}F_{\mu\nu}F^{\mu\nu} + q^2\phi_0^2A_\mu A^\mu, \tag{1.54}$$

$$\mathcal{L}_{int} = q^2A_\mu A^\mu\left(\sqrt{2}\phi_0 h + \frac{h^2}{2}\right) - \frac{m^2h^2}{2\phi_0^2}\left(\sqrt{2}\phi_0 h + \frac{h^2}{4}\right). \tag{1.55}$$

In the $\mathcal{L}_{int}$ a single scalar field $h(x)$ is described corresponding to a spinless boson of mass $\sqrt{2}m$ and a vector field A_μ, corresponding to a vector boson of mass $\sqrt{2}q\phi_0$ with three independent components.

The mechanism for introducing mass is called the **Higgs mechanism** [15, 16] and the particle corresponding to the $h(x)$ field is called the **Higgs boson**. As a consequence of local symmetry breaking the gauge field acquires a mass, and the massless spin-zero Goldstone boson that appeared in the global symmetry breaking 1.2.7 is replaced by the longitudinal polarized state of this massive spin one boson.

In the Glashow-Weinberg-Salam electroweak theory, the masses of the $W^{\pm}$ and Z particles arise as a result of symmetry breaking. The resulting theory can be renormalized.

1.3 The SM Higgs Mechanism

In the standard non-Abelian case of the SM, the theory should reproduce the mass of three gauge bosons $W^{\pm}$ and Z, the γ should remain massless and the QED must stay an exact symmetry [10]. In order to generate masses, the gauge symmetry must break in some way, however the fully symmetric Lagrangian is needed to preserve renormalizability [17].

The Lagrangian should follow the general form:

$$\mathcal{L} = \partial_\mu \phi^\dagger \partial^\mu \phi - V(\phi) \tag{1.56}$$

and the potential is chosen to be of the form:

$$V(\phi) = \mu^2 \phi^\dagger \phi + h(\phi^\dagger \phi)^2. \tag{1.57}$$

In order to have a ground state the potential must be grounded from below, i.e. $h > 0$. Whereas for the μ^2 there are two possibilities, graphically shown in Figure 1.2:

1. $\mu^2 > 0$: the potential has only one minimum ($\phi = 0$) and it describes a massive scalar particle with mass μ and coupling $\sqrt{h}$

2. $\mu^2 < 0$: the minimum is obtained for the ϕ_0 value, $|\phi_0| = \sqrt{\frac{-\mu^2}{2h}} \equiv \frac{v}{\sqrt{2}} > 0$, for which the potential is $V(\phi_0) = -\frac{h}{4}v^4$. v is called the *vacuum expectation value*.

1.3.1 The Mechanism in the SM

For the case of $\mu^2 < 0$, the simplest choice is a complex $SU(2)$ doublet of scalar fields ϕ:

$$\phi(x) \equiv \begin{pmatrix} \phi^+(x) \\ \phi^0(x) \end{pmatrix}, \qquad Y_\phi = +1 \tag{1.58}$$

Figure 1.2: Graphical representation of the potential 1.57 for $\mu^2 \geq 0$ (left) and $\mu^2 < 0$ (right) [18].

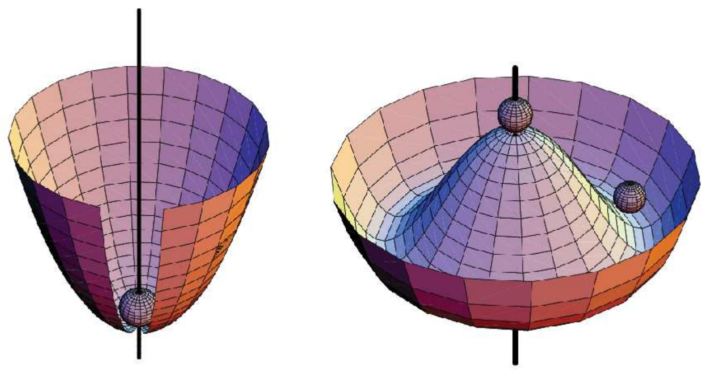

for which there is a finite set of degenerate states with minimum energy satisfying:

$$| \lnsim 0|\phi^0|0 \gnsim | = \sqrt{\frac{-\mu^2}{2h}} \equiv \frac{v}{\sqrt{2}} \tag{1.59}$$

as the previously chosen potential. Rewriting the field Φ as an expansion around the v of the $\theta_i(x)$ fields and H(x), where $i = 1, 2, 3$, at the first order:

$$\Phi(x) = \begin{pmatrix} \theta_2 + i\theta_1 \\ \frac{1}{\sqrt{2}}(v + H) - i\theta_3 \end{pmatrix} = e^{i\theta_a(x)\tau^a(x)/v} \begin{pmatrix} 0 \\ \frac{1}{\sqrt{2}}(v + H(x)) \end{pmatrix}. \tag{1.60}$$

A gauge transformation of this field leads to:

$$\Phi(x) \rightarrow e^{-i\theta_a(x)\tau^a(x)}\,\Phi(x) = \frac{1}{\sqrt{2}} \begin{pmatrix} 0 \\ v + H(x) \end{pmatrix} \tag{1.61}$$

and after the full expansion of terms $|D_\mu\Phi|^2$ as in the Equation 1.34 result to:

$$\begin{aligned} |D_\mu\Phi|^2 &= \left| \left(\partial_\mu - ig_2\frac{\tau_a}{2}W_\mu^a - ig_1\frac{1}{2}B_\mu \right)\Phi \right|^2 \qquad (1.62) \\ &= \frac{1}{2}\left| \begin{pmatrix} \partial_\mu - \frac{i}{2}(g_2W_\mu^3 + g_1B_\mu) & -\frac{ig_2}{2}(W_\mu^1 - iW_\mu^2) \\ -\frac{ig_2}{2}(W_\mu^1 + iW_\mu^2) & \partial_\mu + \frac{i}{2}(g_2W_\mu^3 - g_1B_\mu) \end{pmatrix} \begin{pmatrix} 0 \\ v + H \end{pmatrix} \right|^2 \\ &= \frac{1}{2}(\partial_\mu H)^2 + \frac{1}{8}g_2^2(v + H)^2|W_\mu^1 + iW_\mu^2|^2 + \frac{1}{8}(v + H)^2|g_2W_\mu^3 - g_1B_\mu|^2 \end{aligned}$$

In the above equation, the following fields can be defined:

$$W^{\pm} = \frac{1}{\sqrt{2}}(W^1_\mu \mp iW^2_\mu)\ ,\ Z_\mu = \frac{g_2 W^3_\mu - g_1 B_\mu}{\sqrt{g_2^2 + g_1^2}}\ ,\ A_\mu = \frac{g_2 W^3_\mu + g_1 B_\mu}{\sqrt{g_2^2 + g_1^2}} \tag{1.63}$$

where A_μ is orthogonal to the Z_μ. In this interpretation, the $W^{\pm}$, Z have acquired masses while the photon remained massless:

$$M_W = \frac{1}{2} v g_2\ ,\ M_Z = \frac{1}{2} v \sqrt{g_2^2 + g_1^2}\ ,\ M_A = 0. \tag{1.64}$$

The achievement is that by the spontaneous breaking of the symmetry $SU(2)_L \times U(1)_Y \to U(1)_Q$, three Goldstone bosons have been absorbed by the $W^{\pm}$ and Z bosons to form their longitudinal components and to get their masses. Since the $U(1)_Q$ symmetry is still unbroken, the photon which is its generator, remains massless.

In a similar manner, using the same scalar field Φ and the isodoublet $\tilde{\Phi} = i\tau_2 \Phi^*$, which has hypercharge $Y = -1$, the fermion masses can be generated. The $SU(2)_L \times U(1)_Y$ invariant Yukawa Lagrangian is introduced:

$$\mathcal{L}_F = -\lambda_e\, \bar{L}\, \Phi\, e_R - \lambda_d\, \bar{Q}\, \Phi\, d_R - \lambda_u\, \bar{Q}\, \tilde{\Phi}\, u_R\ +\ h.\,c. \tag{1.65}$$

Taking the electron as an example, one obtains:

$$\begin{aligned} \mathcal{L}_F &= -\frac{1}{\sqrt{2}} \lambda_e\, (\bar{\nu}_e, \bar{e}_L) \begin{pmatrix} 0 \\ v + H \end{pmatrix} e_R\ + \cdots \\ &= -\frac{1}{\sqrt{2}}\, \lambda_e\, (v + H)\, \bar{e}_L e_R\ + \cdots \end{aligned} \tag{1.66}$$

The constant term in front of $\bar{f}_L f_R$ is identified as the fermion mass:

$$m_e = \frac{\lambda_e\, v}{\sqrt{2}}\ ,\ m_u = \frac{\lambda_u\, v}{\sqrt{2}}\ ,\ m_d = \frac{\lambda_d\, v}{\sqrt{2}}. \tag{1.67}$$

The scalar Lagrangian 1.56 is written as:

$$\mathcal{L} = (D_\mu \phi)^\dagger D^\mu \phi - \mu^2 \phi^\dagger \phi + h(\phi^\dagger \phi)^2 \qquad (h > 0,\ \mu^2 < 0) \tag{1.68}$$

and it must be invariant under the $SU(2) \times U(1)$ transformations. If the scalar doublet is parametrized in the general form of:

$$\phi(x) = e^{i \frac{\sigma_i}{2} \theta^i(x)} \frac{1}{\sqrt{2}} \begin{pmatrix} 0 \\ v + H(x) \end{pmatrix} \tag{1.69}$$

The kinematic term of the Lagrangian 1.68 for $\theta^i(x) = 0$, takes the form:

$$\begin{aligned} (D_\mu \phi)^\dagger D^\mu \phi &= \left[\left(\partial^\mu + igW^\mu + ig' \frac{1}{2} B^\mu \right) \phi \right]^\dagger \left(\partial^\mu + igW^\mu + ig' \frac{1}{2} B^\mu \right) \phi \\ &= \frac{1}{2} \partial_\mu H \partial^\mu H + (v + H)^2 \left(\frac{g^2}{2} W^\dagger_\mu W^\mu + \frac{g^2}{8cos^2\theta_W} Z_\mu Z^\mu \right) \end{aligned} \tag{1.70}$$

Through this procedure masses are generated for the $W^{\pm}$ and Z bosons, while the photon remained massless:

$$M_Z\, cos\theta_W = M_W = \frac{1}{2} v g. \tag{1.71}$$

1.3.2 The Higgs Particle in the SM

Finally, the Higgs itself is studied through the kinetic part of the field, $\frac{1}{2}(\partial_\mu H)^2$, of the Lagrangian 1.71 and the potential 1.57:

$$V \;=\; \frac{\mu^2}{2}(0, v+H)\begin{pmatrix} 0 \\ v+H \end{pmatrix} + \frac{\lambda}{4}\left|(0, v+H)\begin{pmatrix} 0 \\ v+H \end{pmatrix}\right|^2. \tag{1.72}$$

Using the relation $v^2 = -\mu^2/\lambda$:

$$V \;=\; -\frac{1}{2}\lambda v^2\,(v+H)^2 + \frac{1}{4}\lambda(v+H)^4 \tag{1.73}$$

and resulting to the Lagrangian containing the Higgs field H:

$$\begin{aligned} \mathcal{L}_H \;&=\; \frac{1}{2}(\partial_\mu H)(\partial^\mu H) - V \\ &=\; \frac{1}{2}(\partial^\mu H)^2 - \lambda v^2\, H^2 - \lambda v\, H^3 - \frac{\lambda}{4}\, H^4 \end{aligned} \tag{1.74}$$

where $M_H^2 = 2\lambda v^2 = -2\mu^2$ is simply the Higgs boson mass and the Feynman rules are given by:

$$g_{H^3} = (3!) i\lambda v = 3i\,\frac{M_H^2}{v}, \qquad g_{H^4} = (4!) i\frac{\lambda}{4} = 3i\frac{M_H^2}{v^2}. \tag{1.75}$$

The Higgs boson couplings to gauge bosons and fermions almost derived previously, when the masses of these particles were calculated:

$$\mathcal{L}_{M_V} \sim M_V^2\left(1 + \frac{H}{v}\right)^2, \qquad \mathcal{L}_{m_f} \sim -m_f\left(1 + \frac{H}{v}\right) \tag{1.76}$$

along with the Higgs boson couplings to gauge bosons and fermions:

$$g_{Hff} = i\frac{m_f}{v}, \quad g_{HVV} = -2i\frac{M_V^2}{v}, \quad g_{HHVV} = -2i\frac{M_V^2}{v^2}. \tag{1.77}$$

In the previous, the vacuum expectation value v is fixed in terms of the W boson mass M_W or the Fermi constant G_μ determined from muon decay:

$$M_W = \frac{1}{2} g_2 v = \left(\frac{\sqrt{2} g^2}{8 G_\mu} \right)^{1/2} \Rightarrow v = \frac{1}{(\sqrt{2} G_\mu)^{1/2}} \simeq 246 \text{ GeV}. \tag{1.78}$$

The Higgs couplings to fermions, massive gauge bosons as well as the self–couplings, are given in Figure 1.3 using both v and G_μ.

The Higgs boson propagator is given, in momentum space, by:

$$\Delta_{HH}(q^2) = \frac{i}{q^2 - M_H^2 + i\epsilon} \tag{1.79}$$

1.4 Higgs System Theoretical Constraints

The Higgs mechanism has various theoretical constraints which are derived from assumptions on the energy range in which the SM is valid before perturbation theory breaks down and new phenomena should emerge [10]. These include constraints from unitarity in scattering amplitudes, perturbativity of the Higgs self–coupling, stability of the electroweak vacuum and fine–tuning, as summarized below.

1.4.1 Perturbative Unitarity

In processes involving the W_L and Z_L bosons, given that the interactions of the longitudinal components grow with momenta, this would eventually lead to cross sections which increase with the energy which would then violate unitarity at some stage [10]. The limit to preserve the unitarity condition if estimated to be:

$$M_H \sim 870 \text{ GeV}. \tag{1.80}$$

Imposing similar criteria on the $Z_L Z_L$, HH and $Z_L H$ the unitarity constraints the Higgs mass below:

$$M_H \sim 710 \text{ GeV}. \tag{1.81}$$

Thus, in the SM, if the Higgs boson mass exceeds values of $\mathcal{O}(700 \text{ GeV})$, unitarity will be violated unless new phenomena appear and restore it.

The perturbation has also to be taken into account in the decays of the Higgs boson to gauge bosons. Using the equivalence theorem and the Lagrangian, the partial decay width of the Higgs boson into two longitudinal Z bosons can be written as:

$$\Gamma(H \to ZZ) = \left(\frac{1}{2M_H}\right) \left(\frac{2!\, M_H^2}{2v}\right)^2 \frac{1}{2} \left(\frac{1}{8\pi}\right) \to \frac{M_H^3}{32\pi v^2}. \tag{1.82}$$

For the decay $H \to WW$, one needs to remove the statistical factor to account for both $W^\pm$ states:

$$\Gamma(H \to W^+W^-) \simeq 2\Gamma(H \to ZZ). \tag{1.83}$$

This means that for high Higgs masses the width becomes comparable to the mass and hence the Higgs cannot be considered as a "real" resonance anymore. The expected width of the Higgs boson is presented in Figure 1.4 and especially in the region $\sim$ 125 GeV, where the Higgs mass is observed, the expectation is below 10^{-2} GeV.

1.4.2 Triviality and Stability Bounds

The variation of the quartic Higgs coupling with the energy scale Q is described by the Renormalization Group Equation [10]:

$$\frac{\mathrm{d}}{\mathrm{d}Q^2}\, \lambda(Q^2) = \frac{3}{4\pi^2}\, \lambda^2(Q^2) \; + \text{higher orders} \tag{1.84}$$

Choosing the natural reference energy point to be the electroweak symmetry breaking scale, $Q_0 = v$, the solution is:

$$\lambda(Q^2) = \lambda(v^2) \left[1 - \frac{3}{4\pi^2}\, \lambda(v^2) \log \frac{Q^2}{v^2}\right]^{-1}. \tag{1.85}$$

If the energy is much smaller than the electroweak breaking scale, $Q^2 \ll v^2$, the quartic coupling becomes extremely small and eventually vanishes, $\lambda(Q^2) \sim \lambda(v^2)/\log(\infty) \to 0_+$. In this case the theory is said to be *trivial*, i.e. non interacting since the coupling is zero. In the opposite limit, where the energy is much smaller than the weak scale, the quartic coupling becomes infinite. The energy where this happens is called *Landau pole* and is equal to:

$$\Lambda_C = v \, \exp\left(\frac{4\pi^2}{3\lambda}\right) = v \, \exp\left(\frac{4\pi^2 v^2}{M_H^2}\right). \tag{1.86}$$

Figure 1.3: The Higgs boson couplings to fermions and gauge bosons and the Higgs self–couplings in the SM. The normalization factors of the Feynman rules are also displayed [10].

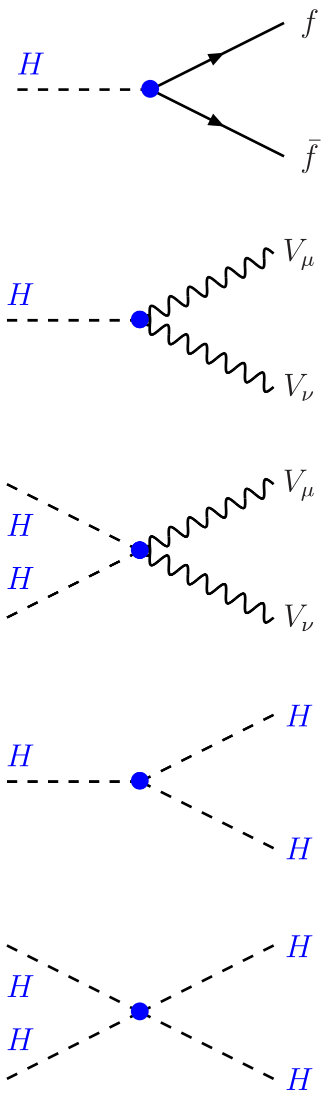

$$g_{Hff} \;=\; m_f/v \;=\; (\sqrt{2}G_\mu)^{1/2}\, m_f \qquad \times\,(i)$$

$$g_{HVV} \;=\; 2M_V^2/v \;=\; 2(\sqrt{2}G_\mu)^{1/2}\, M_V^2 \qquad \times\,(-ig_{\mu\nu})$$

$$g_{HHVV} \;=\; 2M_V^2/v^2 \;=\; 2\sqrt{2}G_\mu\, M_V^2 \qquad \times\,(-ig_{\mu\nu})$$

$$g_{HHH} \;=\; 3M_H^2/v \;=\; 3(\sqrt{2}G_\mu)^{1/2}\, M_H^2 \qquad \times\,(i)$$

$$g_{HHHH} = 3M_H^2/v^2 \;=\; 3\sqrt{2}G_\mu\, M_H^2 \qquad \times\,(i)$$

Figure 1.4: Standard model Higgs boson expected total width [19].

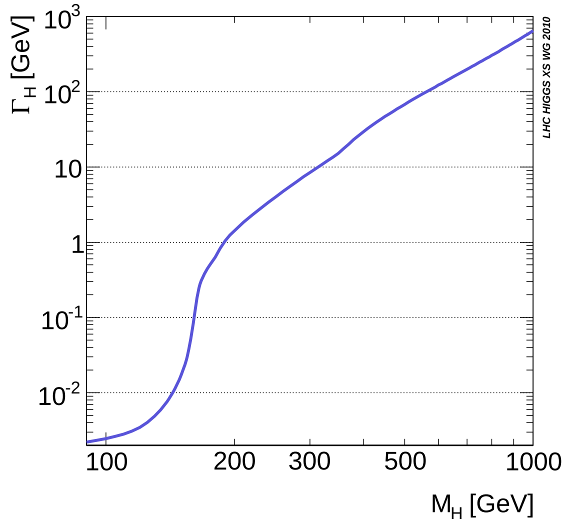

In order for the theory to remain perturbative at all scales a cut-off energy of Λ_c should be defined. From simulations of gauge theories on the lattice, where the non–perturbative effects are properly taken into account, it turns out that the rigorous bound is $M_H < 640$ GeV.

The one–loop renormalization group equation 1.84 for the quartic coupling, including the fermion and gauge boson contributions, becomes:

$$\begin{aligned}\frac{\mathrm{d}\lambda}{\mathrm{dlog}Q^2} &\simeq \frac{1}{16\pi^2}\left[12\lambda^2 + 6\lambda\lambda_t^2 - 3\lambda_t^4 - \frac{3}{2}\lambda(3g_2^2 + g_1^2) + \frac{3}{16}\left(2g_2^4 + (g_2^2 + g_1^2)^2\right)\right] \quad (1.87)\\ &\simeq \frac{1}{16\pi^2}\left[12\lambda^2 - 12\frac{m_t^4}{v^4} + \frac{3}{16}\left(2g_2^4 + (g_2^2+g_1^2)^2\right)\right] \quad (\lambda \ll \lambda_t, g_1, g_2)\end{aligned}$$

where the top quark Yukawa coupling is given by $\lambda_t = \sqrt{2}m_t/v$. Taking the weak scale as a reference point, the solution is:

$$\lambda(Q^2) = \lambda(v^2) + \frac{1}{16\pi^2}\left[-12\frac{m_t^4}{v^4} + \frac{3}{16}\left(2g_2^4 + (g_2^2+g_1^2)^2\right)\right]\log\frac{Q^2}{v^2}. \tag{1.88}$$

If the coupling λ is too small, the top quark contribution can be dominant and could drive it to a negative value $\lambda(Q^2) < 0$, leading to a scalar potential $V(Q^2) < V(v)$. Therefore vacuum is not stable anymore since it has no minimum. The stability argument requires a lower bound in order to have a scalar potential:

$$M_H^2 > \frac{v^2}{8\pi^2}\left[-12\frac{m_t^4}{v^4} + \frac{3}{16}\left(2g_2^4 + (g_2^2+g_1^2)^2\right)\right]\log\frac{Q^2}{v^2}. \tag{1.89}$$

Figure 1.5: The triviality (upper) bound and the vacuum stability (lower) bound on the Higgs boson mass as a function of the cutoff scale Λ_c. The allowed region lies between the bands and the colored bands illustrate the impact of various uncertainties [10].

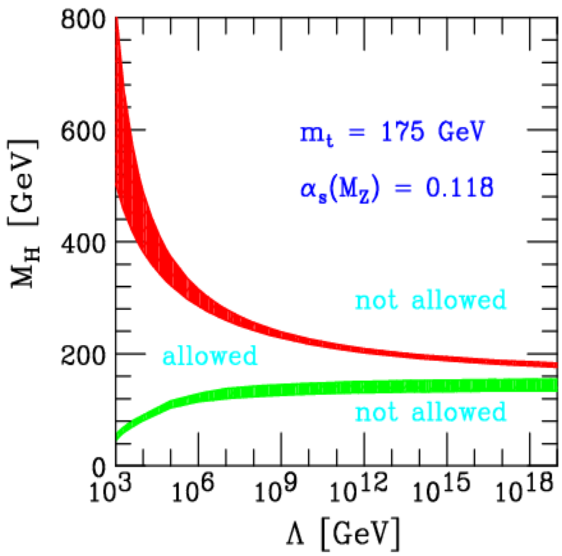

The constraints on the Higgs boson mass depend on the cut–off Λ_C:

$$\begin{aligned} \Lambda_C \sim 10^3 \text{ GeV} &\Rightarrow M_H \gtrsim 70 \text{ GeV} \\ \Lambda_C \sim 10^{16} \text{ GeV} &\Rightarrow M_H \gtrsim 130 \text{ GeV}. \end{aligned} \tag{1.90}$$

Collectively, the limits imposed are the triviality (upper) bound and the vacuum stability (lower) bound of the Higgs mass as a function of the cut–off scale Λ_c, given the top quark mass $m_t = 175 \pm 6$ GeV and $\alpha_s = 0.118 \pm 0.002$, also shown in Figure 1.5.

1.4.3 The Fine–Tuning Constraint

A last theoretical constraint comes from the fine–tuning problem originating from the radiative corrections to the Higgs boson mass [10]. Cutting off the loop integral momenta at a scale Λ, and keeping only the dominant contribution in this scale, one obtains:

$$M_H^2 = (M_H^0)^2 + \frac{3\Lambda^2}{8\pi^2 v^2}\left[M_H^2 + 2M_W^2 + M_Z^2 - 4m_t^2\right] \tag{1.91}$$

where M_H^0 is the bare mass contained in the unrenormalized Lagrangian.

Figure 1.6: Constrains from various theoretical bounds are presented [10]. The dark (light) hatched region marked "1%" ("10%") represents fine–tunings of greater than 1 part in 100 (10). The constraints from triviality, stability and electroweak precision data are also shown. The white region is consistent with all the constraints.

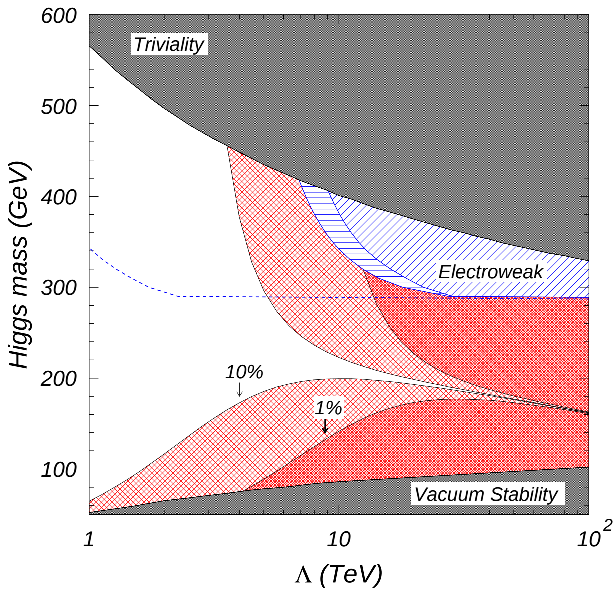

If the cut–off Λ_c is very large, for instance of the order of the Grand Unification scale $\sim 10^{16}$ GeV, one needs a very fine arrangement of 16 digits between the bare Higgs mass and the radiative corrections to have a physical Higgs boson mass in the range of the electroweak symmetry breaking scale, $M_H \sim 100$ GeV to 1 TeV, as is required for the consistency of the SM. This is the naturalness of fine–tuning problem. The acceptable mass regions are presented in Figure 1.6.

1.5 Higgs Beyond the Standard Model

Despite the success of the SM to describe particle physics processes, there are several aspects where it does not provide satisfactory answers. Among these issues, the most important are:

- Gravity is not contained in the SM theory
- Gauge coupling unification is not provided

- Neutrino masses are not included
- SM has no proper candidate for Dark Matter
- The Higgs sector suffers from the instability of the value of the Higgs boson mass when radiative corrections are included in presence of a physical cut-off that is placed at energies far above the electroweak scale (the so called **Hierarchy problem**).

The existence of one new symmetry, or more, relating fermions and bosons is the most popular proposal to solve the hierarchy problem of the SM Higgs sector [20]. This new symmetry is called **Supersymmetry (SUSY)** and generically acts as:

$$\begin{aligned} Q|\text{boson}\rangle &= |\text{fermion}\rangle \\ Q|\text{fermion}\rangle &= |\text{boson}\rangle. \end{aligned} \tag{1.92}$$

This is interpreted as SUSY particles partners (*sparticles*) to the SM particles that share quantum numbers but differ by 1/2 unit in their spin. Exact SUSY requires mass degeneracy between particles and sparticles, however in a realistic model SUSY must be broken, since the SUSY partners with such masses have not been observed. These SUSY-breaking models can be classified in two big groups:

- <u>Unconstrained Models:</u> A general parametrization of all possible SUSY-breaking terms is implemented. The simplest and most popular of these models is the Minimal Supersymmetric Standard Model (MSSM).
- <u>Constrained Models:</u> Specific assumptions on the scenario that achieves the spontaneous SUSY breaking is assumed. There are different kinds of models according to the origin of the SUSY breaking and the way it is transmitted from the so-called "Hidden sector" to the "Visible sector", e.g. Gravity-mediated, Gauge-mediated, Anomaly-mediated, etc.

The MSSM and other SUSY models have an extra symmetry, called the "R-parity", that implies the conservation of a new multiplicative quantum number defined for each particle as:

$$P_R = (-1)^{3(B-L)+2s} \tag{1.93}$$

where B, L and s are the baryon number, the lepton number and the spin of the particle respectively. All the SM-particles have even R-parity, $P_R = +1$, whereas the superpartners have odd R-parity, $P_R = -1$. This symmetry has very important consequences for Dark Matter Physics, since it provides a natural particle candidate for explaining the Dark Matter: the lightest SUSY particle (LSP), that due to the R-parity is stable.

Since the LSP is neutral and uncolored, it leaves no traces in collider detectors and, therefore, the typical SUSY signatures are events with missing energy.

In supersymmetric extensions of the SM, at least two Higgs doublet fields are required for a consistent electroweak symmetry breaking and in the minimal model, the MSSM, the Higgs sector is extended to contain five Higgs bosons: two CP-even h and H, a CP-odd A and two charged Higgs $H^{\pm}$ particles [21]. Besides the four masses, two more parameters enter the MSSM Higgs sector: a mixing angle α in the neutral CP-even sector and the ratio of the vacuum expectation values of the two Higgs fields $tan\beta$. Only two free parameters are needed at tree-level: one Higgs mass, usually chosen to be M_A and $tan\beta$ which is expected to lie in the range $1 \lesssim tan\beta \lesssim m_t/m_b$. In addition, while the masses of the heavy neutral and charged $H, A, H^{\pm}$ particles are expected to range from M_Z to the SUSY breaking scale $M_S = \mathcal{O}(1\ \text{TeV})$, the mass of the lightest Higgs boson h is bounded from above, $M_h \leq M_Z$ at tree-level. This relation is altered by large radiative corrections, the leading part of which grow as the fourth power of m_t and logarithmically with the SUSY scale or common squark mass M_S; the mixing (or trilinear coupling) in the stop sector A_t plays also an important role. The upper bound on M_h is then shifted to $M_h^{\max} \sim$ 110-135 GeV depending on these parameters.

1.6 Higgs Production at Hadron Colliders

In the Standard Model, the main production mechanisms for the Higgs boson at hadron colliders make use of the fact that the Higgs boson couples preferentially to the heavy particles, that is the massive W and Z vector bosons, the top quark and, to a lesser extent, the bottom quark [10]. The four main production processes, the Feynman diagrams of which are displayed in Figure 1.7, are thus: the associated production with W/Z bosons, the weak vector boson fusion processes, the gluon–gluon fusion mechanism and the associated Higgs production with heavy top or bottom quarks:

- Associated production with W/Z (WH/ZH): $q\bar{q} \to V + H$
- Vector Boson Fusion (VBF): $qq \to V^*V^* \to qq + H$
- Gluon-Gluon Fusion (ggF): $gg \to H$
- Associated production with heavy quarks (bbH,ttH): $gg, q\bar{q} \to Q\bar{Q} + H$

The production cross sections of the different mechanisms as a function of the Higgs mass are presented in Figure 1.8. The cross sections are shown for the Run-I center of mass energies (7 and 8 TeV) and the maximum possible energy of the LHC (14 TeV). The missing VH and ttH cross sections for $M_H > 300$ GeV are due to the very small

Figure 1.7: The dominant SM Higgs boson production mechanisms in hadronic collisions.

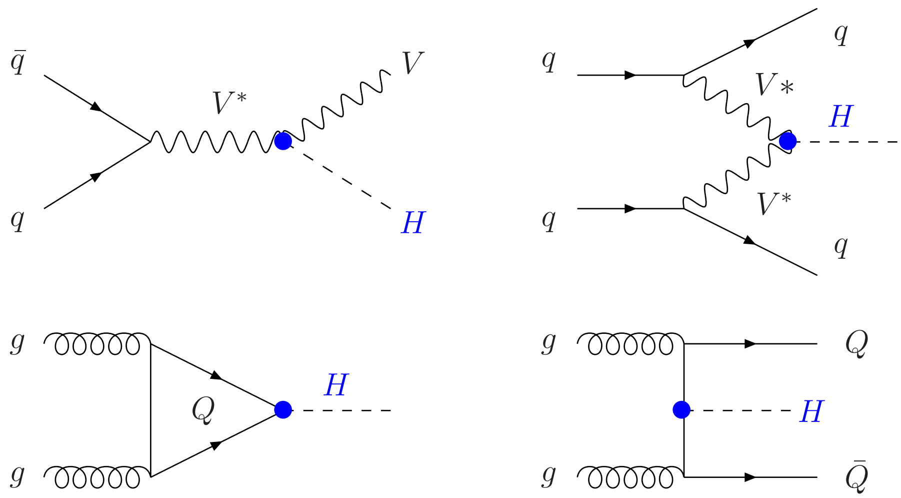

estimated cross sections. Analytically, the theoretical cross sections around the observed Higgs mass at $\sqrt{s} = 7,\ 8,\ 13,\ 14$ TeV are presented in Table 1.4 for all the production mechanisms. Once again the missing estimations are due to very small expected cross sections.

There are also several mechanisms for the pair production of the Higgs particles:

$$\text{Higgs Pair Production :} \qquad pp \rightarrow HH + X \tag{1.94}$$

and the relevant sub–processes are the $gg \rightarrow HH$ mechanism, which proceeds through heavy top and bottom quark loops, the associated double production with massive gauge bosons, $q\bar{q} \rightarrow HHV$, and the vector boson fusion mechanisms $qq \rightarrow V^*V^* \rightarrow HHqq$. However, because of the suppression by the additional electroweak couplings, they have much smaller production cross sections than the single Higgs production mechanisms listed above.

Also suppressed are processes where the Higgs is produced in association with one, two or three hard jets in gluon–gluon fusion, the associated Higgs production with gauge boson pairs, the production with a vector boson and two jets. Other production processes exist, but have even smaller production cross sections (e.g. diffractive processes).

Figure 1.8: Standard Model Higgs boson mechanisms production cross sections at $\sqrt{s} = 7$ (a) and $\sqrt{s} = 8$ TeV (b) as a function of the Higgs mass [19]. (c) shows the total cross sections for $\sqrt{s} = 7,\ 8,\ 14$ TeV. The missing VH and ttH cross sections for $M_H > 300$ GeV are due to the very small estimated cross sections.

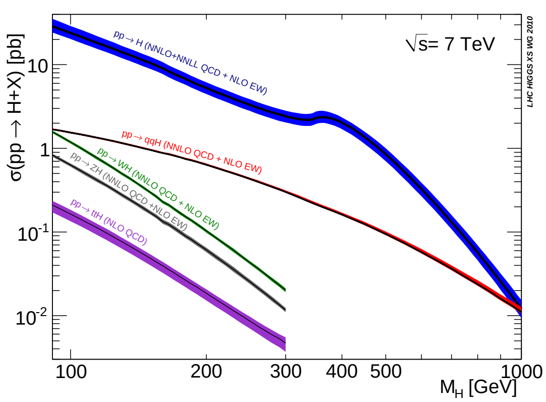

(a)

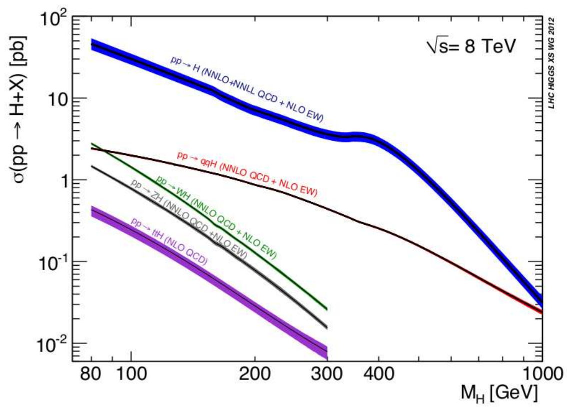

(b)

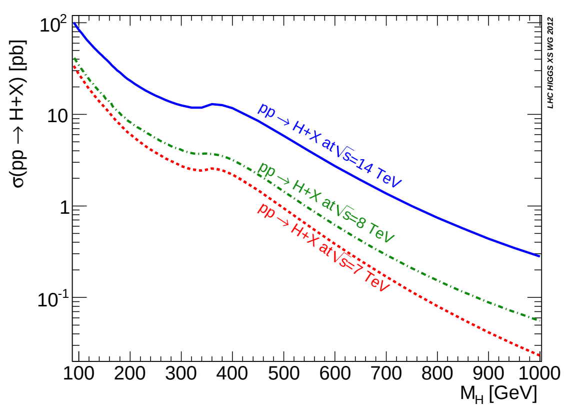

(c)

Table 1.4: SM Higgs production cross sections through ggF, VBF, WH, ZH, bbH (where available) and ttH processes at $\sqrt{s} = 7,\ 8,\ 13,\ 14$ TeV [19] around the around Higgs mass.

m_H (GeV)	ggF σ (pb)	VBF σ (pb)	WH σ (pb)	ZH σ (pb)	bbH σ (pb)	ttH σ (pb)
$\sqrt{s} = 7$ TeV						
125.0	15.13	1.222	0.5785	0.3351	-	0.08632
125.5	15.01	1.219	0.5703	0.3309	-	0.08528
126.0	14.89	1.211	0.5629	0.3267	-	0.08426
$\sqrt{s} = 8$ TeV						
125.0	19.27	1.578	0.7046	0.4153	0.2035	0.1293
125.5	19.12	1.573	0.6951	0.4102	0.2008	0.1277
126.0	18.97	1.568	0.6860	0.4050	0.1979	0.1262
$\sqrt{s} = 13$ TeV						
125.0	43.92	3.748	1.380	0.8696	0.5116	0.5085
125.5	43.62	3.727	1.362	0.8594	0.5053	0.5027
126.0	43.31	3.703	1.345	0.8501	0.4969	0.4966
$\sqrt{s} = 14$ TeV						
125.0	49.47	4.233	1.522	0.9690	0.5805	0.6113
125.5	49.13	4.220	1.502	0.9574	0.5739	0.6043
126.0	48.80	4.206	1.485	0.9465	0.5673	0.5969

Figure 1.9: $\Delta\chi^2$ as a function of m_H, where the solid (dashed) lines give the results when including (ignoring) theoretical errors [23].

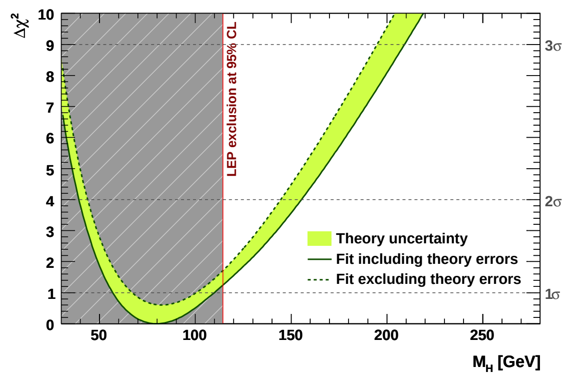

1.7 Higgs Searches and Production at the LHC

The very low mass region, below ~ 110 GeV, was excluded by the Large Electron-Positron Collider (LEP) experiments [22] before the LHC era and hence the LHC studies are focused in the mass region above 100 GeV. Figure 1.9 shows the $\Delta\chi^2$ profile versus the m_H obtained using the Gfitter [23] and the LEP excluded region appears in grey. In the low mass region, the sensitivity is as:

- $ZZ \to 4\ell$: less sensitive but cleanest
- $\gamma\gamma$: is very clean
- $WW \to \ell\ell\nu\nu$: very sensitive and less accurate, no mass reconstruction is possible due to the presence of two neutrinos
- $\tau\tau$: needs distinctive production features to reduce background, e.g. VBF
- bb: huge backgrounds from QCD
- Rest Channels: the background dominates at low center of mass ($\sqrt{s}$) energies

In the high mass region the $WW \to \ell^{\pm}\nu q\bar{q}$, $WW \to \ell^{+}\nu\ell^{-}\bar{\nu}$, $ZZ \to \ell^{+}\ell^{-}q\bar{q}$ and $ZZ \to \ell^{+}\ell^{-}\nu\bar{\nu}$ dominate.

Figures 1.10 present the Higgs channel production branching ratios at $\sqrt{s} = 8$ TeV as a function of the Higgs mass [19]. In the entire possible mass range and separately in the low mass region. The expected significance of the Higgs discovery had been studied prior to the data taking period and the discovery potential found to be significant [24].

Figure 1.10: Standard model Higgs boson decay branching ratios ((a), (b)) and branching ratios to specific channels (c) at $\sqrt{s} = 8$ TeV [19].

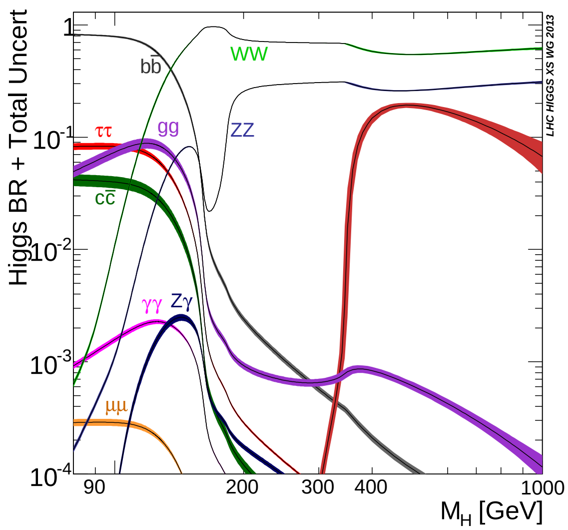

(a)

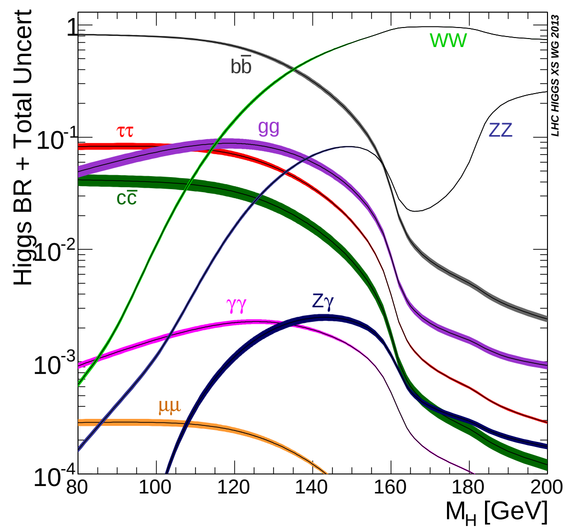

(b)

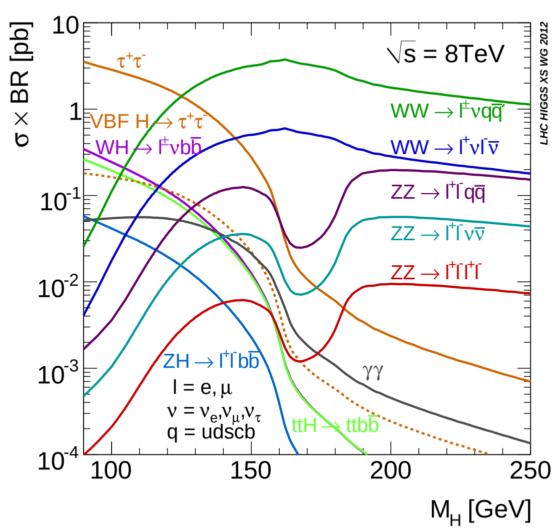

(c)

Chapter Bibliography

[1] Fermi National Laboratory, The science of matter, space and time, http://www.fnal.gov/pub/inquiring/matter/madeof.

[2] J. Beringer et al., Review of Particle Physics (RPP), *Phys.Rev.*, D86:010001, 2012.

[3] C.P. Burgess and G.D. Moore, The standard model: A primer, *Cambridge, UK: Cambridge Univ. Pr. (2007) 542 p.*

[4] Luis Anchordoqui and Francis Halzen, Lessons in particle physics, 2009, arXiv:0906.1271.

[5] S.L. Glashow, Partial Symmetries of Weak Interactions, *Nucl.Phys.*, 22:579–588, 1961.

[6] Steven Weinberg, A Model of Leptons, *Phys.Rev.Lett.*, 19:1264–1266, 1967.

[7] Abdus Salam, Weak and Electromagnetic Interactions, *Conf.Proc.*, C680519:367–377, 1968.

[8] F. Halzen and Alan D. Martin, Quarks and Leptons: An Introductory Course in Modern Particle Physics, *New York, Usa: Wiley (1984) 396 p.*

[9] D.H. Perkins, Introduction to high energy physics, *Reading, USA: Addison-Wesley (1972) 353 p*, 1982.

[10] Abdelhak Djouadi, The Anatomy of electro-weak symmetry breaking. I: The Higgs boson in the standard model, *Phys.Rept.*, 457:1–216, 2008, arXiv:hep-ph/0503172.

[11] Predrag Cvitanovic, Group theory: Birdtracks, Lie's and exceptional groups, *Princeton, USA: Univ. Pr. (2008) 273 p.*

[12] Emmy Noether and M. A. Tavel, Invariant variation problems, 1918, arXiv:physics/0503066.

[13] W.N. Cottingham and D.A. Greenwood, An introduction to the standard model of particle physics, 2007.

[14] J. Goldstone, Field Theories with Superconductor Solutions, *Nuovo Cim.*, 19:154–164, 1961.

[15] Peter W. Higgs, Broken symmetries, massless particles and gauge fields, *Phys.Lett.*, 12:132–133, 1964.

[16] F. Englert and R. Brout, Broken Symmetry and the Mass of Gauge Vector Mesons, *Phys.Rev.Lett.*, 13:321–323, 1964.

[17] Antonio Pich, The Standard model of electroweak interactions, 2007, arXiv:0705.4264.

[18] Jean Iliopoulos, Introduction to the STANDARD MODEL of the Electro-Weak Interactions, *2012 CERN Summer School of Particle Physics, Angers :*, France, 2012, arXiv:1305.6779.

[19] S. Heinemeyer et al., Handbook of LHC Higgs Cross Sections: 3. Higgs Properties, 2013, arXiv:1307.1347.

[20] Maria Herrero, The Higgs System in and Beyond the Standard Model, 2014, arXiv:1401.7270.

[21] Abdelhak Djouadi, Higgs Physics: Theory, *Pramana*, 79:513–539, 2012, 1203.4199.

[22] R. Barate et al., Search for the standard model Higgs boson at LEP, *Phys.Lett.*, B565:61–75, 2003, hep-ex/0306033.

[23] Henning Flacher, Martin Goebel, Johannes Haller, Andreas Hocker, Klaus Monig, et al., Revisiting the Global Electroweak Fit of the Standard Model and Beyond with Gfitter, *Eur.Phys.J.*, C60:543–583, 2009, arXiv:0811.0009.

[24] G. Aad et al., Expected Performance of the ATLAS Experiment - Detector, Trigger and Physics, 2009, 0901.0512.

[25] Michael E. Peskin and Daniel V. Schroeder, An Introduction to quantum field theory, *Reading, USA: Addison-Wesley (1995) 842 p.*

[26] J. Beringer et al., Review of Particle Physics (RPP), *Phys.Rev.*, D86:010001, 2012.

[27] John F. Gunion, Howard E. Haber, Gordon L. Kane, and Sally Dawson, The Higgs Hunter's Guide, *Front.Phys.*, 80:1–448, 2000.

[28] James D. Wells, Lectures on Higgs Boson Physics in the Standard Model and Beyond, 2009, arXiv:0909.4541.

[29] Riccardo Barbieri, Ten lectures on the electroweak interactions, arXiv:0706.0684v1.

[30] Scott Willenbrock, Symmetries of the standard model, pages 3–38, 2004, arXiv:hep-ph/0410370.

[31] S. Heinemeyer, Higgs and Electroweak Physics, pages 37–67, 2009, arXiv:0912.0361.

[32] S.F. Novaes, Standard model: An Introduction, 1999, arXiv:hep-ph/0001283.

[33] Gautam Bhattacharyya, A Pedagogical Review of Electroweak Symmetry Breaking Scenarios, *Rept.Prog.Phys.*, 74:026201, 2011, arXiv:0910.5095.

2

LHC Structure, Operation and Experiments

2.1 Introduction

The Large Hadron Collider (LHC), currently the most powerful particle accelerator [1], is designed to collide two counter rotating beams of protons or heavy ions [2]. The accelerator sits in a circular tunnel of 27 km in circumference [2], between 50 and 175 m under the surface, crossing the Swiss and French borders on the outskirts of Geneva (Figure 2.1). During the Run-I period (2010 - 2013) proton-proton collisions took place at energies of 3.5 and 4.0 TeV per beam and in the Run-II (2015 - 2018) the center of mass energy is foreseen to reach 13 TeV. The capabilities of the collider's technology reach the 14 TeV limit. The beams collision points, as appear in Figure 2.2, are the places where the detectors of the experiments are located. Descriptions of the largest LHC experiments are provided later on this section.

The name of the LHC describes its basic properties [1]:

- **Large :** The size of an accelerator is related to the maximum obtainable energy and therefore the radius of the tunnel is an essential element of the design
- **Hadron :** The LHC accelerates hadrons, either protons or lead ions, using both radio-frequency cavities and dipole magnetic fields in order to generate them and keep them in orbit
- **Collider :** Counter circulate beams collide and the energy of the collision is the sum of the energies of the two beams.

Figure 2.1: Schematic view of the LHC size crossing the Swiss and French borders on the outskirts of Geneva [1].

Figure 2.2: Schematic view of the LHC beam collision points where the experiments are located, specifically the ATLAS, CMS, ALICE and LHC-B sectors can be seen. [3].

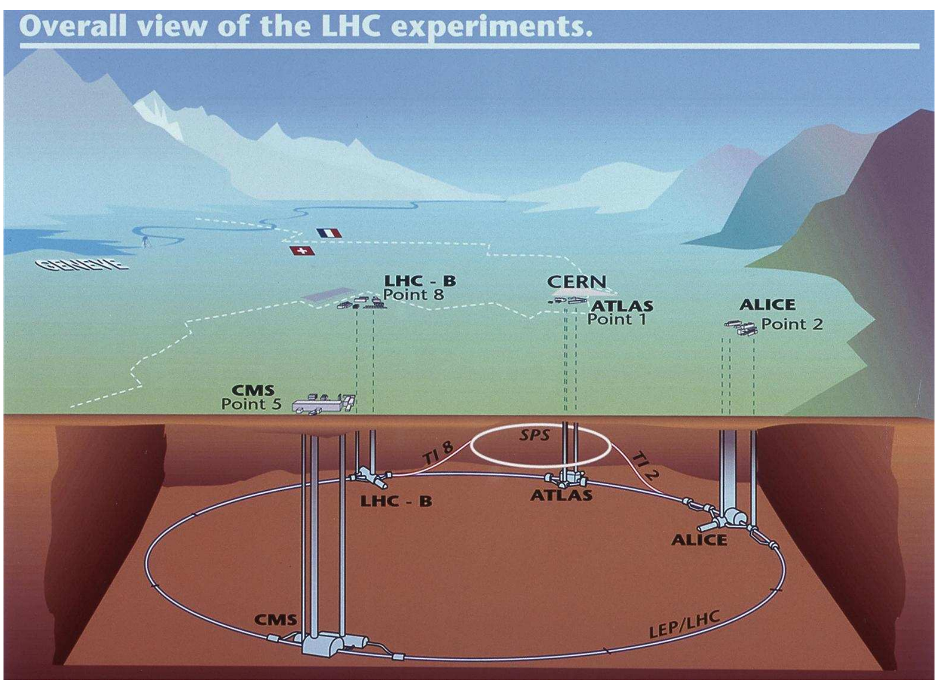

The advantage of circular over linear accelerators is that the ring topology allows continuous acceleration, as the particle can transit several times [2]. Another advantage is that circular accelerators require relatively smaller size than a linear accelerator of comparable power. The beams move around the LHC ring inside a continuous vacuum guided by superconducting magnets that are cooled to 1.9 K by a huge cryogenics system and can be stored at high energies for hours. Even though in the next paragraphs the properties of the colliding mechanism are briefly explained, Table 2.1 presents the most important parameters of the LHC design.

2.2 The CERN Accelerator Complex

The proton beam origin that is accelerated, is the result of a chemical reaction chain [1], analytically:

$$H_2 + e^- \rightarrow H_2^+ + 2e^- \tag{2.1}$$

$$H_2^+ + e^- \rightarrow H^+ + H + e^- \tag{2.2}$$

$$H + e^- \rightarrow H^+ + 2e^- \tag{2.3}$$

This reactions take place when hydrogen gas is injected into a metal cylinder shown in Picture 2.3, called *Duoplasmatron* [1]. That leads to break down of the gas into its constituents protons and electrons. The protons, with energies that can reach 100 keV, then enter the accelerator complex, which is a succession of machines that increasingly accelerate to higher energies [4], as the diagram 2.4 shows. The beam is accelerated gradually as injected through the machines sequence, until it reaches the LHC. The start is the Radio Frequency Quadrupole (QRF), an accelerating component where four vanes (electrodes) provide a quadrupole RF field that both speeds up to 750 keV and focuses the beam [1]. From the quadrupole, the particles are sent to the linear accelerator (LINAC2). The LINAC2 tank is a multi-chamber resonant cavity tuned to a specific frequency which creates potential differences in the cavities that accelerate the particle up to 50 MeV [1]. Protons cross the LINAC2 and reach the 157 m circumference circular accelerator Proton Synchrotron Booster (PSB) in a few microseconds.

A distance of 80 m intercedes between the LINAC2 and the PSB, where twenty quadrupole magnets focus the beam along the line and two bending and eight steering magnets direct the beam. Afterwords, the PS Booster accelerates the beam to 1.4 GeV in 530 ms and injects it in the 628 m circumference circular accelerator Proton Synchrotron (PS) in less than 1 μs [1]. The PS is responsible to feed the Super Proton Synchrotron (SPS) with beam of 25 GeV energy [5] in bunches with the appropriate

Table 2.1: Important parameters of the LHC design [1].

LHC parameters	
Circumference	26659 m
Dipole operating temperature	1.9 K
Number of arcs (2450 m long)	8
Number of lattice cells per arc	23
Number of straight sections (545 m long)	8
Main RF System	400.8 MHz
Number of magnets (dipoles, quadrupoles ... dodecapoles)	9300
Number of dipoles	1232
Number of quadrupoles	858
Number of RF cavities	8/ beam
Nominal energy (protons)	7 TeV
Momentum at collision	7 TeV/c
Momentum at injection	450 GeV/c
Nominal energy (ions)	2.76 TeV/$nucleon$
Peak magnetic dipole field	8.33 T
Current in main dipole	11800 A
Energy density of the LHC magnets	500 kJ/m
Main dipole coil inner diameter	56 mm
Distance between aperture axes (1.9 K)	194.00 mm
Distance between aperture axes (293 K)	194.52 mm
Main Dipole Length	14.3 m
Horizontal force at 8.33 T (inner and outer layer)	1.7 MN/m
Maximum current with NO resistance (1.9 $Ke,\ 8.33\ T$)	17000 A
Maximum current with NO resistance (1.9 $Ke,\ 0\ T$)	50000 A
Number de strands per cable	36
Bending radius	2803.95 m
Minimum distance between bunches	$\sim 7\ m$
Bunch spacing	25 ns
Design Luminosity	$10^{34}\ cm^{-2} \cdot s^{-1}$
Number of bunches / proton beam	2808
Number of protons / bunch (at start)	$1.15 \cdot 10^{11}$
Circulating current / beam	0.54 A
Number of turns / second	11245
Stored beam energy	360 MJ
Stored energy in magnets	11 GJ
Beam lifetime	10 h
Average crossing rate	31.6 MHz
Number of collisions / second	600 $millions$
Radiated Power / beam (synchrotron radiation)	$\sim 6\ KW$
Total crossing angle (collision point)	300 μrad
Emittance ϵ_n	3.75 μrad
Amplitude Function β	0.55 m

Figure 2.3: The proton beam origins from hydrogen gas injected into a metal cylinder, surrounded by electric field [1]. The Figure presents the metal cylinder, also called Duoplasmatron.

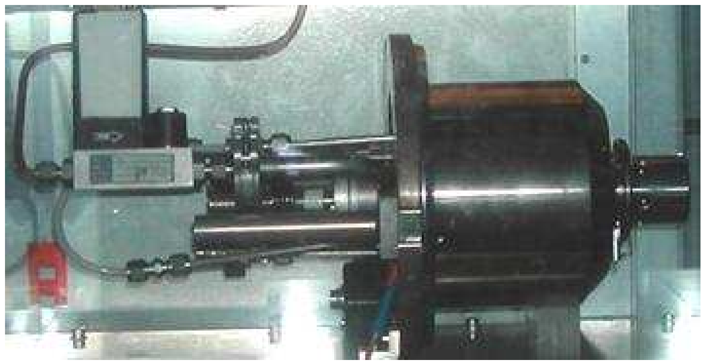

Figure 2.4: Schematic view of the different machines succession through which the proton beams gradually accelerated until they reach their final energy at the LHC [5].

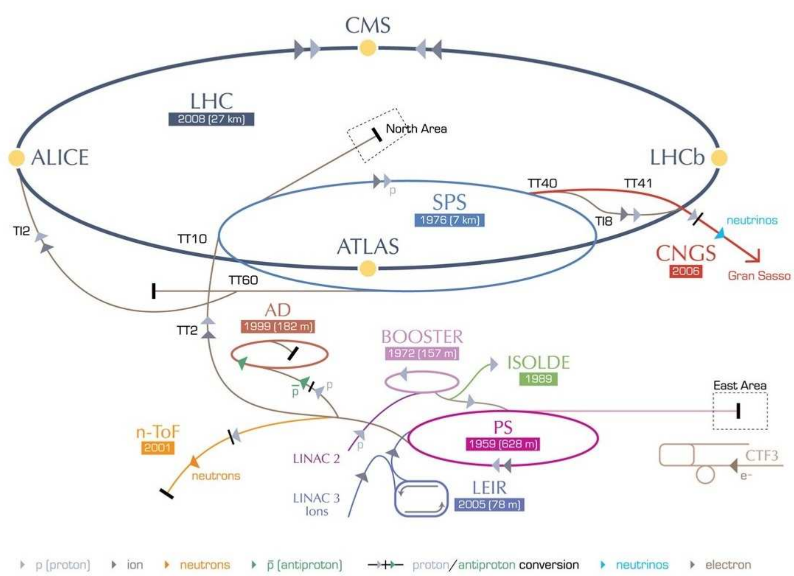

spacing. During the Run-I period the bunch spacing was 50 ns and it is expected to be half during the Run-II operation. The SPS is the final step before the beam transferred to the LHC with an energy of 450 GeV both in clockwise and counter-clockwise directions after a filling time of 4.20 *minutes* per LHC ring. In the LHC, the beams circulate until they ramp to high energy and can be stored up to 10 *hours*, this is the so called "beam lifetime".

The higher the density of the stored particles is, the lower the beam lifetime is. Coulomb scattering of charged particles traveling together causes an exchange of momentum between the transverse and longitudinal directions. Due to relativistic effects, the momentum transferred from the transverse to the longitudinal direction is enhanced by the relativistic factor γ. For stored beam, particles are lost (Touschek effect) if their longitudinal momentum deviation exceeds the RF bucket or the momentum aperture determined by the lattice.

After the dump of the beam, the dipole magnets are ramped down to 0.54 T. Meanwhile beam injection is repeated before the magnets are ramped up again to 8.3 T for another cycle of high energy collisions.

2.3 Proton Beams Collisions

The beams after the acceleration to the desired energy, e.g. 7, 8, 14 TeV, collide at the four collision points of the LHC while circulated in the beam lines. Between each consecutive bunch there is 7.5 m distance, which makes

$$26659\ m/7.5\ m\ \approx 3550\, bunches \tag{2.4}$$

given the LHC circumference of $27km$ [1].

To get a correct sequence of bunches injected into the ring and to be able to insert new bunches when non-useful ones are extracted it is necessary to allow enough space for that. The effective number of bunches per beam is 2808. Each bunch has $1.15 \cdot 10^{11}$ protons (1 cm^3 of hydrogen gas has $\sim 10^{19}$ protons). Each bunch gets squeezed down (using magnetics lenses) to $16 \times 16\ \mu m$ at an interaction point, where collisions take place [6]. The occupied volume for each proton in the interaction point is:

$$(74800 \times 16 \times 16)/(1.15 \cdot 10^{11}) \sim 10^{-4}\ \mu m^3. \tag{2.5}$$

That is much bigger than an atom, so a collision is still rare. The probability of one particular proton in a bunch colliding with a particular proton in the opposite bunch depends roughly on the proton size (d^2 with $d \sim 1\ fm$) and the cross-sectional size of the bunch (σ^2, with $\sigma = 16\ \mu m$) in the interaction point [1]. The exact relation is described by the equation:

$$Probability = \frac{d_{proton}^2}{\sigma^2} = 4 \cdot 10^{-21}. \tag{2.6}$$

A sufficient number of interactions in every crossing is achieved with $N = 1.15 \cdot 10^{11}$ protons/bunch, since the number of interactions per crossing is given by:

$$Probability \times N^2 \approx 50. \tag{2.7}$$

Taking into account that a fraction of $\sim 50\%$ are inelastic scatterings that give rise to particles at sufficient high angles with respect to the beam axis. Therefore, there are about 20 ”effective” collisions at every crossing. With 11245 crosses per second and considering the number of bunches to be equal to the effective (= 2808), the average crossing rate is estimated to be:

$$11245 \times 2808 = 31.6\ million\ crosses. \tag{2.8}$$

The collisions per second can be calculated by multiplying the average crossing rate with the collision probability:

$$(31.6 \cdot 10^6\ crosses/s) \times (20\ collisions/cross) = 600\ k\,collision/s. \tag{2.9}$$

Considering 3550 bunches and the 11245 crossings per second the frequency is $\sim$ 40 MHz.

2.4 The LHC Experiments

As previously mentioned, the LHC ring hosts collision points, where the ATLAS, CMS, ALICE and LHCb experiments are located. The two large experiments, ATLAS and CMS, are based on general-purpose detectors and are designed to investigate the largest range of physics possible. Having two independently designed detectors is vital for cross-confirmation of any new discoveries made. The rest medium-sized experiments, ALICE and LHCb, have specialized detectors for analyzing the LHC collisions in relation to specific phenomena [1]. Two other experiments, the LHCf and the TOTEM, are located very close to the ATLAS and CMS facilities respectively and designed to focus on ”forward particles” (protons or heavy ions). The term forward particles refers to particles that do not meet head-on. In December 2009, the CERN Research Board approved another experiment called “MoEDAL” (the Monopole and Exotics Detector at the LHC) for the research of very specific exotic particles.

The detectors principle is to identify the products of the collisions of the proton beams, based on simple properties:

- *Charged Particles, electrons, protons and muons, leave traces through ionization*
- *Electrons are light particle (0.51 MeV) compared to protons (938.27 MeV) and therefore lose energy quicker (in the calorimeters), while protons penetrate deeper into the detector*
- *Photon traces in the electromagnetic calorimeters are the result of their decay into an electron-positron pair*
- *Neutral hadrons transfer their energy to protons*
- *Muons leave traces in the trackers, pass through the calorimeters loosing a small amount of their energy and reach the outer layers of the detectors, the muon chambers*
- *Neutrinos do not interact with the detector, but can be identified using the missing energy of each event*
- *The trajectories of charged particle are bent by the magnetic fields and the radius of the curvature is used to calculate their momentum.*

The above interactions are summarized in the Figure 2.5 for each particle passing through the different detector components. Heavy collision products, such as the Z or $W^{\pm}$ bosons, are short-lived and decay into lighter particles which are detectable. The complexity of the detectors arises from the ability to built a system able to identify fast enough particles within a harsh background, reading the useful information out reliably and reconstructing it accurately.

In the next paragraphs brief descriptions of the LHC experiments is given.

2.4.1 ATLAS

ATLAS acronym means "A Toroidal LHC ApparatuS" describing the world's largest general purpose particle detector, measuring 46 m long, 25 m high, 25 m wide, weighting 7000 $tons$ and consisting of 100 million sensors [1]. It records sets of measurements on the particles created in collisions - their paths, energies, and their identities [7]. This is accomplished through six different detecting subsystems, shown in Figure 2.6, that identify particles and measure their momentum and energy. The inner layer of the ATLAS is the tracker, which consists of a silicon pixel, a silicon micro-strip and a transition radiation gas detector. The next technology, outer from the tracker is the Liquid Argonne Calorimeter ("LAr"), consisting of a barrel and forward calorimeter. The ATLAS has another calorimeter technology, the Tile Calorimeter, made from plastic scintillator tiles to detect hadrons in the barrel region. The Muon spectrometer

Figure 2.5: Particles interactions as passing through the different layers of a detector [1]. The figure represents the basic principles of the particle identification.

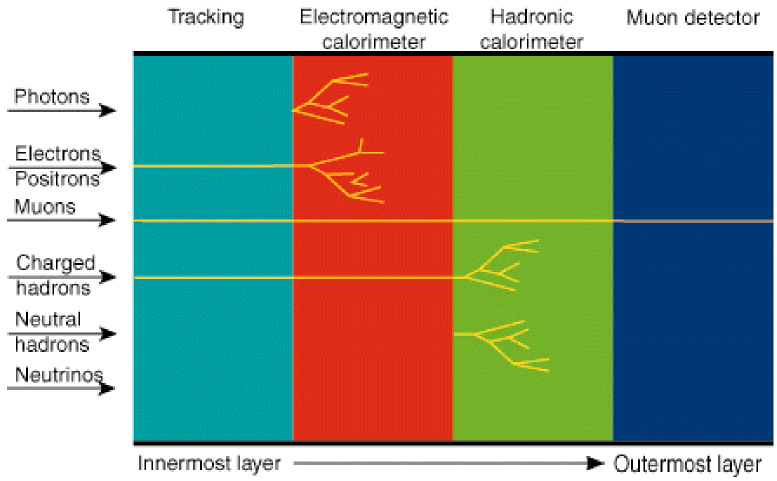

is based on four different technologies, the Cathode Strip Chambers ("CSC") and the Monitored Drift Tubes ("MDT") are used for the precision tracking and the Thin Gap Chambers ("TGC") and the Resistive Plate Chambers ("RPC") provide the trigger. The coverage of the muon spectrometer extends to the very forward region where there is no tracker coverage, with the ability to provide muon track reconstruction. Another vital element is the huge magnet system, combination of toroidal and solenoid magnets, that bends the paths of charged particles for the momentum measurement [8]. In the next chapter, a detailed description of the ATLAS detector is given.

2.4.2 CMS

The Compact Muon Solenoid ("CMS") is the other of the two general-purpose LHC experiments [9]. Although it has the same scientific goals as the ATLAS experiment, it uses different technical solutions and design of its detector magnet system to achieve these [1]. The CMS detector is built around a huge solenoid magnet as shown in Figure 2.7. This takes the form of a cylindrical coil of superconducting cable that generates a magnetic field of 4 T. The main volume of the CMS detector is a multi-layered cylinder, 21 m long, 15 m wide and 15 m high, weighing 12500 $tons$. The innermost layer is a silicon-based particle tracker, surrounded by a scintillating crystal electromagnetic calorimeter which is itself surrounded with a sampling hadronic calorimeter. Both fit inside a central superconducting solenoid magnet, 13 m long and 6 m in diameter, that bents charged particles to allow their momentum measurements. Outside the magnet, are the large muon detectors, which are inside the return yoke of the magnet.

Figure 2.6: Figure of the ATLAS detector [3] showing the constituting subsystems, i.e. Inner Detector, Electromagnetic - Forward - Hadronic Calorimeters, Muon Spectrometer, Toroid and Solenoid Magnets.

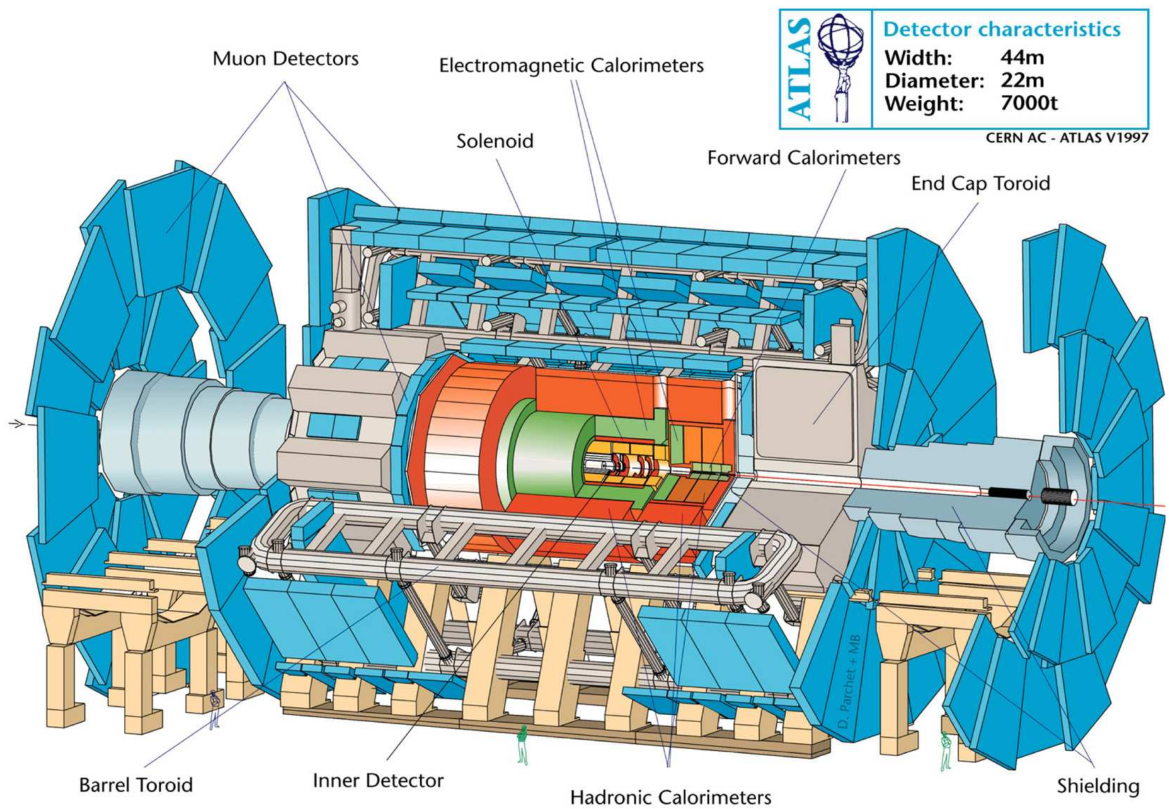

Figure 2.7: The Compact Muon Solenoid ("CMS") detector schematic view [1]. The different components are marked on the Figure.

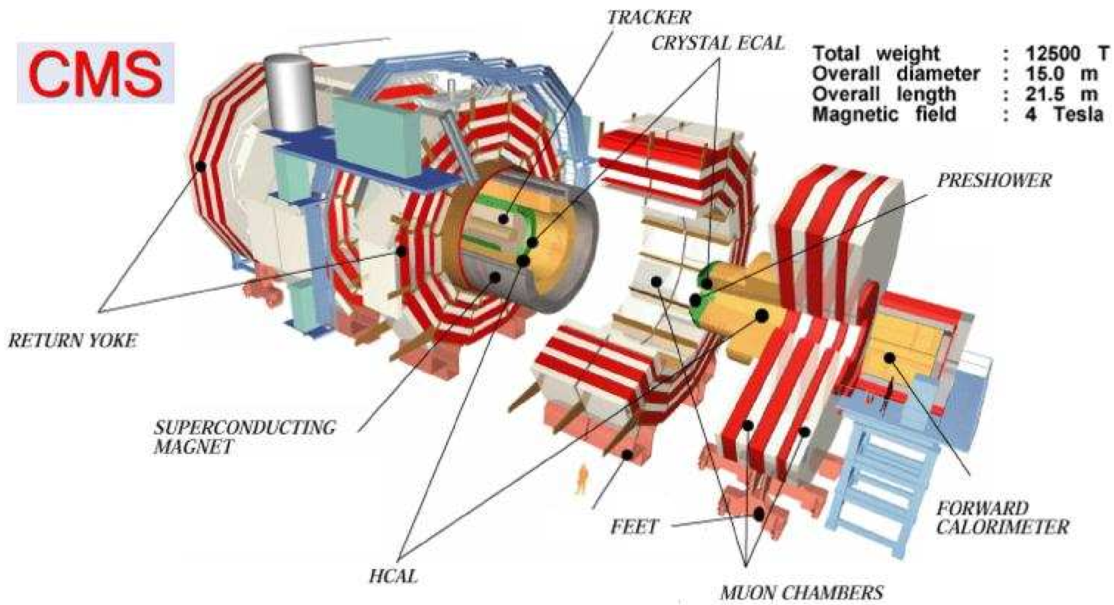

2.4.3 ALICE

ALICE (A Large Ion Collider Experiment) designed to study relativistic heavy ion interactions and the physics of strongly interacting matter at extreme densities where the formation of a new phase of matter, the quark-gluon plasma, is expected [10]. The heavy ions, specifically lead ions, are produced from a highly purified lead sample heated to a temperature of about $550°C$. The lead vapor is ionized by an electron current, which produces many different charged states with a maximum around Pb^{27+}. These ions are selected and accelerated to 4.2 $MeV/nucleon$ before passing through a carbon foil, which strips most of them to Pb^{54+}. The Pb^{54+} beam is accumulated, then accelerated to 72 $MeV/nucleon$ in the Low Energy Ion Ring ("LEIR"), which transfers them to the PS. The PS accelerates the beam to 5.9 GeV/$nucleon$ and sends it to the SPS after first passing it through a second foil where it is fully stripped to Pb^{82+}. The SPS accelerates it to 177 GeV/u then sends it to the LHC, which accelerates it to 2.76 TeV/u.

The detector consists of two main components: the central part composed of detectors dedicated to the study of hadronic signals and electrons, and the forward muon spectrometer dedicated to the study of quarkonia behavior in dense matter. The central part is embedded in a large solenoid magnet with a weak field (full current of 6000 A and magnetic field of 670 mT). The innermost part of the detector is the tracking system, which consists of the inner tracking system ("ITS") and the outer tracking system ("TPC"). TPC is a time projection chamber, a cylindrical device filled with gas and incorporating uniform electric and magnetic fields, ideal for separating, tracking, and identifying thousands of charged particles in a dense environment. A schematic representation of the ALICE detector is given in Figure 2.8.

2.4.4 LHCb

The LHCb detector (Large Hadron Collider beauty experiment) is a 21 m long, 10 m high and 13 m wide detector specializes in investigating the CP violation and other rare phenomena in decays of hadrons with heavy flavors, in particular B-mesons [12]. The interest in CP violation comes not only from the elementary particle physics but also from the cosmology, in an attempt to explain the dominance of matter over antimatter observed in the universe. B-mesons are most likely to emerge from collisions close to the beam direction, so the LHCb detector is designed to catch low-angle particles. The VErtex LOcator ("VELO") is mounted closest to collision point subdetector of the LHCb and uses silicon detector elements to pick out the short-live B-mesons [13]. The products of the B-meson decay, $\pi^{\pm}$, K^0 and protons, can be detected from the two RICH (Ring Imaging Cherenkov) detectors by measuring the cones of the Cherenkov radiation. Precision tracking is provided by the silicon tracker and the gas-filled straw tubes of the outer tracker. The detector also consists of electromagnetic and hadron calorimeters for the energy measurement, as well as a muon system in the far end of the detector, as shown in Figure 2.9. A sophisticated feature of the LHCb is that the tracking detectors are movable close to the path of the beams circling in the LHC in order to catch the b-hadrons from the abundance of different types of hadrons created by the LHC.

2.4.5 TOTEM

The TOTEM (Total Cross Section, Elastic Scattering and Diffraction Dissociation) experiment aims to measure the total p-p cross-section and study elastic and diffractive scattering at the LHC [1]. The hosting point of the TOTEM detectors is near the protons collision point in the center of the CMS detector. The experiment measures particles scattering at very small angles from the LHC's proton-proton collisions, allowing the study of physical processes such as how the shape and size of a proton varies with energy, unable to be measured by any other of the LHC experiments. It includes detectors housed in specially designed vacuum chambers called "Roman pots" connected to the beam pipes in the LHC. There are eight Roman pots, placed in pairs

Figure 2.8: ALICE detector designed for the study of relativistic heavy ion collisions [11].

Figure 2.9: The LHCb detector designed to explore the CP violation and other rare phenomena in decays of hadrons with heavy flavors, in particular B-mesons [13].

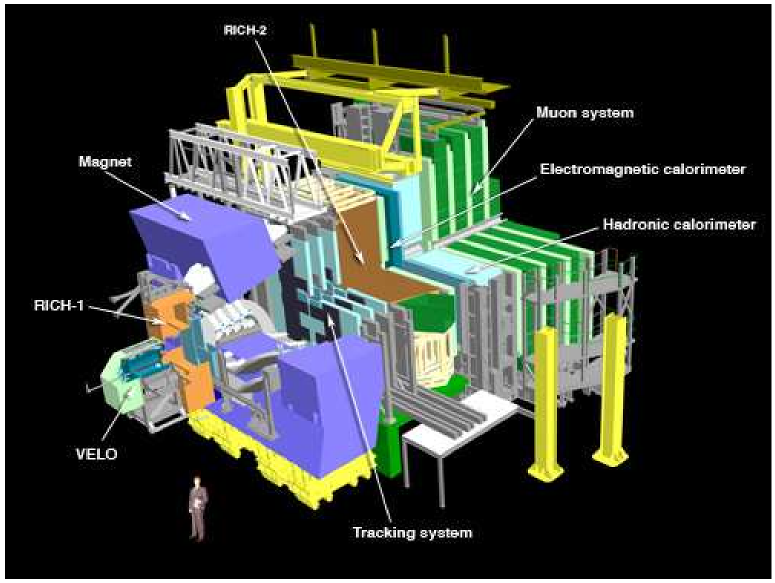

at four locations on either side of the collision point of the CMS experiment, including micro-strip silicon detectors used to detect protons [14]. Although the experiment is scientifically independent from other, TOTEM complements the results from the CMS detector and from other LHC experiments. The 20 tons TOTEM detector, in addition to the 8 Roman pots, is made up of gas-electron-multiplier ("GEM") detectors and cathode strip chambers that measures the jets of forward-going particles that emerge from collisions when the protons break apart [15]. The experiment, schematically presented in Figure 2.10, spans over 440 m and the main detector is 5 m high and 5 m wide.

2.4.6 LHCf

The LHC forward experiment ("LHCf") is placed on either sides of the ATLAS experiment for accurately measuring the number and energy of neutral pions and other forward particles in the ATLAS collisions [1]. The aim of the LHCf experiment is the study of the neutral-particle production cross sections in the very forward region of proton-proton and nucleus-nucleus interactions. The study is essential for the understanding of the development of atmospheric showers induced by very high energy cosmic rays hitting the Earth atmosphere. Studying how collisions inside the LHC cause similar cascades of particles to those of cosmic rays, it will help to interpret and calibrate

Figure 2.10: The Total Cross Section, Elastic Scattering and Diffraction Dissociation experiment ("TOTEM") extended at both sides of the CMS detector [16].

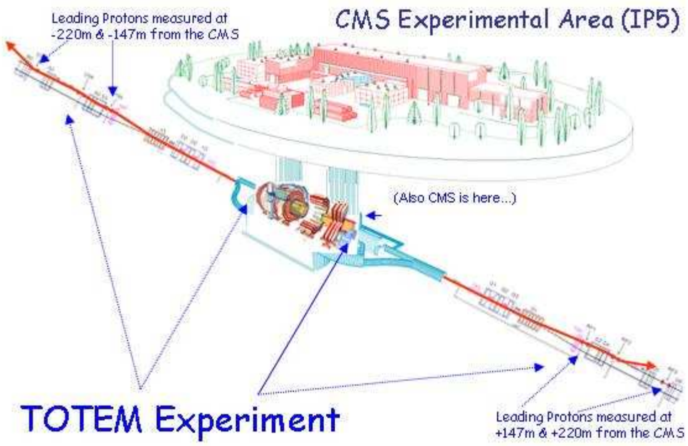

large-scale cosmic-ray experiments that can cover thousands of kilometers. The LHCf detector, presented in Figure 2.11, consists of two electromagnetic calorimeters made of tungsten plates, plastic scintillator and position sensitive sensors, installed at zero degree collision angle ± 140 m from the ATLAS interaction point inside the "TAN" [17]. The TANs (Target Neutral Absorber) are massive zero degree neutral absorbers where charged particles transit from a single common beam tube to two separate beam tubes joining to the arcs of LHC.

2.4.7 MoEDAL

The search strategy for exotics planned for the main LHC detectors can be extended with dedicated experimental designs to enhance, in a complementary way, the physics reach of the LHC [18]. The MoEDAL (Monopole and Exotics Detector at the LHC) project is such an experiment. The prime motivation is to directly search for the Magnetic Monopole or Dyon and other highly ionizing Stable or pseudo-stable Massive Particles ("SMPs") at the LHC. The magnetic monopoles can be detected through the electromagnetic interaction between the magnetic charge and the macroscopic quantum state of a superconducting loop [19]. The Nuclear Track Detectors ("NTD"), shown in Figure 2.12, will be able to record the tracks of highly ionizing particles with electromagnetic charges greater than 206 e. The detection of even one magnetic monopole that fully penetrated a NTD stack is expected to be distinctive. Another important area of physics beyond the Standard Model that can be addressed is the existence of SMPs with single electrical charge which provides a second category of a particle that

Figure 2.11: The LHCf simply consists of two calorimeters to accurately study the number and energy of neutral pions and other forward particles in the ATLAS collisions [1].

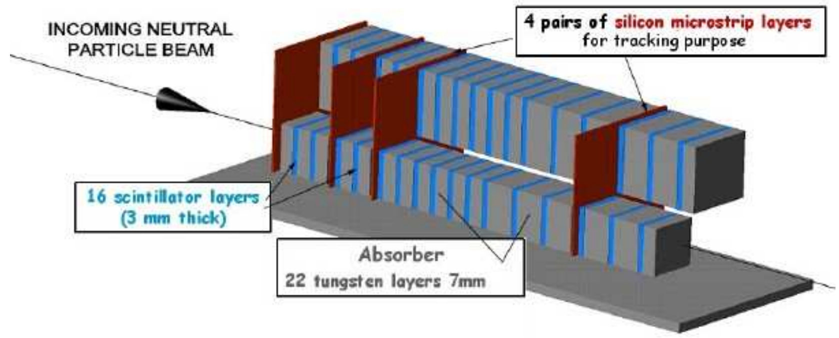

is heavily ionizing by virtue of its small speed. The third class of SMP which could be accessed by MoEDAL has multiple electric charge such as the black hole remnant, or long-lived doubly charged Higgs bosons. SMPs with magnetic charge, single or multiple electric charge and with Z/β ($\beta = v/c$) as low as five can, in principle, be detected by the CR39 nuclear track detectors, putting them within the physics reach of MoEDAL.

Figure 2.12: Schematic view of the MoEDAL Nuclear Track Detectors ("NTD") to enhance the exploration of the exotic searches [1].

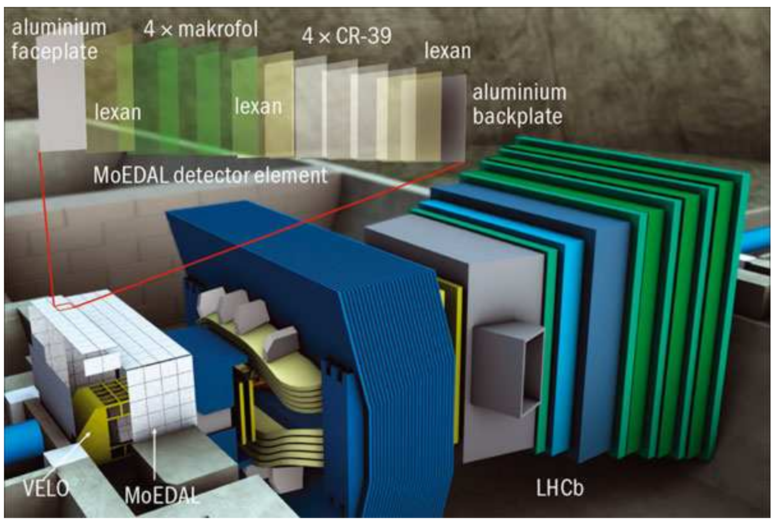

Chapter Bibliography

[1] X. C. Vidal, R. Cid, and M. Rey, Taking a closer look at LHC, http://www.lhc-closer.es.

[2]

[3] ATLAS Collaboration, The ATLAS experiment portal, http://www.atlas.ch/.

[4] C. Lefevre, LHC: the guide, Feb 2009, https://cds.cern.ch/record/1165534.

[5] Christiane Lefvre, The cern accelerator complex, Dec 2008, https://cds.cern.ch/record/1260465.

[6] Lyndon Evans, The Large Hadron Collider: A marvel technology, *Lausanne, Switzerland: EPFL (2009) 251 p*, 2009.

[7] CERN, ATLAS: Detector and physics performance technical design report. Volume 1, 1999.

[8] ATLAS Collaboration, ATLAS: Detector and physics performance technical design report. Volume 2, 1999.

[9] G.L. Bayatian et al., CMS physics: Technical design report, 2006.

[10] ALICE: Technical proposal for a large ion collider experiment at the CERN LHC, 1995.

[11] Berkeley Lab News Center, A flow of heavy-ion results from the LHC, http://newscenter.lbl.gov/2010/12/08/heavy-ion-results-lhc/.

[12] *LHCb : Technical Proposal*, Tech. Proposal. CERN, Geneva, CERN-LHCC-98-004, LHCC-P-4.

[13] LHCb Collaboration, The large hadron collider beauty experiment, http://lhcb-public.web.cern.ch/lhcb-public/en/Detector/Detector-en.html.

[14] TOTEM Collaboration, The TOTEM experiment, http://home.web.cern.ch/about/experiments/totem.

[15] G. Anelli et al., The TOTEM experiment at the CERN Large Hadron Collider, *JINST*, 3:S08007, 2008.

[16] TOTEM Collaboration, Overall view of the totem experiment, BUL Collection - BUL-PHO-2009-080, Aug 2009.

[17] O. Adriani et al., The LHCf detector at the CERN Large Hadron Collider, *JINST*, 3:S08006, 2008.

[18] MoEDAL Collaboration, The MoEDAL experiment, http://moedal.web.cern.ch/.

[19] James L. Pinfold, Searching for the magnetic monopole and other highly ionizing particles at accelerators using nuclear track detectors, *Radiat.Meas.*, 44:834–839, 2009.

[20] Maximilien Brice, First lhc magnets installed at lhc, Apr 2005, https://cds.cern.ch/record/834351.

[21] Lund University, Particle physics - ALICE website, http://www.hep.lu.se/alice/.

[22] James Pinfold et al., Technical Design Report of the MoEDAL Experiment, 2009.

[23] Oliver S. Bruning, P. Collier, P. Lebrun, S. Myers, R. Ostojic, et al., LHC Design Report. 1. The LHC Main Ring, *CERN-2004-003-V-1, CERN-2004-003*, 2004.

[24] The LHC experiments, http://public.web.cern.ch/public/en/lhc.

3

Atlas Detector Description

3.1 Introduction

The ATLAS (A Toroidal LHC Apparatus) experiment is a general-purpose detector at the LHC, whose design was guided by the need to accommodate the wide spectrum of possible physics signatures [1]. The major remit of the ATLAS experiment is the exploration of the TeV mass scale where ground-breaking discoveries are expected, such as the discovery of the Higgs boson. The electroweak symmetry breaking is only one focus of the investigation, as research is also conducted for all kinds of physics beyond the Standard Model.

The design and construction of the ATLAS detector is briefly introduced in this chapter. Summaries of the key aspects and functionalities of each component are reported and their future upgrades are also discussed. Upgrades are expected during the long shutdown periods referred to as ”Phase Upgrades”. The Phase-0 is the era between the Run-I and Run-II, the Phase-I is the long shutdown after the Run-II and later another one will follow in order to transit to the high luminosity LHC scenario (HL-LHC).

3.2 The Coordinate System

The origin of the ATLAS coordinate system is defined as the nominal interaction point in the center of the detector [2]. The z-axis runs parallel to the beam line in counterclockwise direction. Half of the detector that corresponds to positive values of z is referred to as side A and the other half as side C. The x-axis points to the center of the LHC ring and the y-axis points upwards to the surface, resulting in a right-handed orientation. The xy-plane is referred to as the transverse plane. The ATLAS detector has a global cylindrical structure, where each subdetector consists of concentric layers around the beam axis, the barrel component, and two EndCaps formed by disks perpendicular to the z-axis on each side of the interaction point. A coordinate system closely related to cylindrical coordinates is convenient. The radial distance is given by $R = \sqrt{x^2 + y^2}$. The azimuthal angle $\phi \in [-\pi, \pi]$ is the angle with the positive x-axis and increases in clockwise direction when looking down the positive z-axis. The polar angle $\theta \in [0, \pi]$ is defined as the angle with the positive z-axis, albeit generally replaced by the pseudorapidity η, which is given by

$$\eta = -ln(tan\frac{\theta}{2}) \tag{3.1}$$

The preference for this quantity is motivated by the particle flux being roughly constant as a function of η. A direction (η, ϕ) is assigned to the reconstructed final state objects and the opening angle between two of them is denoted ΔR:

$$\Delta R = \sqrt{(\Delta\eta)^2 + (\Delta\phi)^2} \tag{3.2}$$

3.3 Performance Requirements

The performance requirements for the design of the ATLAS detector are based on the processes that may be observed at this new energy scale, such as the production of the Higgs boson, SUSY particles or any kind of Beyond the SM physics. The extensive variety of objects to be detected, the broad energy range of particles to be measured, the high radiation conditions and the high collision rate impose strict requirements on the detectors precision, speed, performance, radiation hardness, efficiency and acceptance. An additional challenge is the instantaneous selection of collisions to be stored, which is taken care of by the trigger system.

3.4 The Inner Detector

The ATLAS inner detector is designed to cope with 10^3 charged particle tracks for every beam collision every 25 ns [1] at the design luminosity of the LHC [1]. A powerful magnetic field causes the particle carrying electric charge tracks to bend, and the curvatures of these tracks allow the momentum and electric charge of each particle to be determined. Concentric layers of high precision tracking detectors are used to record the tracks as they fly away from the interaction point. The inner detector is the first detector layer, very close to the collision point, as seen in Figure 3.1, where the radiation levels are intense, fluxes are up to 10^5 particles per mm^2 per sec, making radiation hardness a top priority for detector and readout electronics. At the same time, the amount of material in the Inner Detector must be minimized to avoid obstructing the particle trajectories (< 0.1 mm [3]). In the next subsections, the different technologies that the ATLAS uses for tracking are briefly described along with the central solenoid that provides the necessary magnetic field.

Figure 3.1: Inner detector schematic where the different technologies that it aparts (Pixel, Silicon and Transition Radiation Tracker) are visible [2].

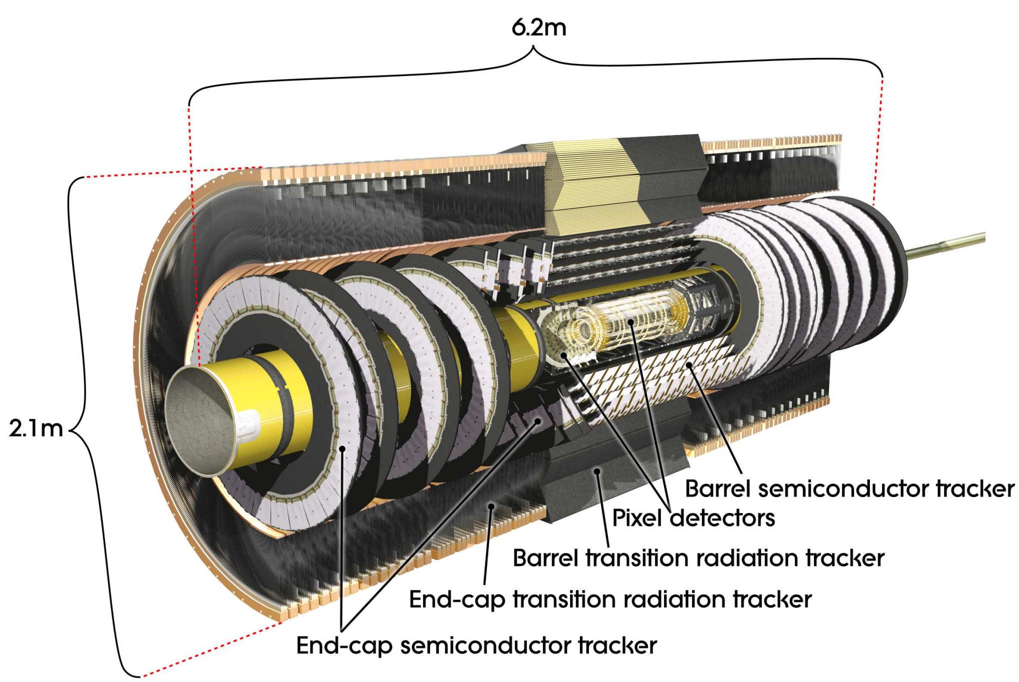

[1] Design value. During the Run-I period it was 50 ns.

Figure 3.2: The B-layer of the inner detector replaced after the Run-I [6]. Figure (a) taken during the extraction which followed by the installation of a new module (IBL) (Figure (b)) as preparation for the Run-II [5]. Due to the high levels of radiation the lifetime of the module is three years of operations [4].

(a) (b)

3.4.1 Pixel Detector

The pixel detector system provides critical tracking information for pattern recognition near the collision point and largely determines the ability of the Inner Detector to find secondary vertices [4]. The pixel system provides three or more space points over the complete acceptance of the Inner Detector, $|\eta| < 2.5$. The innermost pixel layer is called B-layer and located as close as possible to the interaction point to provide the optimal impact parameter resolution. The Insertable B-layer (IBL) operated for the Run-I and replaced for the Run-II, Figure 3.2 shows the extraction followed by the installation of the IBL as preparation for the Run-II [5]. The two other barrel layers and the disk layers are located at radii greater than about 10 cm, for which the useful lifetime is expected to be about seven years at the design luminosity. Four disk layers on either side of the interaction point are required to provide full coverage for $|\eta| < 2.5$.

The layout and parameters of the pixel detector system are determined by performance requirements and by the desired lifetime of the system in the intense radiation environment near the collision point. The detector system is composed of modular units. Read out integrated circuits are mounted on a detector substrate to form barrel and disk modules. The detector substrate is silicon, and the current baseline design is an n^+ in n-bulk sensor. The read out integrated circuits are mounted on the silicon sensor using bump bonding techniques. An additional integrated circuit for control and clock distribution and data compression is mounted on each module, and flexible cables connect each module to data transmission/control circuitry located within the detector volume. Optical fibers or twisted pair cables are used to transmit data to and from the pixel system to read out drivers located outside the ATLAS detector. There are about

1500 identical barrel modules and about 1000 identical disk modules in the system. The barrel modules are mounted on supporting structures (staves) that are also identical throughout the system. Similarly, the disk modules are located on identical support sectors that are joined to form disks. The resulting mechanical structure is very stable and provides the cooling capability to maintain the silicon temperature at $\leq -6°C$ even with the large heat load from the electronics and other sources.

Specifically, a Pixel sensor is a $16.4 \times 60.8\ mm$ wafer of silicon with 46080 pixels, 50 microns each. A Pixel module comprises an un-packaged flip-chip assembly of 16 front-end chips bump bonded to a sensor substrate. There are 1744 modules in the Pixel Detector for nearly 80 million channels in a cylinder 1.4 m long, 0.5 m in diameter centered on the interaction point. The barrel part of the pixel detector consists of the 3 cylindrical layers with the radial positions of 50.5 mm, 88.5 mm and 122.5 mm respectively. These three barrel layers are made of identical staves inclined with azimuthal angle of 20 degrees. There are 22, 38 and 52 staves in each of these layers respectively. Each stave is composed of 13 pixel modules. In the module there are 16 front-end (FE) chips and one Module Control Chip (MCC). One FE chip contains 160 rows and 18 columns of pixel cells, i.e. 2880 pixels per FE chip or 46080 pixels per module. There are three disks on each side of the forward regions. One disk is made of 8 sectors, with 6 modules in each sector. Disk modules are identical to the barrel modules, except the connecting cables. The front-end chips are a major heat source (0.8 W/cm^2) dissipating more than 15 kW into the detector volume. This heat is taken out via integrated cooling channels in the detector support elements: Staves in the barrel region and Sectors in the forward region.

3.4.2 The Semiconductor tracker ("SCT")

The Semiconductor Tracker ("SCT") designed to provide four precision measurements per track in the intermediate radial range, contributing to the measurement of momentum, impact parameter and vertex position, as well as providing good pattern recognition by the use of high granularity [7]. The system is an order of magnitude larger in surface area than any silicon micro-strip detector of previous generations and faces high radiation levels.

The barrel SCT, shown in Figure 3.3 before the installation, uses four layers of silicon micro-strip detectors to provide precision points in the R, ϕ and z coordinates, using small angle stereo to obtain the z measurement. Each silicon detector is $6.36 \times 6.40\ cm^2$ with 768 readout strips each with 80 μm pitch. Each module consists of four detectors. On each side of the module, two detectors are wire-bonded together to form 12.8 cm long strips. Two such detector pairs are then glued together back-to-back at a 40 $mrad$ angle, separated by a heat transport plate, and the electronics are mounted above

Figure 3.3: The Barrel Semiconductor Tracker ("SCT") [8]. The high-precision and high-efficiency semiconductor detector elements near to the collision point distinguish individual tracks from the hundreds produced in each collision [3].

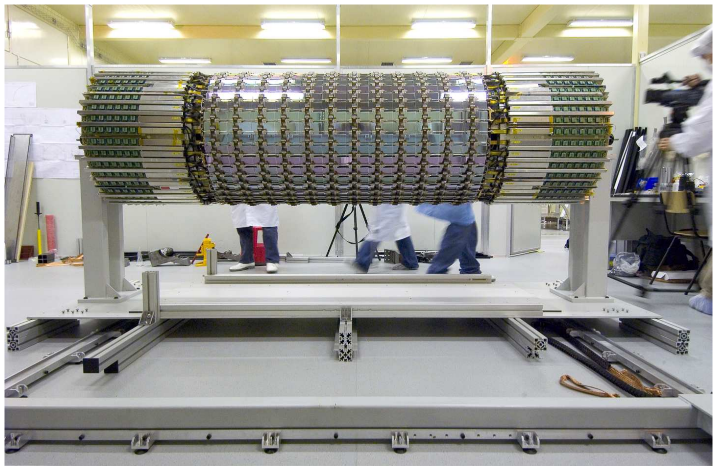

the detectors on a hybrid. The readout chain consists of a front-end amplifier and discriminator, followed by a binary pipeline which stores the hits above threshold until the first level trigger decision. The forward modules are very similar in construction but use tapered strips, with one set aligned radially. Forward modules are made with both 12 and 7 cm lengths.

The detector contains 61 m^2 of silicon detectors, with 6.2 million readout channels. The spatial resolution is 16 μm in $R\phi$ and 580 μm in z. Tracks can be distinguished if they are separated by more than 200 μm.

The barrel modules are mounted on local supports which allow units of six modules to be tested together before mounting on carbon-fibre cylinders which carry the cooling system; the four complete barrels at radii of 300, 373, 447 and 520 mm are then linked together. The forward modules are mounted in up to three rings onto nine wheels, which are interconnected by a space-frame. The radial range of each disk is adapted to limit the coverage to $|\eta| \leq 2.5$ by equipping each one with the minimum number of rings, and by using 6 cm long modules where appropriate.

The system requires a very high stability, cold operation of the detectors, and the evacuation of the heat generated by the electronics and the detector leakage current. The structure is therefore designed with materials with as low a coefficient of thermal expansion as possible. The cooling is a bi-phase system using ice suspended in a methanol-water mixture ("binary ice") to achieve low thermal gradients across the detector. The detector and its front-end electronics are expected to be operational for 10 years, given the irradiation levels [7].

3.4.3 Transition Radiation Tracker ("TRT")

The Transition Radiation Tracker ("TRT"), partially presented in Figure 3.4, is based on the use of straw detectors, which can operate at the very high rates needed by virtue of their small diameter and the isolation of the sense wires within individual gas envelopes [7]. Electron identification capability is added by employing xenon gas to detect transition-radiation photons created in a radiator between the straws. This technique is intrinsically radiation hard, and allows a large number of measurements, typically 36, to be made on every track at modest cost. However, the detector must cope with a large occupancy and high counting rates at the LHC design luminosity.

Each straw is 4 mm in diameter, giving a fast response and good mechanical properties for a maximum straw length of 150 cm. The barrel contains about 50000 straws, each divided in two at the center in order to reduce the occupancy and read out at each end. The EndCaps contain 320000 radial straws, with the readout at the outer radius. The total number of electronic channels is 420000. Each channel provides a drift-time measurement, giving a spatial resolution of 170 μm per straw, and two independent thresholds. These allow the detector to discriminate between tracking hits, which pass the lower threshold, and transition-radiation hits, which pass the higher. The discrimination is needed for the particles identification.

The barrel section is built of individual modules with between 329 and 793 axial straws each, covering the radial range from 56 to 107 cm. The modularity was chosen as a compromise between the ease of construction and maintenance, and the additional structural elements involved. The first six radial layers are inactive over the central 80 cm of their length, in order to reduce their occupancy, while providing extra coverage of the crack between the barrel and EndCap sections.

Each of the two EndCaps consists of 18 wheels. The 14 wheels nearest the interaction point cover the radial range from 64 to 103 cm, while the last four wheels extend to an inner radius of 48 cm in order to maintain a constant number of crossed straws over the full acceptance. To avoid an unnecessary increase in the number of crossed straws at medium rapidity, wheels 7 to 14 have half as many straws per cm in z as the other wheels.

A primary challenge of the design is to obtain good performance at high occupancy and high counting rate. In the barrel, the rate of hits above the lower threshold varies with radius from 6 to 18 MHz, while in the EndCaps the rate varies with z from 7 to 19 MHz. The maximum rate of hits above the higher TR-threshold is 1 MHz. Within a single drift-time bin, the occupancy is about one third of that in the entire straw active time window. A fast, low-noise preamplifier-shaper circuit with active baseline restoration has been developed to process the signals, using a radiation hard bipolar process. Position accuracies of about 170 μm have been achieved in tests at average straw counting rates of about 12 MHz. At these rates, only about 70% of the straws give correct drift time measurements because of shadowing effects, but the large number

Figure 3.4: View of the TRT before the installation [9]. Made from hundreds of thousands of narrow, gas-filled “straws”, each with a high-voltage wire running along its axis. Charged particles passing through the straw ionize the gas producing electrical pulses. The timing of these pulses allows the positions of the particles to be measured with a precision of 0.15 mm. Special materials are embedded between the straw tubes to cause electrons to produce X-rays when they pass through them, essential to distinguish electrons produced in collisions from heavier particles such as pions [3].

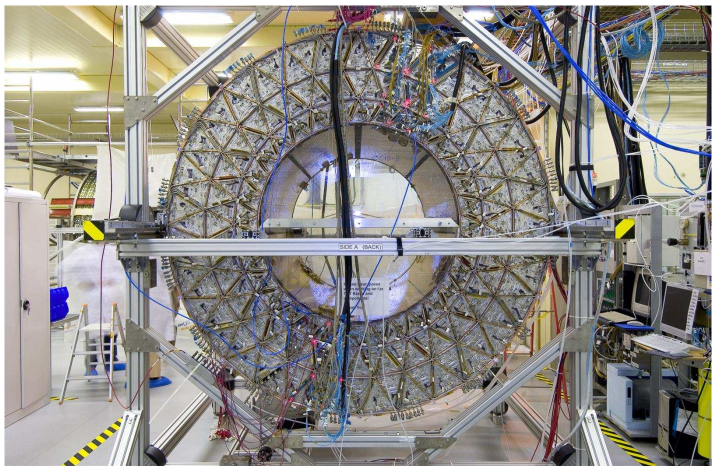

of straws per track guarantees a measurement accuracy of better than 50 μm averaged over all straws at the LHC design luminosity, including errors from alignment.

A good pattern recognition performance is assured by the continuous tracking. Within the radial space available, the straw spacing has been optimized for tracking at the expense of electron identification, which would be improved by a greater path length through the radiator material and fewer active straws. The distribution of the straws over the maximum possible path length also enhances the pattern recognition performance. The TRT contributes to the accuracy of the momentum measurement in the Inner Detector by providing a set of measurements roughly equivalent to a single point of 50 μm precision. It aids the pattern recognition by the addition of around 36 hits per track, and allows a simple and fast level-2 track trigger to be implemented. It allows the Inner Detector to reconstruct V^0s which are especially interesting in CP-violating B decays. In addition it provides additional discrimination between electrons and hadrons, with a pion rejection varying with η between a factor of 15 and 200 at 90% electron efficiency.

3.5 The Calorimeters

Surrounding the Inner Detector are the Calorimeters, which measure the energies of charged and neutral particles of the interaction [3]. The so-called "sampling calorimeters" consist of many layers of dense plates, which absorb incident particles and transform their energies into "showers" of lower energy particles. Between the absorber plates are thin layers of liquid argon or scintillating plastic which sample the energies of the particle showers and produce proportional signals. The calorimeters are designed to trigger on and to provide precision measurements of the energy of electrons, photons, jets, and missing E_T [10].

In order to explore the full physics potential of the LHC, the ATLAS electromagnetic ("EM") calorimeter must be able to identify efficiently electrons and photons within a large energy range (5 GeV to 5 TeV), and to measure their energies with a linearity better than 0.5% [2]. One of the key ingredients for the description of the detector performance is the amount and position of the upstream material. At larger radii, where most of the calorimeter weight is located, and where the radiation levels are low, a less expensive iron-scintillator hadronic "Tile Calorimeter" is used.

The following paragraphs describe the calorimeter technologies used in the ATLAS experiment.

3.5.1 The Liquid Argon ("LAr") Calorimeter

The Liquid Argon sampling calorimeter technique with "accordion-shaped" electrodes, as shown in Figure 3.5, is used for all electromagnetic calorimetry covering the pseudorapidity interval of $|\eta| < 3.2$ [10]. The Liquid Argon technique is also used for hadronic calorimetry from $1.4 < |\eta| < 4.8$. In order to operate a cryogenic system is needed. It includes the system for cooling down and warming up the cryostats and the detectors by circulation of helium. In routine operation, the cooling of the cryostats is achieved using liquid nitrogen produced in a closed loop by a liquefier located in the cryogenics cavern. This equipment has to maintain the temperature of liquid argon in the cryostats constant at approximately 89.3 K and the purity below 2 ppm of oxygen equivalent.

The Barrel EM Calorimeter, presented in Figure 3.6, has a cryostat of 6.8 m long, with an outer radius of 2.25 m, and an inner cavity radius of 1.15 m. Both the inner and the outer shells are in aluminum alloy, with vacuum insulation. The superconducting solenoid uses the same insulation vacuum as the liquid argon vessel. The total thickness of the bare solenoid is 44 mm, amounts to 0.63 X_0 and is supported by the warm flange of the inner shell. Inside the liquid argon vessel, the calorimeter consists of two identical half-barrels, with a gap of a few millimeters in between. Because of

Figure 3.5: Sketch of the accordion geometry structure of the EM calorimeter [10] which provides uniform response in all directions. It consists of closely-spaced absorber layers of stainless steel-clad lead with liquid argon as the sampling material. Particle showers produce ions in the liquid argon which are seen as electric pulses by segmented electrodes.

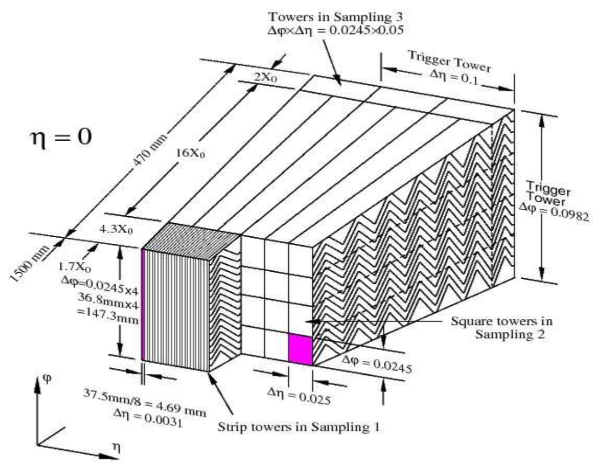

the accordion shape, each half-barrel appears continuous in azimuth. Each half-barrel consists of 1024 lead-stainless-steel converters with copper-polyimide multilayer readout boards in between. Fully pointing readout cells are defined in η and in azimuth by grouping together four (for the central towers) adjacent boards. Connections are made at the front and back face of the calorimeter using motherboards, which also carry the calibrating element (one resistor per readout and calibration signals are routed through cold-to-warm feedthroughs located at each end of the cryostat. Electronics boxes containing the readout elements, including the ADCs, are located on each feedthrough, and provide electrical continuity of the ground so as to form a single Faraday cage out of which come the digital signals.

In the EndCaps, the amplitude of the accordion waves scales with the radius. Given the practical limitations in fabricating the absorber plates, which are arranged like the spokes of a wheel, the ratio of inner to outer radius of a given plate is limited to about three. As a consequence each EndCap EM wheel consists of two concentric wheels, the large one spanning the pseudorapidity interval from 1.4 to 2.5, and the small one from 2.5 to 3.2. There are 768 plates in the large wheel (3 consecutive planes are grouped together to form a readout cell of 0.025 in ϕ) and 256 in the small wheel.

The amount of material, the way it is distributed in space and the presence of a magnetic field combine to necessitate a presampler to correct for the energy lost in front of the calorimeter. The barrel (EndCap) presampler feature, a 1 cm (5 mm) liquid argon active layer instrumented with electrodes roughly perpendicular (parallel) to the

Figure 3.6: View of the LAr Barrel EM calorimeter [11] after the cabling and insertion.

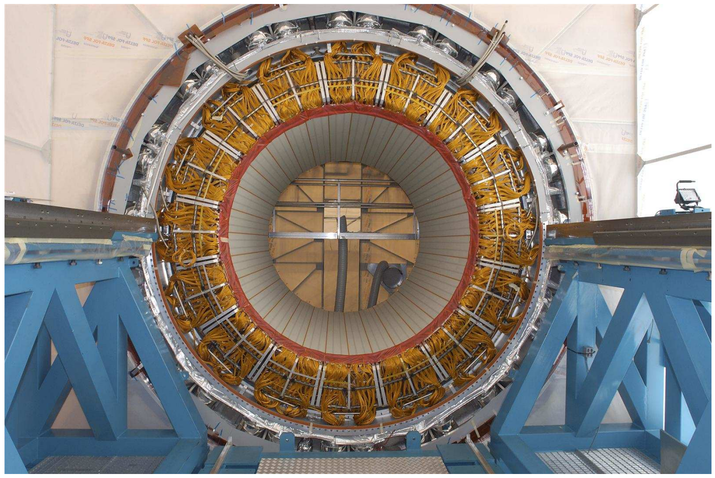

beam axis. In the transition region between barrel and EndCap, around $|\eta| = 1.4$, a scintillator layer, between the two cryostats, is used to recover mainly the jet energy measurement. This also helps for electrons and photons. Beyond a pseudorapidity of 1.8, the presampler is no longer necessary given the more limited amount of dead material and the higher energy of particles for a given p_T. In order to avoid creating a gap in the electromagnetic calorimetry coverage the electromagnetic EndCap wheels have to be as close as possible to the barrel modules. To satisfy this requirement, the gap between the two cryostats (95 mm), and the EndCap presampler, which is of minimum thickness, is encased in a notch of the cryostat cold wall. This takes advantage of the fact that at this radius the mechanical stresses in the EndCap cryostat cold wall are not too large.

The hadronic EndCap calorimeter ("HEC"), is a liquid argon (LAr) sampling calorimeter with copper-plate absorbers, designed to provide coverage for hadronic showers in the range $1.5 < |\eta| < 3.2$. The HEC detector elements are located in the EndCap cryostats at both ends of the ATLAS tracking volume. They share the cryostats with the EM and the forward calorimeter ("FCAL"). The HEC sits behind the EM and FCAL is completely shadowed by it. The boundary between the HEC and the is on a cylinder of radius 0.475 m. Thus the η boundary between the two detectors varies as a function of z. This technology was selected as it allows a simple mechanical design to be produced that is radiation resistant and covers the required area in a cost-effective way. The gaps between the copper plates are instrumented with a readout structure. This structure optimizes the signal-to-noise ratio while reducing the high-voltage requirement and ionization pile-up, and limiting the effect of failure modes such as high-voltage sparks and shorts. The signals are amplified and summed employing the concept of "active pads": the signals from two consecutive pads are fed into a separate amplifier mounted on the outer radius of the HEC. The use of cryogenic preamplifiers provides the optimum signal-to-noise ratio for the HEC. An important aspect of the HEC is its ability to detect muons, and to measure any radiative energy loss.

The FCAL provides electromagnetic and hadronic calorimetry coverage in the range $3.2 < |\eta| < 4.9$. The FCAL is a liquid argon ionization device integrated into the End-Cap cryostat so as to minimize the effects of the transition in the region $|\eta| \sim 3.2$. The three modules of the FCAL are positioned within the forward tube structure of the EndCap cryostat. A fourth module, a passive shielding plug, is also contained within the forward tube. The FCAL is composed of three modules; the electromagnetic (FCAL1) and two hadronic modules (FCAL2 and FCAL3). The FCAL1 module is of copper composition and the hadronic modules of tungsten and sintered tungsten alloy. All three modules have the same nominal outer dimensions (450 mm in z, 455 mm outer radius) and have a centered beam hole of different radius for each module. Structurally, the FCAL modules are quite simple, consisting of single absorber matrix bodies carrying an array of tube electrodes in holes in the matrix bodies. Mechanical stress considerations are, therefore, largely reduced to questions of tube electrode integrity near module bearing points. The modules are supported by contact between their outer circumferences and the inner surface of the cryostat's forward tube. The basic electrode cell used in the FCAL is a tubular electrode with the tube axis parallel to the beam line. The electrode is composed of a rod held within a tube to form an exceptionally thin cylindrical shell liquid argon gap between them. Unit cell dimensions have been optimized for physics performance. The tube electrode signals are summed at the module face to form readout cells. Cell signals are carried on miniature (1 mm diameter) polyimide-copper coaxial cables which run rearward in cable troughs on the module outer surfaces. These cables then emerge from the forward tube via notches in the rear face of the forward tube. A shielding plug is located behind the FCAL modules in the forward tube. This shielding plug acts to provide shielding for the most forward muon chambers and is not instrumented. The FCAL is designed to detect jets with an E_T resolution of $\sigma(E_T)/E_T < 10\%$ for $E_T > 100$ GeV [10]. This requires the FCAL energy resolution to be $\sigma(E)/E < 7\%$ and the jet angle resolution to be $\sigma(q)/q < 7\%$ typically. At the highest $|\eta|$, it is the angular resolution which dominates.

3.5.2 The Tile Calorimeter

The Tile Calorimeter is a large hadronic sampling calorimeter which makes use of steel as the absorber material and scintillating plates read out by wavelength shifting ("WLS") fibres as the active medium [12], to sample the emitted light when charged particles pass through it. A characteristic feature of its design is the orientation of the scintillating tiles which are placed in planes perpendicular to the colliding beams and are staggered in depth. A good sampling homogeneity is obtained when the calorimeter is placed behind an electromagnetic compartment and a coil equivalent to a total of about two interaction lengths (λ) of material.

The absorber structure is a laminate of steel plates of various dimensions, connected to a massive structural element referred to as a girder. Simplicity has been the guideline for the light collection scheme used as well: fibres are coupled radially to the tiles along the outside faces of each module. The laminated structure of the absorber allows for channels in which the fibres run. The use of fibre readout allows to define a tridimensional cell readout, creating a projective geometry for triggering and energy reconstruction. A compact electronics readout is housed in the girder of each module. Finally, the readout of the two sides of each of the scintillating tiles into two separate photomultipliers (PMTs) guarantees a sufficient light yield.

The Tile Calorimeter consists of one barrel, shown in Figure 3.7, and two extended barrel hadron parts. The barrel calorimeter consists of a cylindrical structure with inner and outer radius of 2280 and 4230 mm respectively. The barrel part is 5640 mm in length along the beam axis, while each of the extended barrel cylinders is 2910 mm long. Each detector cylinder is built of 64 independent wedges along the azimuthal direction. Between the barrel and the extended barrels there is a gap of about 600 mm, which is needed for the Inner Detector and the Liquid Argon cables, electronics and services. The barrel covers the region $-1.0 < |\eta| < 1.0$, and the extended barrels cover the region $0.8 < |\eta| < 1.7$. Part of the gap contains an extension of the extended barrel: the Intermediate Tile Calorimeter (ITC), which is a structure stepped in order to maximize the volume of active material in this region, while still leaving room for the services and cables. The ITC consists of a calorimeter plug between the region $0.8 < |\eta| < 1.0$, and, due to severe space constraints, only scintillator between $1.0 < |\eta| < 1.6$. The scintillators in the region $1.0 < |\eta| < 1.2$ are called gap scintillators, and the scintillators between $1.2 < |\eta| < 1.6$ are called crack scintillators. The latter extend down to the region in between the barrel and the EndCap cryostats, while the plug and the gap scintillators primarily provide hadronic shower sampling, the crack scintillator plays a critical role in sampling electromagnetic showers, where the normal sampling is compromised by the dead material of the cryostat walls and the inner detector cables.

The main function of the Tile Calorimeter is to contribute to the energy reconstruction of the jets produced in the pp interactions and, with the addition of the EndCap and forward calorimeters, to provide a good p_T^{miss} measurement. The large center of mass energy requires good performance over an extremely large dynamic range extending from a few GeV up to several TeV. To resolve events over a background of 21 minimum bias events per bunch crossing a fast detector response with fine granularity is required. High radiation resistance is needed to cope with the high particle fluxes expected at the design luminosity over a period of 10 years of operation. The guidelines for the design of this device are derived from the required overall physics performance which call for an intrinsic resolution for jets of $\Delta E/E = \frac{50\%}{\sqrt{E}} \oplus 3\%$ for $|\eta| < 3.0$ with a

Figure 3.7: The Tile Calorimeter Central Barrel assembly and installation [13]. Particle showers are sampled by tiles of scintillating plastic which emit light when charged particles pass through them [3]. The light pulses are carried by optical fibres to photomultiplier tubes behind the calorimeter and converted to electric signals.

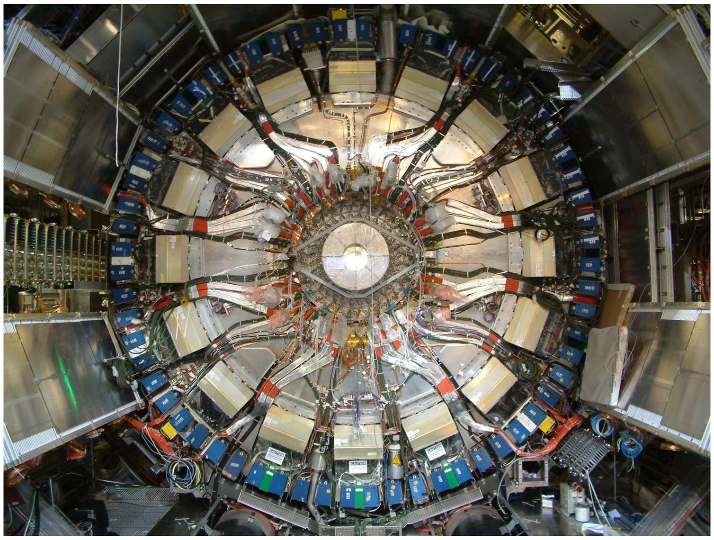

segmentation of $\Delta\eta \times \Delta\phi = 0.1 \times 0.1$.

3.6 The Muon Spectrometer

The ATLAS muon spectrometer, based on the magnetic deflection of muon tracks in a system of three large superconducting air-core toroid magnets instrumented with separate-function trigger and high-precision tracking chambers, deigned to exploit the potential of the most promising and robust signatures of physics at the LHC [14]. Figure 3.8 shows a side view of one quadrant of the spectrometer and its transverse view.

In the pseudorapidity range $|\eta| \leq 1.0$, magnetic bending is provided by a large barrel magnet constructed from eight coils surrounding the hadron calorimeter. For $1.4 \leq |\eta| \leq 2.7$, muon tracks are bent in two smaller EndCap magnets inserted into both ends of the barrel toroid. In the interval $1.0 \leq |\eta| \leq 1.4$ referred to as transition region, magnetic deflection is provided by a combination of barrel and EndCap fields. This magnet configuration provides a field that is mostly orthogonal to the muon trajectories, while minimizing the degradation of resolution due to multiple scattering. In the barrel region, tracks are measured in chambers arranged in three cylindrical layers (stations) around the beam axis; in the transition and EndCap regions, the chambers

Figure 3.8: (a) is the side view of one quadrant of the muon spectrometer and the transverse view is presented in Figure (b). The muon spectrometer measures the trajectories of muons as they bent by a system of large superconducting magnet coils [3]. This allows their momenta and electric charge to be precisely determined.

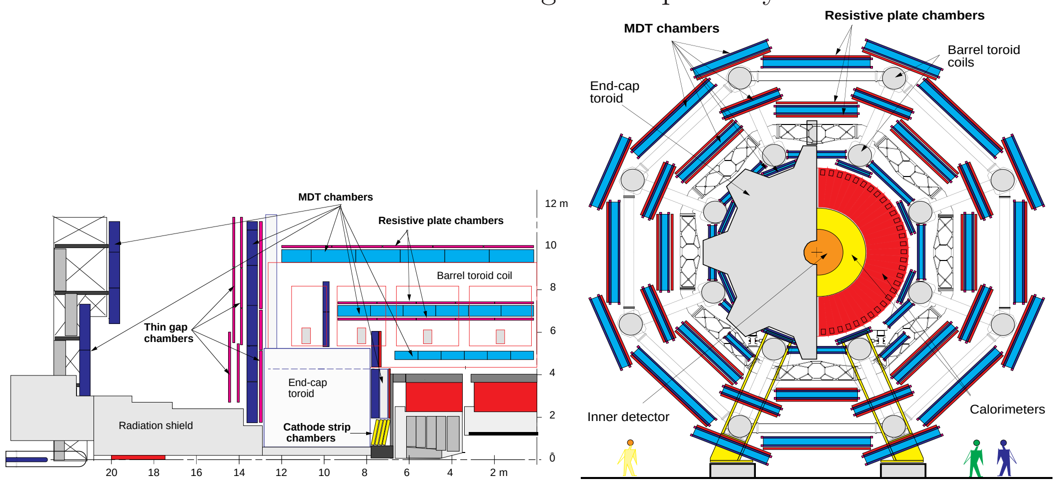

(a) (b)

are installed vertically, also in three stations. Over most of the pseudorapidity range, a precision measurement of the track coordinates in the principal bending direction of the magnetic field is provided by Monitored Drift Tubes (MDT). At large pseudorapidities and close to the interaction point, Cathode Strip Chambers (CSC) with higher granularity are used to sustain the demanding rate and background conditions. Optical alignment systems have been designed to meet the stringent requirements on the mechanical accuracy and the survey of the precision chambers. The trigger system covers the pseudorapidity range $|\eta| \leq 2.4$. Resistive Plate Chambers (RPC) are used in the barrel and Thin Gap Chambers (TGC) in the EndCap region. Both types of trigger chambers also provide a second-coordinate measurement of track coordinates orthogonal to the precision measurement, in a direction approximately parallel to the magnetic field lines. The second-coordinate capability of the trigger chambers is designed to match the acceptance of the precision chambers.

The muon spectrometer designed for a momentum resolution $\Delta p_T/p_T < 10^4 p/\mathrm{GeV}$ for $p_T > 300$ GeV; at smaller momenta, the resolution is limited to a few per cent by multiple scattering in the magnet and detector structures, and by energy loss fluctuations in the calorimeters. To achieve this resolution by a three-point measurement, with the size and bending power of the ATLAS toroids, each point must be measured with an accuracy better than 50 μm.

In the next paragraphs, details for the four different technologies of the muon spectrometer, MDT, CSC, RPC and TGC, are provided [14].

Figure 3.9: Schematic drawing of a rectangular MDT chamber constructed from multilayers of three monolayers each, for installation in the barrel spectrometer [14]. The chambers for the EndCap are of trapezoidal shape, but are of similar design otherwise. The ionized tracks of muons passing through these tubes produce electrical pulses in the wires [3].

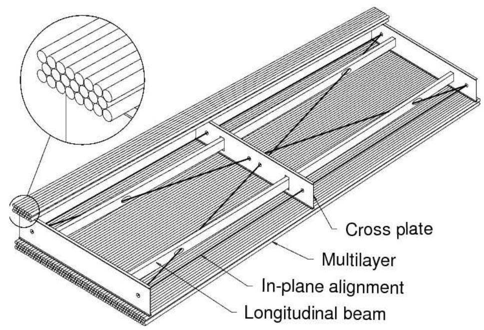

3.6.1 Monitored Drift Tubes (MDT)

Aluminum tubes of 30 mm diameter and 400 μm wall thickness, with a 50 μm diameter central WRe wire, form the detection element of the MDT chambers, shown in Figure 3.9. The tubes operate with a non-flammable $91\% Ar - 5\% CH_4 - 4\% N_2$ mixture at 3 $bars$ absolute pressure. The envisaged working point provides for a highly linear spacetime relation with a maximum drift time of 500 ns, a small Lorentz angle, and good aging properties due to small gas amplification. The single-wire resolution is typically 80 μm, except very close to the anode wire.

The tubes are produced by extrusion from a hard aluminum alloy and are closed by endplugs, which provide accurate positioning of the anode wires, wire tension, gas tightness, and electrical and gas connections. The tube lengths vary from 70 cm to 630 cm. To improve the resolution of a chamber beyond the single-wire limit and to achieve adequate redundancy for pattern recognition, the MDT chambers are constructed from 2×4 monolayers of drift tubes for the inner and 2×3 monolayers for the middle and outer stations. The tubes are arranged in multilayers of three or four monolayers, respectively, on either side of a rigid support structure. The support structures (spacer frames) provide for accurate positioning of the drift tubes with respect to each other, and for mechanical integrity under effects of temperature and gravity; for the barrel chambers which are not mounted in a vertical plane, they are designed to bend the drift tubes slightly in order to match them to the gravitational sag of the wires. The spacer frames also support most of the components of the alignment system.

The structural components of the spacer frames are three cross-plates, to which the drift tube multilayers are attached, and two long beams connecting the cross-plates. The frames constructed to a moderate mechanical accuracy of ± 0.5 mm only and mechanical deformations are monitored by an in-plane optical system; hence the name monitored drift tube chambers.

Each drift tube is read out at one end by a low-impedance current sensitive preamplifier, with a threshold five times above the noise level. The preamplifier is followed by a differential amplifier, a shaping amplifier and a discriminator. The output of the shaping amplifier is also connected to a simple ADC, such that the charge-integrated signal can be used to correct the drift time measurement for time slewing. Eight amplifier/shaper/discriminator (ASD) readout channels are packaged, together with the ADCs, in a single custom-built integrated circuit. Signals from three ASD chips are fed into $24-channel$ time to digital converters (TDC) which measure the drift time with 300 ps RMS resolution. A phase calibration system serves to correct for time offsets between different MDT channels. The ASDs and TDCs are mounted on the chambers by means of simple printed circuit boards. In response to a level-1 trigger, the TDC data are transferred over fast serial links to readout drivers housed in VME (Versa Module Europa) crates in the experimental area.

3.6.2 Cathode Strip Chambers (CSC)

The CSCs are multiwire proportional chambers with cathode strip readout and with a symmetric cell in which the anode-cathode spacing is equal to the anode wire pitch [14]. The precision coordinate is obtained by measuring the charge induced on the segmented cathode by the avalanche formed on the anode wire. Good spatial resolution is achieved by segmentation of the readout cathode and by charge interpolation between neighboring strips. The cathode strips for the precision measurement are oriented orthogonal to the anode wires. Other important characteristics are the small electron drift times ($\leq$ 45 ns), good time resolution (7 ns) [15], good two-track resolution, and low neutron sensitivity. A measurement of the transverse coordinate is obtained from orthogonal strips, i.e. oriented parallel to the anode wires, which form the second cathode of the chamber. The spatial resolution of CSCs is sensitive to the inclination of tracks and the Lorentz angle. To minimize degradations of the resolution, chambers installed in a tilted position such that infinite-momentum tracks originating from the interaction point are normal to the chamber surface. The CSCs are arranged in 2×4 layers. The design utilizes low-mass construction materials to minimize multiple scattering and detector weight. A four-layer multilayer is formed by five flat, rigid panels, each of which is made of Nomex honeycomb and two thin copper-clad FR4 laminates forming the cathodes. The panel frames are made of machined rohacell. Precision machined FR4 strips glued on the panels provide the 2.5 mm step for the $W-Re$ anode wires 30 μm in diameter. A cutout view of one gap is shown in Figure 3.10. In each of the four gaps, the position sensing cathode strips are lithographically etched.

Figure 3.10: Cutout view of a single CSC layer showing the construction details [14]. The CSC are characterized by small drift times and therefore are ideal for the forward region where the radiation backgrounds are high.

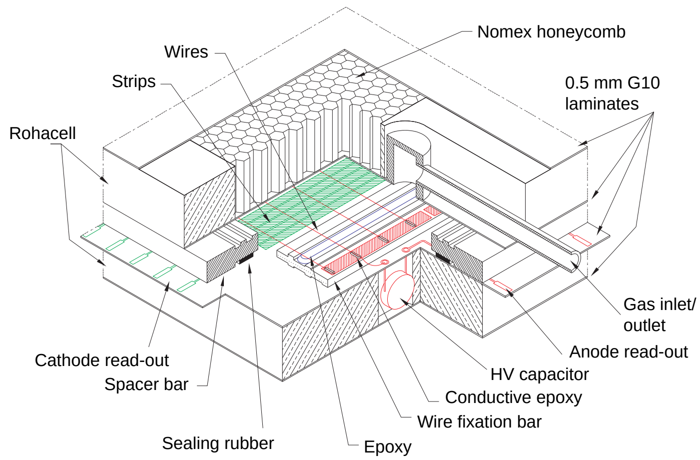

The five panels are precisely positioned with respect to each other with the aid of locating pins. Signals from the cathode strips are transferred via ribbon cable jumpers to the electronic readout boards located on the outer panels. The whole assembly is rigid enough so that no in-plane alignment system is necessary.

The gas is a non-flammable mixture of 80% Ar, 20% CO_2 [15]. The fact that it contains no hydrogen, combined with the small gap width, explains the low sensitivity to neutron background. In general, the CSC performance is less sensitive to variations of the gas parameters than that of the MDTs.

The front-end section of the strip readout electronics consists of a charge-sensitive preamplifier that drives a pulse shaping amplifier. Sixteen channels of preamplifier and shaper are packaged in a complementary metaloxidesemiconductor (CMOS) integrated circuit mounted on an on-detector readout card. This chip is followed by analog storage of the peak cathode pulse-height during the Level-1 trigger latency. Upon a Level-1 trigger, the analog data are multiplexed into a 10-bit ADC. Since the precision coordinate is obtained from charge interpolation, the spatial resolution obtained depends critically on the relative gain of neighboring cathode strips and readout channels.

3.6.3 Resistive Plate Chambers (RPC)

The RPC is a gaseous detector providing a typical spacetime resolution of 1 $cm \times 1$ ns with digital readout [14]. The basic RPC unit is a narrow gas gap formed by two parallel resistive bakelite plates, separated by insulating spacers (Figure 3.11). The primary ionization electrons are multiplied into avalanches by a high, uniform electric field of typically 4.5 kV/mm. Amplification in avalanche mode produces pulses of typically 0.5 pC. The candidate gas mixture is based on tetrafluoroethane ($C_2H_2F_4$), a non-flammable and environmentally safe gas that allows for a relatively low operating voltage. The signal is read out via capacitive coupling by metal strips on both sides of the detector. A trigger chamber is made from two rectangular detector layers, each one read out by two orthogonal series of pick-up strips: the η strips are parallel to the MDT wires and provide the bending view of the trigger detector; the ϕ strips, orthogonal to the MDT wires, provide the second-coordinate measurement which is also required for the offline pattern recognition.

RPCs have a simple mechanical structure, use no wires and are therefore simple to manufacture. The 2 mm thick Bakelite plates are separated by polycarbonate spacers of 2 mm thickness which define the size of the gas gap. The spacers are glued on both plates at 10 cm intervals. A 7 mm wide frame of the same material and thickness as the spacers is used to seal the gas gap at all four edges. The outside surfaces of the resistive plates are coated with thin layers of graphite paint which are connected to the high voltage supply. These graphite electrodes are separated from the pick-up strips by 200 μm thick insulating films which are glued on both graphite layers. The readout strips are arranged with a pitch varying from 30.0 to 39.5 mm.

Each chamber is made from two detector layers and four readout strip panels. These elements are rigidly held together by two support panels which provide the required mechanical stiffness of the chambers. The panels are made of polystyrene sandwiched between two aluminum sheets. One panel is flat, 50 mm thick, with 0.5 mm thick aluminium coatings; the other panel is 10 mm thick with 0.3 mm coatings and is preloaded with a 1 cm sagitta. The two panels are rigidly connected by 2 mm thick aluminium profiles, such that the preloaded support panel provides uniform pressure over the whole surface of an RPC module.

The RPCs are operated with a gas mixture of 97% tetrafluoroethane ($C_2H_2F_4$) and 3% isobutane (C_4H_{10}), with a total volume of 18 m^3. As for the precision chambers, the gas is stored, mixed and purified on the surface and the distribution system is installed underground.

To preserve the excellent intrinsic time resolution of the RPCs, the readout strips are optimized for good transmission properties and are terminated at both ends to avoid signal reflections. The front-end electronics are based on a three-stage voltage amplifier followed by a variable-threshold comparator. The amplifier frequency response is optimized for the typical time structure of RPC avalanches. Eight amplifier-comparator

Figure 3.11: Installation of RPC Muon chambers in the ATLAS cavern (July 2007) [16].

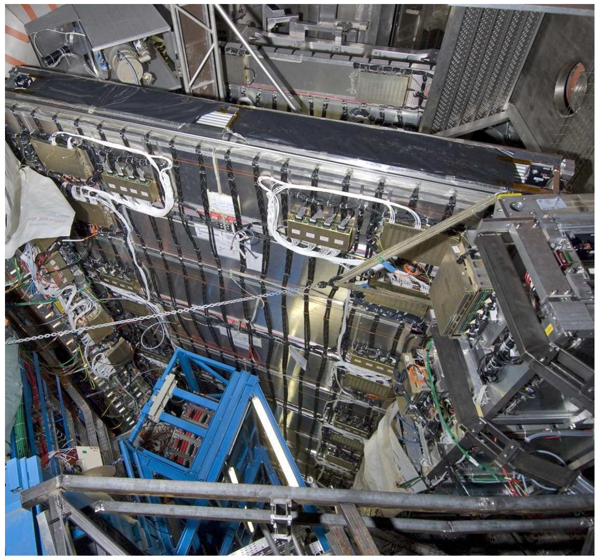

channels are implemented in a VLSI chip in GaAs technology. The chips are mounted on printed circuit boards attached to the edges of the readout panels.

3.6.4 Thin Gap Chambers (TGC)

Thin gap chambers are designed in a way similar to multiwire proportional chambers, with the difference that the anode wire pitch is larger than the cathode-anode distance [14]. Signals from the anode wires, arranged parallel to the MDT wires, provide the trigger information together with readout strips arranged orthogonal to the wires. The readout strips also serve to measure the second coordinate. Using a highly quenching gas mixture of 55% CO_2 and 45% $n - pentane$ $(n - C_5H_{12})$, with a total volume of 16 m^3, this type of cell geometry permits operation in saturated mode, with a number of advantages:

- small sensitivity to mechanical deformations - important for the economical design of large-area chambers
- small dependence of the pulse height on the incident angle, up to angles of 40°
- nearly Gaussian pulse height distribution with small Landau tails and no streamer formation.

Figure 3.12: Schematic cross-section of a triplet (left) and of a doublet of TGCs, where the width of the gas gap is shown enlarged [14]. These detectors, along with the RPC, provide fast information on muon tracks to enable online selection of events containing muons [3].

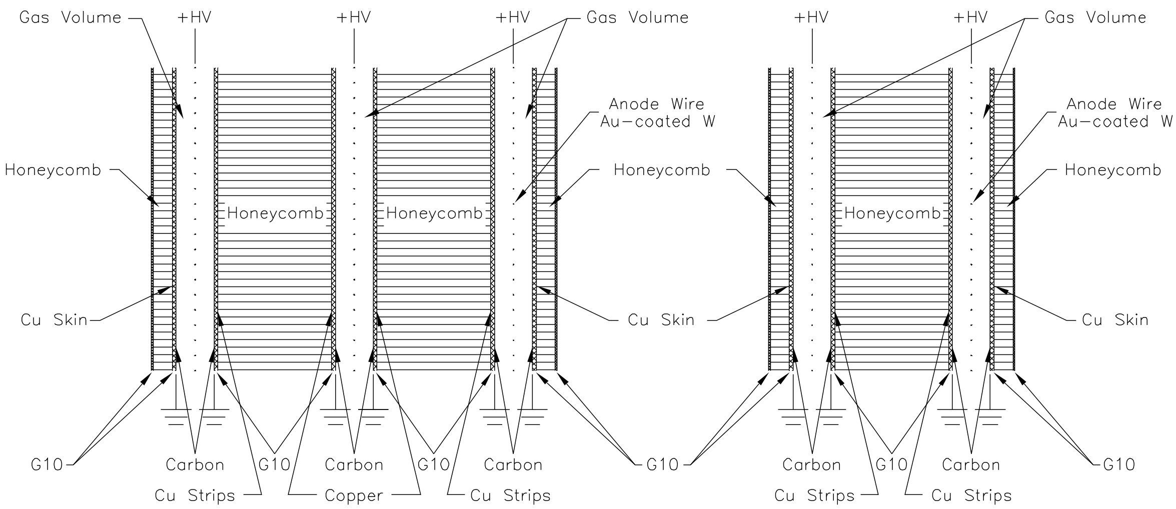

The main dimensional characteristics of the chambers are a cathode-cathode distance (gas gap) of 2.8 mm, a wire pitch of 1.8 mm, and a wire diameter of 50 μm. The operating high voltage foreseen is 3.1 kV. The electric field configuration and the small wire distance provide for a short drift time and thus a good time resolution. As the angle increases, the tracks pass closer to the wire, thus reducing the maximum drift distance and improving the time resolution. In the ATLAS chamber layout, all muons passing through TGCs with transverse momenta above the required threshold have incident angles greater than 10°. Aging properties of the chambers have been investigated in detail and were found to be fully adequate for the expected operating conditions at the LHC, with a large safety margin.

TGCs are constructed in doublets and in triplets. The seven layers in the middle station are arranged in one triplet and two doublets; one doublet is used for the inner station, which only serves to measure the second coordinate. The anode plane is sandwiched between two cathode planes made of 1.6 mm $G-10$ plates on which the graphite cathode is deposited. On the back side of the cathode plates facing the center plane of the chamber, etched copper strips provide the readout of the azimuthal coordinate. The TGC layers are separated by 20 mm thick paper honeycomb panels which provide a rigid mechanical structure for the chambers (Figure 3.12). On the outside, the gas pressure is sustained by 5 mm thick paper honeycomb panels. These are covered in turn by 0.5 mm $G-10$ plates.

The used gas mixture is highly flammable and requires adequate safety precautions. As in the other gas systems, the gas is stored, mixed, and purified on the surface and the distribution system is installed underground. $n-pentane$ has a low vapor pressure and is liquid at room temperature and atmospheric pressure.

To form a trigger signal, several anode wires are grouped together and fed to a common readout channel. The number of wires per group varies between 4 and 20, depending on the desired granularity as a function of pseudorapidity. The grouped signals are fed into a low-impedance two-stage amplifier. The combination of chamber and amplifier yields a rise-time of the amplifier output into the discriminator of 1020 ns. Four amplifier-discriminator (ASD) circuits are integrated into one chip; four ASD chips are grouped in turn on an amplifier-discriminator printed circuit board attached to the edges of the chambers, thus providing the readout of 16 channels. By appropriate adjustment of the threshold, the same ASD chips can be used for wire and strip readout.

3.6.5 Precision Alignment

The requirements on the momentum resolution of the spectrometer call for an accuracy of the relative positioning of chambers traversed by a muon track that matches the intrinsic resolution and the mechanical tolerances of the precision chambers [14]. Over the large global dimensions of the spectrometer, however, it is not possible to stabilize the dimensions and positions of the chamber at the 30 μm level. Therefore, chamber deformations and positions are constantly monitored by means of optical alignment systems and displacements up to about 1 cm are corrected for in the offline analysis.

All alignment systems are based on optical straightness monitors. Owing to geometrical constraints, different schemes are used to monitor chamber positions in the barrel, in the EndCap and the deformations of large chambers, the so called in-plane alignment. Chambers in the small sectors are aligned with particle tracks, exploiting the overlap with chambers in the large sectors. Alignment with tracks also serve to cross-calibrate the optical survey of the large sectors.

Very high accuracy is required only for the positioning of chambers within a projective tower. The accuracy required for the relative positioning of different towers to obtain adequate mass resolutions for multimuon final states is in the millimeter range. This accuracy is easily achieved by the initial positioning and survey of chambers at installation time. The relative alignment of muon spectrometer, calorimeters and inner detector relies on high-momentum muon trajectories.

Figure 3.13: A schematic view of the magnetic field.

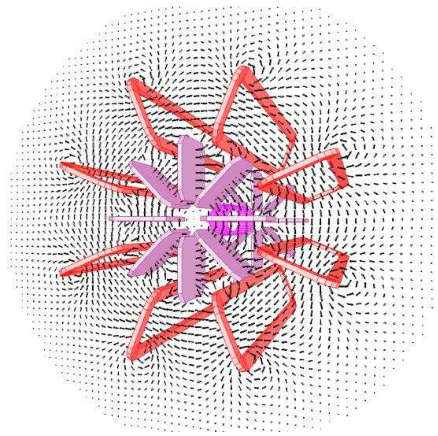

3.7 The Magnet System

An essential part of the ATLAS detector is the magnet systems which provides the bending power required for the momentum measurements of charged particles [17]. ATLAS selected the arrangement of a central solenoid serving the inner tracker with magnetic field, surrounded by a system of 3 large scale air-core toroids, generating the magnetic field for the muon spectrometer.

The superconducting magnets, named Barrel Toroid, EndCap Toroid and Central Solenoid, along with the power system, control, cryogenics and the refrigeration plant compose the magnet system. The overall dimension is 26 m long and 20 m in diameter. A schematic view of the magnetic field is depicted in Figure 3.13.

3.7.1 The Central Solenoid

The Central Solenoid (Figure 3.14) designed to provide an axial magnetic field of 2 T at the center of the tracking volume [18]. It is located in front of the EM calorimeter and therefore the material must be kept minimal for the best calorimeter performance. The technology of a superconducting magnet using indirectly cooled aluminium stabilized superconductor was chosen to achieve the highest possible field with minimum thickness. In order to minimize the material, the vacuum vessels of the Solenoid and of the LAr calorimeter combined into one, eliminating two vacuum walls.

An important safety aspect of the design is the quench protection and recovery, which requires 4 hours recovery time. Except from that, operational factors are set from the alignment, which must be known within ± 1 cm along the beam axis and considering that the coil moves in the cryostat vacuum vessel when it is cooled and shrinks by 2 cm

Figure 3.14: The Central Solenoid before the installation [19]. The 4 *tonne* coil contains 10 km of superconducting cable which is cooled with liquid helium [3]. The nominal current is 8 kA during normal operation.

while the radius changes by 0.5 cm and the radiation exposition (reaches 0.5 $kGy/year$).

3.7.2 The Barrel Toroid

The Barrel Toroid (BT) consists of eight flat coils, shown in Figure 3.15, in a race-track configuration, assembled radially and symmetrically around the beam axis [20]. Each coil contains its own individual cryostat and is supported internally to its vacuum vessel by means of distributed sets of cold-to-warm rods and struts. The only opening in the cryostat are communication ports where electrical and cryogenic lines can be brought out for external connections.

The assembly of coils in the toroid configuration requires a very strong and rigid mechanical structure for supporting both the weights and the magnetic forces. The main magnetic forces are directed symmetrically and radically towards the beam axis. Each coil is submitted to a total radial force of 1100 *tonnes*. The force is transferred from the cold mass to the warm structure by means of titanium rods attached to solid fixtures distributed at 8 locations along the length of the inner leg of the cryostat. The fixtures themselves are linked between adjacent coils by warm voussoirs, which all together constitute 8 solid rings working in compression under the combined radial forces. The above suspension rods work in tension, at a high stress of 400 MPa, and are anticulated in order to accommodate the coil thermal contraction. In addition, cryogenic stops, near the rods, provide lateral bracing against out-of-plane forces, mainly due to the weight and to eventual magnetic unbalance. For the same purpose, the outer legs of

Figure 3.15: A view of the toroid barrel magnets [19]. The ATLAS detector uses an unusually large system of air-core toroids arranged outside the calorimeter volumes to provide a large-volume magnetic field [3].

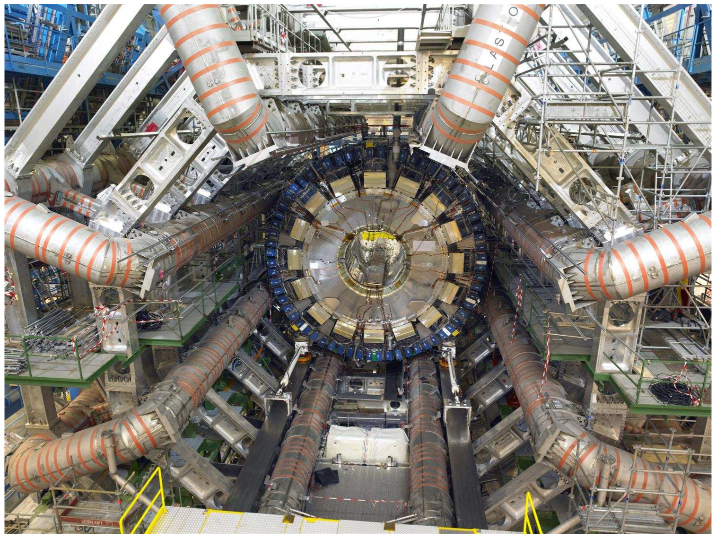

the cryostats are braced by warm structures, concentric to the inner voussoirs internally by similar stops.

The complete toroid is also supported off the ground by a limited number of legs, which are incorporated in the general support structure of the ATLAS detector, namely called the "CERN feet". This structure has also to support the weight of the muon chambers, around 500 *tonnes*.

The indirect cooling eliminates the need for complex and bulky helium vessels and is particularly appropriate for the ATLAS coil configuration. Indirect cooling requires a monolithic coil structure made of high thermal conductivity materials and designed with low levels of stress and strain in order to prevent internal mechanical disturbances. This achieved by the use of a massive aluminium stabilized conductor, impregnated in a rigid alu-alloy structure, and of adequately distributed cooling loops.

The operating current, rated below 65% of the critical current along the load line, provides a temperature margin of 2 K above the operating temperature of 4.5 K, corresponding to an enthalpy margin of about 4000 J/m^3. The coil cooling is achieved by a set of pipes welded in grooves running along the coil casings and fed in parallel with $2 - phase$ helium[2] circulated in forced flow by means of cold pumps.

[2]Refers to helium ^3He and ^4He.

3.7.3 The EndCap Toroid

The design of the EndCap Toroid constrained by the geometry of the experiment and the requirement to produce a high magnetic field across a radial span [21]. The system can be retracted from the operating position to allow access to the central parts of the ATLAS detector. Other constraints of the operation are to transfer the axial force to the Barrel Toroid, support about 100 *tonnes* of shielding at the inner bore, support the BEE muon chambers on the vacuum vessel to enhance the muon spectrometer performance in the critical region between the barrel and the EndCap Toroids and provision the alignment paths for muons detectors alignment through the vessel. One of the two ATLAS EndCap toroid is shown in Figure 3.16 between the Large Muon wheel and close to the Barrel Toroids.

The toroidal fields are generated by 8 superconducting coils, mounted as a single cold mass unit in a large cryostat. The coils are fabricated using aluminium alloy center and side plates to react to the internal coil forces. The cold mass is mounted in a single large cryostat which consists of a large aluminium alloy vacuum vessel, super-insulation, radiation shields and cold mass supports The cryostat performs a number of mechanical force transfer functions in addition to its thermal isolation requirements (transfer of cold mass loads to the rail system within the ATLAS and transfer of axial forces to the Barrel Toroid.

3.8 The Trigger System

The trigger system during the Run-I had three distinct levels: L1, L2, and the event filter. Each trigger level refines the decisions made at the previous level and, where necessary, applies additional selection criteria [22]. The data acquisition system (DAQ) receives and buffers the event data from the detector-specific readout electronics, at the L1 trigger accept rate, over 1600 point-to-point readout links. The first level uses a limited amount of the total detector information to make a decision in less than 2.5 ms, reducing the rate to about 75 kHz. The two higher levels access more detector information for a final rate of up to 200 Hz with an event size of approximately 1.3 $Mbyte$. The trigger flow is schematically presented in Figure 3.17.

The L1 trigger searches for high transverse-momentum muons, electrons, photons, jets, and τ-leptons decaying into hadrons, as well as large missing and total transverse energy. Its selection is based on information from a subset of detectors. High transverse-momentum muons are identified using trigger chambers in the barrel and EndCap regions of the spectrometer. Calorimeter selections are based on reduced-granularity information from all the calorimeters. Results from the L1 muon and calorimeter triggers are processed by the central trigger processor, which implements a trigger menu

Figure 3.16: One of the two EndCap Toroids, siting between the Large Muon wheel and close to the Barrel Toroids [19]. It is movable detector part in order to allow access to the detector inner parts and designed to transfer the axial force to the Barrel Toroid [21].

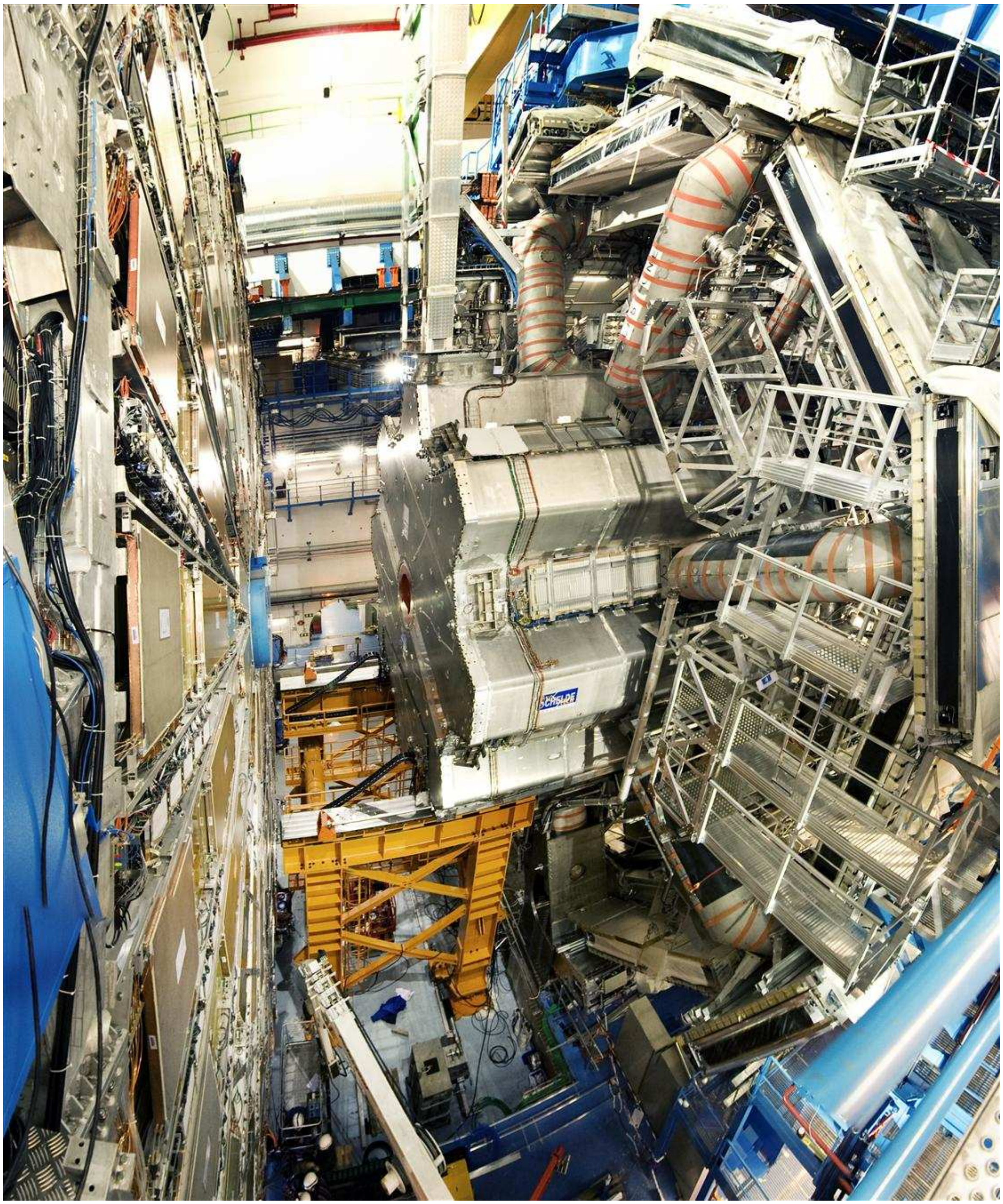

Figure 3.17: Sketch of the ATLAS triggering and DAQ (T/DAQ) system [23]. The places where the HLT and thus the HLT Steering is deployed (L2/EF) are marked in grey.

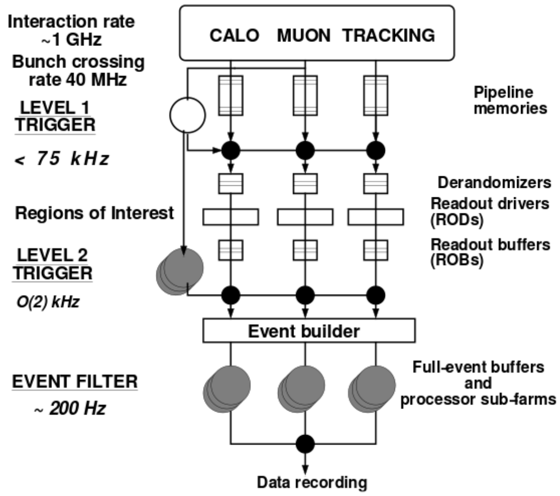

made up of combinations of trigger selections. Pre-scaling of trigger menu items is also available, allowing optimal use of the bandwidth as luminosity and background conditions change. Events passing the L1 trigger selection are transferred to the next stages of the detector-specific electronics and subsequently to the data acquisition via point-to-point links.

In each event, the L1 trigger also defines one or more Regions-of-Interest (RoIs), i.e. the geographical coordinates in η and ϕ, of those regions within the detector where its selection process has identified interesting features. The RoI data include information on the type of feature identified and the criteria passed, e.g. a threshold. This information is subsequently used by the high-level trigger.

The L2 selection is seeded by the RoI information provided by the L1 trigger over a dedicated data path. L2 selections use, at full granularity and precision, all the available detector data within the RoIs (approximately 2% of the total event data). The L2 menus are designed to reduce the trigger rate to approximately 3.5 kHz, with an event processing time of about 40 ms, averaged over all events.

The final stage of the event selection is carried out by the event filter (EF), which reduces the event rate to roughly 200 Hz. Its selections are implemented using offline analysis procedures within an average event processing time of the order of 4 s. The L2 and EF are also called High Level Triggers (HLT).

In the Run-II, the trigger organization will include the first level trigger and the combination of L2 and the EF will be the final level, called High Level Trigger (HLT). The purpose of the upgrade is to add robustness and flexibility to the selection and the conveyance of the physics data, simplify the maintenance of the infrastructure, exploit new technologies and, overall, make ATLAS data-taking capable of dealing with increasing event rates [24].

3.9 The Data Acquisition System (DAQ) and Controls

The Readout Drivers (RODs) of each sub-detector uses standardized blocks which subject to common requirements [22]. After an event is accepted by the L1 trigger, the data from the pipe-lines are transferred off the detector to the RODs. Digitized signals are formatted as raw data prior to being transferred to the DAQ system. The RODs follow some general ATLAS rules, including the definition of the data format of the event, the error detection/recovery mechanisms to be implemented, and the physical interface for the data transmission to the DAQ system.

The first stage of the DAQ, the readout system, receives and temporarily stores the data in local buffers. It is subsequently solicited by the L2 trigger for the event data associated to RoIs. Those events selected by the L2 trigger are then transferred to the event-building system and subsequently to the event filter for final selection. Events selected by the event filter are moved to permanent storage at the CERN computer center. In addition to the movement of data, the data acquisition also provides for the configuration, control and monitoring of the hardware and software components which together provide the data-taking functionality.

The Detector Control System (DCS) permits the coherent and safe operation of the ATLAS detector hardware, and serves as a homogeneous interface to all sub-detectors and to the technical infrastructure of the experiment. It controls, continuously monitors and archives the operational parameters, signals any abnormal behavior to the operator, and allows automatic or manual corrective actions to be taken. Typical examples are high- and low-voltage systems for detector and electronics, gas and cooling systems, magnetic field, temperatures, and humidity. The DCS also enables bi-directional communication with the data acquisition system in order to synchronize the state of the detector with data-taking. It also handles the communication between the sub-detectors and other systems which are controlled independently, such as the CERN technical services, the ATLAS magnets, and the detector safety system.

3.10 Luminosity Determination and Luminosity Detectors

This section provides a description of the detector subsystems and the algorithms used for luminosity measurements [25]. An accurate measurement of the delivered luminosity is a key component of the ATLAS physics program. For cross-section measurements, the uncertainty on the delivered luminosity is often one of the major systematic uncertainties. Searches and discoveries of new physical phenomena rely on accurate information about the delivered luminosity to evaluate background levels and determine sensitivity to the signatures of new phenomena.

3.10.0.1 The Luminosity Detectors

In the early 2010 data taking, MBTS (Minimum Bias Trigger Scintillators), which belong to the category of segmented scintillator counters, were primarily used for luminosity measurements, since they provide efficient triggers at low instantaneous luminosity ($\mathcal{L} < 10^{33}\ cm^{-2}\ s^{-1}$). Located at $z = \pm 365\ cm$ from the nominal interaction point (IP) and covering a rapidity range $2.09 < |\eta| < 3.84$, the main purpose of the MBTS system was to provide a trigger on minimum collision activity during a pp bunch crossing. Light emitted by the scintillators is collected by wavelength-shifting optical fibers and guided to photomultiplier tubes. The MBTS signals, after being shaped and amplified, are fed into leading-edge discriminators and sent to the trigger system.

The Beam Conditions Monitor (BCM), started partially to operate in late 2010. It consists of four small diamond sensors, approximately 1 cm^2 in cross-section each, arranged around the beampipe in a cross pattern on each side of the IP, at a distance of $z = \pm 184\ cm$. The BCM is a fast device originally designed to monitor background levels and issue beam-abort requests when beam losses start to risk damaging the Inner Detector. The fast readout of the BCM also provides a bunch-by-bunch luminosity signal at $|\eta| = 4.2$ with a time resolution of $\sim 0.7\ ns$. The horizontal and vertical pairs of BCM detectors are read out separately, leading to two luminosity measurements labeled BCMH and BCMV respectively. Because the acceptances, thresholds, and data paths may all have small differences between BCMH and BCMV, these two measurements are treated as being made by independent devices for calibration and monitoring purposes, although the overall response of the two devices is expected to be very similar. In the 2010 data, only the BCMH readout was available for luminosity measurements, while both BCMH and BCMV became available in 2011.

Another detector technology specifically designed to measure the luminosity is the Cherenkov detector named LUCID. Sixteen mechanically polished aluminium tubes filled with C_4F_{10} gas surround the beampipe on each side of the IP at a distance of 17 m, covering the pseudorapidity range $5.6 < |\eta| < 6.0$. The Cherenkov photons created by charged particles in the gas are reflected by the tube walls until they reach photomultiplier tubes (PMTs) situated at the back end of the tubes. Additional Cherenkov photons are produced in the quartz window separating the aluminium tubes from the PMTs. The Cherenkov light created in the gas typically produces 6070 photoelectrons per incident charged particle, while the quartz window adds another 40 photoelectrons to the signal. If one of the LUCID PMTs produces a signal over a preset threshold (equivalent to 15 photoelectrons), a hit is recorded for that tube in that bunch crossing. The LUCID hit pattern is processed by a custom-built electronics card which contains Field Programmable Gate Arrays (FPGAs). This card can be programmed with different luminosity algorithms, and provides separate luminosity measurements for each LHC bunch crossing.

Both BCM and LUCID are fast detectors with electronics capable of making statistically precise luminosity measurements separately for each bunch crossing within the LHC fill pattern with no deadtime. These FPGA-based front-end electronics run autonomously from the main data acquisition system, and in particular are not affected by any deadtime imposed by the Central Trigger Processor (CTP).

The Inner Detector, already briefly introduced, is useful for the luminosity measurements by detecting the primary vertices produced in inelastic pp collisions. The vertex data and the MBTS data are components of the events read out through the data acquisition system, and so must be corrected for deadtime imposed by the CTP in order to measure the delivered luminosity. Since not every inelastic collision event can be read out through the data acquisition system, the bunch crossings are sampled with a random or minimum bias trigger. While the triggered events uniformly sample every bunch crossing, the trigger bandwidth devoted to random or minimum bias triggers is not large enough to measure the luminosity separately for each bunch pair in a given LHC fill pattern during normal physics operations. For special running conditions such as the Van der Meer (VdM) scans, where calibration is performed using dedicated beam separation scans, a custom trigger with partial event readout was introduced in 2011 to record enough events to allow bunch-by-bunch luminosity measurements from the Inner Detector vertex data.

In addition to the detectors listed above, further luminosity-sensitive methods have been developed which use components of the ATLAS calorimeter system. These techniques do not identify particular events, but rather measure average particle rates over longer time scales. The Tile Calorimeter (TileCal) provides a signal proportional to the total luminosity summed over all the colliding bunches present at a given time. Similarly, the currents provided by the FCal high-voltage system are directly proportional to the average rate of particles interacting in a given FCal sector.

3.10.0.2 The Luminosity Algorithms

This section describes the algorithms used by the luminosity-sensitive detectors to measure the visible interaction rate per bunch crossing (μ_{vis}). ATLAS primarily uses event counting algorithms to measure luminosity, where a bunch crossing is said to contain an event if the criteria for a given algorithm to observe one or more interactions are satisfied. The two main algorithm types being used are EventOR (inclusive counting) and EventAND (coincidence counting). Additional algorithms have been developed using hit counting and average particle rate counting, which provide a cross-check of the linearity of the event counting techniques.

Figure 3.18 presented the number of interactions per crossing and the total integrated luminosity and data quality in 2011 and 2012 [26]. The mean number of interactions per crossing corresponds the mean of the Poisson distribution on the number of interactions per crossing calculated for each bunch. It is calculated from the instantaneous per bunch luminosity as $\mu = L_{bunch} \times \sigma_{inel}/f_r$, where L_{bunch} is the per bunch instantaneous luminosity, σ_{inel} is the inelastic cross section which considered to be 71.5 mb for 7 TeV collisions and 73.0 mb for 8 TeV collisions and f_r is the LHC revolution frequency. The delivered luminosity accounts for the luminosity delivered from the start of stable beams until the LHC requests ATLAS to put the detector in a safe standby mode to allow a beam dump or beam studies. The recorded luminosity reflects the data acquisition inefficiency, as well as the inefficiency of the so called "warm start": when the stable beam flag is raised, the tracking detectors undergo a ramp of the high-voltage and, for the pixel system, turning on the preamplifiers.

3.11 ATLAS Upgrade

A long shutdown (LS2) is being planned in 2018 to integrate the Linac4 into the injector complex, to increase the energy of the PS Booster to reduce the beam emittance, and to upgrade the collider collimation system. When data taking resumes in 2019 (Phase-I), the peak luminosity is expected to reach $2-3\times10^{34}\ cm^{-2}s^{-1}$ corresponding to 55 to 80 interactions per crossing (pile-up[3]) with 25 ns bunch spacing, well beyond the initial design goals [27]. ATLAS Phase-I upgrades will enable the experiment to exploit the physics opportunities afforded by the upgrades to the accelerator complex. In particular, Phase-I will allow collection of an integrated luminosity of $300-400\ fb^{-1}$, extending the reach for discovery of new physics and the ability to study new phenomena and states. Furthermore, these upgrades are designed to be fully compatible with the physics program of the high luminosity (HL-LHC), where the instantaneous luminosity

[3] The high luminosity conditions at the LHC cause extra jets from other softer proton interactions in the same event, these are called "pile-up".

Figure 3.18: (a) shows the luminosity-weighted distribution of the mean number of interactions per crossing, the integrated luminosities and the mean μ values are given in the figures [26]. (b) presents the cumulative luminosity versus time delivered (green), recorded by ATLAS (yellow), and certified to be good quality data (blue) during stable beams and for pp collisions at 7 and 8 TeV center-of-mass energy in 2011 and 2012.

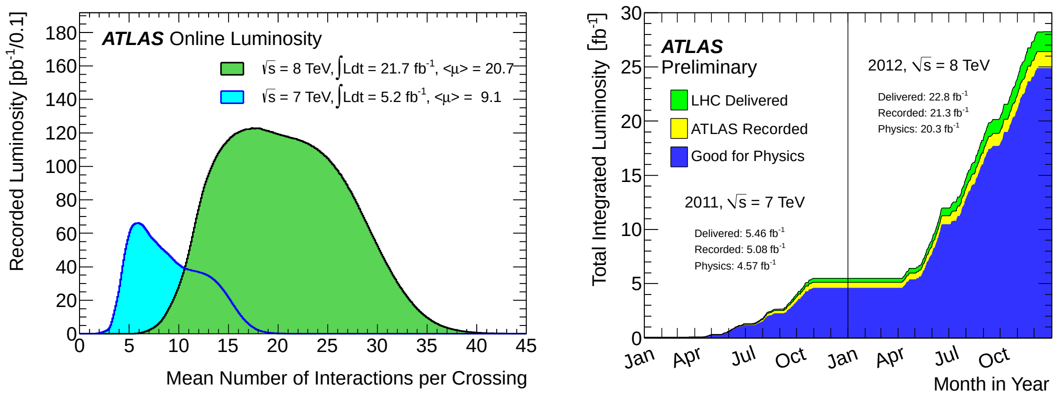

(a) (b)

should reach $5-7\times10^{34}\ cm^{-2}s^{-1}$ for a total integrated luminosity of 3000 fb^{-1} (Phase-II).

The interactions per bunch crossing (μ) during the Phase-I are estimated to be 55. Despite that, it is prudent to plan at this stage an additional safety factor of about 30%, equivalent to an instantaneous luminosity of $3\times10^{34}\ cm^{-2}s^{-1}$ and μ up to 80. The associated integrated luminosity is then 400 fb^{-1}. When estimating the total doses and particle fluences to qualify the electronics for the necessary radiation hardness, a further safety factor of 2 should be applied to take into account the uncertainties on the simulation predictions. Furthermore, any component installed in Phase-I needs to be fully operational in ATLAS also through Phase-II, requiring therefore to be compatible with $7\times10^{34}\ cm^{-2}s^{-1}$, μ 200, and 3000 fb^{-1} of integrated luminosity. How the inner detectors, the calorimeters, the muon spectrometer and the relevant triggers perform under conditions after LS2, is described in the next paragraphs. Detector occupancy, detector resolution, trigger rates and trigger thresholds are discussed in detail, starting from the knowledge acquired from the current operations and data taking.

3.11.1 The Muon Spectrometer Upgrade

The expected rate in the EndCap region, and in particular in the first muon station (small wheel), exceeds the existing detector capability and compromises the muon track-

Figure 3.19: Measured hit rate of cavern background using the MDT and CSC detectors [28]. The discontinuity at R 210 cm is caused by the different sensitivity of the MDTs and CSCs to cavern background particles [27], which indicates possible dependency of the background hit rate on the detector technology. Old simulation studies also appear on the plot.

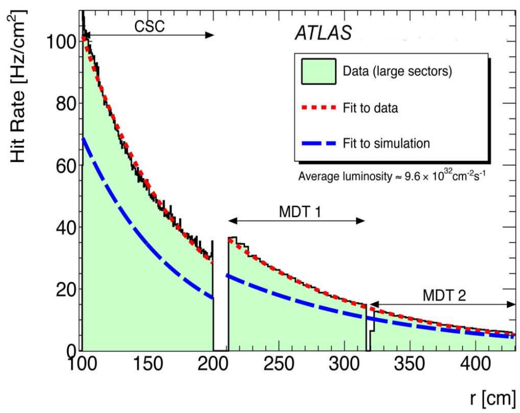

ing performance [27]. The small wheel was designed to be operational and to maintain its performance up to the condition of the nominal LHC luminosity, 1×10^{34} $cm^{-2}s^{-1}$, including a safety factor of 5 with respect to the cavern background level estimated at the time of designing the detector. However, the actual background level has been found to be higher than these original estimates, partially due to shielding which was modified during the Run-I, e.g. a shielding gap in the barrel region lead to higher background in the BI chambers. More recent FLUGG simulations agree much better with the hit rate measurements (presented in Figure 3.19), providing a more reliable estimate of the expectations for future operation, but the safety margins are significantly reduced.

Sharpening the Level-1 threshold is necessary for the data taking in Phase-I and beyond. The Level-1 trigger upgrade addresses both the suppression of the fake triggers and improvement of the p_T resolution. Presently, the Level-1 muon trigger in the EndCap is operating as follows. A track segment is identified first using hits on the 7 layers in the TGC. Then, the p_T is determined from the deviation of the segment angle from the direction pointing towards the nominal interaction point (IP) position (assuming that the track produced at the IP). As a result of the assumption, there is unexpectedly high rates of fake triggers in the EndCap region. This may be removed by requiring a corresponding activity in the small wheel. Studies have been made to see how well such approach works using collision data by emulating the small wheel segments in an upgraded detector using data from the existing detectors (CSC, MDT, TGC). The L1MU20 [4] rate is reduced by about one order of magnitude compared to

[4] L1 muon trigger with p_T threshold of 20 GeV

Figure 3.20: Sketch of the layout and operating principle of a MM detector [29].

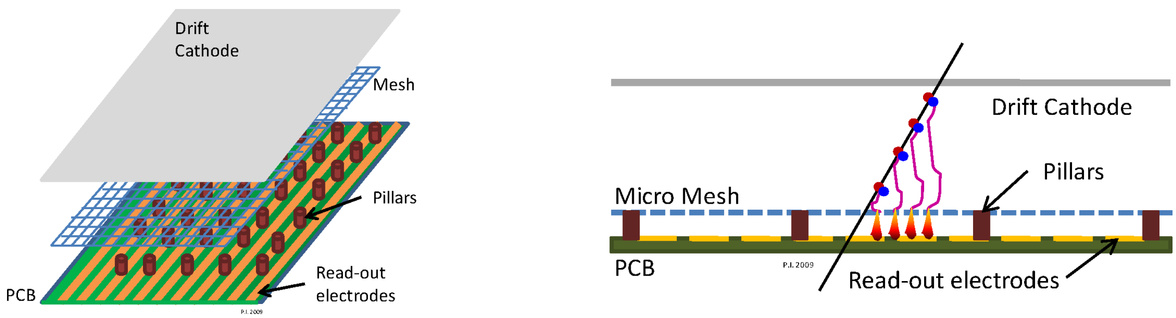

the initial rate and the efficiency of high p_T muons is 95%. The detector technologies chosen to replace the existing small wheel are the Micromegas and sTGCs [29].

3.11.1.1 The MicroMegas Detectors

The micromegas, "micro mesh gaseous structure" (MM), technology permits the construction of thin wireless gaseous particle detectors [29]. MM detectors consist of a planar (drift) electrode, a gas gap of a few millimeters thickness acting as conversion and drift region, and a thin metallic mesh at typically 100-150 m distance from the readout electrode, creating the amplification region. A sketch of the MM operating principle is shown in Figure 3.20. The HV potentials are chosen such that the electric field in the drift region is a few hundred V/cm, and 40-50 kV/cm in the amplification region. Charged particles traversing the drift space ionize the gas; the electrons liberated by the ionization process drift towards the mesh. With an electric field in the amplification region 50-100 times stronger than the drift field, the mesh is transparent to more than 95% of the electrons. The electron avalanche takes place in the thin amplification region, immediately above the readout electrode. The drift of the electrons in the conversion gap is a relatively slow process; depending on the drift gas, the drift distance, and the drift field it typically takes several tens of nanoseconds. On the other hand the amplification process happens in a fraction of a nanosecond, resulting in a fast pulse of electrons on the readout strip. The ions that are produced in the avalanche process move, in the opposite direction of the electrons, back to the amplification mesh. Most of the ions are produced in the last avalanche step and therefore close to the readout strip. Given the relatively low drift velocity of the ions, it takes them about 100 ns to reach the mesh, still very fast compared to other detectors. It is the fast evacuation of the positive ions which makes the MM particularly suited to operate at very high particle fluxes.

Figure 3.21: The sTGC internal structure sketch [29].

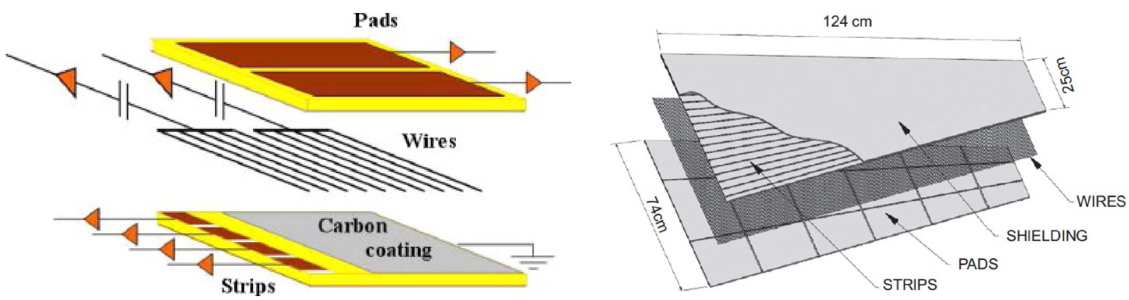

(a) (b)

3.11.1.2 The sTGC Detectors

The basic Small strip Thin Gap Chamber (sTGC) structure is shown in Figure 3.21. It consists of a grid of 50 μm gold-plated tungsten wires, sandwiched between two cathode planes [29]. The cathode planes are made of a graphite-epoxy mixture with a typical surface resistivity of 100 $k\Omega$ sprayed on a thick $G-10$ plane, behind which there are on one side strips (that run perpendicular to the wires) and on the other pads (covering large rectangular surfaces), on a thick PCB with the shielding ground on the opposite side. The strips are much smaller than the TGC pitch, hence the name Small TGC for this technology.

The TGC system, used in the present ATLAS muon EndCap trigger system, has passed a long phase of R&D and testing. The basic detector design for the NSW has two quadruplets 35 cm apart in z. Each quadruplet contains four TGCs, each TGC with pad, wire and strip readout. The pads are used to produce a 3-out-of-4 coincidence to identify muon tracks roughly pointing to the interaction point. They are also used to define which strips are to be readout to obtain a precise measurement in the bending coordinate, for the online muon candidate selection. The azimuthal coordinate, where only about 10 mm precision is needed, is obtained from grouping wires together. The charge of all strips, pads and wires are readout for offline track reconstruction.

3.11.2 The Calorimeters Upgrade

Higher transverse granularity and depth information is required by the Level-1 trigger system to reduce the rates and improve resolution for several trigger objects as Figure 3.22 shows [27]. Rejection factors of about $3-5$ for low p_T jets faking electrons can be achieved by implementing shower shape algorithms using the 2nd sampling layer of the EM calorimeters. Furthermore, studies of discriminant variables using the 3^{rd} sampling layer of the EM and the hadronic Tile Calorimeter layers are in progress and

Figure 3.22: Expected Level-1 rates for different algorithms and conditions calculated from Monte Carlo simulations with the current Level-1 trigger system [28]. The pileup corresponds to $\mu = 46$ with a bunch spacing of 25 ns [27].

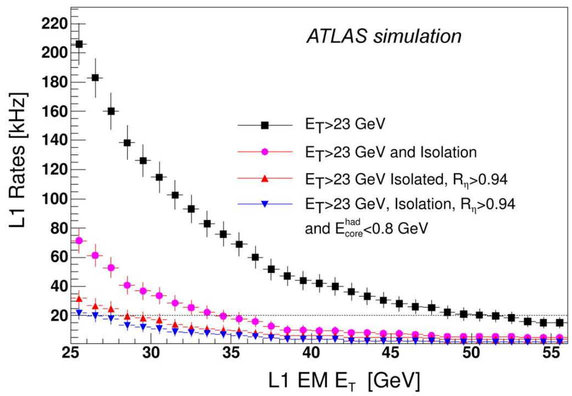

could potentially lead to substantial improvements of the resolution of τs, jets and more importantly, missing E_T (MET) triggers.

This additional information will require a partial upgrade of the calorimeter front-end readout architecture, part of the input stage of the Level-1 calorimeter trigger and the interfaces among the two systems. The upgrade plan for Phase-I is part of a more general staged program to be implemented over the next decade for the entire HL-LHC lifetime: the ultimate goal is a free-running digital architecture of all individual LAr and Tile calorimeter channels. The proposed architecture will be validated by an in-beam system test planned for installation in ATLAS during the Phase-0 shutdown. The system will be run seamlessly within ATLAS during the Run-II. It is aimed at improving the granularity in one $\Delta\eta \times \Delta\phi = 0.4 \times 0.4$ slice of the LAr and Tile barrel calorimeters, matching the size of the current L1Calo electron algorithm window. Two trigger Tower Builder Boards and four new Tile drawers with digitization of data at the front-end will be installed in order to test the digital trigger path and hardware implementations of novel single-object triggers.

For the Phase-I, an intermediate stage will be applied. It combines analog and digital trigger readout, fully compatible with the present analog transmission of the trigger primitives but with a digital readout path that contains many of the elements required by the final upgrade.

For the LAr calorimeters, this will be implemented by means of new Tower Builder Boards (sTBBs) that are modified by adding a digital readout path. This provides the trigger with finer granularity data in depth and in η.

The full digital readout of the Tile calorimeter is planned for Phase-II. For Phase-I, an upgrade based on using the "D-cell outputs" (the outermost layer of TileCal) that are already available is being considered, if it can be motivated by simulations results.

3.11.3 The Fast Tracker

The FastTracKer (FTK) [27], is a pipelined electronics system that rapidly finds and fits tracks in the inner-detector silicon layers for every event that passes the Level-1 trigger. Its goal is global track reconstruction with near offline resolution at a maximum Level-1 rate of 10^5 events per second and a latency per event of less than 100 μs. This can be compared with the time to carry out full track reconstruction in the Level-2 processors which is estimated to be several hundred milliseconds at Phase-I luminosity. FTK uses 11 silicon layers over the full rapidity range covered by the barrel and the disks. It receives a copy of the pixel and silicon strip (SCT) data at full speed as it moves from the RODs to the ROSs following a Level-1 trigger, and after processing it provides the helix parameters and χ^2 of all tracks with p_T above a minimum value, typically 1 GeV. The Level-2 processors can request the track information in a Region of Interest or the entire detector.

FTK has been designed as a highly parallel system that is segmented into η and ϕ towers, each with its own pattern recognition hardware and track fitters, and the installation milestone target is the Long Shutdown starting at 2018.

3.11.4 The Forward Physics Upgrade

ATLAS considers to install a Forward Proton (AFP) detector in order to detect protons at 206 and 214 m on both side of the ATLAS experiment at very small scattering angles [27]. The physics motivation is to identify and record events with leading intact protons emerging from diffractive collisions occurring in ATLAS, for both "exploratory" physics, e.g. anomalous couplings between W/Z bosons and γ, and QCD physics in new kinematical domain. These studies could not be performed using the other ATLAS forward detectors.

The AFP detector will consist of three parts: movable beam pipe, silicon position detectors and quartz timing detectors. The movable beam line specializes in the measurement of scattered protons, the silicon tracker in combination with the LHC dipole and quadrupole magnets forms a powerful momentum spectrometer and the quartz detector will provide a fast timing system.

3.11.5 The T/DAQ Upgrade

As mentioned in the previous paragraphs, the replacement of the Small wheel and the partial replacement of the LAr on-detector electronics will impose changes to the L1 Muon and Calorimeter triggers. On top of that, upgrades to the Level-1 trigger electronics are expected to improve performance at higher pile-up and provide increased trigger flexibility without major architectural changes to the current detector readout and data acquisition [27].

Following the L1 trigger changes, the HLT needs to adapt the selection software for higher luminosity. The HLT steering software will be upgraded to provide greater flexibility, to optimize the event processing, to minimize average execution times and prevent excessive times in the case of events with many RoIs. The HLT tracking code will be upgraded to limit the rise of algorithm execution times as events become more complex due to the higher levels of pile-up and cavern background, affecting the muon detectors, as the luminosity increases. In addition to minimizing the average per-event processing time, it is important to prevent very long execution times which would otherwise cause time-outs. The HLT muon code must be adapted for the new small muon wheels and the ID tracking must be adapted for the insertable B-layer and to use FTK information. The FTK will provide initial track parameter information which can be used to guide (seed) the HLT tracking that will add TRT information and refine and refit the tracks.

The current DAQ/HLT architecture is expected to meet the needs of the experiment with respect to Level-1 rate and bandwidth. However, a new version of the readout link (RoL), whose current implementation runs at 160/200 $Mbytes/s$, may be needed to provide increased bandwidth for new detectors. The physics demands of ATLAS have pushed the operation of the ROS a factor of two beyond its original design specification. The performance is currently network bandwidth limited (2 $Gbits/s$). This limit constrains some Level-2 trigger chains and in order to remove this limitation and re-establish some of the operational headroom originally provided in the system, the data flow network will be upgraded to a 10 $Gbits/s$ Ethernet connection at the ROS and, via link aggregation, 100 $Gbits/s$ Ethernet connections to a central core. This upgrade would also allow the rate at which events are built to be increased. A sub-component of the ROS is the ROBIN, a PCI-X card. By the Phase-I shutdown, it is anticipated that PCI-X slots will no longer be deployed in sufficient numbers on commercially available computers, having been replaced by PCI-express. The ROBIN will be re-designed and re-implemented to follow this technological trend and support readout links of higher speeds than the current.

By the end of Phase-I operations, the custom VMEbus electronics implementing the Region of Interest Builder (RoIB) will have been in operation for sixteen years. Two upgrade paths are currently being investigated. The first aims to exploit the continued advances in server technology. It is expected to be able to implement the RoIB functionality in one or more servers housing one or more custom mezzanine cards that handle the small data packets arriving at up to 100 kHz from the Level-1 system. This will remove or reduce the dependency on custom electronics and introduce additional operational flexibility into the system. The alternative of re-implementing the RoIB in modular electronics will also be investigated as a back-up solution.

Figure 3.23: Schematic view of the signatures the different physics objects leave in the detector. The ATLAS detector layout is consider for the graph.

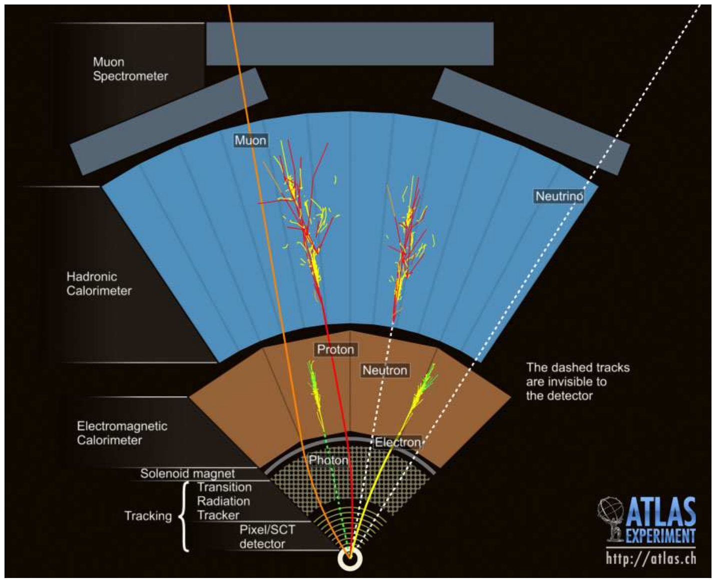

Other upgrades to the ATLAS detector imply the deployment of additional DAQ/HLT hardware. Additional RoLs and ROSs (including ROBINs) will be deployed to readout the new small wheels and the upgraded LAr electronics.

The deployed software will have become obsolete and in some cases no longer meet the requirements on the DAQ/HLT system, which will necessitate its upgrade.

3.12 Summary

In this chapter, the technologies on which the ATLAS detector is based are extensively described. The combination of the information from the tracking detectors, the calorimeters and the muon chambers leads to the identification of physics objects as Figure 3.23 shows. The triggering and the data acquisition are of high importance for fruitful and efficient data taking, especially in harsh pile-up conditions. At the end of this chapter the future plans for the detector upgrade are presented.

Chapter Bibliography

[1] G. Aad et al., Expected Performance of the ATLAS Experiment - Detector, Trigger and Physics, 2009, 0901.0512.

[2] CERN, ATLAS: Detector and physics performance technical design report. Volume 1, 1999.

[3] ATLAS Collaboration, Technical challenges of atlas, http://atlas.ch/atlas_brochures/atlas_brochures_pdf/atlas_tech_full.pdf.

[4] Norbert Wermes and G Hallewel, *ATLAS pixel detector: Technical Design Report*, Technical Design Report ATLAS. CERN, Geneva, ATLAS-TDR-11, CERN-LHCC-98-013.

[5] Maximilien Brice, Re-insertion of the pixel detector, CERN-HI-1312311.

[6] Atlas Collaboration, Atlas interior 2013, http://www.atlas.ch/photos/atlas-interior.html.

[7] ATLAS inner detector: Technical design report. Vol. 1, 1997, CERN-LHCC-97-16, ATLAS-TDR-4.

[8] ATLAS Collaboration, ATLAS SCT public twiki page, https://twiki.cern.ch/twiki/pub/Atlas/SctWiki.

[9] Maximilien Brice, ATLAS experiment - view of the inner detector ATLAS TRT, Sep 2005, http://cds.cern.ch/record/889555.

[10] ATLAS liquid argon calorimeter: Technical design report, 1996, CERN-LHCC-96-41.

[11] ATLAS Collaboration, Liquid Argon Barrel ATLAS Photos, http://www.atlas.ch/photos/calorimeters-lar-barrel.html.

[12] ATLAS Tile calorimeter: Technical design report, 1996, CERN-LHCC-96-42.

[13] ATLAS Collaboration, Combined Barrel ATLAS Photos, http://www.atlas.ch/photos/calorimeters-combined-barrel.html.

[14] ATLAS muon spectrometer: Technical design report, 1997, CERN-LHCC-97-22, ATLAS-TDR-10.

[15] T. Argyropoulos, K. A. Assamagan, B. H. Benedict, V. Chernyatin, E. Cheu, et al., Cathode strip chambers in ATLAS: Installation, commissioning and in situ performance, *IEEE Trans.Nucl.Sci.*, 56:1568–1574, 2009.

[16] ATLAS Collaboration, RPC ATLAS Photos, http://www.atlas.ch/photos/muons-rpc.html.

[17] CERN, *ATLAS magnet system: Technical Design Report, 1*, Technical Design Report ATLAS. CERN, Geneva, 1997, ATLAS-TDR-6, CERN-LHCC-97-018.

[18] CERN, *ATLAS central solenoid: Technical Design Report*, Technical Design Report ATLAS. CERN, Geneva, ATLAS-TDR-9, CERN-LHCC-97-021.

[19] ATLAS Collaboration, Magnets ATLAS Photos, http://www.atlas.ch/photos/magnets.html.

[20] J P Badiou, J Beltramelli, J M Baze, and J Belorgey, *ATLAS barrel toroid: Technical Design Report*, Technical Design Report ATLAS. CERN, Geneva, 1997, ATLAS-TDR-7, CERN-LHCC-97-019.

[21] CERN, *ATLAS end-cap toroids: Technical Design Report*, Technical Design Report ATLAS. CERN, Geneva, 1997, ATLAS-TDR-8, CERN-LHCC-97-020, Electronic version not available.

[22] P.J. Clark, The ATLAS detector simulation, *Nucl.Phys.Proc.Suppl.*, 215:85–88, 2011.

[23] N. Berger, T. Bold, T. Eifert, G. Fischer, S. George, et al., The ATLAS high level trigger steering, *J.Phys.Conf.Ser.*, 119:022013, 2008.

[24] A Krasznahorkay, The evolution of the Trigger and Data Acquisition System in the ATLAS experiment, Technical Report ATL-DAQ-PROC-2013-018, CERN, Geneva, Sep 2013.

[25] Georges Aad et al., Improved luminosity determination in pp collisions at $\sqrt{s}$ = 7 TeV using the ATLAS detector at the LHC, *Eur.Phys.J.*, C73:2518, 2013, 1302.4393.

[26] ATLAS Collaboration, ATLAS Luminosity Public Results Twiki, *https://twiki.cern.ch/twiki/bin/view/AtlasPublic/LuminosityPublicResults*.

[27] Letter of Intent for the Phase-I Upgrade of the ATLAS Experiment, Technical Report CERN-LHCC-2011-012, LHCC-I-020, CERN, Geneva, Nov 2011.

[28] ATLAS Collaboration, ATLAS public results, https://twiki.cern.ch/twiki/bin/view/AtlasPublic/WebHome.

[29] S. Gadomski, Updated impact parameter resolutions of the ATLAS Inner Detector, 2000, ATL-INDET-2000-020, ATL-COM-INDET-2000-026, CERN-ATL-INDET-2000-020.

[30] Georges Aad et al., Measurement of the muon reconstruction performance of the ATLAS detector using 2011 and 2012 LHC proton-proton collision data, *Eur.Phys.J.*, C74(11):3130, 2014, 1407.3935.

[31] Georges Aad et al., Electron and photon energy calibration with the ATLAS detector using LHC Run 1 data, *Eur.Phys.J.*, C74(10):3071, 2014, 1407.5063.

[32] X. C. Vidal, R. Cid, and G. M. Rey, Taking a closer look at LHC, http://www.lhc-closer.es.

[33] CERN, ATLAS: Detector and physics performance technical design report. Volume 2, 1999.

[34] M Capeans, G Darbo, K Einsweiller, M Elsing, T Flick, M Garcia-Sciveres, C Gemme, H Pernegger, O Rohne, and R Vuillermet, ATLAS Insertable B-Layer Technical Design Report, Technical Report CERN-LHCC-2010-013, ATLAS-TDR-19, CERN, Geneva, Sep 2010.

[35] ATLAS inner detector: Technical design report. Vol. 2, 1997, CERN-LHCC-97-17.

[36] A. Artamonov, D. Bailey, G. Belanger, M. Cadabeschi, T.Y. Chen, et al., The ATLAS forward calorimeters, *JINST*, 3:P02010, 2008.

[37] J.C. Barriere, F. Bauer, M. Fontaine, A. Formica, V. Gautard, et al., The alignment system of the ATLAS barrel muon spectrometer, 2008.

[38] S Aefsky, C Amelung, J Bensinger, C Blocker, A Dushkin, M Gardner, K Hashemi, E Henry, B Kaplan, M Ketchum, P Keselman, U Landgraf, A Ostapchuk, J E Rothberg, A Schricker, N Skvorodnev, and H Wellenstein, The Optical Alignment System of the ATLAS Muon Spectrometer Endcaps, *J. Instrum.*, 3:P11005. 49 p, Feb 2008, ATL-MUON-PUB-2008-003, ATL-COM-MUON-2008-005.

[39] R (SLAC) Bartoldus, C (Marseille CPPM) Bee, D (CERN) Francis, N (RAL) Gee, S (London RHBNC) George, R (Michigan SU) Hauser, R (RAL) Middleton, T (CERN) Pauly, O (KEK) Sasaki, D (Oregon) Strom, R (Roma I) Vari, and S (Roma I) Veneziano, Technical Design Report for the Phase-I Upgrade of the ATLAS TDAQ System, Technical Report CERN-LHCC-2013-018, ATLAS-TDR-023, CERN, Geneva, Sep 2013, Final version presented to December 2013 LHCC.

[40] dE/dx measurement in the ATLAS Pixel Detector and its use for particle identification, Technical report, CERN, Geneva, Mar 2011, ATLAS-CONF-2011-016.

[41] Basic ATLAS TRT performance studies of Run 1, Technical report, CERN, Geneva, Mar 2014, ATL-INDET-PUB-2014-001.

[42] Georges Aad et al., Monitoring and data quality assessment of the ATLAS liquid argon calorimeter, *JINST*, 9:P07024, 2014, 1405.3768.

[43] Georges Aad et al., Performance of the ATLAS muon trigger in pp collisions at $\sqrt{s} = 8$ TeV, 2014, 1408.3179.

4

Cathode Strip Chambers (CSC)

4.1 Introduction

In this chapter, the performance and operational properties of the Cathode Strip Chambers (CSC) are studied. Starting from the basic construction properties, the readout of the chambers is described. The on-detector electronics send the collected information to the off-detector for enhanced processing and signal allocation. The major operational problem during the Run-I was the deadtime caused by the off-detector system. A variety of methods were applied to resolve the problem and a new system was designed for the Run-II.

The reconstruction software is explained in all steps until the required CSC muon signal is extracted and performance summaries are also given in this chapter. The resolution and the alignment of the detector are explored, given their importance on the muon quality.

At the end, the repair of chambers and their functionality is reported.

4.2 Principle of Operation

The CSC, introduced in Section 3.6.2, are well suited to meet the requirements for the precision measurement of muons in ATLAS [1]. Precision tracking at the innermost station (Small Wheel) in the high pseudorapidity regions, $2.04 \leq |\eta| \leq 2.70$, is performed by 16 four-layered Cathode Strip Chambers on each EndCap [2]. These are multi-wire proportional chambers with segmented cathodes providing excellent spatial resolution and high counting rate capability. The second cathode of each layer is coarsely segmented, providing the transverse coordinate [2]. The sensitivity to neutrons is low, $\epsilon_n < 10^{-4}$, due to the small gas volume and the lack of hydrogen in the operating gas. Photon sensitivity is also small, $\epsilon_\gamma \sim 1\%$ for $E_\gamma = 1\ MeV$. The rather large chamber dimension and high operating pressure, however, make them unsuitable for use in areas where high ($> 200\ Hz/cm^2$) counting rates are expected [1].

Following the overall ATLAS geometry, there are two chamber versions, Large and Small, which differ slightly in the active area [2]. These are installed alternately and overlap partially to seamlessly cover the 27% of the Muon Spectrometer's pseudorapidity acceptance. The large chambers of one out of the two small wheels are presented in Figure 4.1. Multiple measurements of the same track are provided, since every chamber consists of four identical layers each with 192 precision and 48 transverse coordinate strips, which are lithographically etched for highest precision. The precision strips have a readout pitch of 5.308 and 5.556 mm for the Large and Small chambers respectively. The basic operation and design parameters are presented in Table 4.1.

Table 4.1: Basic CSC Operation Parameters [2].

Number of chambers	2×16	
Number of layers / chamber	4	
Layers separation	25 mm	
Inclination angle	11.6°	
Gas mixture	$Ar/C0_2$ (80% : 20%)	
Wire material	$W - Re$ (97% : 3%)	
Operating voltage / gain	1900 V / 10^4	
Anode - cathode distance	2.5 mm	
Anode wire pitch	2.5 mm	
	Small	Large
Number of wires / layers	250	420
Number of η readout strips	192	192
η readout strip pitch (mm)	5.566	5.308
Number of ϕ readout strips	48	48
ϕ readout strip pitch (mm)	12.922	21.004
Active area (m^2) / chamber	0.50	0.78
Gas volume (l) / chamber	10.0	15.5
Chamber total weight (kg)	70	92

Figure 4.1: One of the two ATLAS Small Wheels in the assembly building before the installation [3]. In the inner radius the eight CSC large chambers are visible and partially overlapping from the backside (not visible) with the eight small chambers.

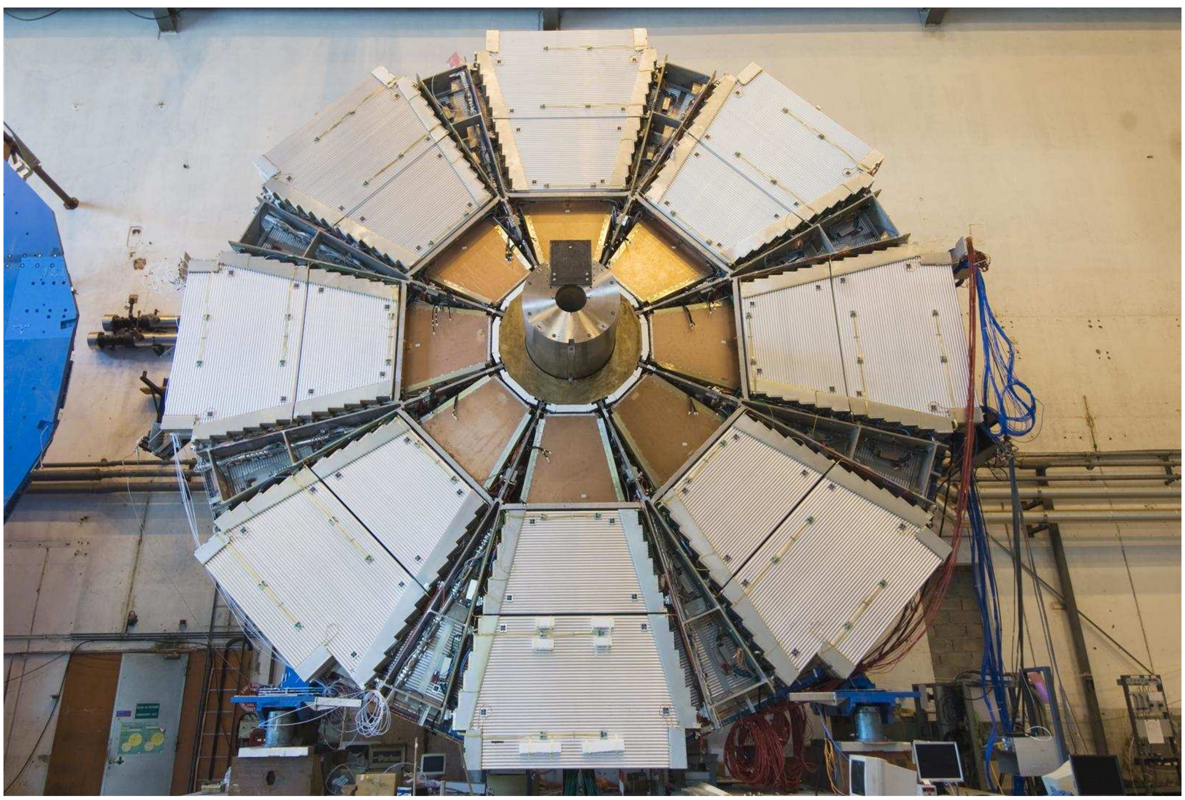

Figure 4.2: Schematic diagram of the cathode strip chamber (side view) [2].

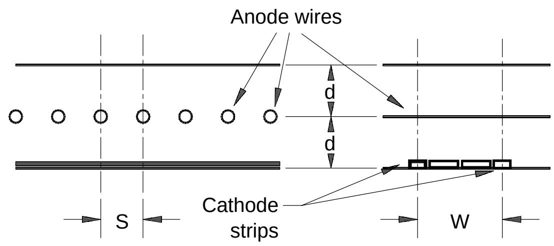

The gas used is a mixture of Ar/CO_2 which comply the characteristics of high drift velocity, low Lorentz angle and is non-flammable. Despite the fact that a high drift velocity is needed to ensure that the bunch-crossing identification can be performed [1], for the position measurement, variations of the drift velocity or non-uniform drift velocities as a function of E/p are inconsequential to the performance. For the same reason, the CSC operation is immune to modest variations of temperature and pressure. Similarly, variations in the absolute gas gain do not, to first order, affect the CSC operation since a relative charge measurement in adjacent strips is involved.

4.3 Signal Formation

The CSCs are multiwire proportional chambers with a symmetric cell in which the anode-cathode spacing (d) is equal to the anode wire pitch (S), which has been fixed at 2.5 mm, as schematically shown in Figures 4.2,4.3. In a typical multiwire proportional chamber the anode wires are read out limiting the spatial resolution to an R.M.S. of $S/\sqrt(12)$ [2]. In a CSC the precision coordinate is obtained by measuring the charge induced on the segmented cathode by the avalanche formed on the anode wire. The induced charge distribution as a function of the variable $\lambda = x/d$, where x is the precision coordinate (transversely to the strips), is given by:

$$\Gamma(\lambda) = K_1 \frac{1 - tanh^2 K_2 \lambda}{1 + K_3 tanh^2 K_2 \lambda} \tag{4.1}$$

where the constants K_2, K_3 are related by the empirical formula:

$$K_2 = \frac{\pi}{2}\left(1 - \frac{1}{2} K_3^{1/2}\right). \tag{4.2}$$

Using the equation 4.2 and the constraint that the total charge induced on one cathode equals half the avalanche charge, Equation 4.1 can be reduced to a one-parameter

Figure 4.3: The principle of operation is illustrated in the diagram, this particular cathode geometry is called ”Two Intermediate Strips”, which improves the position linearity using capacitive charge division [4, 5].

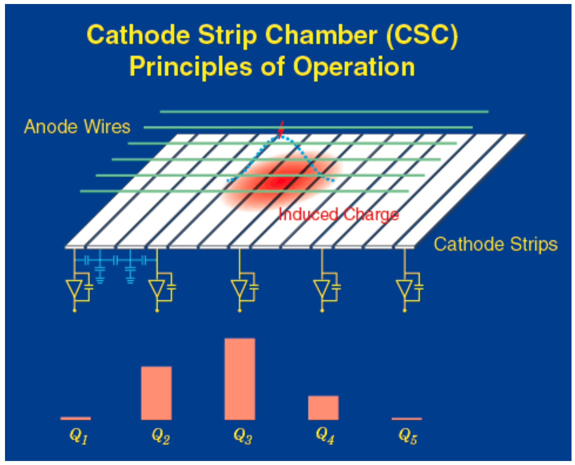

expression. The optimum cathode readout pitch W is determined by the width of the induced charge and the desire to keep the number of readout channels to a minimum while maintaining a linear response.

Optimal capacitive coupling requires that the inter-strip capacitance (C_1) be much larger than the capacitance of a strip to ground, (C_2). Specifically for the ATLAS CSC design $C_1/C_2 \approx 10$ [1]. Since the preamplifier noise is dominated by the input capacitance an additional advantage from the use of two intermediate strips (graphically presented in Figure 4.3) is a reduction by a factor between two and three of the inter-node capacitance. Further optimization of the linearity can be accomplished by making the width of the intermediate strip slightly larger than that of the readout strips. It is necessary to provide a high resistance path to ground to maintain the intermediate strips at the proper DC potential. A thin strip of resistive epoxy (conductivity 6 $M\Omega$ per square) is silk screened on the tips of the strips at the end of the cathode opposite to the amplifiers.

4.4 Spatial resolution of the CSCs

In a CSC the precision coordinate is obtained by a relative measurement of charges induced by the avalanche on adjacent cathode strips. Therefore modest (< 20%) variations in the chamber's gas gain do not affect the spatial resolution [1]. For this reason the CSC performance is immune to variations in temperature and pressure commonly encountered in the experimental hall. Since no precision time measurement is involved, the CSC operation is insensitive to the drift properties of the operating gas. A modest 34 *ns* R.M.S. time resolution is sufficient to determine the bunch crossing with high efficiency.

The primary factor limiting the CSC spatial resolution is the electronic noise of the preamplifier. The precision in the determination of the center of gravity of the induced charge depends linearly on the signal-to-noise ratio. Eventually other factors, such as uncertainty in electronic gain, calibration and geometrical cathode distortions, set the limit for this technique at about 30 μm. A design consideration of the readout amplifier is an electronic noise level such that the chamber can be operated with a total anode charge of about 1 pC per minimum ionizing particle at the target spatial resolution.

Assuming that the projection of the avalanche position on the cathode strip plane is at a point $x = 0$. The position of the center of gravity is given by the ratio of the first and second moments of the charge distribution on the strip plane

$$x_{cg} = \frac{\sum\limits_{i=1}^{N} x_i q_i}{\sum\limits_{i=1}^{N} q_i} \tag{4.3}$$

where $x_i = iW$ and W is the pitch of the cathode readout. If the charges q_i are the measured with an R.M.S. error of σ then the uncertainty in x_{cg} is:

$$\sigma_{cg} = \frac{\sigma}{Q}\sqrt{2\sum_i x_i^2} \tag{4.4}$$

or

$$\sigma_{cg} = \frac{\sigma}{Q}\sqrt{2W^2 + 2(4W^2) + 2(9W^2) + ...} \tag{4.5}$$

Therefore, the resolution depends on the number of strips used. The optimum lies between three and five strips, as estimated from Monte Carlo studies. The resolution deteriorates rapidly for one or two (due to lack of information), while it increases slowly when more than five strips are used because the electronic noise of more channels is added in quadrature.

4.5 The Effect of Inclined Tracks and the Lorentz Angle

The second most significant contribution to the spatial resolution of the CSC is the effect of the inclined tracks and the Lorentz angle. The charge interpolation is optimum when the avalanche is formed on a single point along the wire. A finite spatial extent of the anode charge results in a resolution degradation [1]. Such non-local charge deposition can be caused by a number of factors such as delta electrons, inclined tracks, and a Lorentz force along the anode wire in the presence of a magnetic field which is not collinear with the electric field of the chambers. It should be noted, however, that the Lorentz effect in the CSC does not result in a systematic shift of the measured coordinate. It does not, therefore, require a correction. In fact, no correction is possible. Simply the resolution degrades because of the spread of the charge along the wire. The effect of the inclined tracks is minimized by tilting the chamber by an angle of 11.59° so that, on the average, the tracks are normal to the plane of the chambers [1].

4.6 Timing Resolution

The maximum drift distance of the ionization electrons for a track traversing a chamber exactly between two anode wires is 1.25 mm. With a drift velocity of 60 $\mu m/ns$, typical of the chosen operating gas, the maximum drift time is about 30 ns [1]. A time of arrival distribution has been measured to have an R.M.S. of about 7 ns. It exhibits, however, significant tails due to very low drift fields in the boundary of two adjacent cells. In any case, this resolution is not sufficient to permit efficient tagging of the bunch crossing of a given muon traversing the chamber. For this reason, the following technique is used to determine the bunch crossing. The earliest time of arrival in a four-plane multilayer is determined by connecting the four signals from these planes in an OR circuit. Test beam measurements of the timing obtained with such an arrangement show a timing resolution of 3.6 ns R.M.S. with a symmetric, nearly Gaussian, distribution.

4.7 Mechanical Design and Construction

4.7.1 Description of the Basic Four-Layer Module

The CSC design utilizes low-mass construction materials to minimize multiple scattering and detector weight [1]. A four-layer multilayer is formed by five flat, rigid panels, each of which is made of an 18.75 mm thick sheet of nomex honeycomb (hexcel) and two 0.5 mm thick copper-clad FR4 laminates, the 17 μm thick copper cladding forming the cathodes. The panel frames are made of machined rohacell, a closed-cell, high stiffness lightweight foam. Precision machined FR4 strips glued on the panels provide the step for the anode wire plane. The anode wires are made of gold-plated tungsten with 3% rhenium and have a diameter of 30 μm. The high voltage (HV) distribution system and all the passive components are encapsulated in the rohacell frames. A rubber gasket between two adjacent planes provides the gas seal for the assembly. No components under high voltage are outside the seal, thus minimizing the risk of high voltage breakdowns. These panels weigh approximately 1 kg/m^2.

In each of the four gaps, the position-sensing cathode strips are lithographically etched. One of the cathodes has precision strips, parallel to the corresponding MDT anode wires. The second cathode is segmented in coarser strips parallel to the CSC wires. They provide the transverse coordinate and bunch crossing timing. The five panels are precisely positioned with respect to each other with the aid of locating pins. The outer copper-clad laminates of each module form an electromagnetic shield for the detector. A cutout view of one gap formed by two panels has been already presented in Figure 3.10. Signals from the cathode strips are transferred via ribbon cable jumpers to the electronic readout boards located on the chamber edges. The whole assembly is rigid enough so that no in-plane alignment system is necessary.

4.7.2 Assembly Procedure

Key elements in the construction of the cathode strip chambers are the lithographically segmented precision cathodes. These cathodes are produced in industry using standard lithographic techniques. The design of the cathodes is done using printed circuit layout tools and incorporates, in the perimeter of the boards, the necessary circuitry for the signal routing and HV distribution and filtering. The design is then electronically transmitted to an industrial firm for the photo-plotting of the artwork and the etching of the boards. The rest of the assembly procedure is schematically shown in Figure 4.4.

4.7.3 Support Structure and Alignment of the CSC System

The sixteen chambers in each EndCap are mounted on a rigid support structure, as seen in Figure 4.1 in the form of a wheel, inclined in order to reduce the resolution degradation due to inclined tracks [1]. The support structure is aligned, as a unit, within the EndCap global alignment system and no individual chamber alignment is needed.

Figure 4.4: The chamber assembly sequence [1].

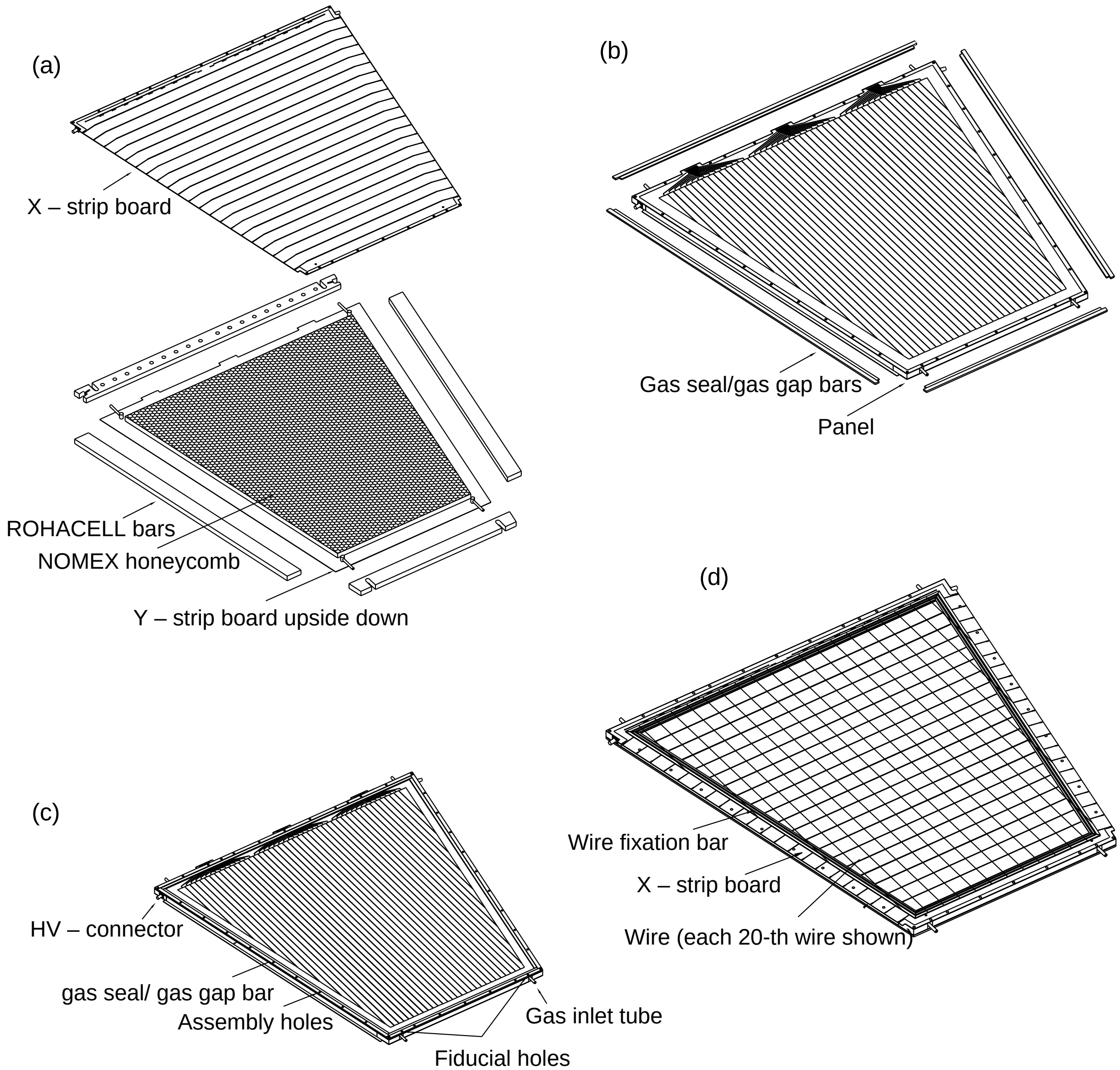

4.8 The Readout Complex

The severe radiation levels where the CSC chambers operate imposes the minimum of the electronics to be located on the detector [6]. The on-detector electronics amplifies and shapes the cathode strip signals, and stores the analog pulse height information during the first-level trigger latency. When a trigger is received, four consecutive time samples are digitized and transmitted via fiber-optic links to the off-detector electronics. Sampling and digitization are performed on-detector but are controlled by the off-detector electronics.

The off-detector electronics operated during Run-I and replaced with new ones for the Run-II, due to limitations of the former to operate beyond 70 kHz. The hardware of the two systems is based on different technologies but the processing of the information is similar. It contains the sparsification stage, during which hits below the threshold and hits not associated with the current bunch crossing are suppressed. The rejection stage identifies hits possibly belonging to tracks by removing isolated background hits. The remaining data are formatted and sent to the ATLAS Trigger/DAQ System (TDAQ) for further processing.

4.8.1 The On-Detector Electronics

The CSC on-detector electronics consists of two layers of amplifier-storage module (ASM) boards [6]. Each strip is connected to a preamplifier and shaper circuit, implemented as a radiation-tolerant custom ASIC, which forms a bipolar pulse with a 70 ns peaking time to mitigate pile-up effects. The shaped pulses are sampled every 50 ns, and the analog pulse height information is stored in a custom radiation tolerant CMOS switched capacitor array (SCA) for the duration of the first-level trigger latency, which for the CSCs is estimated to reach 188 bunch crossings in the worst case scenario. The SCA provides an effective pipeline depth of 288 bunch crossings. Following a trigger, those cells of the SCAs specified by the ROD are time multiplexed and digitized using $12-bit$ Analog Devices AD9042 ADCs. Custom ASICs multiplex the data from 16 ADCs to two G-Link serializers configured to operate with $16-bit$ input words at 40 MHz single frame rate.

Eight preamplifier/shaper ICs supporting a total of 96 channels reside on a printed circuit board (ASM-I). Two ASM-I boards piggyback on one ASM-II which contains the 16 SCAs, ADCs, multiplexors serving 192 channels total, and two fiber optic G-Link transmitters. A total of five such ASM-I/ASM-II combinations are needed to read out one chamber, four for the precision coordinate strips and one for the transverse coordinate strips from all four layers. Four ASM-I/ASM-II configurations are attached to the narrow edge of the chamber and share a common Faraday cage and cooling

Figure 4.5: CSC fiber connections for the small (Figure (a)) and large (Figure (b)) chambers [7].

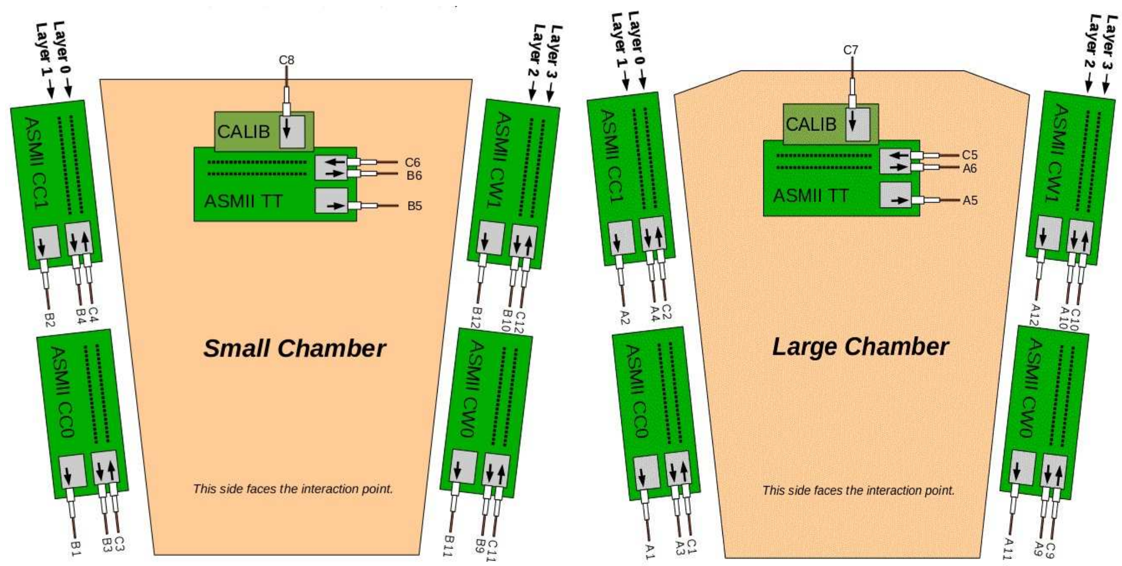

(a) (b)

fixture. The transverse strip ASM-I/ASM-II package is attached to the broad side of the chamber, together with circuitry for injecting a pulse onto the wires of each layer for calibration purposes.

Each of the on detector electronic package is connected to the off detector electronics by two data fibers and one control fiber. The data fiber transmits the detector information, whereas the control fiber is used for the protocol establishment between the on and off electronics for the control of the latter. The connections for each chamber type are presented in Figure 4.5. It has to be noted that each fiber bundle contains twelve fibers, two of which are used as spares.

4.8.1.1 Calibration

The calibration of the on-detector electronics is done by a pulser [8], which practically provides a fast voltage step. Control is delivered by a fiber optic link from the off-detector electronics and deserialized by a "G-Link" receiver. The deserialized data directly feeds the pulse drivers, attenuator level select lines, and analog switches. The pulse drivers are gated out and the analog switches ground the output when the G-Link Rx receives fill frames or is unlocked to prevent spurious pulses. The comparison of known input and the measured output is used as a calibration constant.

The calibration procedure also includes daily pedestal runs. These runs are taken during the operations period and the procedure is to record the electronics noise when

Figure 4.6: Pedestal noise pattern used for the Run-I operations. Side C sectors appear with negative numbers as well as the ϕ channels [9].

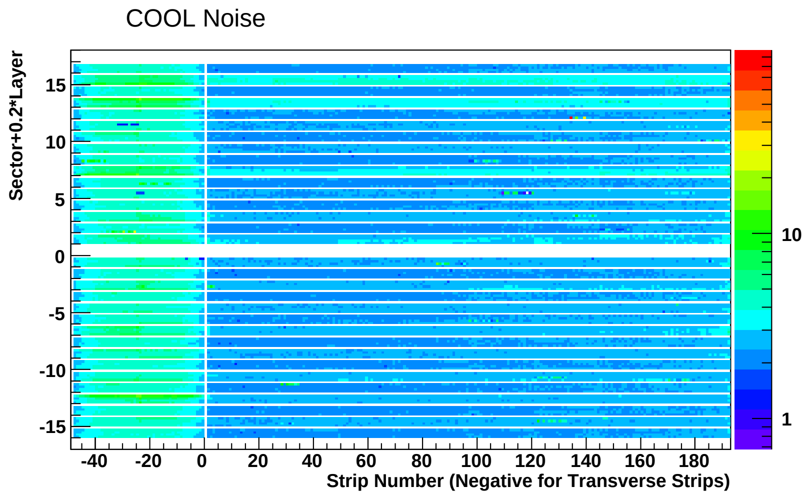

the chamber HV is off (no gas amplification). When a pedestal is taken, a histogram is filled with ADC values and the pedestal is defined as the mean of the Gaussian distribution. The thresholds for the data acquisition are set to a few σ from the pedestal value of each channel and the pedestal values itself are used to define the charge measurement uncertainty, as is discussed later.

A typical pedestal pattern, the one used for the Run-I operations, is presented in Figure 4.6. Side C sectors appear with negative numbers as well as the ϕ channels. All the pedestal runs taken, were analyzed and no significant variation found in the three years of operations, which proves the pedestal stability. The deviations from the database pattern (Figure 4.7) recorded are within the uncertainties and consequently the database pattern remain unchanged.

Apart from the pedestal, other calibration constants are monitored and these are the peaking time, the time of the maximum of each channel relative to the first sample which might show variation between groups of 12 channels up to 10 ns, dead and hot channels are kept for the accurate offline reconstruction, gain constants, defined as the amplifier's sensitivity in ADC counts per fC for each channel, the linearity and saturation points, which describe deviations from the ideal proportionality between the pulser amplitude and the measured amplitude.

Especially for the problematic channels, detailed studies conducted periodically to reveal possible degradation, based on occupancy histograms of hits on muon tracks (excluding the dead layers[1]). Figure 4.8 shows the map of the dead channels in the

[1]As will be discussed later, the HV failures in layers was the main source of channels disfunctionality.

Figure 4.7: The average pedestal noise for each sector shows small deviation with respect to the database pattern used for the operations [9]. The differences are within the uncertainties, are considered marginal and prove the pedestal stability.

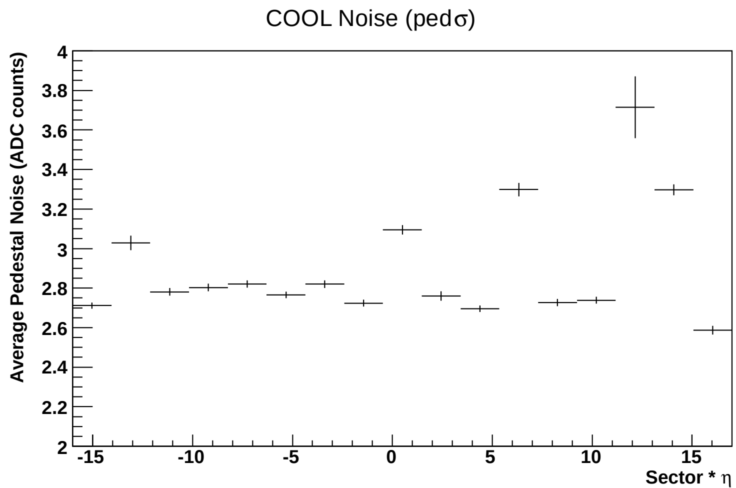

beginning of the 2012 data taking, where dead channels appear with no entries and hot channels have relatively high entries. Overall, the problematic precision channels corresponded to 3.6% and the transverse ones to 4.3%. By the end of 2012 the only degradation was coming from the two dead layers of one sector, which resulted to 5.0% η channels and 5.9% ϕ dead channels.

In the long shutdown of $2013-2015$ the dead layers were repaired and the expected numbers of problematic channels is predicted to be 1.1% and 2.0% for the η and ϕ respectively, though new studies based on actual data need to be conducted at the beginning of the Run-II.

4.8.2 The Off-Detector Electronics

Signals associated with a particle trajectory must be correlated with adjacent strips and time [6]. The consecutive time samples retrieved from each strip provide pulse shape information. An example is shown in Figure 4.9 for four samples. The effective trigger latency is adjusted so that the second and third sample are closest to the peak of the positive lobe. Receipt of a first-level trigger automatically leads to readout of the four or two samples associated with the event.

Signal below a predefined threshold, either the pedestal value of the channel or a user-defined threshold[2], are rejected and calibration constants are applied to the

[2]The higher than the pedestal thresholds could be imposed due to stuck bit or dead channels or

Figure 4.8: Dead and hot channels showing as zero entries bins and relatively high entries bins respectively. The study based on the exclusion of dead layers and the histograms with the occupancy of hits on muon tracks separately for the η (Figure (a)) and ϕ (Figure (b)) channels in the beginning of 2012. At the end of the Run-I operations the only degradation was due to additional dead layers.

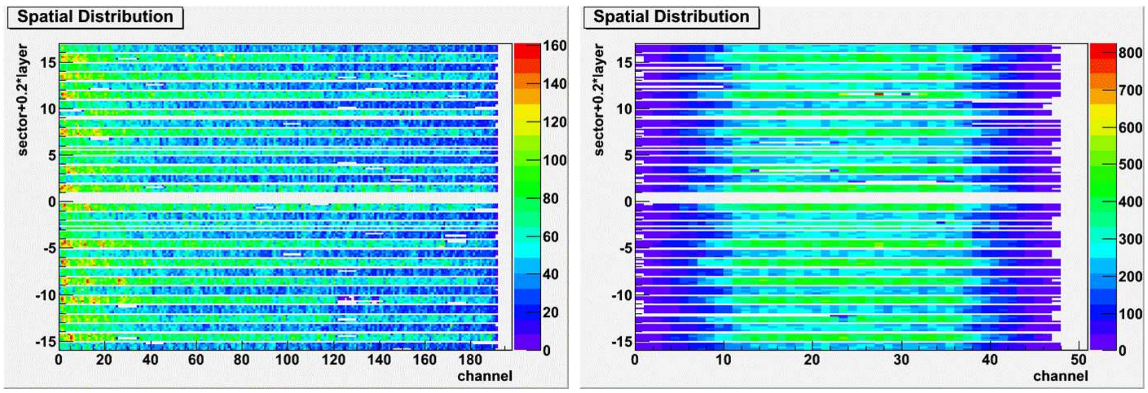

(a) (b)

Figure 4.9: CSC pulse shape, with sampling times (of arbitrary latency) indicated by dashed lines [6].

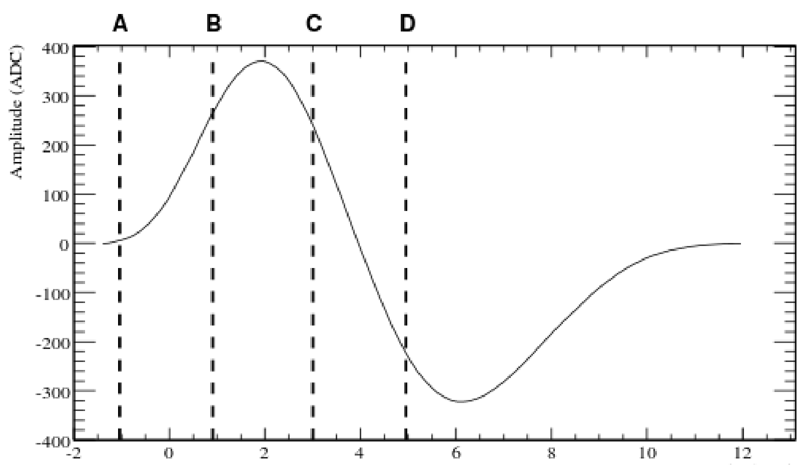

Figure 4.10: CSC dead-time, during the Run-I, as a function of the trigger rate during physics runs [11]. Special handling methods invented to allow the operation within the allowed by the experiment 2% dead-time. The curves corresponds to different data taking conditions that is discussed later.

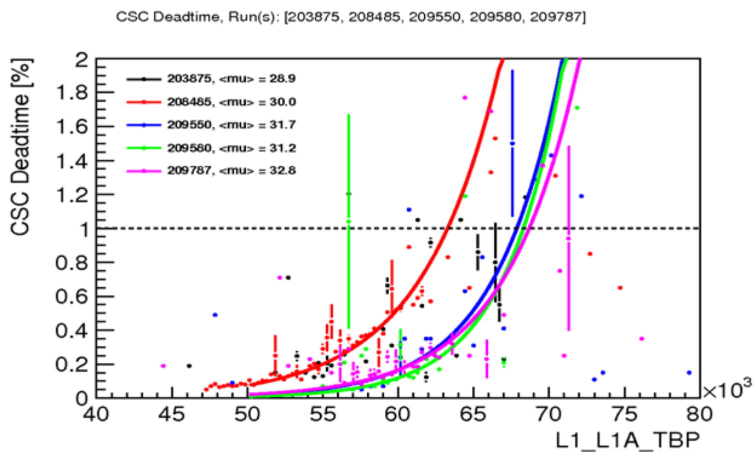

rest. The next step is to identify the clusters by finding groups of contiguous hit channels [10], taking into account that stuck bit channels can create spurious clusters and dead channels can split a cluster in two. The cluster identification is performed via a parabola interpolation and the peaking time is also determined. Overlapping clusters are not a concern during the data taking and the offline reconstruction deals with them.

Except from the nominal data taking acquisition the off-detector electronics control the pulser used for the on-detector electronics calibration, reported in Section 4.8.1.

Between the Run-I and the Run-II the off-detector electronics had to be replaced due to limitations of the initial design. As Figure 4.10 shows, the system could not sustain high trigger rates and the corresponding occupancy [11]. Even from the Run-I period special busy handling methods had to be invented to anticipate the trigger rates and allow running below the maximum allowed dead-time of 2% by the ATLAS experiment. This methods is analyzed in detail in this chapter, focused on the studies performed to evaluate the physics impact on each one of them and the actual impact, after the application, is also be reported.

The description of the off-detector readout technologies are briefly discussed in the next paragraphs. Both of them, as well as the rest of the ATLAS detectors, are configured through the “Object Kernel Support (OKS)” database [12].

---

data suppression strategy (to be discussed later).

Figure 4.11: CSC readout information flow schema [11].

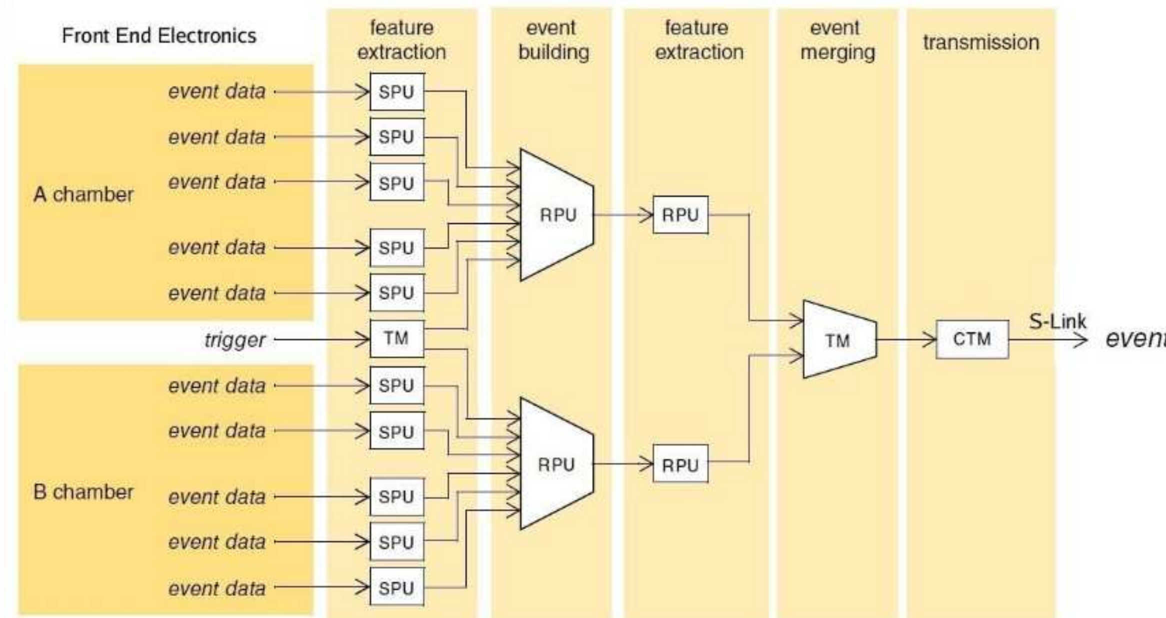

4.8.2.1 The Run-I off-Detector Electronics

The Run-I off-detector electronics consists of 16 readout drivers (RODs), each coupled with a transition module (CTM) [6]. Each ROD/CTM pair handles the incoming data of two chambers, i.e. from 10 ASM-II boards as shown in Figure 4.11. It also controls the ASM-II, in particular the readout of the SCA when a trigger has been received.

The CTM provides three major functions: the logic to monitor, control and receive data from the FEE of its corresponding chambers; the logic and buffering to respond appropriately to trigger requests; and a single fiber-optic transmitter, referred to as the Read-Out Link (ROL), used to send event data to the ATLAS Trigger and Data Acquisition (TDAQ) system [11]. The responsibilities of each ROD are twofold: setting up, controlling and monitoring the on-detector electronics and the CTM; and extracting data from the chambers and sending the resulting event to the ROL.

The CSC ROD is a $9U$ VME board encapsulating thirteen 300 MHz digital signal processors (DSPs) and 40 Xilinx Spartan II field programmable gate arrays (FPGAs). Ten such units are used as Sparsification Processing Units (SPU) and two as Rejection Processing Units (RPU). Each ROD has two identical halves, known as side A and side B, one for each serving chamber. The naming schema for identifying the chambers, starts by defining the wheel, "A" or "C" side, followed by the chamber number, e.g. $A12$. The sectors are numbered on the wheel so that the closest to the ground chamber

Figure 4.12: Number assignment of the CSC chambers for the EndCap A as viewed from the interaction point or EndCap C as seen from outside [7].

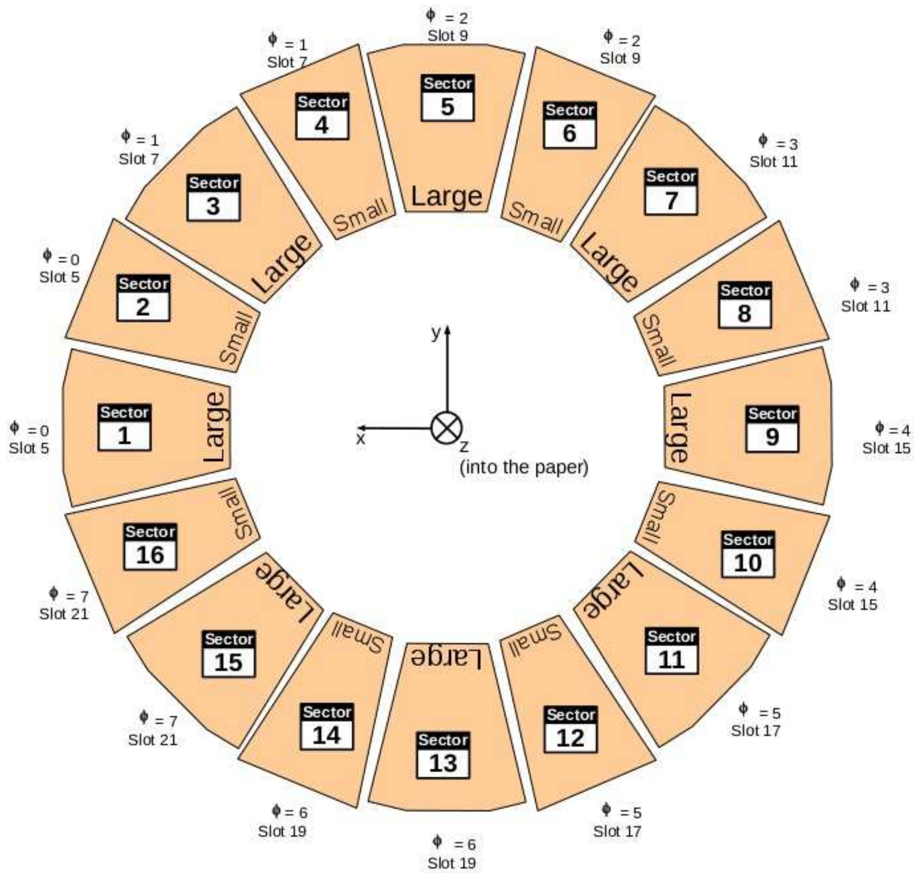

is the number "13" and the sequence, as seen from the interaction point, is clockwise and counterclockwise for the side "A" and "C" respectively. The small chambers have even numbers whereas the large chambers have odd. The convention is to measure the layers of each chamber starting from the IP and pointing to the outside, usually starting from "0". The chamber number assignments are schematically presented in Figure 4.12 along with the slot numbers that the corresponding board is housed.

Each crate houses also a Timing Interface Module (TIM), a Local Trigger Processor (LTP) and a ROD crate controller (RCC). The RCC functions as the crates VME bus master and executes ATLAS specified run control software, used to orchestrate and monitor the behavior of the RODs operating as one component of the ATLAS TDAQ system.

Figure 4.13: The Run-II readout system is based on boards hosted on an ATCA crate. The front view is shown in Figure (a) and the back view in Figure (b) where the RTM are hosted and the fibers are connected.

(a) (b)

4.8.2.2 The Run-II Off-Detector Electronics

The new off-detector electronics are based on the Reconfigurable Cluster Element (RCE), a 6−*slot* ATCA (Advanced TeleCommunication Architecture) shelf which hosts the boards and is equivalent to the VME crate and a LINUX server to adapt and host the TDAQ software [13].

The shelf hosts the front boards and the corresponding Rear Transition Modules (RTM), shown in Figure 4.13. A key component of the ATCA is the shelf manager which provides Ethernet access and controls, monitors and maintains the safety of the infrastructure (i.e. temperature, fan speed, power).

The front board, also called Cluster-On-Board (COB), is the carrier of the RCE and hosts the firmware and software. The connection of the various components of the COB is succeeded with high speed communication paths. Each COB has a Real Transition Module (RTM) which provides a useful extension of the front board for the input/output (I/O) interface (e.g S-Link, G-Link) and increases the useful footprints. Every board contains one Data Transport Module (DTM) bay and four Data Processing Modules (DPM) bays. The DTM holds a mezzanine board which contains one RCE and interacts with the self manager via interconnections. The DPM acquires and processes data originating from the RTM with use of a number of RCEs. The RCE itself, the computational element, is a bundled set of hardware, firmware and software (FPGA+processor+DSP, using the System-On-Chip technology, both running on ZYNQ). It contains soft (programmable) and hard (resources) silicon (hence the name "Cluster Element"). The fact that it is highly parallel and inhomogeneous, because data are carried over a variety of media employing various inhomogeneous protocols, makes its performance significant.

The system is composed of six COBs, four of them acting as Front-End and two as Back-End (Formatters). The corresponding RTMs serve the CSC chambers and the RoL (16 channels) respectively. With the new readout, 8 chambers are read by one board whereas the new system needs 6 boards to read the same number of chambers.

The new system is a plug compatible replacement of the Run-I system and this means that no modification is needed either on the on-detector electronics. The requirements that is satisfies are the same as for the old system: interacts with the on-detector electronics to lock the fibers, control the pulser, set the number of samples, the sampling frequency and the latency, receives and processes trigger and timing signals with the ability to re-synchronize, performs the feature extraction, monitors and asserts busy, sends the data to the ROS, handles the TDAQ control and monitoring (including functionalities that the old system did not support, e.g. stopless recovery and TTC restart) and the infrastructure is remotely controlled.

To make the use of the old readout possible while the new system was under development, a patch panel installed to allow reverting between the two system in a simple way. After the installation, even though the additional fibers added only a few meters to overall fiber path, the system was re-evaluated to measure the attenuation losses and the length of the fibers by two independent methods. One of them used an OTDR machine (Optical Time Domain Reflectometer), connected to one end of the fibers (before the off-detector electronics) and extracted the scattered or reflected light after the injection of an optical pulse. A typical distribution of the OTDR output, for the CSC fibers, is presented in Figure 4.14. The peaks are connections and from the left to right these are: fan-out connection with the CSC fibers, fibers up to the patch panel, two connections of the 30 cm fibers on the patch panel, patch panel connection with the small fiber extension, extension connection with the 80 m long fiber that goes to the cavern, 80 m fiber connection with the cavern patch panel, fiber connection from the cavern patch panel to the on-detector electronics. The comparison of the signal intensity at the beginning and the end of the fibers path is the signal loss. The second method used, is more direct compared to the previous one but applicable only to the detector fibers and not the control fibers. It was performed by plugging a light receiver before the on-detector electronics and measuring the light that the ASMs send to the off-detector electronics when operated at nominal low voltage (LV). The method could not be used to measure the control fiber losses because in this case the optical signal is send from the off-detector electronics to the on-detector electronics and not vice versa. The light measurements for all sectors are summarized in Table 4.2. Both methods shown marginal losses, except from a few cases which were resolved by replacing the fibers.

Table 4.2: Measurements of the data transmission light (in dBm) at the end of the fiber paths before the on detector electronics. The fibers with numbers "7" and "8" are not included in the table because they are not used.

Side A										
Sector	Fiber-1	Fiber-2	Fiber-3	Fiber-4	Fiber-5	Fiber-6	Fiber-9	Fiber-10	Fiber-11	Fiber-12
A01	-8.96	-7.97	-8.85	-10.1	-8.22	-7.9	-9.45	-10.31	-9.14	-8.56
A02	-7.98	-8.87	-8.22	-8.02	-7.71	-10.41	-6.91	-9.46	-6.71	-8.35
A03	-8.35	-18.22	-7.94	-7.86	-8.06	-7.44	-7.65	-9.97	-7.5	-8.72
A04	-11.6	-7.18	-8.12	-8.54	-7.63	-8.23	-9.11	-9.27	-7.6	-7.65
A05	-8.64	-7.86	-6.8	-10.41	-7.92	-8.81	-8.26	-9.68	-7.65	-8.54
A06	-9.58	-8.64	-7.2	-8.79	-8.85	-7.53	-7.19	-7.88	-9.18	-8.17
A07	-8.85	-10.44	-7.91	-8.49	-7.9	-8.08	-8.21	-8.28	-8.36	-10.13
A08	-8.27	-8.39	-7.88	-7.37	-9.04	-9.08	-8.6	-8.24	-13.94	-8.51
A09	-7.62	-7.90	-7.07	-8.30	-8.43	-8.35	-7.66	-8.41	-7.27	-8.79
A010	-9.03	-7.02	-7.78	-8.00	-7.82	-9.04	-6.60	-7.41	-6.96	-7.71
A011	-7.40	-8.24	-7.73	-8.91	-8.95	-10.72	-7.73	-7.49	-7.05	-7.48
A012	-9.02	-9.49	-8.43	-8.10	-8.61	-8.56	-7.09	-9.10	-8.01	-8.02
A013	-7.68	-8.74	-8.22	-9.03	-9.88	-8.30	-8.09	-8.35	-6.86	-7.53
A014	-8.80	-9.03	-10.06	-9.09	-9.13	-8.23	-7.61	-9.77	-10.25	-9.44
A015	-8.12	-8.54	-8.69	-10.13	-13.31	-10.06	-8.51	-9.88	-14.89	-8.82
A016	-9.15	-8.06	-7.20	-9.21	-8.02	-7.96	-7.46	-8.29	-7.40	-8.28

Side C										
Sector	Fiber-1	Fiber-2	Fiber-3	Fiber-4	Fiber-5	Fiber-6	Fiber-9	Fiber-10	Fiber-11	Fiber-12
C01	-7.86	-8.64	-6.63	-7.86	-8.69	-7.59	-8.53	-9.5	-7.94	-8.47
C02	-7.39	-8.32	-7.03	-7.98	-9.44	-6.83	-7.26	-7.72	-7.53	-8.60
C03	-10.09	-7.33	-6.93	-8.32	-8.81	-7.37	-8.34	-8.65	-8.15	-9.19
C04	-7.34	-8.99	-7.53	-9.12	-7.92	-8.23	-8.06	-7.65	-6.87	-8.58
C05	-7.59	-7.63	-7.36	-7.02	-8.78	-8.11	-7.53	-11.03	-8.35	-7.90
C06	-9.33	-7.07	-6.97	-11.79	-7.29	-7.59	-7.63	-8.06	-8.43	-7.83
C07	-9.14	-7.46	-7.35	-7.95	-7.85	-7.34	-7.62	-8.13	-6.83	-7.29
C08	-7.10	-8.56	-16.23	-9.45	-8.30	-7.45	-7.44	-7.81	-7.20	-8.51
C09	-9.09	-7.90	-7.03	-10.08	-9.22	-7.65	-7.29	-12.06	-7.59	-7.41
C10	-11.38	-9.05	-8.38	-9.05	-8.85	-10.24	-12.81	-8.99	-8.53	-9.33
C11	-9.17	-9.51	-9.15	-9.27	-9.00	-9.52	-8.06	-11.64	-10.51	-9.85
C12	-9.62	-10.33	-8.54	-9.70	-10.15	-12.3	-9.61	-9.99	-10.33	-10.24
C13	-9.01	-9.02	-9.02	-9.35	-12.52	-9.92	-9.03	-16.11	-9.34	-11.18
C14	-9.21	-8.04	-8.59	-8.09	-7.75	-6.75	-7.88	-9.45	-12.01	-8.38
C15	-7.56	-7.31	-7.84	-7.53	-8.87	-7.24	-7.88	-9.25	-8.12	-8.06
C16	-6.61	-7.28	-6.89	-7.36	-7.50	-7.65	-8.24	-7.56	-9.01	-8.42

Figure 4.14: An example output of the OTDR (Optical Time Domain Reflectometer) measurements performed on the CSC fibers, to measure pulse losses and attenuation. The peaks are connections and from the left to right these are: fan-out connection with CSC fibers, fibers up to the patch panel, two connections with the 30 cm fibers on the patch panel, patch panel connection with the small fiber extension, extension connection with the 80 m long fiber that goes to the cavern, 80 m fiber connection with the cavern patch panel, fiber connection from the cavern patch panel to the on-detector electronics.

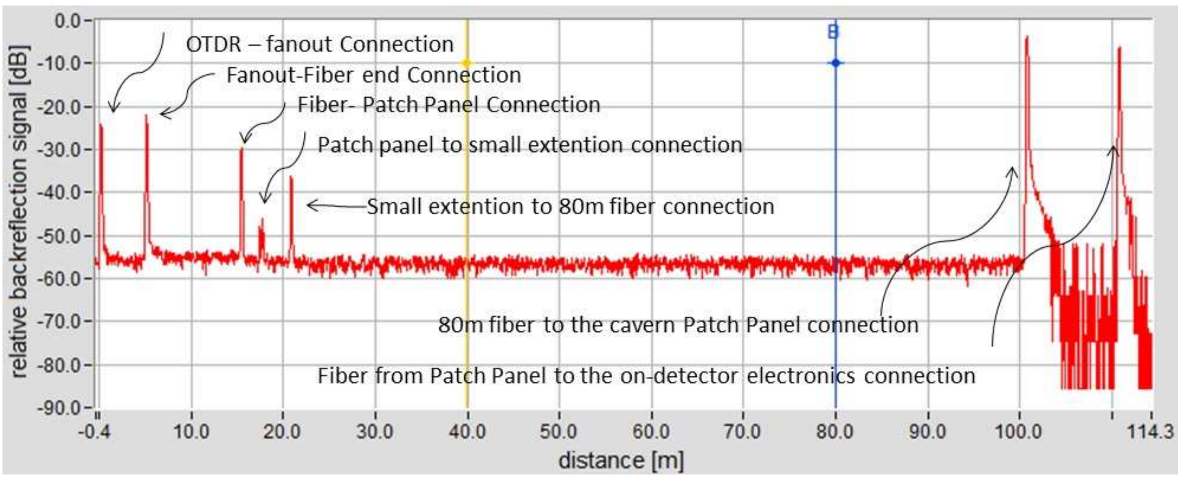

4.8.2.3 The Trigger and Timing (TTC) Unit

The trigger and timing crate (TTC), as Figure 4.15 shows, is the same for the Run-I and Run-II electronics and contains the modules for the control of the timing and trigger signals. The modules in the crate consist of the SBC (Single Computer Board), the LTPi (Local Trigger Processor interface), two LTPs (Local Trigger Processors), two TTCvis and one TTCex module. The local trigger processor contains a pattern generator, that can generate all TTC trigger signals. This generator can run in continuous mode or in single-shot operation. The TTCvi module passes on the signals from the LTP and adds the Bunch Counter Reset (BCR) signals.

The busy modules propagate the busy signal from the readout electronics to ATLAS. Once a detector component raise busy the so called “Simple Deadtime” increases and trigger the raise of the so called “Complex Deadtime”. The latter causes a global deadtime rise to avoid mix of the various readout information between different events. The maximum allowed busy by the ATLAS experiment is 2%. If it is exceeded then an automatic procedure removes the part that creates the busy (the action is called “Stopless Removal”). The electronics that will be used for the Run-II allow removal of the CSC detector components with better granularity compared to the old system,

Figure 4.15: The trigger and timing unit (TTC), which is the same for the Run-I and the Run-II. The modules are responsible for the synchronization of the system with the rest ATLAS components and the trigger handling.

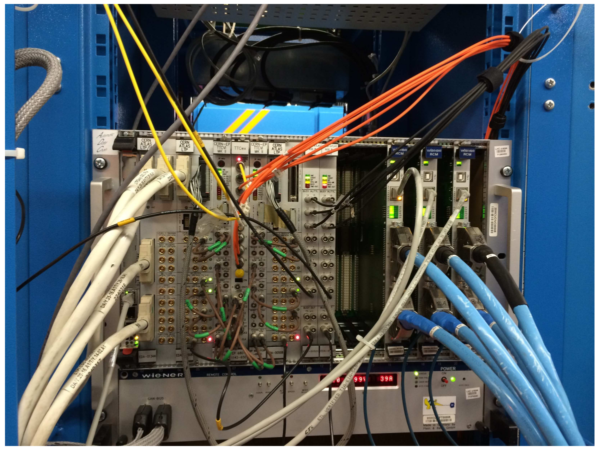

where the entire detector side had to be removed.

The new readout electronics also allow the so called “TTC Restart”, which is not possible with the old system. This allows the re-synchronization of a detector part with ATLAS in the case where it is lost.

To avoid deadtime originating from the readout links (RoLs), the Run-I 16 readout links were used for the data transmission from the off detector electronics to the ATLAS Readout System (ROS). For Run-II, the RoLs are doubled and replaced by the so called “3^{rd} generation“ ones. This means that each RoL serves one chamber instead of two. The two ROSes, each one reads out a detector side, were also replaced by modern machines with bigger capabilities. These changes were motivated by the amount of the predicted data volume that is expected to be transferred during the Run-II.

The system is in place for the Run-II and an event display showing a cosmic track on top of the pedestal noise is shown in Figure 4.16. The pedestal had not been subtracted from this run for testing reasons.

4.9 Offline Reconstruction

4.9.1 Strip Charge Reconstruction

The offline reconstruction starts by defining the charge of each strip. This is done by performing a parabolic interpolation between the samples, in the case of four samples, and calculating the peaking time as the time of the largest sample corrected by the

Figure 4.16: Cosmic track passing through the CSC recorded with the new readout complex. The pedestal had not been subtracted from this run for testing reasons.

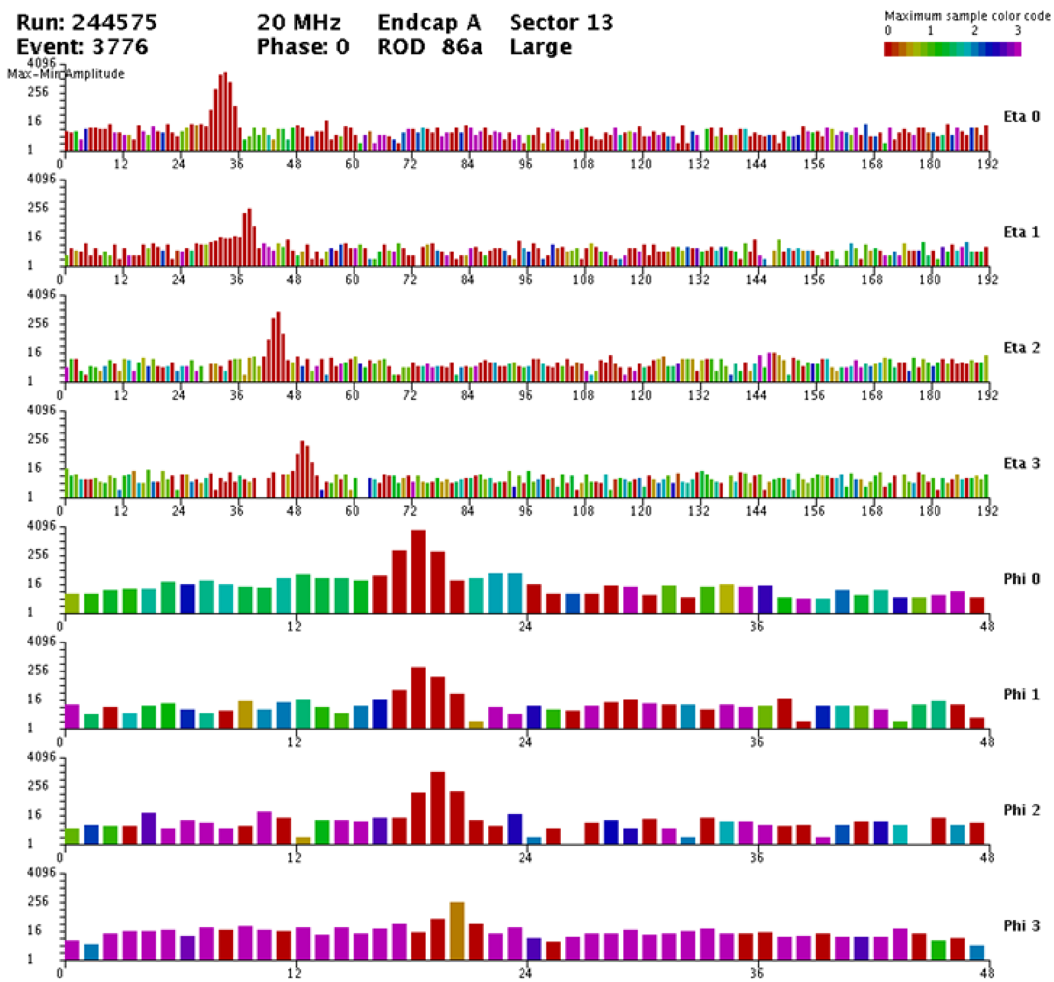

"time offset" estimated from the interpolation. In case of two samples data taking, the parabolic interpolation is not possible. In this case, the charge is the result of a linear interpolation and the time information can be retrieved by making use of the "asymmetry", defined as:

$$Asymmetry = \frac{Time_{1st\ Sample} - Time_{2nd\ Sample}}{Time_{1st\ Sample} + Time_{2nd\ Sample}}. \tag{4.6}$$

From a $4-samples$ recorded run, the time as a function of the asymmetry of the 2^{nd} and the 3^{rd} samples (middle samples, i.e. in Figure 4.9 the "B" and "C" samples) found to follow a 2^{nd} order polynomial, as shown in Figure 4.17. The time reconstruction using this formula provides a very close result to time reconstruction using the $4-samples$ information, also shown in Figure 4.17. The time information is very important for beam halo and cavern background studies.

Figure 4.17: Study for the time reconstruction of data recorded with $2-samples$, based on a $4-samples$ recorded run using the 2^{nd} and the 3^{rd} sample (Figure 4.9). Figure (a) shows the time vs the asymmetry, defined as in Equation 4.6. The distribution is fitted with a 2^{nd} order polynomial and the obtained formula used to reconstruct the time. Figure (b) shows the comparison of the time as reconstructed using the asymmetry, denoted as "2 $Samples$", and the nominal "4 $Samples$" reconstruction.

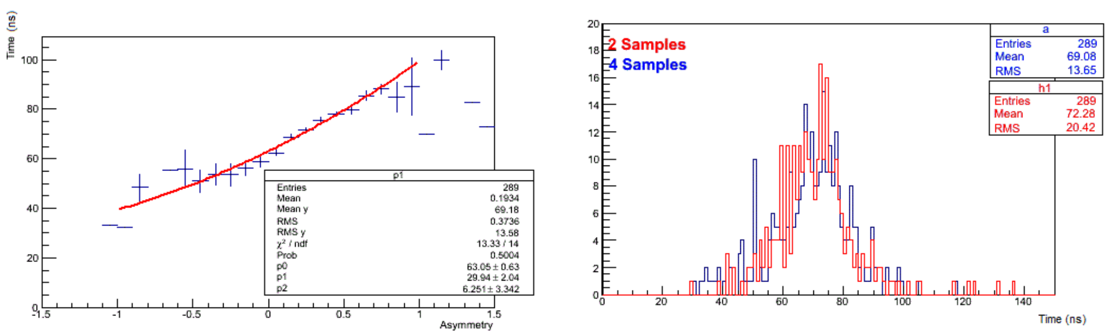

(a) (b)

The hit is kept only if the charge exceeds the noise level and the channel does not belong to the known problematic channels, e.g. dead channels. The threshold of the offline reconstruction is set to $(pedestal + 2(f001 - pedestal))$, even though in some data taking periods the online charge threshold exceeded the offline threshold as it is discussed later.

At this reconstruction levels, the charges of the η and ϕ strips are presented in Figure 4.18 for $4-samples$ data. $2-samples$ data are extensively studied in a following section (4.11.1).

Figure 4.18: The charge distributions of each strip that exceeds the thresholds separately for η (a) and ϕ (b) hits in logarithmic scale. This charge deposition, formed from $4-samples$ data, includes background hits and muon tracks. The tails of the distributions are formed by the saturation peaks.

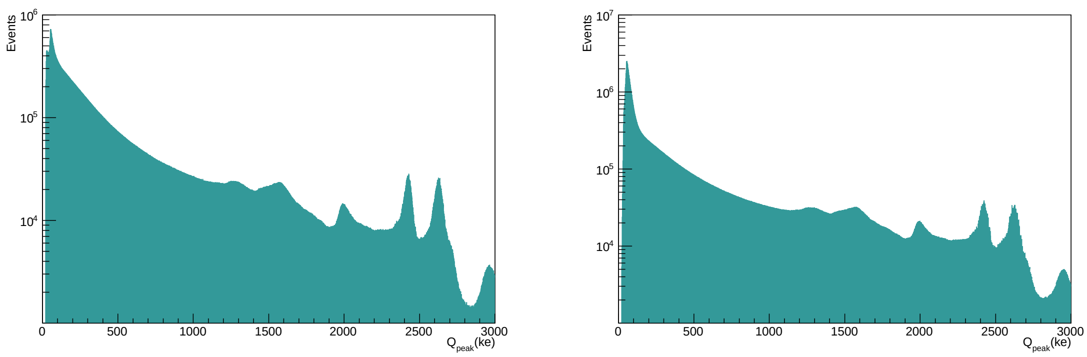

(a) (b)

4.9.2 Cluster Formation

The next step is the clustering, during which hits of neighboring channels are combined to reconstruct the charge deposition left by particles crossing the detector layers. The process is different for the precision (η) and the transverse (ϕ) layers due to the different pitches. The size of the pitch defines how extensive the charge deposition of a charged particle is, hence it imposes different approaches for the clusters identification.

4.9.2.1 The η Clustering

The η strips clustering algorithm was modified during the Run-I (specifically, in the end of the 2011 data taking) in order to provide more accurate position reconstruction based on a calibration directly obtained from real data (the previous calibration had been obtained from the Monte Carlo (MC)).

The process starts by identifying the highest channel charge among the lowest neighboring and forming the charge ratios:

$$Q_{RAT1} = Q_{left}/Q_{peak} \tag{4.7}$$

$$Q_{RAT2} = Q_{right}/Q_{peak} \tag{4.8}$$

where Q_{left} and Q_{right} are the left and the right channels respectively to the one with the highest charge (Q_{peak}). The initial Run-I reconstruction applied a correction to this

Figure 4.19: Interstrip position as a function of the charge ratio, separately for large (a) and small (b) chambers due to different pitches. The distributions, which are made from data, are the inputs of the "S-Curve" calibration. The red line indicates the old calibration.

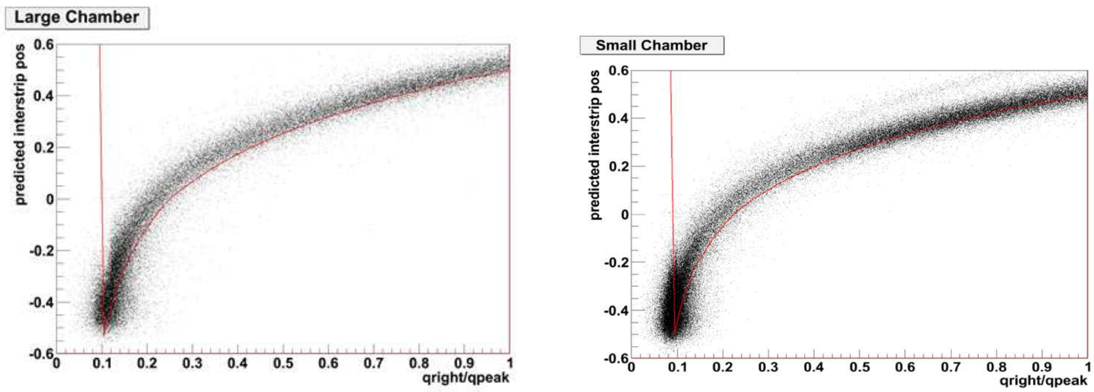

(a) (b)

ratios based on the simulation, whereas later a more sophisticated method invented. The interstrip position[3], defined as:

$$Interstrip\ Position\ x = \frac{Position\ (mm)}{Pitch} + 96 - ChannelNumber \tag{4.9}$$

plotted as a function of the charge ratios, is shown in Figure 4.19, separately for the large and small chambers due to the different pitches. The distributions are fitted with a hyperbolic tangent and a correction is applied based on the inverse of the function:

$$x = \frac{atanh\left(\frac{Q_{RAT}-a}{b}\right)}{c} + x_0 \tag{4.10}$$

where a, b, c, x_0 are parameters estimated from the fit. The method is called the "S-Curve" calibration and the performance results are shown later on this section.

The position corresponds to the weighted average between the charge ratios and the uncertainty is estimated from the error propagation in this formula. The interstrip positions from the improved and original calibrations are presented in Figure 4.20. For a sufficient number of data, the position within the strip is flat, as expected, for the new calibration.

The inconsistency, i.e. large asymmetry, between the two charge ratios (Equations 4.7 and 4.8), along with the information of the width (in strips) of the clusters, define the quality of the hit. Based on this, each cluster is categorized to be either a clean cluster

[3]There are 192 channels, and the number 96 corresponds to half of the channels number.

Figure 4.20: Interstrip position (Figure (a)) for the improved (red) and old (black) calibration. As expected, for the new calibration the distribution is flat for a large number of measurements. Additional check performed by taking advantage of the other layers information and performing a line fit to estimate the position in the given layer. The result shows good agreement between the measured and the predicted position within the strip (Figure (b)).

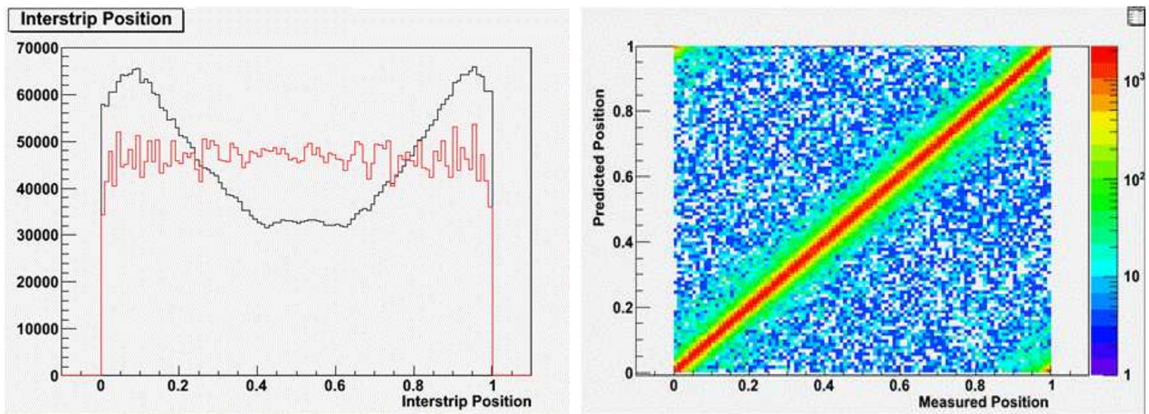

(a) (b)

precisely fitted (unspoiled) or a spoiled hit. The spoiled category includes clusters that are on the edge of the plane, have multiple peaks, are too narrow (less than three strips), too wide, skewed, show inconsistency between the charge ratios, the parabolic interpolation failed in the peak charge or the left and/or the right strips are saturated. The most common spoiled reason is the inconsistency between the charge ratios, which appeared more frequently in the initial reconstruction, as Figure 4.21 presents, and corrected by the improved reconstruction. Figure 4.22 shows the η charge with and without the spoil requirement. The flag of too wide clusters is removed because the width is amplitude dependent.

4.9.2.2 The ϕ Clustering

The non-precision transverse ϕ hits form clusters using the strip with the highest charge and the two adjacent strips (left and right). The position of the cluster is simply the mean of the strip with the highest charge. By definition, ϕ clusters are three strips wide, whereas the η clusters usually have three strips as Figure 4.23 shows.

Figure 4.24 shows the clusters charge, defined as the sum of the charge of the strips that form the cluster, separately for the η and ϕ strips.

Figure 4.21: Unspoiled hits (1^{st} bin) and spoiled hits (the rest bins) percentages between the old and the new reconstruction. The spoiled bins correspond to: 2^{nd} non-η hits, 3^{rd} on edge of the plane, 4^{rth} has multiple peaks, 5^{th} too narrow, 6^{th} too wide, 7^{th} skewed, 8^{th} show inconsistency between the charge ratios, 9^{th} parabolic interpolation failed in the peak charge, 10^{th} the left and/or the right strips are saturated. The most common spoiled category is due to the inconsistency of the charges, which was improved with the new reconstruction.

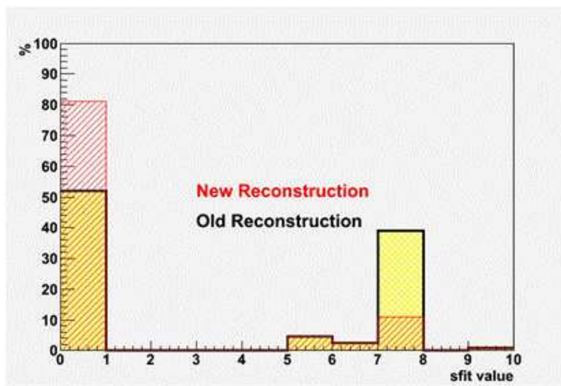

Figure 4.22: Precision charge for unspoiled hits (a) and spoiled hits (b) from 4$-$*samples* data. The saturation is included in the spoil flags and hence the saturation peaks, at the end of the distribution, appear in (b).

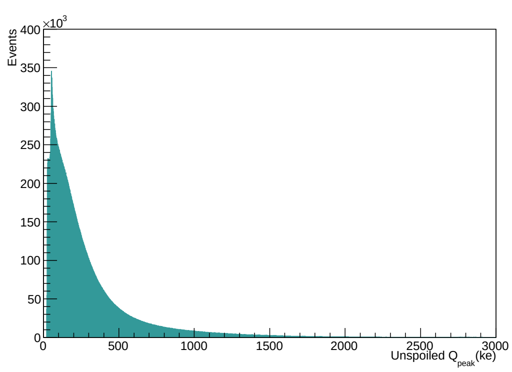

(a)

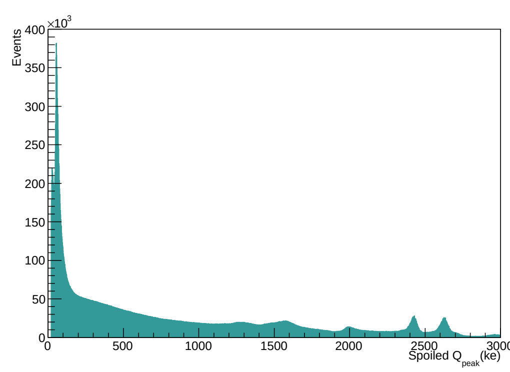

(b)

Figure 4.23: Precision cluster width measured in strips. The usual width case is clusters of three strips. Non-precision clusters have three strips by definition due to the largest strip pitch.

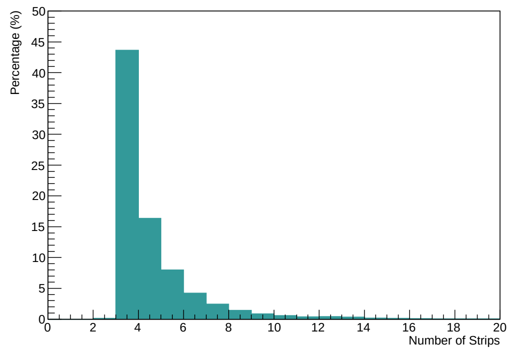

Figure 4.24: Cluster charge distributions, defined as the sum of the strips charge that forms the cluster, separately for precision (a) and non precision (b) strips from $4-samples$ data.

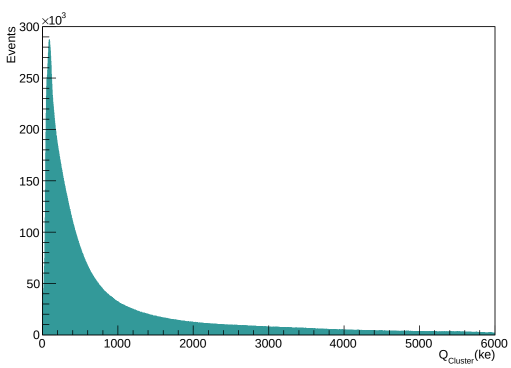

(a)

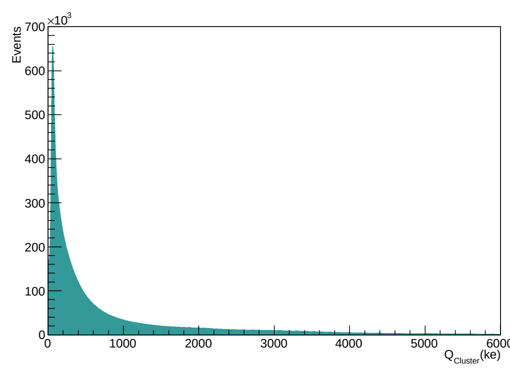

(b)

Figure 4.25: Peak strip charge distributions separately for precision (a) and non precision strips (b) from $4 - samples$ data. The clusters were preselected to belong to segments and the shapes are different compared to Figure 4.18 without the preselection requirement. The fit parameters of the Landau distributions are presented and as expected the MPV value is higher for the ϕ hits because of the largest strip pitch.

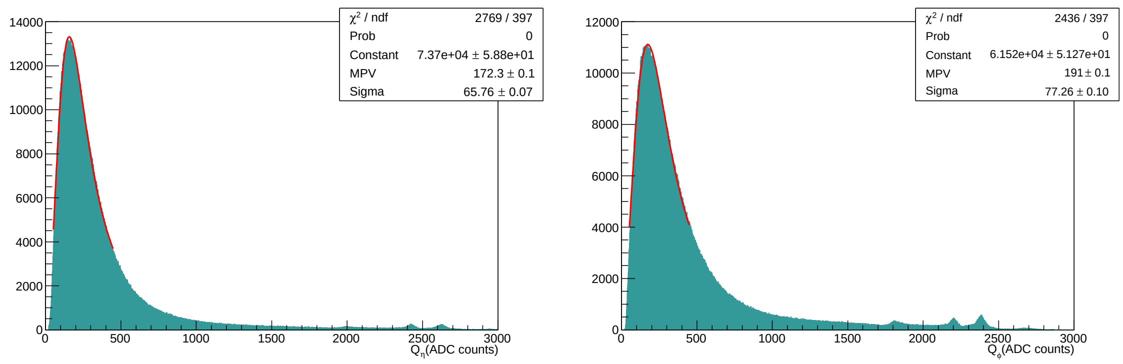

(a) (b)

4.9.3 The Segments Reconstruction

After the cluster finding, clusters from different layers are associated in space and time to reconstruct the particle track within the CSC detector, to form the "segment". There are two possible segment combinations, called the $2d$ and $4d$ segments. The former measures the position and direction for one orientation, either η or ϕ, and the latter provide a complete measurement of both coordinates and directions.

The cluster charge distribution, for clusters that are part of segments, is presented in Figure 4.25. The peak shape is clearer compared to the single clusters distributions, already presented (Figure 4.18), because these clusters are part of tracks. The peaks are modeled by Landau distributions and the fitting parameters are also presented on the same Figure. The effect on the η charge distribution of the spoil requirement when the cluster is part of a segment is presented in Figure 4.26 fitted with a Landau.

The CSC reconstruction is finished after the segments formation. The reconstructed information is combined with the information from other detector technologies, i.e. inner detector or other muon detectors, to form muons. During the Run-I period two muon algorithms existed, the STACO (STatistical COmbination of the different vectors) and the MUID (algorithm which refits the combined tracks starting from the ID track and then adding the muon measurements) [14]. For the upcoming Run-II, these two algorithms will be replaced by the unified "Muon" or "3^{rd}" chain, which performs muon identification by a chain of algorithms starting from the pattern recognition inside the Muon Spectrometer and ending with the final definition of the muon object using

Figure 4.26: η peak charge distributions on segments when are required to be unspoiled (a) and spoiled (b) for $4-samples$ data. The peaks are fitted with Landaus and the parameters appear on the Figures.

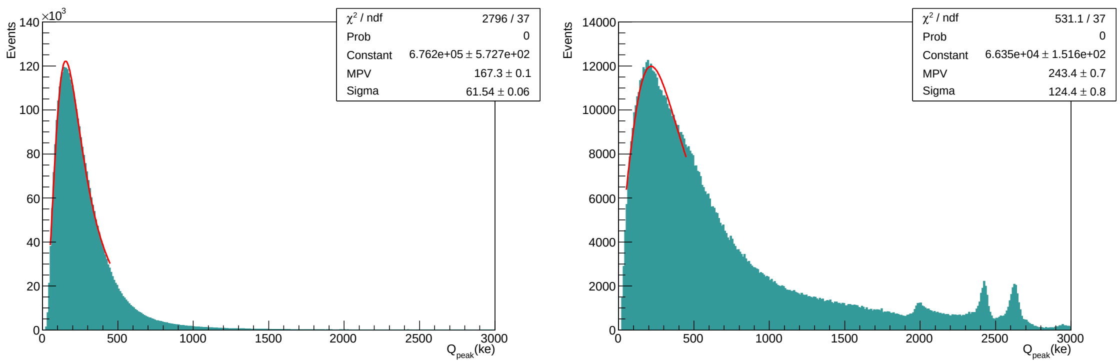

(a) (b)

information from all detectors.

The tracks passing through the CSC detector have the momentum profile shown in Figure 4.27. The peak in the low region is normally excluded in track-related analysis, since it is the result of background processes.

4.10 CSC Simulation

The MC production starts from the so called "Generation" stage, during which the interaction of two protons is simulated producing a list of particles. The final state products of the interaction are propagated through the detector using $GEANT4$, this step is called "Propagation". Afterwords, the first detector specific stage follows, the "Digitization".

Specifically for the CSCs, the digitization is performed for each hit and defines how a cluster is created. For the production of more accurate MC, when the reconstruction improved, new "Charge Sharing Profiles" were created. This means, that data distributions of $Q_{peak}/(Q_{left}+Q_{right}+Q_{peak})$ as a function of the interstrip position were created, as shown in Figure 4.28. Then, the distributions are fitted by the functions:

$$f(x) = \frac{Q}{1+ax^2+bx^4} \tag{4.11}$$

separately for the large and small chambers due to different pitches. The obtained formula is used for the digitization.

The reconstruction, as described for the data in Section 4.9, follows the digitization.

Figure 4.27: Momentum distribution of tracks going through the high η region where the CSC detectors are located. In muon analysis good tracks selection includes a cut of $p > 50$ GeV to reject background processes, which form the low region peak.

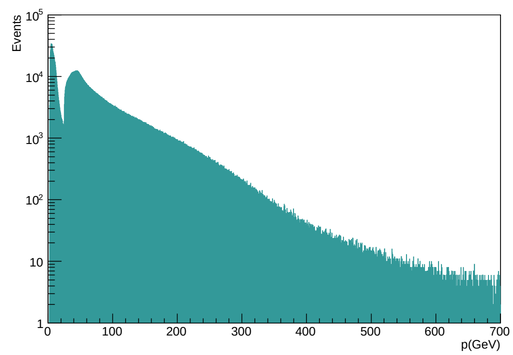

4.11 CSC Operational Conditions During the Run-I

The overall CSC operation during the ATLAS Run-I period was smooth, without significant data acquisition losses or operational problems. The hardware limitation of the off-detector electronics was a serious concern during the entire Run-I. Concerning the detector operation, before the 2012 data taking, the year that the majority of Run-I data were collected ($20.3fb^{-1}$), and the operating rate was high, the only problems were the HV failure in three layers in different chambers ($C03$, $A05$, $A09$). In June 2012, $C05L1$ showed less occupancy in the half plane and in August 2012 one chamber showed failure in two consecutive layers ($C01$). In a following section the physics impact of this malfunctions is investigated in details.

In 2010 data taking, the off-detector electronics charge threshold corresponded to the $(pedestal + 3.1(f001 - pedestal))$ noise of each channel and in 2011 raised to $(pedestal + 5.1(f001 - pedestal))$. The motivation was both physics and mostly the deadtime increase. The former was based on the fact that physics objects leave higher charge signatures (as can be concluded from Figures 4.18 and 4.25) and the latter was caused by the hardware limitation of the off-detector electronics.

In 2012, when the trigger rate increased even more, the first step taken in the direction of decreasing the input occupancy was to raise the charge thresholds to 40 ADC counts (1 ADC count = 1100 e) at the RODs level or above the noise level in case it was higher. Typical charge distributions of the η and ϕ peak charges when the cluster belongs to segment, have already been presented in Figure 4.25. The applied threshold modification in the beginning of 2012 suppressed further hits coming mainly from background processes, cross talk and echos and deteriorated the efficiency by less than

Figure 4.28: Fitted data distributions of the charge ratios as a function of the interstrip position, defined as in Equation 4.9. The obtained formulas are used to produce charge, at the digitization level, given the interstrip position.

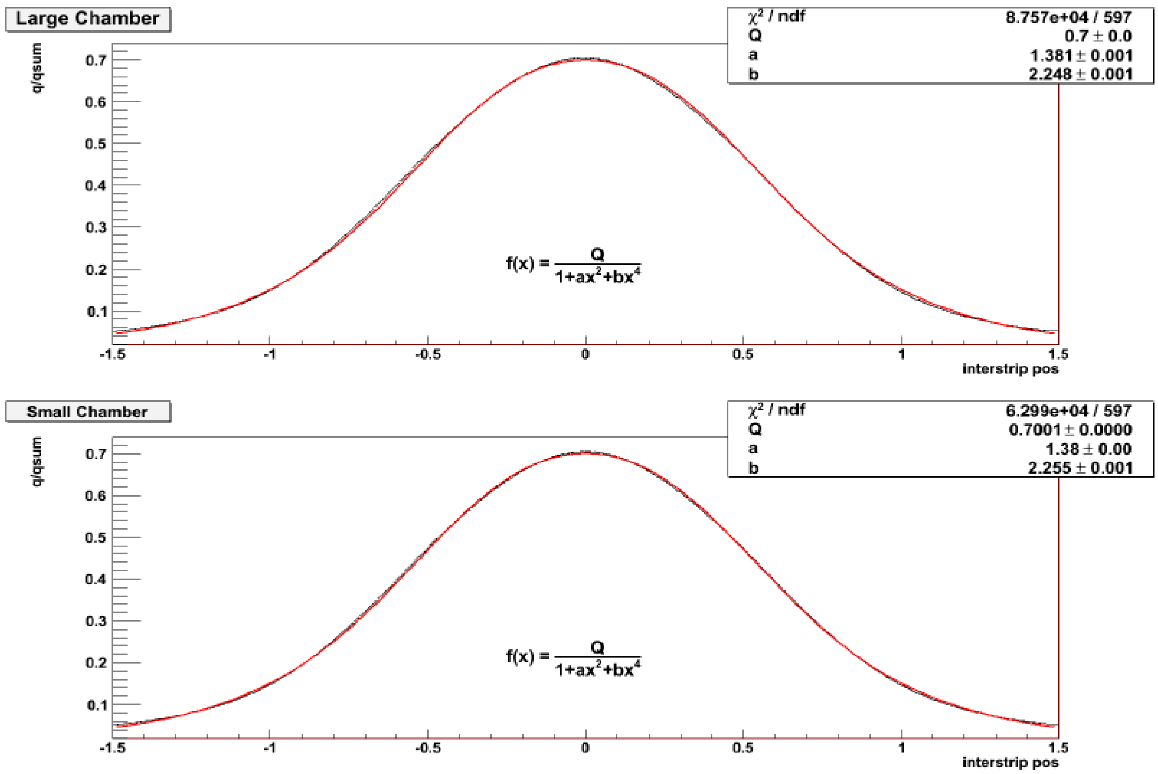

0.7%.

The rate continued to increase gradually, during 2012, until it reached $\sim 70\ kHz$ and a number of possible temporary solutions explored, tested and some of them applied in order to compensate the high rates and allow the operation under the conditions that the experiment required. All the introduced methods aimed to reduce the data volume and/or the cluster volume. Before the application of each method a careful evaluation of the advantages and the disadvantages was conducted. In the next paragraphs the deadtime reduction methods are explored in chronological order.

4.11.1 2-Samples Data Taking

When the deadtime started becoming non negligible [4] a drastic solution was applied. The RODs sampling changed from four samples to two samples. The outer samples, i.e. "A" and "D" in Figure 4.9, were discarded and the latency settings were modified so that the pulse peak is between the two inner samples. In addition to the sampling changes, fiber extensions were installed and perplexed the latency choice. A wrong value was chosen and but it was corrected after a few runs.

The sampling method itself did not affect the efficiency though it required different reconstruction handling as previously mentioned in Section 4.9. The performance is discussed in Section 4.15 and it slightly deteriorated due to the non accurate hit charge and peaking time reconstruction.

The modified two sample reconstruction helped to restore the timing measurement lost by the application of this method.

4.11.2 Charge Thresholds

In the end of August 2012, the deadtime had to be further reduced to anticipate the gradually increasing trigger rate. At this point the charge threshold was increased to lower the data volume. A detailed study was performed in advance to evaluate the physics impact. Because of the different shapes of the η and ϕ distributions, as shown in Figure 4.25, and the early peaking of the precision - η charge, from the beginning different thresholds were considered.

Clusters that are part of tracks were studied for the calculation of the efficiency losses with higher thresholds. The number of the CSC hits on track is presented analytically in Table 4.3 for different thresholds and also in Figure 4.29 as a percentage. The study was performed using runs taken with low thresholds and at the reconstruction level they were increased to the values reported in the Table.

Based on the above Table, the decision taken to raise the thresholds to 50 and 60 ADC counts for the η and ϕ hits respectively. The performance prediction was confirmed by the observations after the deployment of this data taking schema.

In parallel, ROD monitors were deployed to unveil the actual source of busy within the ROD. Figures 4.30 show the sources of busy during a typical run separately for large and small chambers. As expected, the large chambers contribute to the busy more compared to the small, due to higher data volume, but the majority of the dead-time was a result of the ϕ channels processing. The ϕ channels per layer are 48 and are processed together for all the layers (in total $4 \times 48 = 192$ channels) by one processing

[4] The maximum acceptable dead-time by the experiment is 2%. When a sub-detector's dead-time increases the complex dead-time also increases.

Table 4.3: Percentage of CSC hits on track for different charge thresholds. The study was performed using runs taken with low thresholds and at the reconstruction level they were increased.

Threshold	$N = 0$ (%)		$N = 1$ (%)		$N = 2$ (%)		$N = 3$ (%)		$N = 4$ (%)	
	η	ϕ	η	ϕ	η	ϕ	η	ϕ	η	ϕ
20 ke	0.24	0.04	0.03	0.04	0.2	0.7	19.19	22.12	80.33	77.1
45 ke	0.24	0.04	0.04	0.05	0.55	1.05	20.69	23.04	78.47	75.82
50 ke	0.24	0.04	0.05	0.06	0.83	1.23	21.71	23.55	77.18	75.11
55 ke	0.24	0.04	0.06	0.09	1.15	1.47	22.96	24.23	75.59	74.18
60 ke	0.24	0.04	0.1	0.1	1.6	1.86	24.45	24.95	73.62	73.04
70 ke	0.25	0.04	0.2	0.2	2.9	2.76	27.85	26.76	68.8	70.24
75 ke	0.25	0.04	0.26	0.28	3.86	3.34	29.59	27.81	66.04	68.54
85 ke	0.26	0.05	0.49	0.45	6.03	4.8	33.12	30.11	60.1	64.58
90 ke	0.26	0.06	0.71	0.6	7.22	5.72	34.87	31.08	56.93	62.54

unit. For each η layer, one unit is assigned for the processing (192 channels). This means that eventually the ϕ unit processes the exact same number of channels as each of the η processing units, however the ϕ unit was busier than the rest. The problem was considered to originate from some sort of trafficking during the data transmission. The assumption was enhanced by the fact that the readout links showed relatively high busy.

The evaluation of the busy monitors led soon to the decision to revert the η threshold back to 40 ADC counts and left the ϕ threshold unchanged to 60 ADC counts. As had been predicted, the busy did not increase with this choice and the efficiency was partially restored.

4.11.3 Non Applied Busy Reduction Methods

Other methods were also considered and evaluated because of the rather exponential increase of the busy at $\sim 70\ kHZ$, as Figure 4.10 shows. Despite that, eventually there was no need for any of these methods to be applied. The most important of them included higher ϕ thresholds (with the losses reported in Table 4.3) different or not for the large and small chambers, use only the peak strip for the ϕ hits[5], reduced time

[5]The ϕ strips are wider than the η and the charge is mostly deposited at the peak strip. Along with the fact that the transverse coordinate is the non-precision one, no major efficiency discrepancies predicted. The study showed that the probability of having ≥ 2 ϕ hits on track is $97.5 \pm 0.5\%$ whereas

Figure 4.29: η (a) and ϕ (b) percentage of hits on tracks as a function of the charge thresholds. The study was performed using runs taken with low thresholds and at the reconstruction level they were increased.

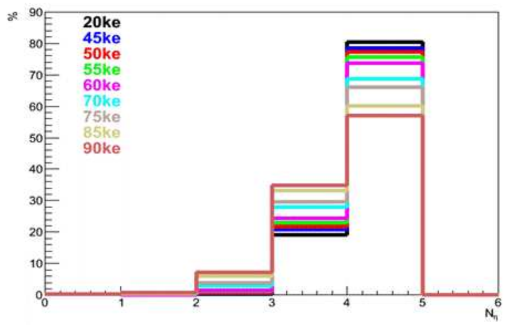

(a)

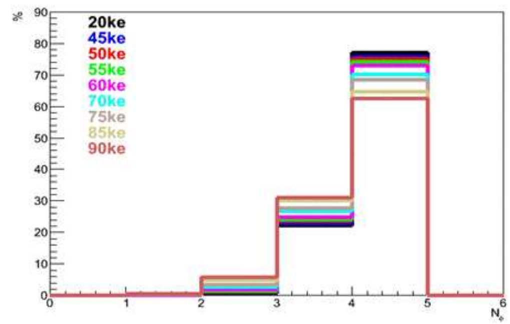

(b)

Figure 4.30: Large (a) and small (b) chambers busy source monitoring (in arbitrary units). The bin assignments are: the first 4 bins correspond to the processing units of the η channels of the 4 layers consecutively, the 5^{th} is the unit that processes all the ϕ channels, the 6^{th} bin corresponds to the RPU, the 7^{th} to the stream caring the trigger information summary and the last one is the readout link. The large chambers contributed to busy more, due to higher data volume, but the majority of the dead-time was a result of the ϕ channels processing.

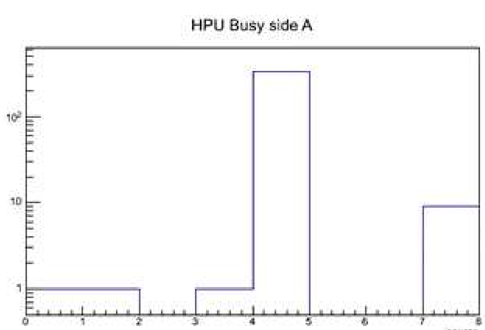

(a)

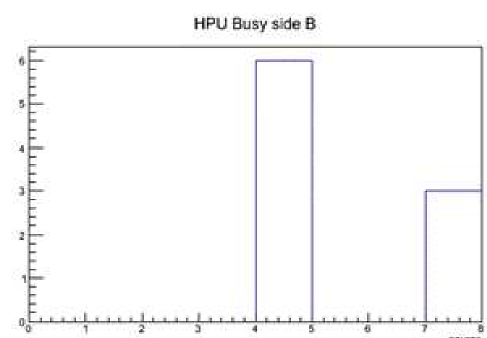

(b)

Figure 4.31: Investigation of the impact of the reduced time window in order to reduce the busy. The number of clusters are reported for a sample taken with the nominal time-window and then reprocessed offline with reduced time range. The major physics impact of this method would be the loss of hits primarily originate from beam halo and other cavern background processes. The method was never applied in the data taking, except from one test run which showed that the processing time due to the time calculation was a significant busy factor.

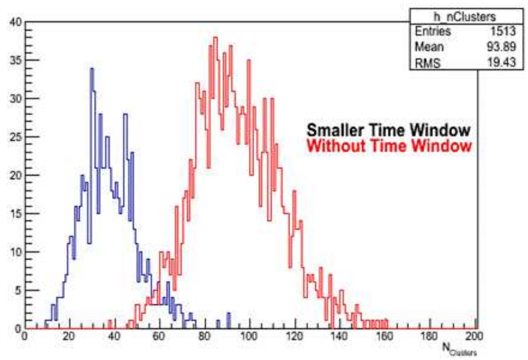

windows (expected to reduce the cluster volume, as Figure 4.31 shows, and cut all hits essential for beam halo and cavern background studied).

All these method implemented in the software and the OKS configuration was updated to include them. The actual application would only require a parameter change in the database.

4.12 Resolution and Angle Dependence

An indication of the good performance is the track resolution. The $3-point$ residuals, defined as:

$$R_1 = x_1 - \frac{1}{2}(x_0 + x_2) \qquad (4.12)$$
$$R_2 = x_2 - \frac{1}{2}(x_1 + x_3)$$

are formed from the middle layers, i.e. "1" and "2", and the adjacent outer, i.e. either "0" and "2" or "1" and "3" respectively[6], are used to predict the hit position. The

by using the neighboring strips is $97.68 \pm 0.17\%$.

[6] The measuring of the layers starts from 0.

Figure 4.32: The residuals distribution, defined as in Equation 4.13, fitted with a double Gaussian to account for both the signal (red line) and the background (blue line). The resolution is estimated to be 78.6 μm for $4 - samples$ runs.

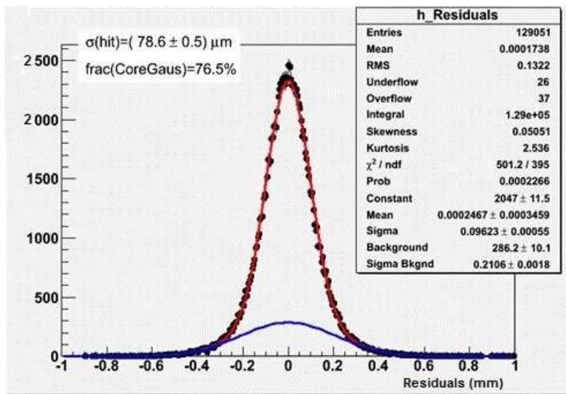

resolution is estimated by fitting the residuals distribution, shown in Figure 4.32, with a double-Gaussian, one for the signal and one for the cavern background. The resolution is obtained by multiplying the width of the inner Gaussian by a factor of $\sqrt{\frac{2}{3}}$ to account for the error propagation in the residual. In the case of $4 - samples$ the resolution is measured to be 78.6 μm.

The resolution is not similar for inclined and perpendicular tracks, but depends on the segment angle shown in Figure 4.33. Figure 4.34 shows the resolution as a function of the incident angle. The curve follows the formula $\sqrt{p_0^2 + (p_1 \times tan\theta)^2}$, where p_0 is the resolution for tracks with perpendicular incidence and the p_1 term describes the resolution degradation for larger angles, experimentally measured to be:

$$\begin{aligned} p_0 &= 73.4 \pm 0.3 \\ p_1 &= 954 \pm 34. \end{aligned} \tag{4.13}$$

4.13 Alignment Checks

The mean value of the residuals is a clear indication of the alignment of the system (discussed in Section 4.7.3). Figure 4.35 shows the mean values, theoretically expected to be 0.00, for each sector with the final alignment values for Run-I. The deviations observed are too small and this indicates how well the wheels are aligned. The analysis is based on the 2012 data and the final alignment constants for the Run-I.

Except from this detector specific alignment checks, regular checks of the alignment

Figure 4.33: The segment angle for the tracks passing through the CSC detector. The resolution is different for perpendicular and inclined tracks, but the observed positive and negative asymmetry is due to lower efficiency of sectors with dead layers.

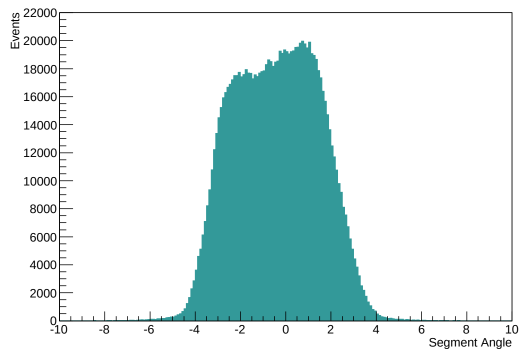

Figure 4.34: The resolution as a function of the incident angle. The curve follows the function $\sqrt{p_0^2 + (p_1 \times tan\theta)^2}$, where $p_0 = (73.4 \pm 0.3)$ μm is the resolution for tracks with perpendicular incidence and the $p_1 = (954 \pm 34)$ term describes the resolution degradation for larger angles.

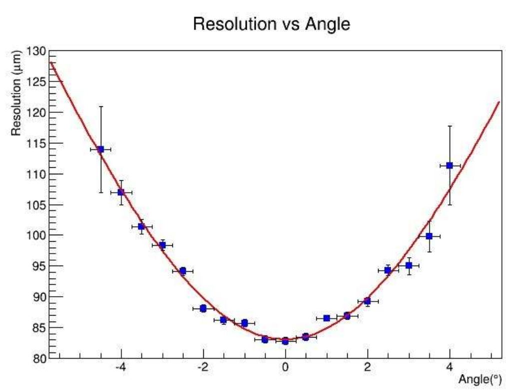

Figure 4.35: Plot of the residuals mean (in cm) for each sector, which proves the good alignment of the wheels given the small deviation from the expected value of 0.00. The analysis performed on 2012 data with the final alignment constants for the Run-I. Sectors with dead layers were not included since the $3-point$ residuals formation was not possible.

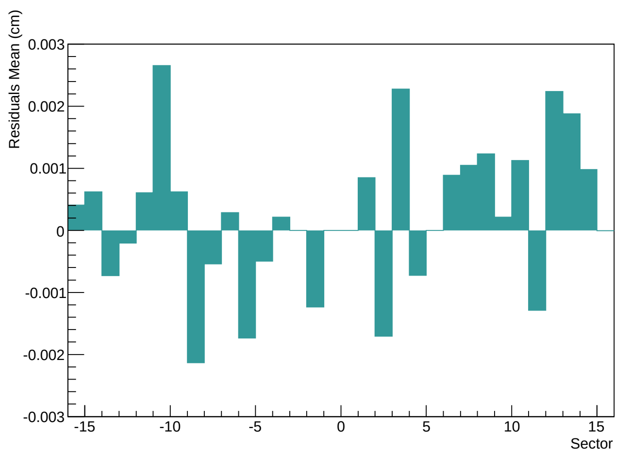

are performed for the muons to measure the misalignment not only between the muon detectors but between the inner detector and the muon spectrometer.

4.14 Lorentz Angle Effect Measurement

In 2011, a few runs were recorded with stable beams and the toroids and solenoids magnets switched off. The motivation was various studies for the different detector components.

The resolution analysis of the inclined tracks of these runs and the comparison with the runs taken with nominal magnets operation, provides a measurement of the effect of the Lorentz force on the charged tracks. Specifically, the resolution is slightly decreased as Figure 4.36 shows. The run reconstructed with the initial Run-I method and is compared to a run similarly reconstructed, hence the resolution is different from previously reported value.

Figure 4.36: In 2011, a few runs were recorded with stable beams and without magnetic field. The runs reconstructed with the initial Run-I method and compared to a similarly reconstructed run (red line). The resolution dependence on the incident track angle is studied separately for the large (a) and small (b) chambers, following the method presented in Section 4.12. As expected smaller resolution values are estimated.

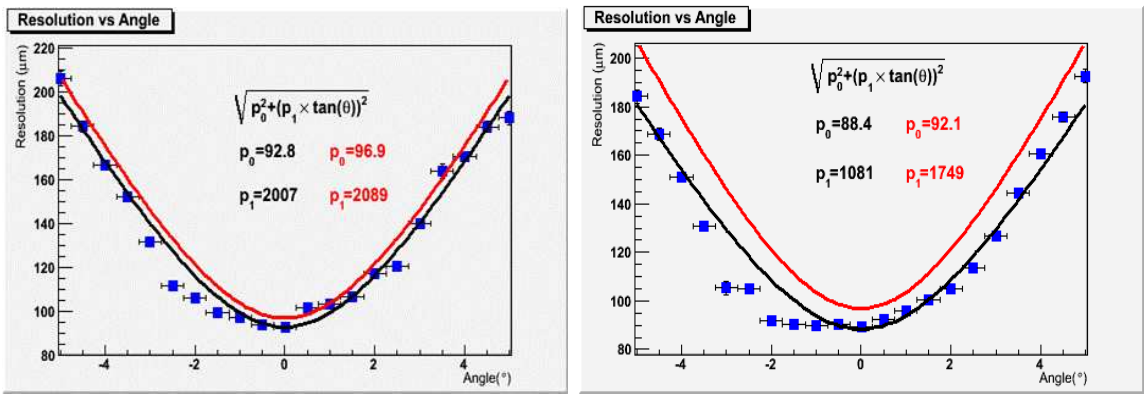

(a) (b)

4.15 2 vs 4-Samples Data Taking Performance

The $2 - samples$ data taking, applied to reduce the data volume, even though is expected not to reduce the hit-finding efficiency, it deteriorates slightly the accuracy of the reconstruction reconstruct the time and the charge of the hits (as introduced in Section 4.9).

Figure 4.37 presents the fitted reconstructed η peak charge, for clusters belonging to segments, in order to be compared to Figure 4.25. The MPV value, of the fitted Landau, is different between the $2-samples$ and $4-samples$. This charge difference is reflected also in the unspoiled fraction, which is increased to 85% with respect the $4 - samples$ value of 80%. The source is the decrease of the ”inconsistency” between the charge ratios, apparently related to the charge reconstruction. The η position reconstruction is therefore affected, in contrast to the ϕ clusters position which position is defined as the middle of the peak strip.

These changes are also reflected in the residuals and the resolution as shown in Figure 4.38. In the case of $4 - samples$ the resolution is measured to be 78.6 μm and in the case of $2 - samples$ is increased to 84.1 μm. The outliers in the residual distributions, another indication of the performance, is also increased from 0.05 % to

Figure 4.37: The η charge distribution, for clusters on segments with $2-samples$ data taking, fitted with Landau. The MPV is shifted compared to $4-samples$ to higher values, consequently the position reconstruction is affected, as well as the spoil fraction.

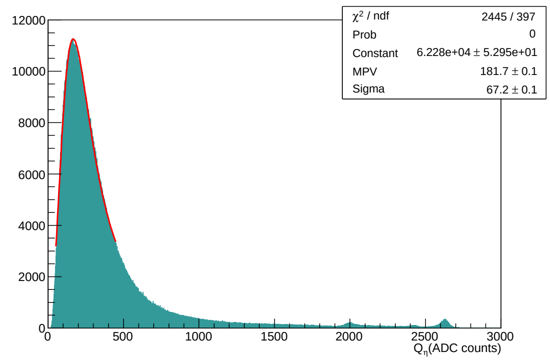

0.13% respectively. The pulls, defined from the error propagation in the residuals:

$$\delta R_1 = \sqrt{\delta x_1^2 + 0.25(\delta x_0^2 + \delta x_2^2)} \tag{4.14}$$
$$\delta R_2 = \sqrt{\delta x_2^2 + 0.25(\delta x_1^2 + \delta x_3^2)}$$

also deviate slightly more from the expected value of 1.000 when migrated to the $2-samples$ data taking. The fitted with a Gaussian pulls distributions are presented in Figure 4.39 and the estimated means are $\sigma = 1.044$ and $\sigma = 1.064$ for the $4-$ and $2-samples$ respectively. The $2-samples$ data taking was crucial for the operation of the system and the efficiency deterioration was considered acceptable, otherwise the operation would have been impossible.

4.16 CSC Efficiency in the Muon Algorithm

In this section the CSC efficiency in the STACO muon algorithm [14] is investigated using the tag and probe method. In the beginning, the muon spectrometer reconstruction efficiency is extracted in the high η region, where the CSC detectors are located, and then the efficiency of the CSC segments, when a STACO muon exists, is estimated.

Figure 4.38: The residuals distribution for $2-samples$ data, defined as in Equation 4.13, fitted with a double Gaussian to account for both the signal (red line) and the background (blue line). The resolution is estimated to be 78.6 μm for the $4-samples$ runs (in Section 4.12) and for the $2-samples$ is 84.1 μm. The outliers correspond to 0.05 % and 0.13% respectively. The differences are attributed to the non-accurate charge reconstruction when two of the four samples are not recorded.

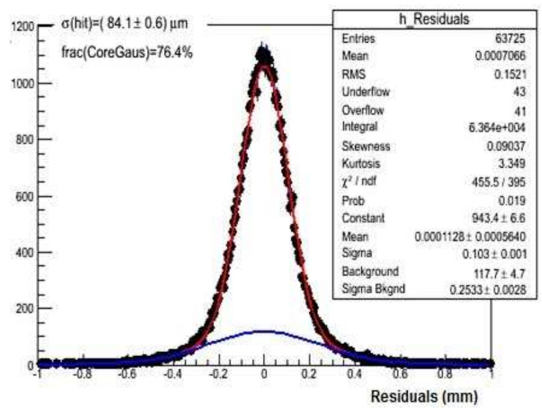

Figure 4.39: The pulls distributions, defined as in Equation 4.15, are fitted with a Gaussian. The measured pulls are $\sigma = 1.044$ and $\sigma = 1.064$ for the $4-samples$ (a) and $2-samples$ (b) respectively. The deviation from the expected zero value is due to the less accurate reconstruction.

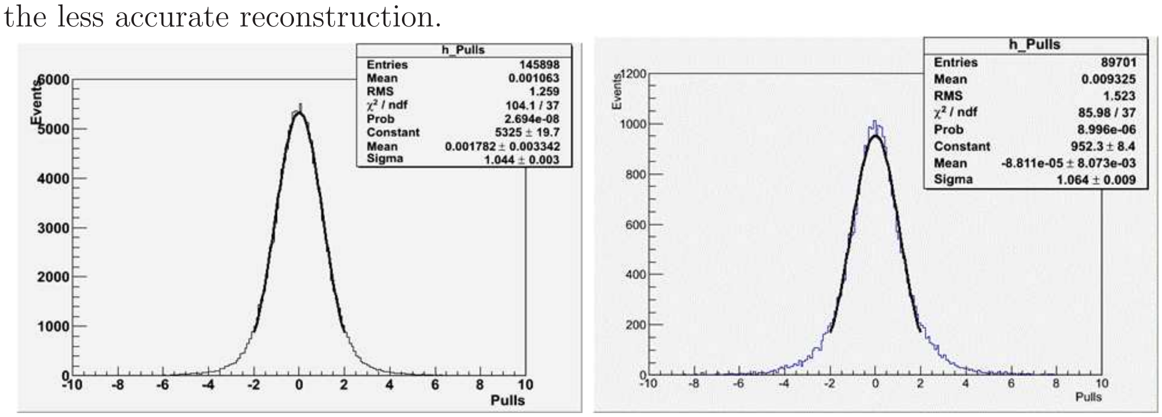

(a) (b)

Figure 4.40: Mass distribution formed by the tag muon and the probe charged track for a subset of the Run-I data. The Z-resonance can be seen above a constant background.

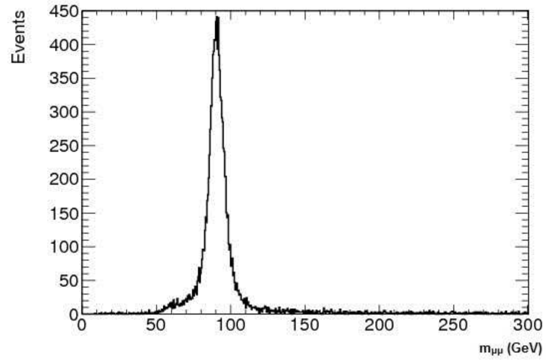

4.16.1 The Tag and Probe Method

The tag and probe method relies on the preparation of an unbiased sample of physics objects and uses a well-known resonance or PDF for a data-driven efficiency estimation. Specifically, the $Z \to \mu^+\mu^-$ decays are used in this section. The "tag" muon is selected using tight selection (for fake rate elimination) and the "probe" muon selection is looser. The so called "passing probe" has stricter criteria than the probe, but looser compared to the tag. The ratio of the passing probes over probes is defined as the efficiency of the technique:

$$Efficiency = \frac{N_{Passing\,Probes}}{N_{Probes}}. \tag{4.15}$$

The tag muon is a combined (both ID and MS information) or segment tagged (ID and partial MS information), with $p_T > 20$ GeV, satisfying a number of inner detector criteria, B-Layer/SCT/Pixel hits and a successful TRT extension. Isolation criteria, both track based and calorimeter based, are also applied. The probe object is an inner detector opposite charged track, going through the CSC region ($2.0 < \eta < 2.7$), with $p_T > 20$ GeV. The tag and probe objects form the Z mass above a constant background, shown in Figure 4.40. A mass cut, $|m - m_Z| < 15$ GeV is applied to suppress non Z-resonant events. The passing probe is associated with the probe inner detector track by requiring $\Delta R < 0.1$ between them. All the selection criteria are summarized in Table 4.4.

The efficiencies in η bins are presented in Figure 4.41 and they are relatively high. The error bars correspond to the binomial errors and no systematic uncertainty is included. Further investigation follows for better understanding of the inefficiency concerning only the CSC segments and hits information. It has to be noted that the CSC detectors are only 1/3 of the muon spectrometer stations in the forward region.

Table 4.4: Selection criteria for the tag and probe objects used for the efficiency extraction of the STACO muon algorithm in the high η region.

Object Type	Selection
Tag	Combined or Segment Tagged Muon $p_T > 20$ GeV $N_{B-Layer\,Hits} > 0$ when B - Layer Hit expected $N_{Pixel\,Hits} + N_{Crossed\,Dead\,Pixel\,Sensors} > 1$ $N_{SCT\,Hits} + N_{Crossed\,Dead\,SCT\,Sensors} \geq 6$ $N_{Pixel\,Holes} + N_{SCT\,Holes} < 3$ ${n_{TRT}}^{hits}$ = number of TRT hits, ${n_{TRT}}^{outliers}$ = number of TRT outliers n = ${n_{TRT}}^{hits} + {n_{TRT}}^{outliers}$ $\|\eta\|$ <1.9 : $n > 5$ and ${n_{TRT}}^{outliers} > 0.9n$ $\|\eta\|$ ≥1.9 : $n > 5$ and ${n_{TRT}}^{outliers} > 0.9n$ $\Sigma p_T/p_T < 0.15(\Delta R = 20)$ $\Sigma E_T/E_T < 0.30(\Delta R = 20)$
Probe	Opposite Charged Inner Detector Track in the CSC region $p_T > 20$ GeV
Tag & Probe	$\|m - m_Z\| < 15$ GeV
Passing Probe	Muon Associated to the Probe Track ($\Delta R < 0.1$)

Figure 4.41: Efficiency of the STACO muon algorithm as estimated from the tag and probe method. Results are provided for the high η region where the CSC detectors are located. The estimated efficiency depends on all the muon technologies in the region where the probe object passes.

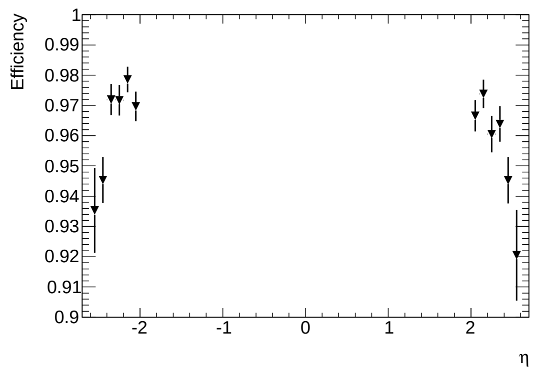

The classification of the CSC segments conditions is the following in the inefficiency cases:

- *33.6% segment with 4 unspoiled hits*
- *33.7% segment with 3 unspoiled hits*[7]
- *13.4% segment with <3 unspoiled hits*
- *19.3% segments with no track association.*

The tag and probe estimated efficiency depends on all the muon technologies in the region where the probe object passes. To optimize the result for the CSC detectors another tag and probe method is used. The CSC reconstruction contributes to the muon object reconstruction with segments. These segments are formed from the layer hits, which might be unspoiled hits or not. The CSC segment efficiency is estimated using the same tag selection as previously and now the probe is required to be a STACO muon passing through the CSC region. The efficiency is estimated as the number of muons related to a CSC segment divided by the number of probe muons. Table 4.5 presents analytically the selection. The resulting efficiencies are shown in Figure 4.42. The overall efficiency is $(98.85 \pm 0.10)\%$ and the variations between sectors or the different η, ϕ regions are small.

[7] The cases of less than four unspoiled hits can be partially explained from the dead layers and the stuck bit channels.

Table 4.5: Selection criteria for the tag and probe objects used for the CSC segment efficiency extraction in the STACO muon algorithm.

Object Type	Selection
Tag	Combined or Segment Tagged Muon $p_T > 20$ GeV $N_{B-Layer\,Hits} > 0$ when B - Layer Hit expected $N_{Pixel\,Hits} + N_{Crossed\,Dead\,Pixel\,Sensors} > 1$ $N_{SCT\,Hits} + N_{Crossed\,Dead\,SCT\,Sensors} \geq 6$ $N_{Pixel\,Holes} + N_{SCT\,Holes} < 3$ ${n_{TRT}}^{hits}$ = number of TRT hits, ${n_{TRT}}^{outliers}$ = number of TRT outliers n = ${n_{TRT}}^{hits} + {n_{TRT}}^{outliers}$ $\|\eta\|$ <1.9 : $n > 5$ and ${n_{TRT}}^{outliers} > 0.9n$ $\|\eta\|$ ≥1.9 : $n > 5$ and ${n_{TRT}}^{outliers} > 0.9n$ $\Sigma p_T/p_T < 0.15(\Delta R = 20)$ $\Sigma E_T/E_T < 0.30(\Delta R = 20)$
Probe	Opposite Charged STACO Muon passing through the CSC region $p_T > 20$ GeV
Tag & Probe	$\|m - m_Z\| < 15$ GeV
Passing Probe	STACO Muon with Associated CSC Segment

4.17 Performance of Sectors with Problematic Layers

During the Run-I, sectors $A05$, $A09$, $C03$ lost one layer because of HV failure (before 2012) and in the middle of 2012 $C01$ lost two consecutive layers. In addition, the second layer of chamber $C05$ showed less occupancy, starting from the middle of 2012, and this is also be investigated in this section.

The performance of sectors already presented with the tag and probe method in Figures 4.42, including those with dead layers. Since the muon algorithms are robust against the detector efficiency and can work with a few hits on each subsystem, no significant loss is observed. Even though, in terms of detector performance, specifically in the case of $C01$ the real loss is visible in the segment angle determination.

Using a data sample taken when the $C01$ was fully operated, a study conducted to simulate the loss of the two outer layers. Pseudo-segments are defined by using the first two layers, simply by requiring the same event clusters within 5 strips apart[8]. This

[8] Assuming that clusters part of the same track cannot be more strips apart given the layers distance and the pitch

Figure 4.42: CSC segment efficiencies in the STACO muon algorithm using the tag and probe method. Overall, the efficiency as a function of the passing probe muon in the η - ϕ range (a) and the sectors efficiencies (b) are presented. Partial cause of the inefficiency cases are TGC holes. The study performed with the 2012 data.

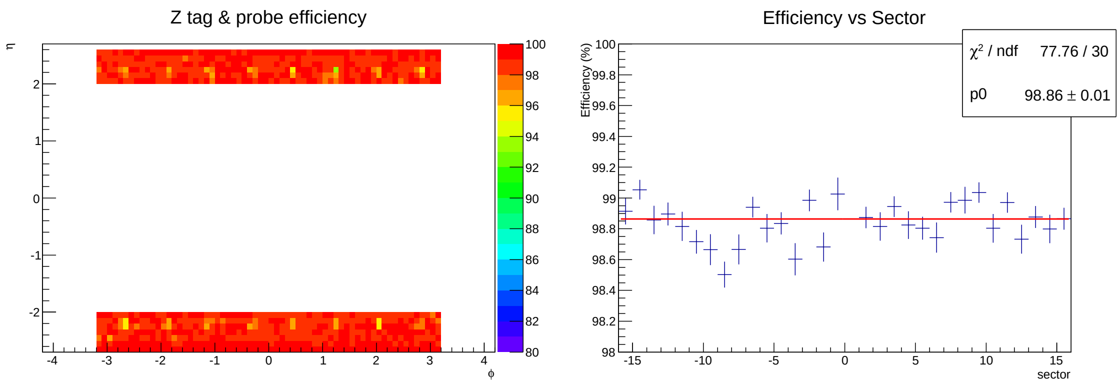

(a) (b)

segments are compared to the real segments found by the nominal segment algorithm. The fake rate, defined as:

$$Fake\ Rate = \frac{Pseudo - segments\ unassociated\ with\ real\ segments}{Total\ pseudo - segments} \tag{4.16}$$

was estimated to be 3.6% and the probability of not finding a pseudo-segment when a real segment exists is negligible ($\sim 0.01\%$). Despite the low fake rate, further investigation was performed for possible fake reduction. Specifically, the association of the clusters charges was used to reveal possible patterns. As Figure 4.43 shows, no correlation could be revealed. The real cost of the loss of the two layers is in the segment angle, the estimated pseudo-segment angle shows non-marginal deviation from the real angle (Figure 4.44).

Except from the dead layers, $C05$ showed less occupancy in half of one plane (Figure 4.45) and the analysis showed that the hit finding efficiency deteriorated as Table 4.6 reports. The cause is probably a failure in the HV distribution line. This assumption is supported by the evidence that when the occupancy reduction occurred, the HV value on this layer was less than expected (Figure 4.45).

4.18 Run-I Performance Summary

Table 4.7 summarizes the efficiency during the Run-I operations for fully operating sectors, i.e. without dead layers. The time intervals are defined as the eras with the

Figure 4.43: Possible correlation of the fake rate with the cluster charges investigated for the C01 pseudo-segments after the two dead layers appeared. No pattern is visible. Figures show the charge of the inner layers separately for true (a) and for fake pseudo-segments (b). Sector C01 study of the segment identification, after the loss of the two outer layers, estimated to have a fake rate of 0.036.

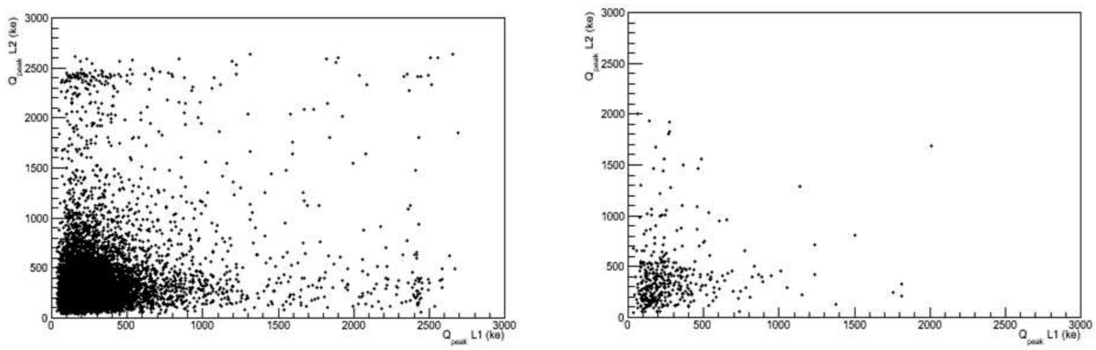

(a) (b)

Figure 4.44: $C01$ pseudo-segments angle difference from the real angle. The loss of the two layers is visible at this estimation.

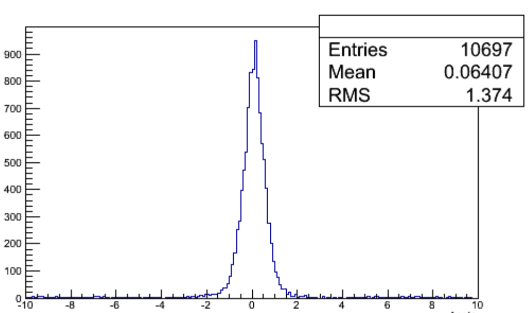

Figure 4.45: $C05L1$ shows less occupancy than expected (red line). The problem is associated with lower current drawn from this plane.

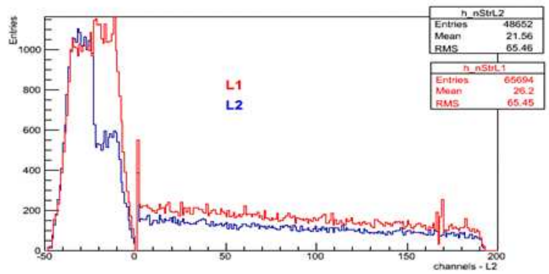

Figure 4.46: $C05L1$ less occupancy associated with the lower current drawn in the middle of the data taking (June 13^{th}, 2012). The source is probably due to a failure in the HV distribution line. The image is a screen shot from the DCS viewer.

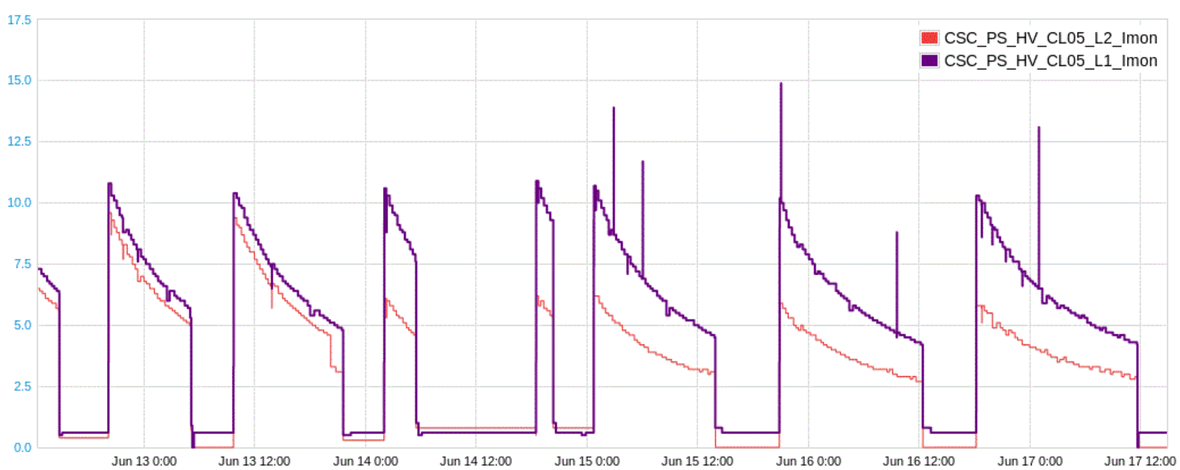

Table 4.6: The Table summarizes the performance of $C05L1$ after found to show less occupancy in half of the plane. For comparison reasons other sectors are presented.

Hits on Tracks	$C05$	Rest Sectors without dead layers
$> 1\ \eta$	94.0 ± 0.3	98.77 ± 0.12
$> 1\ \phi$	93.5 ± 0.3	97.68 ± 0.17
$> 1\ Unspoiled\ \eta$	85.6 ± 0.4	91.4 ± 0.3

same data acquisition conditions. These are in chronological order: the $4 - samples$ data taking, the $2 - samples$ data taking with wrong latency settings and increased thresholds ($\eta > 50$ and $\phi > 60$ ADC counts) and correct latency with restored η thresholds (40 ADC counts). Schematically the inefficiency of all runs included in the "Good Runs List" [15] (GRL, in total 474 runs) are presented in Figure 4.47. The performance, excluding the runs taken with wrong latency settings, was overall stable and high.

Table 4.7: Summary Table of the Run-I performance in eras with the same data acquisition conditions for fully operating sectors. Run to run deviations observed only for runs taken with wrong latency settings. The quoted uncertainties are statistical only.

Selection	Efficiency (%)			
	$4 - samples$	$2 - samples$	Wrong Latency, $\eta > 50,\ \phi > 60$ ADC counts	Correct Latency, $\eta > 40,\ \phi > 60$ ADC counts
$> 1\ \eta$ on track	98.947 ± 0.014	98.956 ± 0.014	~ 94	98.744 ± 0.008
$> 1\ \phi$ on track	97.746 ± 0.017	97.729 ± 0.020	~ 87	97.699 ± 0.012
$> 1\ Unspoiled\ \eta$ on track	91.77 ± 0.04	91.92 ± 0.04	~ 85	90.870 ± 0.023
$Z\ Tag\&Probe$	98.915 ± 0.014	98.873 ± 0.016	~ 98	98.764 ± 0.019

The efficiency of sectors with malfunctions was studied separately since they do not reflect the general performance. The results of the study are summarized in the Table 4.8 for the time period starting from the appearance of the problem and excluding the time period with the wrong latency settings. The efficiency is very close to the efficiency of the rest sectors reported in Table 4.7.

Figure 4.47: The fraction of tracks with less than 2 η (a) and less than 2 ϕ hits are presented for all runs in the good runs lists of the Run-I for fully operating sectors. The x-axis are the runs (in total 474 runs) in chronological order. Excluding the period where the latency set wrongly, motivated by the installation of fiber extensions and sampling changing, the inefficiency was low and stable over time. This is a strong indication of the robust detector performance.

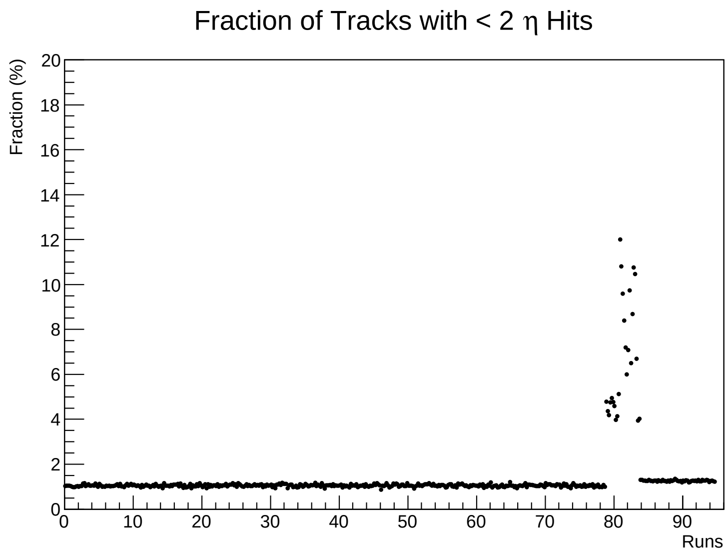

(a)

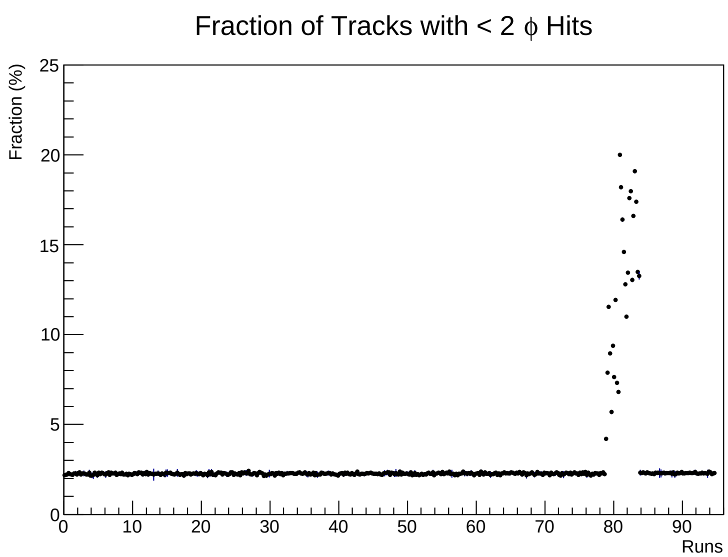

(b)

Table 4.8: Summary Table of the Run-I performance for sectors with malfunctions starting from the appearance of the problem and excluding the period with wrong latency settings. The efficiencies are comparable with the fully working chambers, reported in Table 4.7.

Selection	Efficiency (%)		
	$C03,\ A05,\ A09$ 1 dead layer	$C01$ 2 dead layers	$C05$ Less occupancy
$> 1\ \eta$ on track	98.671 ± 0.025	$85.30 \pm 0.0.14$	89.70 ± 0.04
$> 1\ \phi$ on track	96.96 ± 0.04	91.67 ± 0.14	97.20 ± 0.06
> 1 *Unspoiled* η on track	89.75 ± 0.08	59.4 ± 0.19	86.40 ± 0.12
Z Tag&Probe	98.52 ± 0.04	97.52 ± 0.04	98.71 ± 0.04

4.19 25ns Runs

At the end of the 2012 data taking, runs with 25 ns bunch spacing, instead of the 50 ns, recorded with $2-samples$. The reason was to conduct a preliminary study of the detectors operation and be better prepared for the Run-II, during which the bunch spacing will be decreased. The specific conditions of the recorded three runs are summarized in Table 4.9. The run was analyzed in multiple levels. Figure 4.48 presents the occupancies for relatively low and high charges and for comparison the 50 ns occupancies are presented. The 50 ns run was chosen to have roughly the same instantaneous luminosity in order to have the same pile up conditions.

Table 4.9: Summary of the exact conditions of the 25 ns runs recorded in 2012 at $\sqrt{s} = 8$ TeV center of mass energy.

Run	Trains	Colliding Bunches	Peak Instantaneous Luminosity ($cm^{-2}\ s^{-1}$)	ATLAS Delivered Luminosity (pb^{-1})	Lumi Blocks	Recorded Events (Hz)
216399	2	48	5.83×10^{32}	10.942	1095	357.5
216419	3	48	3.44×10^{32}	2.174	271	479.0
	3	42				
216432	3	48	1.70×10^{32}	0.876	435	158.5
	1	42				

The offline analysis of the precision charge shows certain differences in the peaks positions when no further requirement is imposed. As Figure 4.37 shows, the peak shapes are different. Despite that, when the cluster on segment requirement is imposed

Figure 4.48: Comparison of the occupancies of 25 ns bunch spacing data with 50 ns as recorded from the online monitor. The latter data run chosen to have similar pile up conditions in order to be comparable. Figure (a) shows the 25 ns data with $Q_{peak} <$ 100 ke, (b) the 50 ns with $Q_{peak} < 100$ ke, (c) shows the 25 ns with $Q_{peak} > 100$ ke and (d) the 50 ns with $Q_{peak} > 100$ ke cases. The negative channels correspond to the ϕ channels, whereas as the positive are the η.

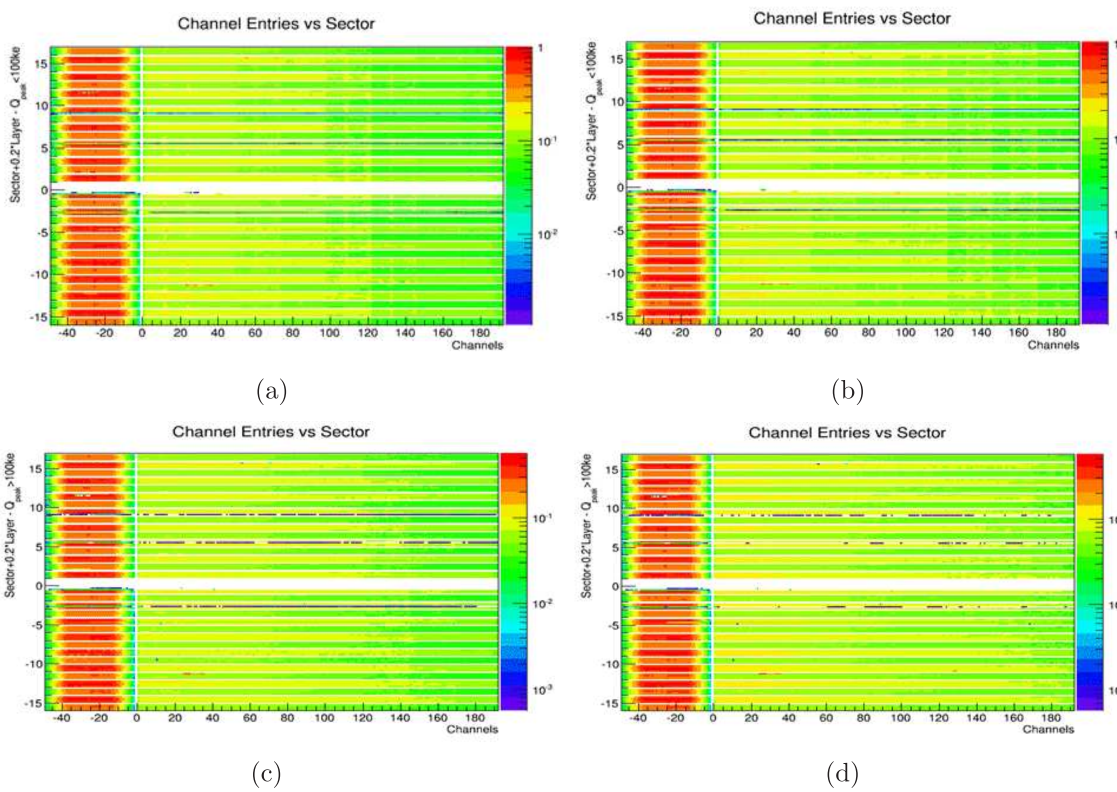

(a) (b) (c) (d)

Figure 4.49: Comparison of the 25 ns data η charge (red line) with the 50 ns (blue line). Figure (b) is the zoomed Figure (a). The shapes are different but restored when clusters on segments are required (see Figure 4.37), which indicates different background composition.

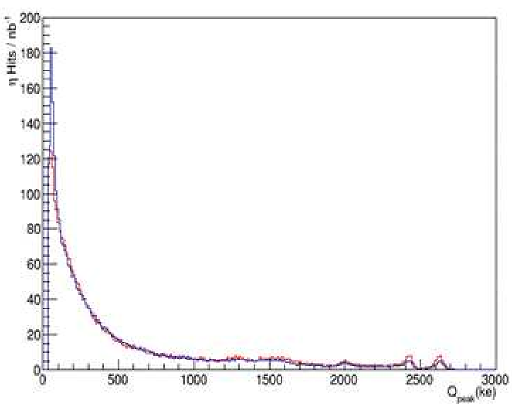

(a)

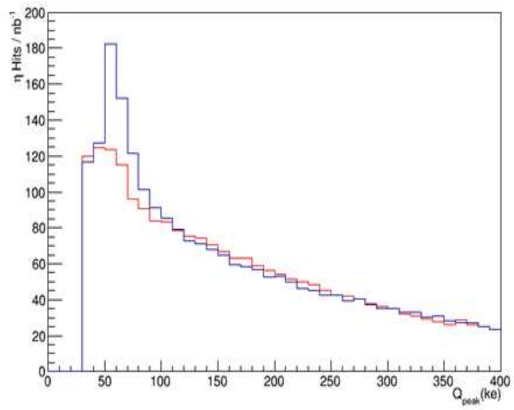

(b)

(Figure 4.50, a Landau MPV value of (172 ± 36) ke) is found similar to the 50 ns value of (181.7 ± 0.1) ke) (Figure 4.37, which indicates different background composition. The peaking time of the small hits is further investigated and reveals that the 50 ns excess contamination concentrates around 0 ns (Figure 4.51). The overall time distributions do not look significantly different though (Figure 4.52).

The unspoiled hits on segments are also higher for the 25 ns, which is probably due the smaller contamination with small amplitude hits, as Figure 4.53 presents. Despite that, the resolution slightly degraded to (87.9 ± 0.6) μm (the residuals are presented in Figure 4.54) with the respect to the measured $2-samples$ resolution (Figure 4.38) of (84.1 ± 0.6) μm.

The founding are used for precision 25 ns simulation production.

4.20 Post-Run-I Chambers Repair

During the Long Shutdown (LS1), between the Run-I and Run-II, the sectors with dead layers were repaired. Initially, the plan was to repair only the side C broken sectors, because only that wheel was lifted to the surface for the Insertable B-Layer replacement (mentioned in Section 3.4.1). However, the design of a new chamber extraction tool, schematically presented in Figure 4.55, made possible the side A chambers repair, owing to the small required space, which was enough to fit the space between the Barrel MDT

Figure 4.50: η charge on segments for 25 ns data fitted with a Landau distribution. The MPV is estimated to be (172 ± 36) ke and is well compared to the (181.7 ± 0.1) ke (see Figure 4.37) obtained with the 50 ns data.

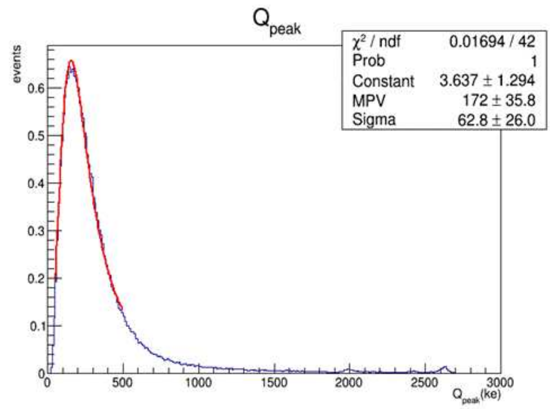

Figure 4.51: The peaking time (ns) of hits is presented as a function of the peak charge amplitude (ke) separately for 25 ns (a) and 50 ns (b) data. The hits excess in the case of 50 ns data is concentrated around 0 ns.

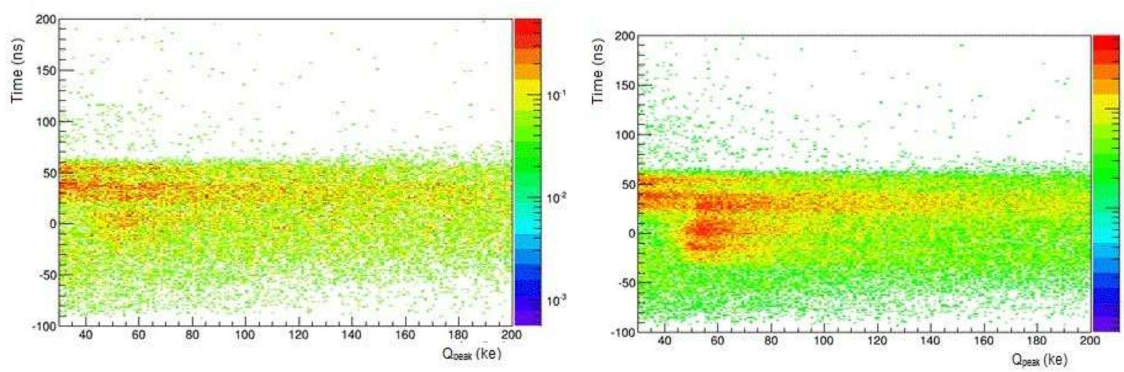

(a) (b)

Figure 4.52: The peaking time of hits is presented for 25 ns (red line) and 50 ns (blue line).

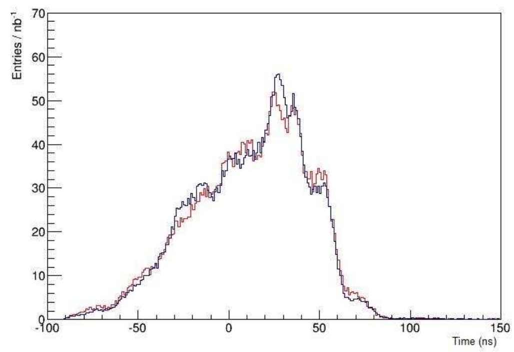

Figure 4.53: The unspoiled hits on segments for 25 ns (red line) and 50 ns (blue line) data. Due to the smaller contamination with small amplitude hits, the unspoiled fraction is higher for the 25 ns data.

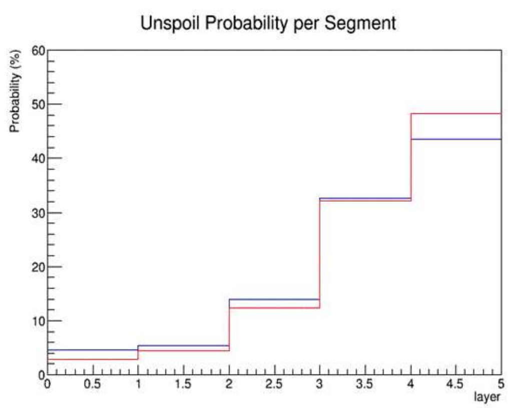

Figure 4.54: The residuals of 25 ns data fitted to give a resolution of (87.9 ± 0.6) μm, slightly higher than the $2 - samples$ resolution of (84.1 ± 0.6) μm (4.38).

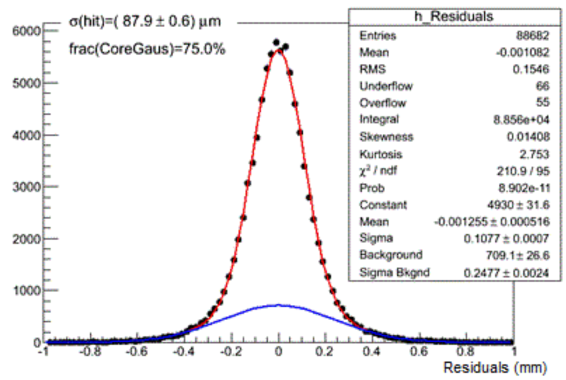

and the EndCap Toroid.

The chambers extracted were the $C01$, $C03$, $A05$ and $A09$ which had at least one dead layer. The sector's $C05$ problem of less occupancy in half of one plane was not repair. The assumption is that the problem is due to partial HV distribution failure, but lack of absolute determination of the cause led to the decision of not extracting the chamber.

After the dismounting from the wheel, the chambers were moved to the laboratory (Figure 4.56) where the surrounding copper shield, the on-detector electronics, the cooling system and the gas were removed. The dead cables showed as curled, were replaced and all the pieces put back together. The chambers in the laboratory run on HV for one night and the DAQ tests showed no significant change of the pedestal pattern which indicates the good operational level. Finally, the chambers were installed on the wheel and further commissioning tests were followed to verify the functionality of the chambers. The pedestal differences from the database values were not significant, as shown in Figure 4.57 and this strongly proves the success of the repairs.

4.21 Summary

In this chapter, the CSC operations and performance during the Run-I presented. Despite the problems occurred, caused by the dead layers and mainly by the limitation of the readout electronics, the efficiency remained high. The official ATLAS reports, presented in Figure 4.58, shows that the overall deadtime originating from the CSC was marginal compared to other subsystems [17] and the online data quality was 100% during the 2012 [18], i.e. the year that the majority of the Run-I data recorded.

Figure 4.55: Schematic view of the chamber removal tool used for the chambers extraction [16]. Due to the small required space the dismount of chambers from the cavern became possible.

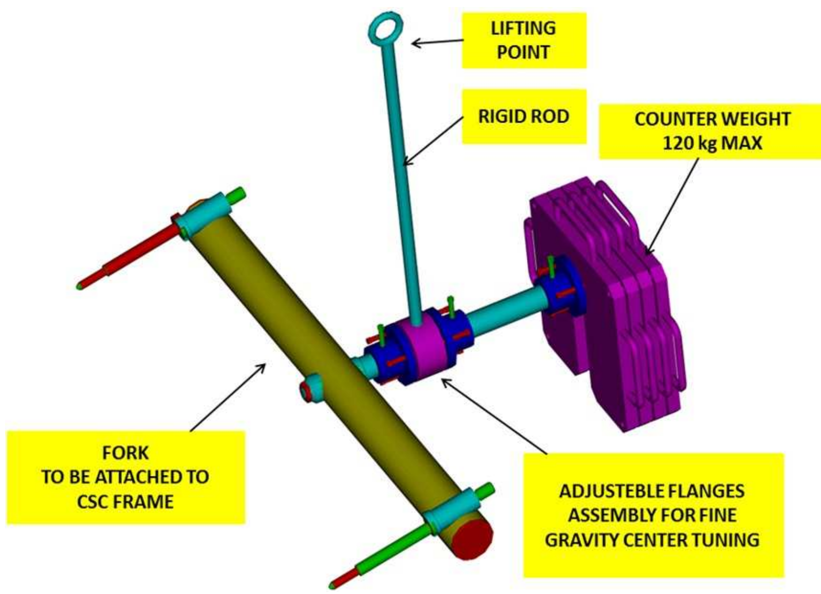

Figure 4.56: Pictures taken during the repair of the chambers. (a) shows the extraction of a broken chamber from the Wheel C (on the surface), (b) shows a chamber in the laboratory with the copper protection removed as well as the on-detector electronics (sitting on the planes), the colling system and the gas, (c) shows the layer with the damaged wire at the time of its removal (too delicate wires to be seen on the Picture) and (d) shows the chamber after the repair when the DAQ test took place. The final step was the installation and connection of the service on the wheel and another DAQ test for the absolute verification of the successful installation and repair.

(a) (b)

(c) (d)

Figure 4.57: Pedestal runs deviations from the database values of Run-I for the repaired sectors after the installation for each channel (the ϕ channels are denoted with negative numbers). No significant change, above the uncertainty value, is observed.

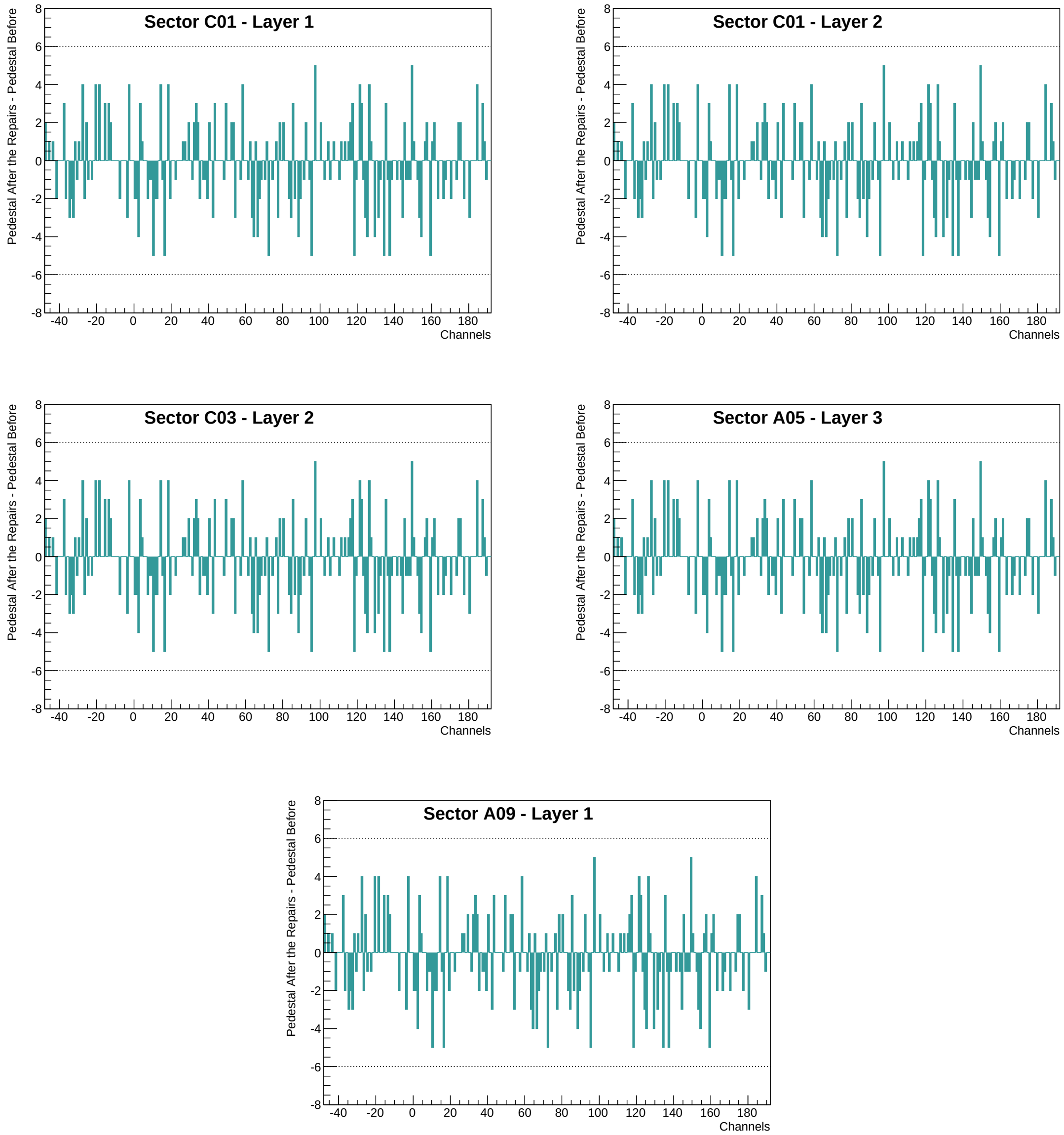

Figure 4.58: ATLAS official reports for the deadtime [17] and the online data quality efficiency [18]. Figure (a) shows that the deadtime caused by the CSC was marginal (8.1 *seconds*, 0.2%) compared to other subsystems and Figure (b) presents the luminosity weighted relative fraction of good quality data delivery by the various ATLAS subsystems during LHC fills with stable beams in pp collisions at $\sqrt{s} = 8$ TeV. Runs between April 4th and December 6th, corresponding to a recorded integrated luminosity of 21.3 fb^{-1}, are accounted. The CSC had 100% efficiency.

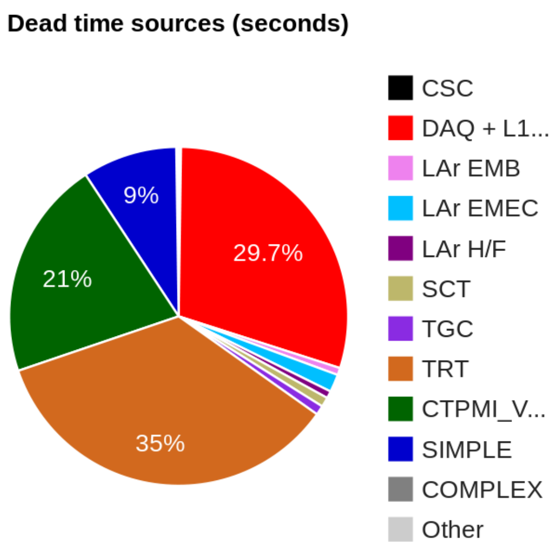

(a)

ATLAS p-p run: April-December 2012										
Inner Tracker			Calorimeters		Muon Spectrometer				Magnets	
Pixel	SCT	TRT	LAr	Tile	MDT	RPC	CSC	TGC	Solenoid	Toroid
99.9	99.1	99.8	99.1	99.6	99.6	99.8	100.	99.6	99.8	99.5
All good for physics: 95.5%										

Luminosity weighted relative detector uptime and good quality data delivery during 2012 stable beams in pp collisions at √s=8 TeV between April 4th and December 6th (in %) – corresponding to 21.3 fb-1 of recorded data.

(b)

Chapter Bibliography

[1] ATLAS Collaboration, ATLAS muon spectrometer: Technical design report, 1997, CERN-LHCC-97-22, ATLAS-TDR-10.

[2] T. Argyropoulos, K. A. Assamagan, B. H. Benedict, V. Chernyatin, E. Cheu, et al., Cathode strip chambers in ATLAS: Installation, commissioning and in situ performance, *IEEE Trans.Nucl.Sci.*, 56:1568–1574, 2009.

[3] ATLAS Collaboration, Csc atlas photos, http://www.atlas.ch/photos/muons-csc.html.

[4] Brookhaven National Laboratory Instrumentation Division, Cathode strip chambers, http://www.inst.bnl.gov/programs/gasnobledet/hepnp/csc.shtml.

[5] E Mathieson, Induced charge distributions in proportional detectors, $http : //www.inst.bnl.gov/programs/gasnobledet/publications/Mathieson\%27s_Book.pdf$.

[6] I. Gough Eschrich, Readout electronics of the ATLAS muon cathode strip chambers, pages 247–250, 2008.

[7] M. Schernau, CSC website, http://positron.ps.uci.edu/∼schernau.

[8] ATLAS Collaboration, CSC pulser calibration website, https://twiki.cern.ch/twiki/pub/Atlas/Pulser/CSC_Pulser_H.pdf.

[9] ATLAS Collaboration, CSC calibration monitoring website, https://atlas-csc-calib.web.cern.ch.

[10] D. L. Hawkins, ATLAS particle detector CSC ROD software design and implementation, and, Addition of K physics to chi-squared analysis of FDQM.

[11] R. Murillo, M. Huffer, R. Claus, R. Herbst, A. Lankford, et al., Software design of the ATLAS Muon Cathode Strip Chamber ROD, *J.Phys.Conf.Ser.*, 396:012031, 2012.

[12] I. Soloviev, User's Guide Tools Manual, OKS Documentation, 2002, ATLAS DAQ Technical Note: 033.

[13] SLAC, Muon CSC readout upgrade, https://confluence.slac.stanford.edu/display/Atlas.

[14] ATLAS Collaboration, Muon Performance in Minimum Bias pp Collision Data at $\sqrt{s} = 7$ TeV with ATLAS, 2010.

[15] ATLAS Collaboration, Data quality information public results, https://twiki.cern.ch/twiki/bin/view/AtlasPublic/RunStatsPublicResults2010.

[16] A. Gordeev (BNL), Graphics and design of the CSC Removal Tool.

[17] ATLAS Collaboration, ATLAS daq efficiency summary, https://atlasdaq.cern.ch/daq_eff_summary.

[18] ATLAS Collaboration, Data quality information for 2010 and 2011 data, https://twiki.cern.ch/twiki/bin/view/AtlasPublic/RunStatsPublicResults2010.

[19] G. C. Smith, J. Fischer, and V. Radeka, Capacitive Charge Division in Centroid Finding Cathode Readouts in MWPCs, *IEEE Trans.Nucl.Sci.*, 35:409–413, 1988.

[20] E Mathieson and G C Smith, Reduction in Non-Linearity in Position-Sensitive MWPCs, *IEEE Trans.Nucl.Sci.*, 36:305–310, 1989.

[21] J. Dailing, N. Drego, D. Hawkins, A. Lankford, Y. Li, et al., Performance and radiation tolerance of the ATLAS CSC on-chamber electronics, pages 196–200, 2000.

[22] J. Dailing, N. Drego, A. Gordeev, V. Grachev, D. Hawkins, et al., Off-detector electronics for a high-rate CSC detector, *IEEE Trans.Nucl.Sci.*, 51:461–464, 2004.

[23] UCL, ATLAS TIM website, http://www.hep.ucl.ac.uk/atlas/sct/tim/tim-muons.shtml.

5

Search for $H \rightarrow ZZ^{(*)} \rightarrow 4\ell$ Decays

5.1 Introduction

The decay channel $H \rightarrow ZZ^{(*)} \rightarrow 4\ell$, where $\ell = e, \mu$, is one of the experimentally cleanest signatures for the search of the Standard Model Higgs boson. The main backgrounds to the $H \rightarrow ZZ^{(*)} \rightarrow 4\ell$ search at the LHC are the irreducible $ZZ^{(*)}/\gamma^* \rightarrow 4\ell$, while the reducible backgrounds are mainly $Z + QQ$ (Q=b or c quark), $t\bar{t}$, and $Z + light\,jets$ with one or more "fake" leptons in the final state.

For the high mass region, $m_H \geq 160$ GeV, the two on-shell Z bosons from the Higgs decay allow for a selection which strongly suppresses the reducible backgrounds leaving only the irreducible $ZZ^{(*)} \rightarrow 4\ell$ component. At low Higgs masses, where one of the decay bosons is off-shell, contributions from $Z + jets$ and $t\bar{t}$ can be significant and tighter cuts are therefore applied to reduce these backgrounds to a level safely below the $ZZ^{(*)}$ continuum.

Previous direct searches for the Higgs boson performed at the CERN Large Electron-Positron Collider (LEP) excluded at 95% confidence level (CL) the production of a SM Higgs boson with mass, m_H, less than 114.4 GeV [1]. The searches at the Fermilab Tevatron $p\bar{p}$ collider have excluded at 95% CL the region between $156 < m_H < 177$ GeV [2]. At the LHC, results from data collected in 2010 extended the search in the region between $200 < m_H < 600$ GeV by excluding a Higgs boson with cross section larger than $5 - 20$ times the SM prediction [3].

This analysis presents a general, model independent, search for Higgs candidate

Table 5.1: Luminosity collected during the 2011 and 2012 data taking [4], the data taking conditions and the data quality are also presented [5].

Year	Energy ($\sqrt{s}$)	Peak luminosity	Pile-up ($<\mu>$)	Integrated luminosity	Data taking efficiency	Data quality efficiency
2011	7 TeV	$3.65\times10^{33}cm^{-2}s^{-1}$	9.1	$4.5\ fb^{-1}$	~96.5%	~89.9%
2012	8 TeV	$7.73\times10^{33}cm^{-2}s^{-1}$	20.3	$20.3\ fb^{-1}$	~95.5%	~95.3%

events and background measurements, with focus on the muons background, using data collected from the ATLAS experiment in 2011 and 2012. The available data were analyzed per year of data taking due to different center of mass energies ($\sqrt{s}$), 7 TeV for 2011 and 8 TeV for 2012.

Several control regions are constructed by relaxing or inverting cuts applied for the Higgs search and then are fitted simultaneously to extract the background contribution. Estimations in the signal region are based on transfer factors. Hence, the efficiency of the leptons in background environments is also studied, as an important factor of the search. Comparisons between real data and Monte Carlo expectations are performed in each of the analysis steps. Multiple cross checks are also presented to guaranty the validity of the result.

5.2 Data Samples

The data, collected during the 2011 and 2012 years, are subjected to quality requirements and are rejected when recorded during periods when either the LHC declared unstable beams or the relevant ATLAS detector components were not operating nominally. The events surviving this quality requirements are said to belong to the "Good Runs List". The resulting integrated luminosity is $\mathcal{L} = 4.5\ fb^{-1}$ for $\sqrt{s} = 7$ TeV and $\mathcal{L} = 20.3\ fb^{-1}$ for $\sqrt{s} = 8$ TeV, respectively, for all the final states. Details about the data taking conditions [4] and efficiencies [5] are presented in Table 5.1.

5.3 Monte Carlo (MC) samples

5.3.1 Signal MC Samples and Cross Sections

The $H \to ZZ^{(*)} \to 4\ell$ signal is modeled using the POWHEG Monte Carlo (MC) event generator [6, 7], which calculates separately the gluon-gluon fusion and vector-boson fusion production mechanisms with matrix elements up to next-to-leading order (NLO). The Higgs boson transverse momentum (p_T) spectrum in the gluons fusion process is re-weighted to follow the calculation of Reference [8], which includes QCD corrections up to NLO and QCD soft-gluon re-summations up to next-to-next-to-leading logarithm (NNLL). POWHEG is interfaced to PYTHIA8.1 [9] for showering and hadronization, which in turn is interfaced to PHOTOS [10] for quantum electrodynamics (QED) radiative corrections in the final state. PYTHIA is used to simulate the production of a Higgs boson in association with a W or a Z boson as well as the associated production with a top quark pair.

The Higgs boson production cross sections and decay branching ratios, as well as their uncertainties, are taken from References [11, 12]. The cross sections for the gluons fusion process have been calculated to next-to-leading order (NLO) [13, 14, 15] and next-to-next-to-leading order (NNLO) [16, 17, 18] in QCD. In addition, QCD soft-gluon resummations calculated in the next-to-next-to-leading logarithm (NNLL) approximation are applied for the gluons fusion process [19]. NLO electroweak (EW) radiative corrections are also applied [20, 21]. These results are compiled in References [22, 23, 24] assuming factorization between QCD and EW corrections.

The cross sections for the vector-boson fusion process are calculated with full NLO QCD and EW corrections [25, 26, 27], and approximate NNLO QCD corrections are available [28]. The cross sections for the associated WH/ZH production processes are calculated at NLO [29] and at NNLO [30] in QCD, and NLO EW radiative corrections [31] are applied. The small contribution from the associated production with a $t\bar{t}$ pair ($q\bar{q}/gg \rightarrow t\bar{t}H$, denoted $t\bar{t}H$) is now taken into account in the analysis. The cross sections for the $t\bar{t}H$ process are estimated up to NLO QCD [32, 33, 34, 35, 36].

The Higgs boson decay branching ratio [37] to the four-leptons final state is predicted by PROPHECY4F [38, 39], which includes the complete NLO QCD+EW corrections, the interference effects between identical final-state fermions, and the leading two-loop heavy Higgs boson corrections to the four-fermion width. Table 5.2 gives the production cross sections and branching ratios for $H \rightarrow ZZ^{(*)} \rightarrow 4\ell$ which are used to normalize the signal MC samples for several Higgs boson masses.

The QCD scale uncertainties for $m_H = 125$ GeV amount to $^{+7}_{-8}\%$ for the gluons fusion process and $\pm1\%$ for the vector-boson fusion and associated WH/ZH production processes. The mass-dependent uncertainty in the production cross section due to uncertainties in the parton distribution function (PDF) and α_s are $\pm8\%$ for gluon-initiated processes and $\pm4\%$ for quark-initiated processes, estimated in the mass range around 125 GeV by following the prescription in Reference [40] and by using the PDF sets of CTEQ [41], MSTW [42] and NNPDF [43]. The PDF uncertainties are assumed to be 100% correlated for processes with identical initial states, regardless of their being signal or background [40, 44, 41, 42, 43].

Table 5.2: Higgs boson production cross sections for gluons fusion, vector-boson fusion and associated production with a W or Z boson in pp collisions at $\sqrt{s}$ of 7 TeV and 8 TeV [11]. The quoted uncertainties correspond to the total theoretical systematic uncertainties. The production cross section for the associated production with a W or Z boson is negligibly small for $m_H > 300$ GeV. The decay branching ratio for $H \to ZZ^{(*)} \to 4\ell$, with $\ell = e$ *or* μ, is reported in the last column [11].

m_H [GeV]	$\sigma\,(gg \to H)$ [pb]	$\sigma\,(qq' \to Hqq')$ [pb]	$\sigma\,(q\bar{q} \to WH)$ [pb]	$\sigma\,(q\bar{q} \to ZH)$ [pb]	$\sigma\,(gg \to Htt')$ [pb]	BR $\left(H \to ZZ^{(*)} \to 4\ell\right)$ $[10^{-3}]$
			$\sqrt{s} = 7\ Tev$			
123	15.6 ± 1.6	1.25 ± 0.03	0.61 ± 0.02	0.35 ± 0.01	0.09 ± 0.01	0.103 ± 0.005
125	15.1 ± 1.6	1.22 ± 0.03	0.58 ± 0.02	0.34 ± 0.01	0.09 ± 0.01	0.125 ± 0.005
127	14.7 ± 1.5	1.20 ± 0.03	0.55 ± 0.02	0.32 ± 0.01	0.08 ± 0.01	0.148 ± 0.006
			$\sqrt{s} = 8\ Tev$			
123	19.9 ± 2.1	$1.61^{+0.04}_{-0.05}$	0.74 ± 0.02	0.44 ± 0.02	$0.14^{+0.01}_{-0.02}$	0.103 ± 0.005
125	19.3 ± 2.0	1.58 ± 0.04	0.70 ± 0.02	0.42 ± 0.02	$0.13^{+0.01}_{-0.02}$	0.125 ± 0.005
127	18.7 ± 1.9	1.55 ± 0.04	0.67 ± 0.02	0.40 ± 0.02	$0.13^{+0.01}_{-0.02}$	0.148 ± 0.006

5.3.2 MC Background Samples

The $ZZ^{(*)}$ continuum background is modeled using POWHEG [45] for quark-antiquark annihilation and GG2ZZ [46] for gluon fusion. The mass-dependent PDF and α_s scale uncertainties are parametrized as recommended in Reference [12]. The QCD scale uncertainty has a $\pm 5\%$ effect on the expected $ZZ^{(*)}$ background at 125 GeV, and the effect due to the PDF and α_s uncertainties is $\pm 4\%$ ($\pm 8\%$) at 125 GeV for quark-initiated (gluon-initiated) processes.

The $Z +$jets production is modeled using ALPGEN [47] interfaced to PYTHIA for hadronization and showering and is divided into two sources: $Z +$ light jets, which includes $Zc\bar{c}$ in the massles c-quark approximation, $Zb\bar{b}$ from parton showers, and $Zb\bar{b}$ using matrix element calculations that take into account the b-quark mass. The MLM [48] matching scheme is used to remove any double counting of identical jets produced via the matrix element calculation and the parton shower, but this scheme is not implemented for b-jets. Therefore, $b\bar{b}$ pairs with separation $\Delta R = \sqrt{(\Delta\phi)^2 + (\Delta\eta)^2} > 0.4$ between the b-quarks are taken from the matrix-element calculation, whereas for $\Delta R < 0.4$ the parton-shower $b\bar{b}$ pairs are used. In this search the $Z+$jets background is normalized using control samples from data. For comparisons with simulation, the QCD NNLO FEWZ [49, 50] and MCFM [51] cross section calculations are used for inclusive Z boson and $Zb\bar{b}$ production, respectively.

The $t\bar{t}$ background is modeled using POWHEG interfaced to PYTHIA for parton shower hadronization, to PHOTOS for quantum electrodynamics (QED) radiative corrections and TAUOLA [52, 53] for the simulation of τ lepton decays.

SHERPA [54] is used for the WZ production simulation.

Generated events are fully simulated using the ATLAS detector simulation [55] within the GEANT4 framework [56]. The simulation of the additional pp interactions (pileup) is done in a separate step in the simulation chain, during digitization. Here minimum bias events, which were previously simulated, are superimposed on the simulated signal event. The distribution of the number of pileup events reproduces the bunch structure and the average number of interactions of the run periods.

The cross sections and background samples used for the data comparison are summarized in Table 5.3. The corresponding Feynman diagrams of the processes are presented in Figure 5.1. All the MC samples used for this analysis are summarized in the Appendix A analytically.

Figure 5.1: Production mechanisms of the ZZ, $Zb\bar{b}$ and $t\bar{t}$ backgrounds of the $H \to ZZ^{(*)} \to 4\ell$.

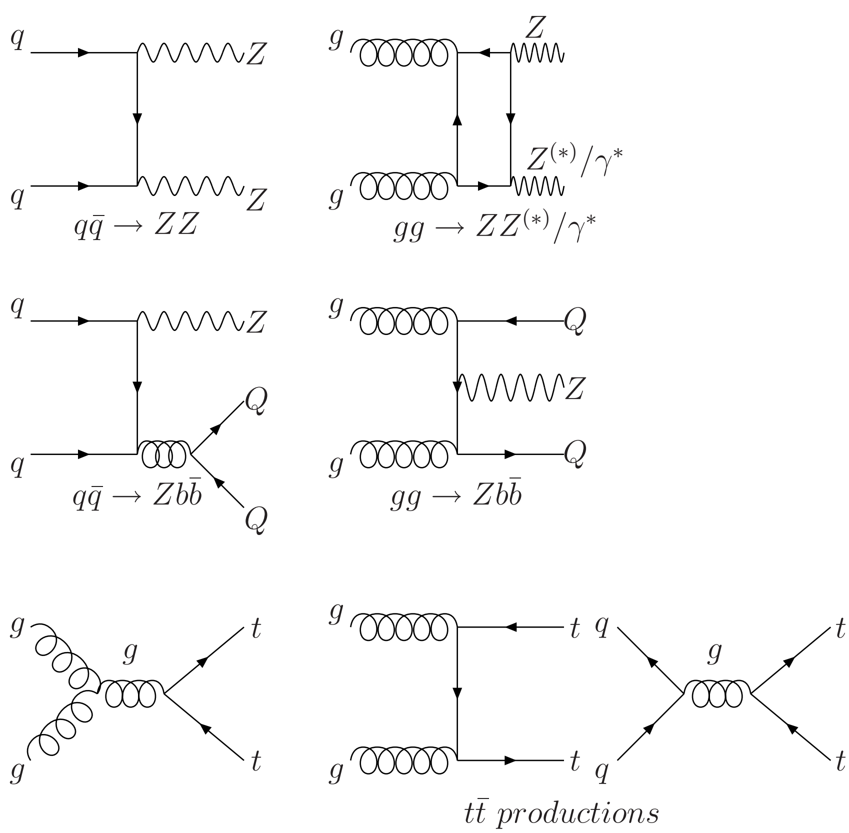

Table 5.3: Higgs backgrounds cross sections in pp collisions at $\sqrt{s}$ of 7 TeV and 8 TeV and the generated MC events.

	$\sqrt{s}=7$ TeV			$\sqrt{s}=8$ TeV		
Background Sample	Cross Section (pb)	k-factor	Events	Cross Section (pb)	k-factor	Events
$Z(\to \mu^+\mu^-)bb$ 3ℓ filter Np0	646.234	1.6	249899	837.906	1.6	499897
$Z(\to \mu^+\mu^-)bb$ 3ℓ filter Np1	328.405	1.6	148000	438.495	1.6	297899
$Z(\to \mu^+\mu^-)bb$ 3ℓ filter Np2	116.831	1.6	91500	159.779	1.6	169499
$Z(\to e^+e^-)bb$ 3ℓ filter Np0	645.316	1.6	249998	834.997	1.6	499995
$Z(\to e^+e^-)bb$ 3ℓ filter Np1	328.759	1.6	148000	437.617	1.6	297998
$Z(\to e^+e^-)bb$ 3ℓ filter Np2	116.276	1.6	91000	158.952	1.6	169499
$Z(\to \mu^+\mu^-)bb$ 4ℓ filter Np0	29.820	1.6	1194396	38.533	1.6	2488592
$Z(\to \mu^+\mu^-)bb$ 4ℓ filter Np1	21.159	1.6	678199	28.081	1.6	1383294
$Z(\to \mu^+\mu^-)bb$ 4ℓ filter Np2	9.886	1.6	241296	13.592	1.6	479518
$Z(\to e^+e^-)bb$ 4ℓ filter Np0	29.620	1.6	1195393	38.146	1.6	2488990
$Z(\to e^+e^-)bb$ 4ℓ filter Np1	21.033	1.6	678599	27.905	1.6	1453390
$Z(\to e^+e^-)bb$ 4ℓ filter Np2	9.786	1.6	241076	13.520	1.6	479018
$Z(\to \mu^+\mu^-)$ Np0	712000	1.23	6615230	718910	1.18	12907286
$Z(\to \mu^+\mu^-)$ Np1	155000	1.23	1334296	175810	1.18	6533889
$Z(\to \mu^+\mu^-)$ Np2	48800	1.23	1999941	58805	1.18	3580483
$Z(\to \mu^+\mu^-)$ Np3	14200	1.23	549896	15589	1.18	204799
$Z(\to \mu^+\mu^-)$ Np4	3770	1.23	150000	3907	1.18	129800
$Z(\to \mu^+\mu^-)$ Np5	1120	1.23	50000	1193	1.18	239200
$Z(\to e^+e^-)$ Np0	712000	1.23	6618284	718890	1.18	12908972
$Z(\to e^+e^-)$ Np1	155000	1.23	1334897	75600	1.18	7029177
$Z(\to e^+e^-)$ Np2	48800	1.23	2004195	58849	1.18	3580989
$Z(\to e^+e^-)$ Np3	14200	1.23	549949	15560	1.18	1004994
$Z(\to e^+e^-)$ Np4	3770	1.23	149948	3932	1.18	428597
$Z(\to e^+e^-)$ Np5	1120	1.23	50000	1199	1.18	239700
$t\bar{t}$	80070	1.203	9984443	252890	0.105	37909974
WZ	11485	1.00	999896	9757*0.274	1.06	5998980
$ZZ^* \to 4\mu$	46.6	1.00	100000	69.75	1.00	1081496
$ZZ^* \to 4e$	46.6	1.00	100000	69.75	1.00	1081496
$ZZ^* \to 2e2\mu$	99.1	1.00	199900.	145.37	1.00	1599696
$gg \to ZZ^* \to 4\mu$	0.43	1.00	65000	0.6725	1.00	90000
$gg \to ZZ^* \to 4e$	0.43	1.00	65000	0.6725	1.00	90000
$gg \to ZZ^* \to 2e2\mu$	0.86	1.00	65000	1.345	1.00	90000

5.4 Leptons Definition

Leptons identification and reconstruction are of particular importance for the $H \rightarrow ZZ^{(*)} \rightarrow 4\ell$ channel. In this section, the algorithms are briefly described and the baseline electron/muon selection for the analysis is defined.

5.4.1 Electron reconstruction and identification

Electron candidates are required to have a well-reconstructed ID track pointing to an electromagnetic calorimeter cluster [57]. The cluster longitudinal and transverse shower profiles are required to be consistent with those expected for the electromagnetic showers. Tracks associated with electromagnetic clusters are fitted using a Gaussian-Sum Filter [58], which allows for bremsstrahlung energy losses to be taken into account.

The electron identification is based on requirements on variables that provide good separation between isolated electrons and hadronic jets faking electrons. In the central region of $|\eta| < 2.47$, variables describing the longitudinal and transverse shapes of the electromagnetic showers in the calorimeters, the properties of the tracks in the inner detector, e.g. number of b-layer and silicon hits, signal in the TRT, or change in the momentum from the beginning to the end of the track from bremsstrahlung, as well as the matching between tracks and energy clusters are used to discriminate against the different background sources.

5.4.1.1 Electron Identification and Reconstruction in the 2011

For the 2011 dataset, the identification criteria for central-electron candidates are implemented based on rectangular cuts on the calorimeter, tracking, as well as on combined track-cluster variables [59]. These requirements are optimized in 10 detector-motivated cluster-η bins and 11 E_T bins (from 5 to 80 GeV), in order to provide good separation between signal (isolated) electrons and background from hadrons faking electrons, non-isolated electrons (e.g. from semi-leptonic decays of heavy-flavors quarks), and electrons from photon conversions.

For the 2011 analysis the selection criteria are designed for general physics-analysis use and the menu is called "loose++". It corresponds to an intermediate menu between the loose and medium working points. Shower shape variables in both the first and the second layers of the EM calorimeter are used and cuts are applied on the fraction of the energy deposited in the hadronic and the electromagnetic calorimeters. Requirements on the quality of the electron track and track-cluster matching are also applied.

5.4.1.2 Electron Identification and Reconstruction in the 2012

For the 2012 dataset a multivariate analysis (MVA) technique [60] is employed to define the electron identification, since it allows for simultaneous evaluation of several properties when making a selection decision [59]. Out of the different MVA techniques, the maximum Likelihood (LH) approach has been chosen for the electron identification because of its simple construction.

The electron LH makes use of signal and background probability density functions (PDFs) of the discriminating variables. Based on these PDFs, an overall probability is calculated for the object to be signal or background-like. The signal and background probabilities for a given electron are combined into a discriminant on which a cut is applied:

$$d_{\mathcal{L}} = \frac{\mathcal{L}_S}{\mathcal{L}_S + \mathcal{L}_B}, \qquad \mathcal{L}_S(\vec{x}) = \prod_{i=1}^{n} P_{s,i}(x_i) \tag{5.1}$$

where $\vec{x}$ is the vector of variable values and $P_{s,i}(x_i)$ is the value of the signal probability density function of the i^{th} variable evaluated at x_i. In the same way, $P_{b,i}(x_i)$ refers to the background probability function. The choice of the cut value on the discriminant determines the signal efficiency/background rejection of the Likelihood working point.

Signal and background PDFs used for the electron LH Particle Identification (PID) are obtained from data. The variables counting the hits on the track are not used as PDFs in the LH, but are left as simple cuts, since every electron should have a high quality track to allow for a robust 4-vector measurement. The LH menu cuts on the LH discriminant called Loose-LH has been chosen to define the electron identification of this analysis out of the three possible working points namely loose, medium, tight.

5.4.1.3 Electrons E-p Combination

In order to improve the energy resolution of low E_T electrons and electrons in problematic regions of the electromagnetic calorimeter, such as the crack region of the EM calorimeter in $1.37 < |\eta| < 1.52$, where its response tends to be poorer, a combination of the track momentum and the cluster energy is performed [59]. Specifically, the combination is applied to electrons with $E_T < 30$ GeV and $\eta < 1.52$, which have consistent Inner Detector and cluster energy measurements, as judged by the ratio:

$$\text{Significance}\ (\mathrm{E_{Cluster}} - \mathrm{p_{Track}}) = \frac{|\mathrm{E_T^{Cluster}} - \mathrm{E_T^{Track}}|}{\sqrt{\sigma^2_{\mathrm{E_T^{Cluster}}} + \sigma^2_{\mathrm{E_T^{Track}}}}} < 5. \tag{5.2}$$

The combination method employs a maximum likelihood fit of E_T^{Track} and $E_T^{Cluster}$, using probability density functions (PDFs) which are generated by fitting the E_T^{Track}/E_T^{Truth} and $E_T^{Cluster}/E_T^{Truth}$ distributions with a Crystal Ball in order to take into account both

Table 5.4: Electron selection criteria for 2011 and 2012 analysis.

Electron Selection	
Menu	Loose++ (2011), Loose-LH (2012)
Kinematics	$E_T > 7$ GeV
$\|\eta\|$ Region	< 2.47
Improved Resolution	E-p Combination

the Gaussian core resolution and the tails of the distributions. The events used to build the PDFs come from single $e^{\pm}$ Monte Carlo samples with flat E_T spectra on $7 < E_T < 80$ GeV, with all constituent electrons required to have Significance $(\mathrm{E_{Cluster}} - \mathrm{E_{Track}}) < 5$.

Electrons are placed into categories according to their E_T and $|\eta|$ along with their approximate bremsstrahlung loss (quantified as $|\Delta E_{Track}|/E_{Track}$ between the momentum at the perigee and the momentum at the last track measurement), with separate distributions of $\mathcal{F}_1(\frac{E_T^{Track}}{x})$ and $\mathcal{F}_2(\frac{E_T^{Cluster}}{x})$ for each category, where $x = (E_T^{Track} + E_T^{Cluster})/2$. The product:

$$-\,log\left[\mathcal{F}_1(\frac{E_T^{Track}}{x}) \cdot \mathcal{F}_2(\frac{E_T^{Cluster}}{x})\right] \tag{5.3}$$

is minimized with respect to the variable x, yielding the combined transverse momentum for a given electron, as well as its error. Any electrons which do not meet the requirements on E_T, $|\eta|$, and significance$(\mathrm{E_{Cluster}} - \mathrm{E_{Track}})$ instead have their four momenta built using the default cluster energy and the track direction.

The likelihood combination method shows the greatest potential for improvement in cases of low E_T electrons, and electrons in the central $|\eta|$ region of the detector. For electrons in the forward region ($1.37 < |\eta| < 2.5$), or those with high E_T the cluster-based transverse momentum is used. For the $H \to ZZ^{(*)} \to 4\ell$ case the improvement of the E-p combination is seen in the $4e$ and $2\mu 2e$ channels and corresponds to an approximate reduction of 4% and 3.5% respectively in the width of the $m_{4\ell}$ distribution.

The electron criteria are summarized in Table 5.4 for both 2011 and 2012 analysis selection.

5.4.2 Muon Identification and Reconstruction

In the ATLAS four kind of muon candidates are distinguished depending on the way they are reconstructed: *standalone muons, combined muons, segment tagged muons,* and *calorimeter tagged muons* [61].

- *Standalone muons* (SA): This reconstruction is based entirely on the muon spectrometer information, independently of the inner detector. It is initiated locally in a muon chamber by a search for straight line track segments in the bending plane. A minimum of two track segments in different muon stations are combined to form a muon track candidate using three - dimensional tracking in the magnetic field. The track parameters are obtained from the muon spectrometer track fit and are extrapolated to the interaction point taking into account both multiple scattering and energy loss in the calorimeters. These muons are used in the $|\eta| > 2.5$ region outside the ID coverage, to increase the overall analysis acceptance.

- *Combined muons* (CB): The trajectory measured by the ID is associated with a previously defined Standalone muon, by performing a χ^2-test, defined by the difference between the respective track parameters weighted by their combined covariance matrices. The parameters are evaluated at the point of the closest approach to the beam axis. The track parameters are derived from a χ^2 fit on the two tracks or the refit of the ID and MS hits associated with the track.

- *Segment tagged muons* (ST): A track in the ID is identified as a muon if the trajectory extrapolated to the MS can be associated with track segments in the precision muon chambers. If a segment is sufficiently close to the predicted track position, then the inner detector track is tagged as corresponding to a muon. ST muons adopt the measured parameters of the associated ID track.

- *Calorimeter tagged muons* (Calo Muons): A trajectory in the ID is identified as a muon if the associated energy depositions in the calorimeters are compatible with the hypothesis of a minimum ionizing particle. Their use in the analysis is to cover the region of $|\eta| < 0.1$, which is not equipped with muon chambers, and only if $p_T > 15$ GeV, since the calorimeter muon identification algorithm is optimized for muons with $p_T > 15$ GeV. The material thickness traversed by the muons is over 100 radiation lengths (X_0), as presented in Figure 5.2. By passing through this material, muons undergo electromagnetic interactions which result in a partial loss of their energy. Since over 80% of this material is in the instrumented areas of the calorimeters, the energy loss can be measured.

In the first years of the LHC operation, ATLAS used two reconstruction algorithms [63], the STACO and MUID, as already discussed in Section 4.9, following different pattern recognition strategies. In this analysis the STACO algorithm is used. Between the years of 2011 and 2012 data taking, the changes in the muon reconstruction do not concern the algorithmic part of the STACO but were a mixture of software and hardware updates, the list of which is given below:

Figure 5.2: Material distribution before the Muon Spectrometer in ATLAS as a function of η. The material is expressed in radiation lengths (X_0) [62].

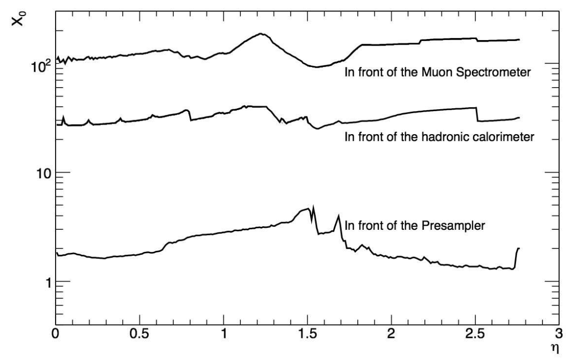

- *Inclusion of EE chambers*: During the Christmas shutdown of 2011, the staged Extended EndCap chambers in the η region between 1.1 and 1.3 namely the *EE* chambers have been installed and commissioned. More specifically the totality of the *EE* chambers in side C and 3 out of 16 sectors in side A have been installed, resulting in an improved reconstruction efficiency in the transition region between the barrel and the EndCap ($\eta \approx -1.2$), as they allow for a three-point momentum measurement in this region.

- *Improved reconstruction in the CSC chambers*: As already discussed in Section 4.9, the reconstruction of the Cathode Strip Chambers that equip the Muon Spectrometer in the $|\eta|$ region > 2.0 has been considerably improved as described in Chapter 4, resulting in an overall improvement of the momentum resolution in this region.

- *Inner Detector hit requirements*: The ID hit quality requirements of the muon tracks of all categories (except SA tracks) have been slightly modified. This allowed to remove some inconsistency with respect to the calorimeter muon selection, to fix a problem in the 2012 data of the Pixel sensor status not propagated to the offline reconstruction and to remove non-uniformity of the ID efficiency as a function of η.

- *ID, MS alignment improvement*: Improved alignment constants were provided during the 2012 reprocessing for both the ID and the MS system.

The list of the ID hit requirements that the combined, segment tagged and calo muons are required to fulfill is given in Table 5.5. The standalone muons do not have an ID track, consequently there are no ID requirements, but they are required

Table 5.5: List of the Inner Detector hit requirements for combined, segment tagged and calo muons for the 2011 and 2012 datasets.

ID Hit Requirements 2011	
ID Si hit requirement	Expect B-layer hit = false or Number of B-layer hits ≥ 1
	No. of Pixel hits + No. of crossed inactive Pixel sensors > 1
	No. of SCT hits + No. of crossed inactive SCT sensors > 5
	No. of Pixel holes + No. of SCT holes < 3
TRT hit requirements: $\lvert\eta\rvert < 1.9$	Hits + Outliers > 5 & $Outliers < 0.9(Hits + outliers)$
TRT hit requirements: $\lvert\eta\rvert \geq 1.9$	if (Hits + Outliers > 5): $Outliers < 0.9(Hits + outliers)$
ID Hit requirements 2012	
ID Si hit requirement	No. of Pixel hits + No. of crossed inactive Pixel sensors > 0
	No. of SCT hits + No. of crossed inactive SCT sensors > 4
	No. of Pixel holes + No. of SCT holes < 3
TRT hit requirements: $0.1 < \lvert\eta\rvert \leq 1.9$	Hits + Outliers > 5 & $Outliers < 0.9(Hits + outliers)$

Table 5.6: Muon selection Criteria in both 2011 and 2012.

2011 and 2012 Muon Selection	
ID cuts	as in Table 5.5
	CB,ST $p_T > 6$ GeV, $\lvert\eta\rvert < 2.7$
Kinematics	Calo Muons $p_T > 15$ GeV, $\lvert\eta\rvert < 0.1$
	SA $p_T > 6$ GeV, $2.5 < \lvert\eta\rvert < 2.7$
Overlap	Reject Calo if $DR_{Calo-STACO} < 0.1$
Removal	Reject SA if $DR_{SA-ST} < 0.1$
Allow maximum one Calo muon or SA	

to be identified by all three available muon stations. The muons selection criteria are summarized in Table 5.6.

5.5 Trigger

The trigger signatures for the online selection of four-lepton events are single and di-lepton triggers. Due to the higher instantaneous luminosity and pile-up levels of the 2012 data-taking, both single- and di-lepton trigger thresholds have been raised, and isolation cuts have been introduced for single lepton triggers. A summary of the triggers that are used in the 2011 analysis is shown in Table 5.7 and the corresponding 2012 triggers are shown in Table 5.8. The "i" in the name denotes that the trigger item is required to be isolated. The isolation cut is applied at the Event Filter level only and requires the sum of the p_T of tracks (with $p_T > 1$ GeV) in a cone of size $\Delta R < 0.2$ around the lepton track, to be less than 10% of the lepton p_T. The same trigger criteria applied also on MC to achieve the same level of efficiency with the data.

In the four-lepton event selection it is required that either one of the leptons matches the single-lepton trigger, or that two leptons match the di-lepton trigger, even though the requirement of trigger matching has a negligible impact on the total event selection efficiency.

The trigger efficiency with respect to the 2012 offline analysis requirements for a simulated Higgs signal (gluon-fusion with $m_H = 130$ GeV) is estimated to be:

- 4μ: 97.6%
- $2e2\mu/2\mu2e$: 97.3%
- $4e$: 99.7%

Table 5.7: Summary of the triggers used during the 2011 data taking. In each data taking period, the OR of single and di-lepton triggers is used to select each signature. The naming convention is explained in the text.

		Single-lepton triggers		
Period	B-I	J	K	L-M
4μ	EF_mu18_MG	EF_mu18_MG_medium	EF_mu18_MG_medium	EF_mu18_MG_medium
$4e$	EF_e20_medium	EF_e20_medium	EF_e22_medium	EF_e22vh_medium1
$2e2\mu$	4μ OR $4e$			
		Di-lepton triggers		
Period	B-I	J	K	L-M
4μ	EF_2mu10_loose	EF_2mu10_loose	EF_2mu10_loose	EF_2mu10_loose
$4e$	EF_2e12_medium	EF_2e12_medium	EF_2e12T_medium	EF_2e12Tvh_medium
$2e2\mu$	4μ OR $4e$ OR EF_e10_medium_mu6			

The trigger efficiency in data and MC is measured using tag and probe methods [64] based on $Z \rightarrow \mu^+\mu^-$ and $Z \rightarrow e^+e^-$ events. The efficiency is computed in bins of the phase space $\epsilon_i = (p_{T_i}, \eta_i, \phi_i)$ and is defined for p_T values above the trigger threshold. Differences between trigger efficiency in data and MC is accounted for re-weighting MC events according to the single-lepton efficiency computed in phase-space bins η_i of all the reconstructed leptons in the event. The trigger efficiency scale factor for the single lepton triggers is computed as:

$$SF_{trigger} = \frac{[1 - \Pi_i(1 - \epsilon(\eta_i))]_{Data}}{[1 - \Pi_i(1 - \epsilon(\eta_i))]_{MC}}. \tag{5.4}$$

No correction is applied for the dilepton triggers.

Table 5.8: Summary of the triggers used during the 2012 data taking for the four analysis channels. When multiple chains are indicated, it is intended that the OR among them is requested. The naming convention is explained in the text.

Channel	Single-lepton	Di-lepton
4e	e24vhi_medium1, e60_medium1	2e12Tvh_loose1, 2e12Tvh_loose1_L2StarB(data only)
4μ	mu24i_tight, mu36_tight	2mu13, mu18_mu8_EFFS
$2e2\mu$	4μ OR $4e$ OR e12Tvh_medium1_mu8 OR e24vhi_loose1_mu8	

5.6 Events selection

5.6.1 Analysis Events Selection

The analysis starts by pre-selecting leptons as described in Section 5.4. The standard selection of primary vertexes is used in this analysis, meaning that the vertex selected as the primary one is the vertex with the largest p_T sum in the event. Since the four leptons emerge from the primary vertex, the lepton tracks must have distances $|\Delta z_0| < 10\ mm$ from the primary vertex along the proton beam pipe. To reduce the cosmic background an additional cut on the transverse impact parameter is required ($|\Delta d_0| < 1\ mm$).

The event selection criteria (consisting of lepton quality, kinematic, isolation and impact parameter significance cuts) are presented in Table 5.9. The candidate quadruplet is formed by selecting two opposite sign, same flavor di-lepton pairs in an event. Muons are required to have $p_T > 6$ GeV and $|\eta| < 2.7$, while electrons are required to have $E_T > 7$ GeV and $|\eta| < 2.47$. In each quadruplet the p_T thresholds for the three leading leptons are 20, 15 and 10 GeV. The four leptons of the quadruplets are required to be well separated, $\Delta R = \sqrt{\Delta\eta^2 + \Delta\phi^2} > 0.10$ for same flavor leptons and $\Delta R > 0.20$ for different flavor leptons.

The di-lepton of the quadruplet with a mass m_{12} closest to the nominal Z boson mass is called the leading di-lepton, while the second di-lepton of the quadruplet with a mass m_{34} is the sub-leading one. For each event there is a mass window requirement applied to the invariant mass of each of the two di-leptons. The cut values are chosen event-by-event using the reconstructed four-leptons invariant mass, resulting in a single mass spectrum for each background regardless of the hypothesized Higgs mass. m_{12} is required to be between 50 and 106 GeV, m_{34} is required to exceed a threshold, $m_{threshold}$, which varies as a function of the four-leptons invariant mass, $m_{4\ell}$, and it should always be below 115 GeV. The value of $m_{threshold}$ is 12 GeV for $m_{4\ell} < 140$ GeV, rises linearly to 50 GeV with $m_{4\ell}$ in the interval $m_{4\ell} \in [140\text{ GeV}, 190\text{ GeV}]$ and stays at 50 GeV for $m_{4\ell} > 190$ GeV. Table 5.10 summarizes the m_{34} cut values. In the case that more than one quadruplet survive the kinematic selection, the one with m_{12} closest the m_Z mass is retained, if multiple quadruplets have the same m_{12} the one with the highest m_{34} is

Table 5.9: Summary of the $H \to ZZ^{(*)} \to 4\ell$ candidate selection requirements. The two lepton pairs are denoted as m_{12} and m_{34}. The choice of the threshold value $m_{threshold}$ for m_{34} can be found in Table 5.10.

Kinematic Selection	Require at least one quadruplet of leptons consisting of two pairs of same-flavor (SF) opposite-charge (OS) leptons fulfilling the following requirements: p_T thresholds for three leading leptons in the quadruplet 20, 15 and 10 GeV Select best quadruplet to be the one with the leading dilepton mass being the one closer to the Z mass and the second mass closer to the Z one, to be the subleading one. Leading di-lepton mass requirement 50 GeV $< m_{12} <$ 106 GeV Sub-leading di-lepton mass requirement $m_{threshold} < m_{34} <$ 115 GeV Remove quadruplet if alternative same-flavor opposite-charge di-lepton gives $m_{\ell\ell} <$ 5 GeV $\Delta R(\ell, \ell') > 0.10(0.20)$ for all same (different) flavor leptons in the quadruplet.
Isolation	Isolation cut applied on all leptons of the quadruplet Contribution from the other leptons of the quadruplet is subtracted Lepton track isolation ($\Delta R = 0.20$): $\Sigma p_T / p_T < 0.15$ Electron calorimeter isolation ($\Delta R = 0.20$) : $\Sigma E_T / E_T < 0.20$ Muon calorimeter isolation ($\Delta R = 0.20$) : $\Sigma E_T / E_T < 0.30$ Standalone muons calorimeter isolation ($\Delta R = 0.20$) : $\Sigma E_T / E_T < 0.15$
Impact Parameter Significance	Apply impact parameter significance cut to all leptons of the quadruplet. For electrons : $d_0/\sigma_{d_0} < 6.5$ For muons : $d_0/\sigma_{d_0} < 3.5$

Table 5.10: The m_{34} mass cut depends on the $m_{4\ell}$ value. For the intermediate values the cuts increase linearly.

$m_{4\ell}$ GeV	< 140	140	190	> 190
m_{34} cut GeV	12	12	50	50

selected.

The normalized track isolation discriminant is defined as the sum of the transverse momenta of tracks, Σp_T, inside a cone of $\Delta R < 0.2$ around the lepton, excluding the lepton track, divided by the lepton p_T. The tracks are considered in the sum are of good quality; i.e. they have at least four hits in the pixel and silicon strip detectors ("silicon hits") and $p_T > 1$ GeV for muons, and at least nine silicon hits, one hit in the innermost pixel layer (the b-layer) and $p_T > 0.4$ GeV for electrons. Each lepton is required to have normalized track isolation smaller than 0.15.

The normalized calorimetric isolation discriminant for muons is defined as the sum of the calorimeter cells, ΣE_T, inside an isolation cone of 0.20 around the muon, after having subtracted the muon ionization energy which is calculated as the sum of cells in a much smaller cone around the muon, divided by the muon p_T. In the case of electrons, the normalized calorimetric isolation is computed as the sum of the topological cluster transverse energies inside a cone of 0.2 around the electron cluster divided by the electron E_T, the cells corresponding to the core of the electron cluster are excluded from the sum. Muons are required to have a normalized calorimetric isolation of less than 0.30, while for electrons the corresponding value is 0.20. For both the track- and calorimeter-based isolation any contributions arising from other leptons of the quadruplet are subtracted. For the track isolation the contribution from any other lepton in the quadruplet within $\Delta R < 0.2$ is subtracted. For the calorimetric isolation, the contribution of any electron in the quadruplet within $\Delta R < 0.18$ is subtracted. The impact parameter significance, d_0/σ_{d0}, is required to be lower than 3.5 for muons and 6.5 for electrons. The electron impact parameter is affected by bremsstrahlung and is thus broader. The final discrimination variable is the mass of the leptons quadruplet.

5.6.2 FSR recovery

$H \to ZZ^{(*)} \to 4\ell$ decays include low E_T photon Final State Radiation (FSR) [65]. The QED process of radiative photon production in Z decays is well modeled by the MC. Some of the FSR photons can be identified in the detector as incorporated directly into the four lepton measurement. This can recover events which have their reconstructed four lepton mass moved out of the signal region.

FSR recovery is allowed only for one photon per event and can be added to the leading Z for $m_{4\ell} < 190$ GeV or any of the two Zs above this threshold. The candidate FSR photons, nominally calibrated, in case they are collinear within a cone of $\Delta R < 0.05$ around a muon, 400 MeV of energy is removed from the photon measured energy to account for the average contribution from muon ionization. Collinear FSR search is performed only for muons. The photon candidates are obtained from any of the two different objects:

- 3×5 clusters seeded by clusters satisfying the requirements:
  - cluster transverse energy between 1.5 GeV $< E_T <$ 3.5 GeV,
  - the cone between the cluster and the muon $\Delta R_{\text{cluster},\mu} = \sqrt{\Delta\eta^2 + \Delta\phi^2} < 0.08$,
  - the fraction of the cluster energy deposited in the front sampling of the calorimeter over the total energy $(f_1) > 0.2$.
- Standard photons or electrons satisfying the requirements:
  - cluster transverse energy $E_T > 3.5$ GeV

– the cone between the cluster and the muon $\Delta R_{\text{cluster},\mu} = \sqrt{\Delta\eta^2 + \Delta\phi^2} < 0.15$,

– the fraction of the cluster energy deposited in the front sampling of the calorimeter over the total energy $(f_1) > 0.1$.

If more than one cluster are found in the cone, then the one with the highest E_T is selected. The cut on the fraction f_1 is effective only in low energies ($E_T < 15$ GeV) where a large fraction of the EM energy is deposited in the front sampling and helps in discriminating against background induced by the muon itself via ionization at energies where the muon energy loss Landau tail is still significant (i.e. cluster energies up to 3 GeV).

The non collinear search is performed for both electrons and muons. Candidates are required to satisfy the following requirements :

- the FSR photon candidate to pass the tight identification criteria,
- the cone between the cluster and the lepton $\Delta R_{\text{cluster},\ell} = \sqrt{\Delta\eta^2 + \Delta\phi^2} > 0.15$,
- the transverse energy of the cluster $E_T > 10$ GeV,
- the FSR photon candidate to be isolated $E_T^{cone40} < 4$ GeV

In this analysis the FSR photon addition is applied on the events that pass all selections. FSR photons are searched for all lepton candidates of the final quadruplet but at maximum one FSR photon candidate is added to the 4ℓ system. The FSR correction is applied only to the on-shell Z. Priority is given to collinear photons associated to the leading $Z \to \mu^+\mu^-$. The correction is applied if $66 < m_{\mu\mu} < 89$ GeV and the $m_{\mu\mu\gamma} < 100$ GeV. In the case the collinear search has failed then the non collinear FSR photon with the highest E_T, if found, is added provided it satisfies the following requirements:

- $m_{4\ell} \leq 190$ GeV, $m_{ll} < 81$ GeV and $m_{ll\gamma} < 100$ GeV $\to$ the on-shell Z is corrected
- $m_{4\ell} > 190$ GeV, $m_{ll} < 81$ GeV and $m_{ll\gamma} < 100$ GeV $\to$ the pair with the $m_{ll\gamma}$ closest to the Z pole is corrected since both Zs are on shell.

The lower cut on E_T reduces the hadronic background (mainly due to π^0 decays), whereas the upper cut on the M_{ll} is applied in both cases in order to reduce the Initial State Radiation (ISR), the π^0 and muon ionization backgrounds for a very small loss of efficiency of a few percent. FSR photons correspond to events with m_{ll} below the Z pole mass while the ISR photons, π^0's and muon ionization clusters do not.

The effect of the FSR recovery in $Z \to \mu^+\mu^-$ events recovers 70% of the collinear FSR photons, whereas the non-collinear FSR selection has an efficiency of $\approx 60\%$ and a purity of $\geq 95\%$ [65]. Similarly, the addition of FSR in $Z \to e^+e^-$ significantly improves the tails and the bulk of the mass resolution.

5.6.3 Z Mass Constraint

In the $H \to ZZ^{(*)} \to 4\ell$, the first lepton pair is predominately produced in a decay of an on-shell Z boson and hence allows for the improvement of the di-lepton mass resolution exploiting the Z line shape given the knowledge of the lepton momentum measurement uncertainties. The probability of observing a Z boson having a true mass m_{12}^{true} and decaying to two leptons with true 4-momenta, $\mathbf{p}_{1,2}^{true}$, while measuring the 4-momenta $\mathbf{p}_{1,2}^{rec}$ is given by the product:

$$L(\mathbf{p}_1^{true}, \mathbf{p}_2^{true}, \mathbf{p}_1^{rec}, \mathbf{p}_2^{rec}) = B(\mathbf{p}_1^{true}, \mathbf{p}_2^{true}) \cdot R_1(\mathbf{p}_1^{true}, \mathbf{p}_1^{rec}) \cdot R_2(\mathbf{p}_2^{true}, \mathbf{p}_2^{rec}), \quad (5.5)$$

where B is the probability density function (PDF) of the Z line shape at generator level and the PDFs $R_{1,2}$ of the energy or momentum response functions for the two leading leptons.

The m_{12}^{true}, in the case that the lepton energies are much higher than the lepton mass, is given by:

$$\left(m_{12}^{true}\right)^2 = 2 \cdot E_1^{true} E_2^{true} \left(1 - \cos\theta\right) \quad (5.6)$$

where $E_{1,2}^{true}$ denotes the true lepton energies and θ the opening angle between the two decay leptons depending on the true lepton angles $\eta_{1,2}^{true}$ and $\phi_{1,2}^{true}$. The lepton angles are measured very precisely such that the values $\eta_{1,2}^{rec}$ and $\phi_{1,2}^{rec}$ effectively correspond to $\eta_{1,2}^{true}$ and $\phi_{1,2}^{true}$, respectively. Therefore, the lepton response functions are essentially PDFs of the true energies for certain measurement of the lepton 4-momenta:

$$R_{1,2}(\mathbf{p}_{1,2}^{true}, \mathbf{p}_{1,2}^{rec}) = R_{1,2}(E_{1,2}^{true} \,|\, \mathbf{p}_{1,2}^{rec}). \quad (5.7)$$

In summary, the only uncertainty comes from the measured lepton energies, $E_{1,2}^{true}$.

The likelihood (L), defined in Equation 5.5, is maximized for a given event over the true lepton energies, to give the maximum likely 4-momenta, $\mathbf{p}_{1,2}^{ml}$. B is modeled with a relativistic Breit-Wigner function, $\mathcal{F}_{\mathrm{BW}}(m_{12}^{true} \,|\, m_Z, \Gamma_Z)$, with mean and width parameters set to the Z boson mass (m_Z) and natural width (Γ_Z) respectively. Furthermore, the single lepton response functions are approximated by a Gaussian distribution, $\mathcal{F}_{\mathrm{G}}(E_{1,2}^{true} \,|\, E_{1,2}, \sigma_{1,2})$, with mean set to the measured lepton energies ($E_{1,2}$) and variance ($\sigma_{1,2}^2$, lepton momentum resolution squared obtained from simulation).

The improvement for all channels from the Z mass constrained fit is $\sim 15\%$ in the mass resolution.

5.7 Reducible Background Estimation Methods

The backgrounds in the $H \to ZZ^{(*)} \to 4\ell$ analysis are the $ZZ^{(*)}$ SM production, which has exactly the same topology as the signal and is therefore referred to as the irreducible background, and the reducible ones from $Z + jets$ (comprised of both the heavy and light flavor jets) and top quark pairs ($t\bar{t}$). The $ZZ^{(*)}$ background has good quality and isolated leptons in the final state. Its normalization and shape is fine-tuned from the data fit in the low mass region where the single Z resonant appears and the high mass region formed by the spectrum of the two on-shell Zs. For the estimation of the reducible background processes, which originate from fake or non-isolated leptons, data-driven methods using control regions are used. The WZ production contribution is also taken into account as it is predicted from the MC.

The background methods are divided into two subcategories, the so called "muons" and "electrons" backgrounds. The final states of $Z + \mu\mu$ and $Z + ee$ are strongly dependent on the muons and electrons, that form the secondary pair since the on-shell Z is a clean signature, and therefore are studied separately. $Z + \mu\mu$ states accept significant contribution from $Zb\bar{b}$ mostly and smaller contributions come from $t\bar{t}$ and $Zlight$, whereas the dominant background in the $Z + ee$ are Z bosons accompanied by jets misidentified as electrons.

The following section describes the data-driven reducible background estimation concept, primarily focused on the muons background. The general procedure is as follows:

- The background composition and shapes are studied in special control regions (CR) constructed by relaxing or inverting selection and/or lepton identification requirements on the secondary pair only. The selection of the leading pair follows the nominal Higgs selection, described in Section 5.6. The higher statistics in the control regions, enriched in the reducible background, permit several distributions to be compared between data and simulation.

- An unbinned simultaneous fit is performed on the control regions for the extraction of the reducible background, which treats the backgrounds globally and allows the minimization of the statistical uncertainty.

- The expected background in the signal region (SR) is computed by extrapolating the background from the control region using the so-called transfer factors. These factors are determined from the per event efficiency of a given background in a control region with respect to the signal region from the MC.

5.8 Background Discrimination Variables

In order to reduce $Z + jets$ and $t\bar{t}$ below a safety level, isolation and impact parameter criteria are used, as described in Section 5.6. These criteria are also called additional lepton selection [62]. In this section they are extensively discussed since

Figure 5.3: (a) Track - based and (b) calorimeter-based isolation distributions in cone $\Delta R = 0.3$ for muons originating from Higgs decays and jets ($m_H = 120$ GeV). The isolation cuts at low values of the relative isolation variable suppress the background. The cut values are chosen to be < 0.15 and < 0.30 for the relative track- and calorimeter-based isolation respectively.

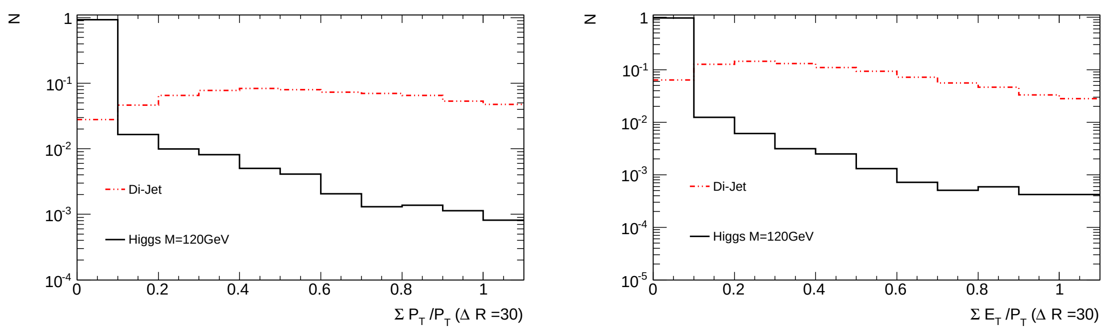

(a) (b)

they are essential for measuring the background. Focus is given on muons since the presented background method is applied to the 4μ and $2e2\mu$ final states.

5.8.1 Isolation

Muons that originate from light quark jets, from $Z + light\ Jets$ decays, populate in general the low p_T spectrum and are characterized by relatively large difference between the transverse momenta measured in the inner detector and the muon spectrometer. Consequently, such muons are not isolated. Muons coming from either heavy hadrons or fakes are expected to be in jet environment and therefore they tent not to be isolated. As opposed to these, the prompt muons from W or Z boson decays have on average just the opposite properties except that they originate from the interaction point.

The imposal of calorimetric and track isolation, especially on muons, reduces drastically the reducible backgrounds, including the "fake" muons of the $Z + jets$ background. As an example the distributions of the isolation variables used in this analysis for muons originating from Higgs decays as well as muons originating from jets are shown in Figure 5.3. The isolation distributions of $H \to ZZ^{(*)} \to 4\ell$ ($m_H = 120$ GeV) and a dijet sample are presented. It can be observed that the signal peaks at zero whereas the backgrounds extends to higher values.

Figure 5.4: $d_0/\sigma d_0$ significance distribution of muons from Higgs decays and muons from jets. The application of this cut (specifically $-3.5 < d_0/\sigma d_0 < 3.5$) leads to background rejection.

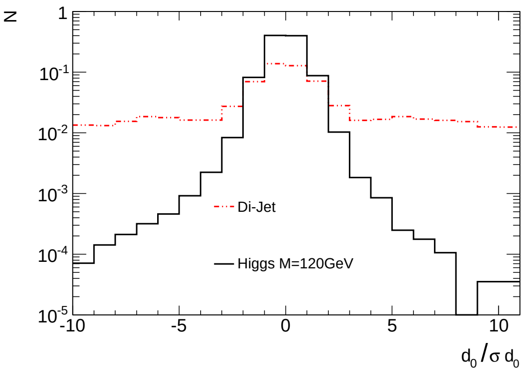

5.8.2 Impact Parameter Significance

Due to the appreciable life time of the b–hadrons, some of the leptons from the $Zb\bar{b}$ and $t\bar{t}$ processes are expected to originate from displaced vertexes, which can be used for further rejection of the reducible backgrounds. The impact parameter significance, defined as the impact parameter of the lepton normalized to its measurement error, is required not to exceed 3.5 for muons. In Figure 5.4, where the distributions of a $H \to ZZ^{(*)} \to 4\ell$ ($m_H = 120$ GeV) and a dijet sample are presented, it is visible how this requirement rejects the background [62].

5.9 Muon Efficiencies in Background Environments

From the previous Section 5.8 it is clear that the additional lepton selection plays an important role on the discrimination of the Higgs and $ZZ^{(*)}$ candidates against the reducible background. This section presents the efficiency extraction of background-like muons, performed in a control region (CR) which allows quantitative comparisons for the additional muons in the $Z + \mu$ final state. Table 5.11 summarizes the selection, which includes a Z candidate decaying either to muons or electrons, isolated and passing impact parameter criteria, with p_T thresholds of 20 and 15 GeV and the mass window is strictly set within 15 GeV from the nominal Z mass. The muon accompanying the Z is required to pass only the muon pre-selection criteria.

Figure 5.5 presents the muon additional selection variables and the p_T spectrum after the selection of Table 5.11 for the 2011 and Figure 5.6 for the 2012 data. For combined muons, Figure 5.7 shows the difference of the transverse momentum as measured in the

Table 5.11: Summary of the $Z + \mu$ selection for the study of the muon additional selection (isolation and impact parameter significance) efficiencies.

Z Candidate Selection	
Leptons	e or μ
p_T Thresholds	20, 15 GeV
Mass Cut	$\lvert m_{\ell\ell} - m_Z \rvert < 15$ GeV
Additional Selection	Imposed
Overlap Removal	$DR > 0.1$
Additional Muon	
Overlap Removal	$DR > 0.1$ Same Flavor (SF), $DR > 0.2$ Opposite Flavor (OF)
J/Ψ Veto	$m_{\mu^+\mu^-} > 5$ GeV

inner detector and the muon spectrometer. The structure at high $(p_{T_{ID}} - p_{T_{MS}})/p_{T_{ID}}$ from fake leptons (i.e. muons from π and K decays) is well described by the simulation.

The $Z + \mu$ efficiencies after the additional selection cuts, separately and combined for the two possible Z decays, are presented in Table 5.12. As expected, no difference is observed between the $Z \rightarrow e^+e^- + \mu$ and $Z \rightarrow \mu^+\mu^- + \mu$ channels. The overall discrepancy between data and MC is small and is attributed squared as a systematic uncertainty in the $Z + \mu\mu$ final state.

5.10 Muons Reducible Background Estimation

5.10.1 The Simultaneous Fit Concept

The muons background estimation is based on an unbinned maximum likelihood fit, which is performed simultaneously to four orthogonal control regions in order to achieve a better statistical uncertainty and global handling of the three reducible background sources, $Zb\bar{b}$, $Zlight$ and $t\bar{t}$. The fit is performed on the leading di-lepton mass (m_{12}) distribution, since it allows separation of the Z component from the $t\bar{t}$ due to the on-shell Z peak of the former, of both the 4μ and $2e2\mu$ channels.

The four CRs used for the fit are chosen to be non-overlapping to both each other and the SR. The fit aim is to estimate the background contribution in a fifth CR, which is formed by opposite sign secondary muon pairs, $Z + \mu^+\mu^-$, without isolation and impact parameter criteria on them. This control region is referred to as "OS CR" or "reference CR". The reference CR contains also the SR and that is the reason why

Figure 5.5: Properties of the muons accompanying a Z candidate before the application of the isolation and impact parameter selection using the 2011 data: (a) p_T spectrum, (b) normalized track-based isolation, (c) normalized calorimeter-based isolation and (d) $d_0/\sigma d_0$.

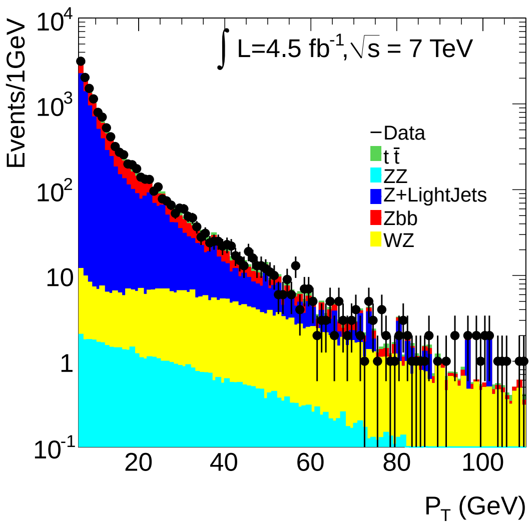

(a)

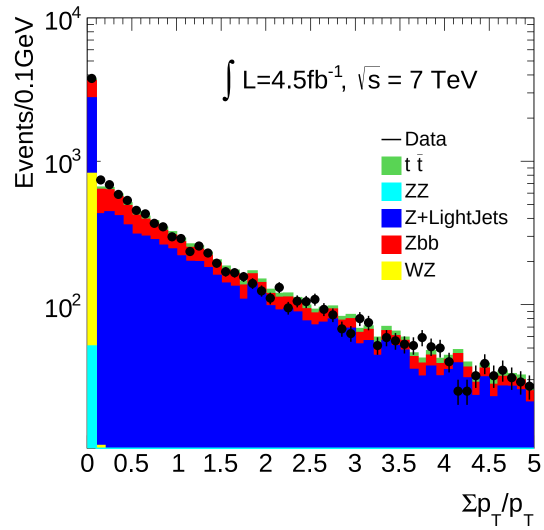

(b)

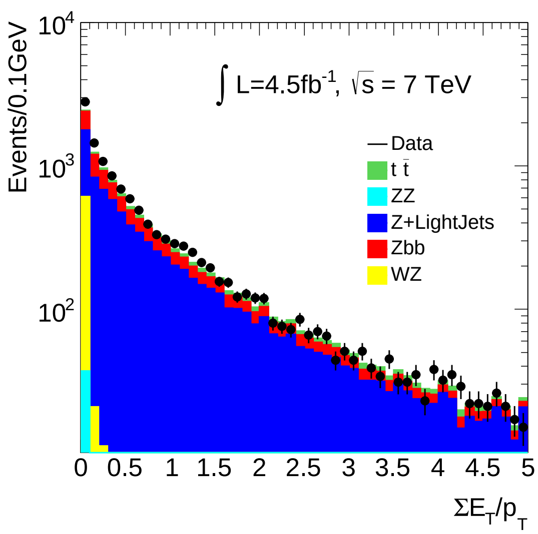

(c)

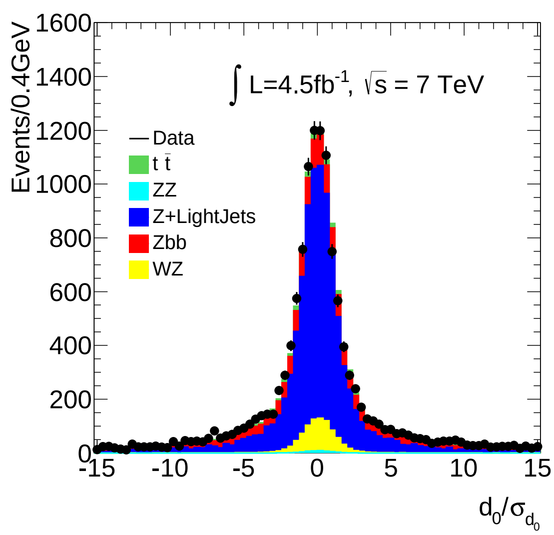

(d)

Figure 5.6: Properties of the muons accompanying a Z candidate before the application of the isolation and impact parameter selection using the 2012 data: (a) p_T spectrum, (b) normalized track-based isolation, (c) normalized calorimeter-based isolation and (d) $d_0/\sigma d_0$.

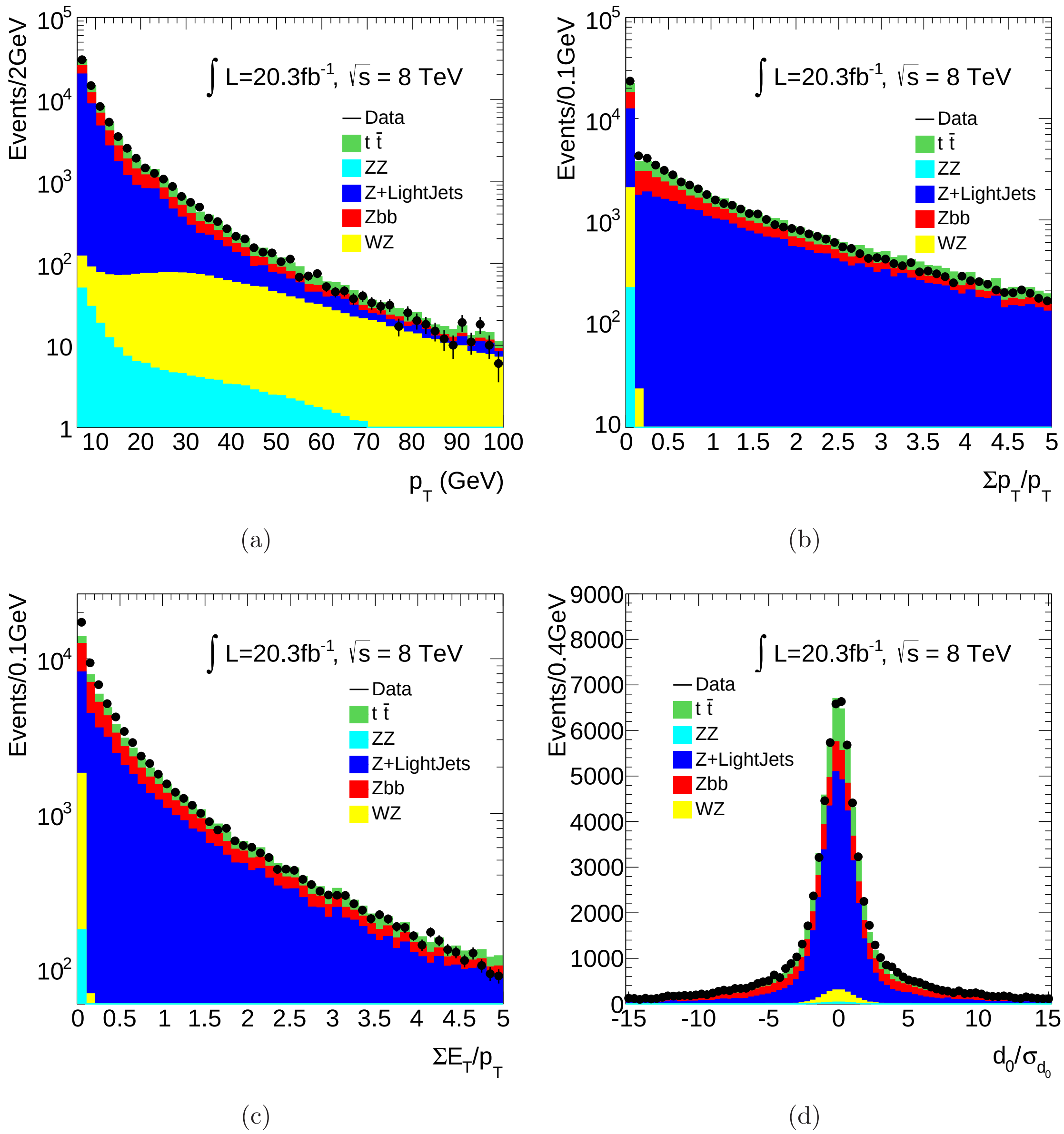

Figure 5.7: The 2011 (a) and 2012 (b) distributions of the difference between ID and MS transverse momentum estimates normalized to the ID measurement, $(p_{T_{ID}} - p_{T_{MS}})/p_{T_{ID}}$, for combined muons accompanying a $Z \to \ell^+\ell^-$ candidate. This control plot for the background estimate demonstrates that the pi/K in-flight decays are well-described by the simulation.

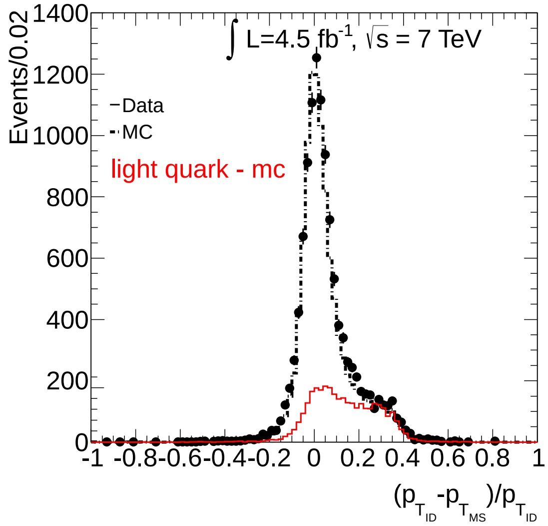

(a)

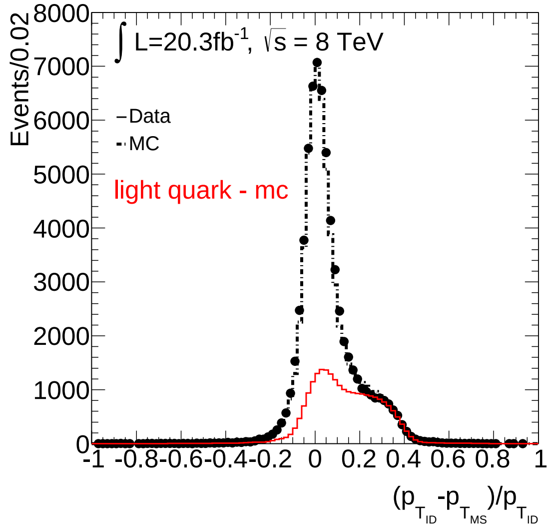

(b)

Table 5.12: 2011 and 2012 efficiencies of muons accompanying a Z candidate. The combined and separate efficiencies according to the possible Z decays are reported. As expected, no difference is observed between the $Z \to e^+e^- + \mu$ and $Z \to \mu^+\mu^- + \mu$ channels.

Selection	Data (%)	MC (%)
2011		
$Z \to \mu^+\mu^- + \mu$	20.1 ± 0.5	18.9 ± 0.4
$Z \to e^+e^- + \mu$	19.6 ± 0.5	18.0 ± 0.4
$Z \to \ell^+\ell^- + \mu$	19.6 ± 0.3	18.5 ± 0.3
2012		
$Z \to \mu^+\mu^- + \mu$	19.71 ± 0.19	19.32 ± 0.15
$Z \to e^+e^- + \mu$	19.04 ± 0.21	18.79 ± 0.17
$Z \to \ell^+\ell^- + \mu$	19.38 ± 0.14	19.07 ± 0.09

it cannot be included directly in the fit. However, indirectly is used in the model describing each CR as:

$$
\begin{aligned}
PDF_{CR} \;=\;& N_{t\bar{t}} \cdot f_{t\bar{t}} \cdot M_{t\bar{t}} && (t\bar{t}) \\
&+N_{Zb\bar{b}} \cdot f_{Zb\bar{b}} \cdot M_{Zb\bar{b}} && (Zb\bar{b}) \\
&+N_{Zlight} \cdot f_{Zlight} \cdot M_{Zlight} && (Zlight) \\
&+N_{ZZ+WZ} \cdot f_{ZZ+WZ} \cdot M_{ZZ+WZ} && (ZZ+WZ)
\end{aligned}
\tag{5.8}
$$

where:

- N_x: is the number of the $x-$background events in the OS CR,
- f_x: is the ratio of the x-background between the under study CR and the OS CR (estimated from the MC),
- M_x: is the shape model of the x-background.

It should be noted that despite the small ZZ and WZ contribution in the control regions used for the fit, due to the inverted cuts, the remaining contributions are included for accuracy in the fit unified and fixed to the values estimated from the MC.

The m_{12} shapes, included in the Equation 5.8, for the backgrounds are:

- $t\bar{t}$ background: is modeled by a 2^{nd} order Chebychev polynomial (parameters c_0, c_1)
- $Zb\bar{b}$, $Zlight$ and $WZ+ZZ$ backgrounds: are modeled by a convolution of a Crystal Ball with a Breit-Wigner (parameters μ, α, η, σ and m_Z). The same shape parameters are used for the $Zb\bar{b}$, $Zlight$ and $WZ+ZZ$ models[1], given that there is no physics motivation for them to be different, and the same shapes are considered in the different CR with only the number of events left to be estimated from the fit.

The four CR are described by one separate model each of the Form 5.8. For better handling of the uncertainties, the ratios and shape parameters are promoted to nuisance parameters with Gaussian constraints. The m_{12} data distributions are fitted with the minimization requirement. *MINOS* errors are enabled to obtain better estimation of asymmetric errors and to change the *MINUIT* verbosity level to its lowest possible value [66].

At the end, the reference CR fit estimations are extrapolated to the SR with use of transfer factors. Transfer factors are estimated from the MC and correspond to the efficiency of a reference CR event to pass the additional selection, i.e. isolation and $d_0/\sigma d_0$ criteria, and be detected in the SR.

[1]Later in this Chapter a check is performed with different parameters and the result is almost identical.

5.10.2 Fit Control Regions

The control regions used for the fit are selected such that there is no contamination from the Higgs signal and as little as possible contamination from the irreducible $ZZ^{(*)}$. Below a brief description of the four control regions is given:

(1) Inverted $d_0/\sigma d_0$ CR
The standard four-lepton analysis selection is applied on the leading dilepton, whereas the subleading dilepton pair has the impact parameter significance selection inverted for at least one lepton in the pair and no isolation selection is applied. This control region is enhanced primarily in $Zb\bar{b}$ and secondarily in $t\bar{t}$ since leptons from b-quark mesons are characterized by large d_0 significance.

(2) Inverted Isolation CR
The standard four-lepton analysis selection is applied on the leading dilepton and the subleading dilepton pair passes the standard impact parameter significance selection and at least one lepton in the pair fails the isolation selection. Relative to the previous CR, this control region aims to enhance the $Zlight$ jet component (π/K in-flight decays) over the $Zb\bar{b}$ component by requiring the impact parameter significance selection. These two background processes are described by the same model and would be consequently highly correlated.

(3) Same Sign (SS) CR
The standard four-lepton analysis selection is applied on the leading dilepton and the subleading dilepton has neither the impact parameter significance nor the isolation selection applied while the leptons are required to have same charge. This same sign control region is not dominated by a specific background; all the reducible backgrounds have a significant contribution.

(4) $e\mu + \mu\mu$ CR
This is a $t\bar{t}$ targeted CR and the decays to $e\mu + \mu\mu$ are expected to be as many as the sum of the $4\mu + 2e2\mu$. The events of this control region are opposite-charge different-flavor leading dileptons which must satisfy the standard four-lepton analysis selection. The subleading dilepton has neither the impact parameter significance nor the isolation selection applied, while both same and opposite charge leptons are accepted to increase statistics. Events with a Z boson decaying to a pair of electrons or muons are vetoed in this CR, by vetoing events where any combination of same flavor opposite sign leptons have an invariant mass in the region $50-106$ GeV.

In Figure 5.8 the m_{12} distributions of the inverted $d_0/\sigma d_0$, inverted isolation and SS CRs are presented for data and MC simulation, where MC contributions are normalized to the theoretical cross sections. A visible discrepancy is reported which leads to the need of a data-driven based estimation of the background.

Figure 5.8: The m_{12} distributions for the 2012 data and MC simulation, normalized to the theoretical cross sections, are presented for the inverted $d_0/\sigma d_0$ CR (a), inverted isolation CR (b) and the SS CR (c). An excess is observed to the data with respect to the theoretical expectations.

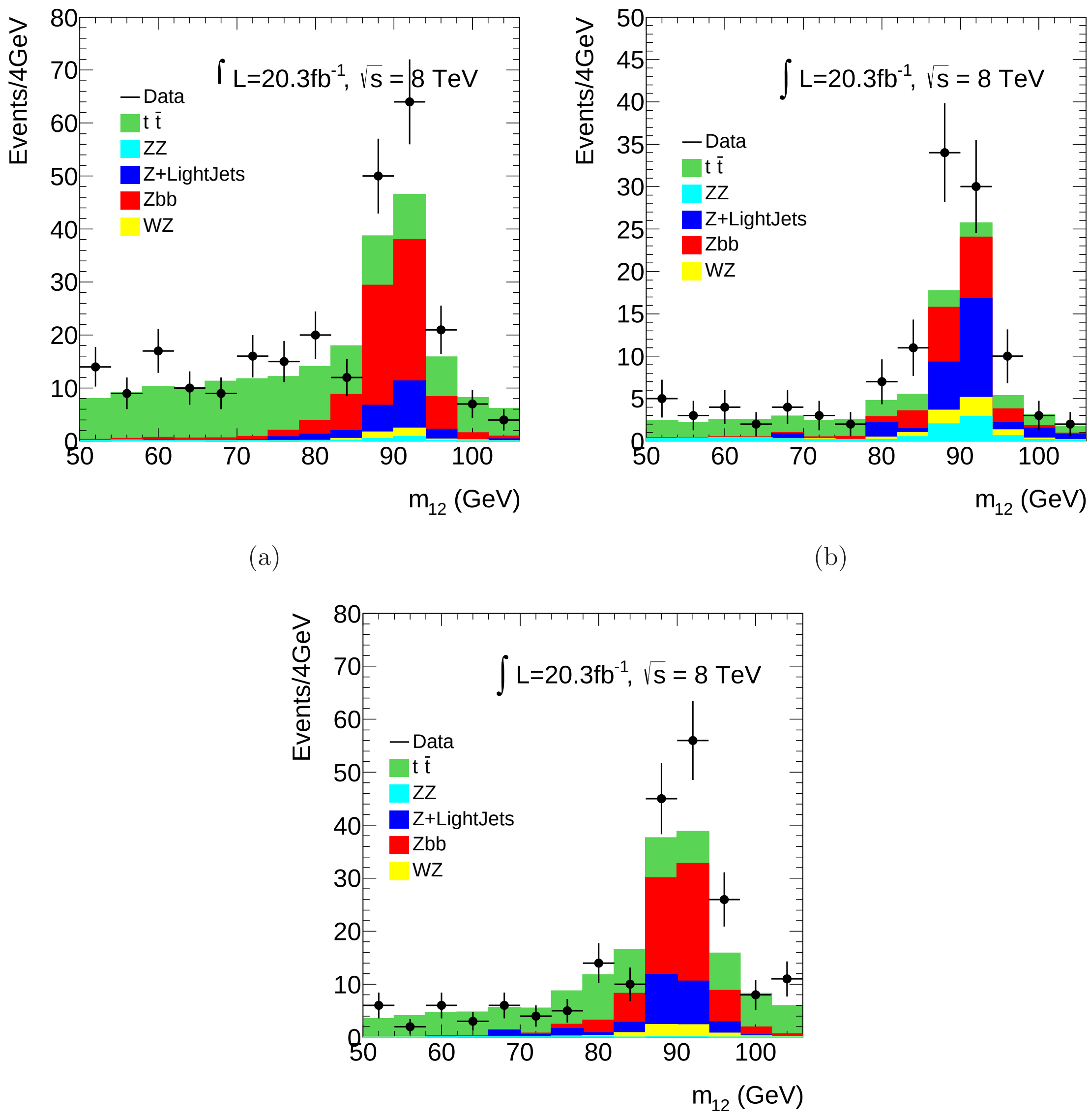

(a)

(b)

(c)

The $e\mu+\mu\mu$ CR is dominated by $t\bar{t}$ events, however a check for possible contributions from QCD is performed. The QCD CR is formed by same sign leading $e\mu$ events ($e^{\pm}\mu^{\pm}+\mu$ or $e^{\pm}\mu^{\pm}+\mu\mu$). In this CR any difference between data and the known MC ($t\bar{t}$, diboson and Z) is attributed to QCD and $W+jets$ and a "QCD factor" is estimated from the formula:

$$f_{QCD} = (Data - Known\ MC)_{e^{\pm}\mu^{\mp}+\mu}/(Data - Known\ MC)_{e^{\pm}\mu^{\pm}+\mu}. \tag{5.9}$$

The 3ℓ final state is used since it allows quantitative comparisons. In the 4ℓ final state of $e^{\pm}\mu^{\mp}+\mu\mu$, the QCD is estimated by:

$$N_{QCD}^{e^{\pm}\mu^{\mp}+\mu\mu} = f_{QCD} \times N^{e^{\pm}\mu^{\pm}+\mu\mu} \tag{5.10}$$

and the shape is considered to be the shape of the $e^{\pm}\mu^{\pm}+\mu\mu$ events. The m_{12} and m_{34} distributions of the $e^{\pm}\mu^{\mp}+\mu\mu$ CR are presented in Figure 5.9. The QCD estimated events correspond to 3.0 ± 2.1 and 2.5 ± 1.7 in the OS and SS secondary pair final states respectively. This contribution will not be taken into account for the simultaneous fit, because it is very small, the uncertainty is significant and the shape is based on the observed events.

Figure 5.9: (a) m_{12} and (b) m_{34} mass distributions of $e^{\pm}\mu^{\mp}+\mu\mu$ events, where both OS and SS secondary pairs are considered. The comparison is performed between data and $t\bar{t}$, diboson, Z MC and the measured QCD.

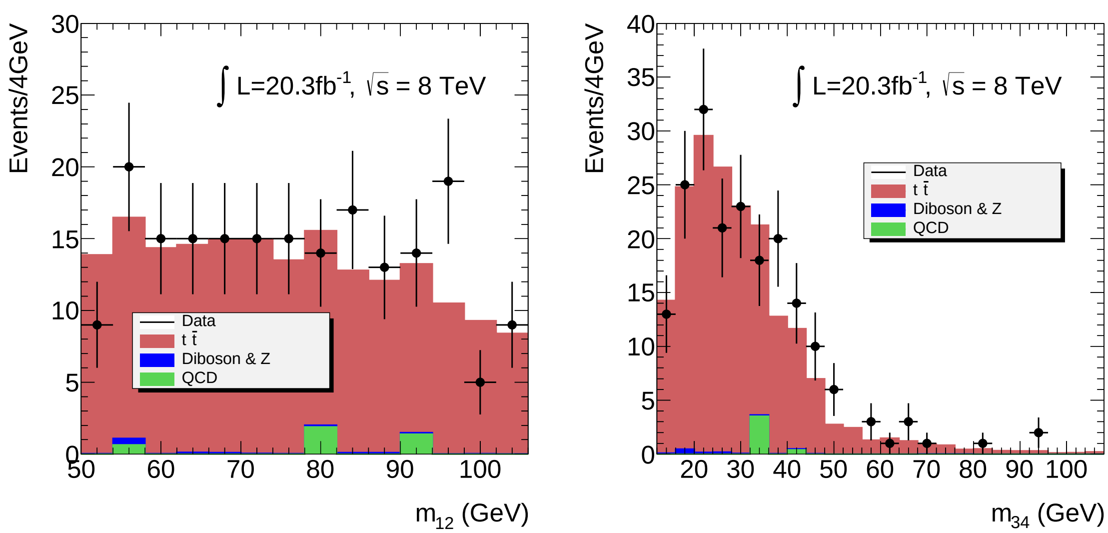

(a) (b)

For the four presented control regions, the MC contributions of the background sources normalized to the theoretical cross sections are quoted in Table 5.13. The

Table 5.13: 2012 MC estimated contributions of the reducible background sources normalized to the theoretical cross sections in the four fit CRs.

Background	$inv - d_0/\sigma d_0$ CR	$inv - iso$ CR	SS CR	$e\mu + \mu\mu$ CR
$Zb\bar{b}$	70.5 ± 0.6	19.5 ± 0.3	47.0 ± 0.7	0.4 ± 1.9
$Zlight$	20 ± 3	29 ± 3	26 ± 3	0.0 ± 1.3
$t\bar{t}$	124.6 ± 1.3	25.2 ± 0.6	80.6 ± 1.1	159.6 ± 1.6

Table 5.14: MC estimated ratios for the reducible background of the fit CR with respect to the OS CR at $\sqrt{s} = 8$ TeV, following the naming convention $f_x = CR_x/CR_{OS}$. The uncertainties correspond to the MC statistical errors. These fractions are used by the fit, as the Equation 5.8 describes, after being promoted to nuisance parameters for better handling of the uncertainties.

Background	f_{inv-d0}	$f_{inv-iso}$	f_{SS}	$f_{e\mu+\mu\mu}$
$Zb\bar{b}$	0.751 ± 0.010	0.209 ± 0.005	0.653 ± 0.012	0.0005 ± 0.0003
$Zlight$	0.44 ± 0.09	0.52 ± 0.09	0.59 ± 0.10	0.000 ± 0.003
$t\bar{t}$	0.828 ± 0.012	0.167 ± 0.004	0.539 ± 0.009	1.201 ± 0.023

relevant ratios of each background type in each CR with respect to the OS CR are presented in Table 5.14, as estimated from the simulation. The uncertainties are the MC statistical uncertainties. These fractions are used for modeling each CR after being promoted to nuisance parameters.

5.10.3 MC Closure Test

To validate the fit method, the consistency of the results and to extract the shape parameters a closure test is performed on MC events. Inputs from $Zb\bar{b}$, $Zlight$ and $t\bar{t}$[2] simulated events feed the four CR and an unbinned simultaneous fit is performed. Each control region is fitted by the model described by the Equation 5.8, since the values of the fractions reported in Table 5.14 are treated as nuisance parameters and the shape parameters are set free. The test is performed on 2012 MC since the amount of events allows more accurate quantitative comparisons.

The fitted distributions are presented in Figure 5.10 and the reducible background estimations in the OS CR are presented in Table 5.15. The results are in agreement with the expected values and hence the method is proved to work. The shape param-

[2]For the $t\bar{t}$ MC the generator MC@NLO is used.

Table 5.15: Closure test of the simultaneous fit method using MC inputs at $\sqrt{s} = 8$ TeV. The reducible background events in the OS CR as predicted from the MC and estimated from the fit shows no discrepancy. This proves the validity of the method.

Reducible Background	MC prediction	MC Fit estimation
$Zb\bar{b}$	93.5 ± 0.7	94.1 ± 0.8
Zlight	43 ± 5	43.7 ± 1.1
$t\bar{t}$	106.1 ± 1.9	107.5 ± 0.9

Table 5.16: Shape parameters for the Chebychev polynomials (c_0, c_1) and the Crystal Ball convoluted with a Breit-Wigner (μ, α, η, σ and m_Z) as estimated from the MC closure test fit. The parameters are used for the data fit with Gaussian constraints in their uncertainties.

Shape Parameter	MC fit estimated value
c_0	-0.230 ± 0.020
c_1	-0.182 ± 0.011
μ	-0.32 ± 0.22
α	1.35 ± 0.07
η	4 ± 3
σ	1.69 ± 0.28
m_Z	91.0 ± 0.3

eters estimated from the fit are presented in Table 5.16 and are used later in the data simultaneous fit with Gaussian constraints within their uncertainties.

5.10.4 2012 Data Unbinned Simultaneous Fit

Since the fit validity and consistency is proved from the MC closure test, the method can be safely applied on the data. Each control region is fitted by the model described by the Equation 5.8. As fractions, the values reported in Table 5.14 are used and the shape parameters are taken from the MC (Table 5.16). Both are promoted to nuisance parameters with Gaussian constraints in their uncertainties for better error handling.

Figure 5.11 shows the simultaneous fit PDFs as well as the separate background components for the four CRs in the data as estimated from the fit. The number of events in the reference CR are presented in Table 5.17 for both the fit results and

Figure 5.10: Closure test of the simultaneous fit method using MC inputs at $\sqrt{s}$ = 8 TeV. The data m_{12} distributions are presented after the unbinned simultaneous fit in the control regions of inverted $d_0/\sigma d_0$ (a), inverted isolation and passing $d_0/\sigma d_0$ (b), SS (c) and $e\mu + \mu\mu$ (d).

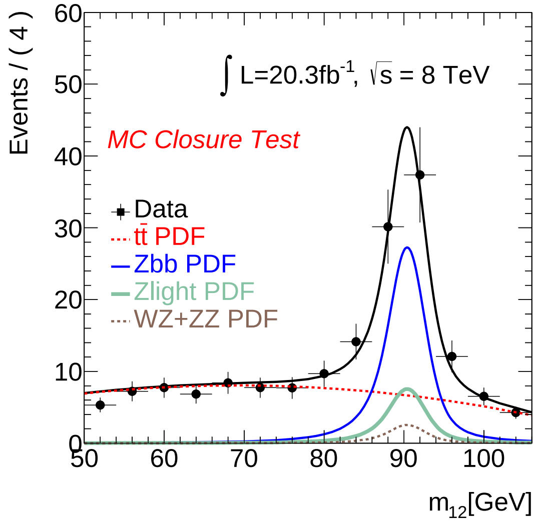

(a)

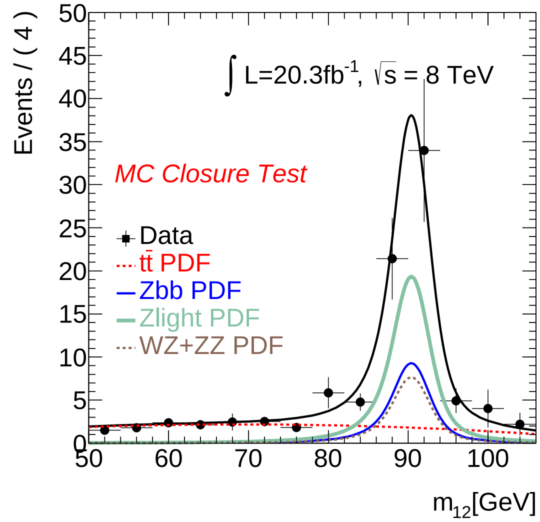

(b)

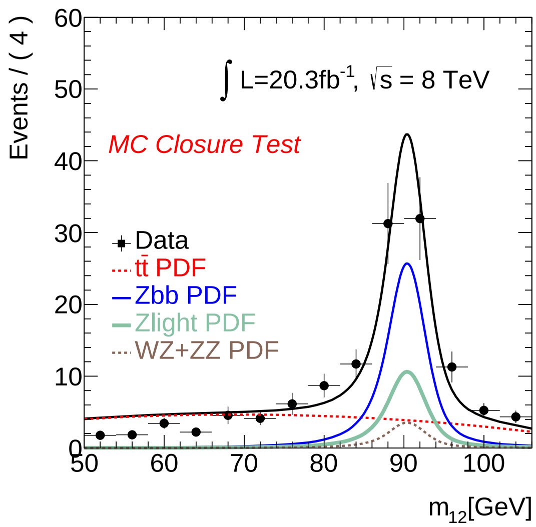

(c)

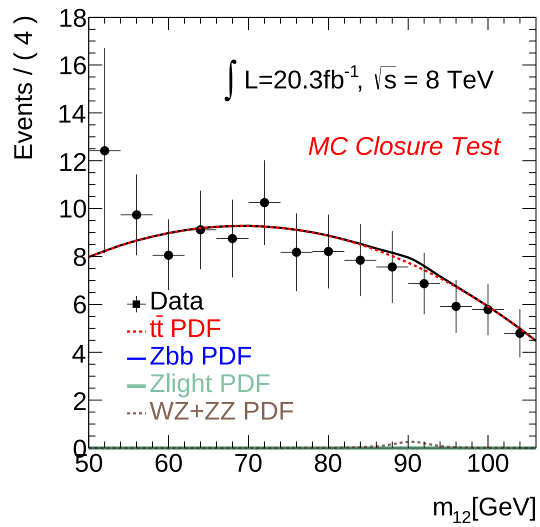

(d)

Table 5.17: Estimations of the reducible background contributions made from the 2012 data simultaneous fit in the OS CR and the relevant MC expectations. The difference between the two is quoted as "scaling". The presented uncertainties are the statistical uncertainties estimated from the fit and the MC available statistics respectively.

Reducible Background	MC prediction	Fit estimation	Scaling
$Zb\bar{b}$	93.5 ± 0.7	139 ± 16	1.49 ± 0.17
Zlight	43 ± 5	46 ± 9	1.07 ± 0.24
$t\bar{t}$	150.6 ± 1.5	181 ± 11	1.20 ± 0.07

Table 5.18: Correlation values of the $Zb\bar{b}$, $Zlight$ and $t\bar{t}$ with each other as estimated from the simultaneous fit of the 2012 data.

Reducible Background	$Zb\bar{b}$	$t\bar{t}$	$Zlight$
$Zb\bar{b}$	1.000	-0.506	0.028
$t\bar{t}$	-0.506	1.000	-0.020
$Zlight$	0.028	-0.020	1.000

the MC expectations. The corresponding ratio called "scaling" also appears on the Table. The correlation matrix of the fit parameters is presented in Figure 5.12 and the corresponding pulls are presented in Figure 5.13. The pulls are defined as $(p_{fit} - p_{nominal})/\delta p_{nominal}$, where the "nominal" values correspond to the pre-fit values, and are expected to be distributed around 0.00. The pull error bars correspond to the ratio of the estimated fit uncertainty divided by the pre-fit assigned uncertainty. Table 5.18 presents the correlation of the parameters of interest, i.e. the OS CR events of $Zb\bar{b}$, $Zlight$ and $t\bar{t}$, with each other.

The m_{12}, m_{34} and $m_{4\ell}$ masses in the reference OS CR are presented in Figure 5.14, where the reducible backgrounds are scaled to the fit estimation and the ZZ and WZ are taken from the MC. The exact numbers of each background are mentioned on the legends. The Higgs signal contribution is not included.

5.10.5 2012 Data Unbinned Simultaneous Fit Validity

Even though, the method of the simultaneous fit is validated and proved to work on the MC, as described in Section 5.10.3, a number of other sanity checks are performed to further ensure the validity of the results. This includes the following cross checks

Figure 5.11: The 2012 data m_{12} distributions are presented after the unbinned simultaneous fit in the control regions of inverted $d_0/\sigma d_0$ (a), inverted isolation (b), SS (c) and $e\mu + \mu\mu$ (d). The WZ and ZZ contamination is fixed to the MC estimation and the rest of the background results estimated from the fit.

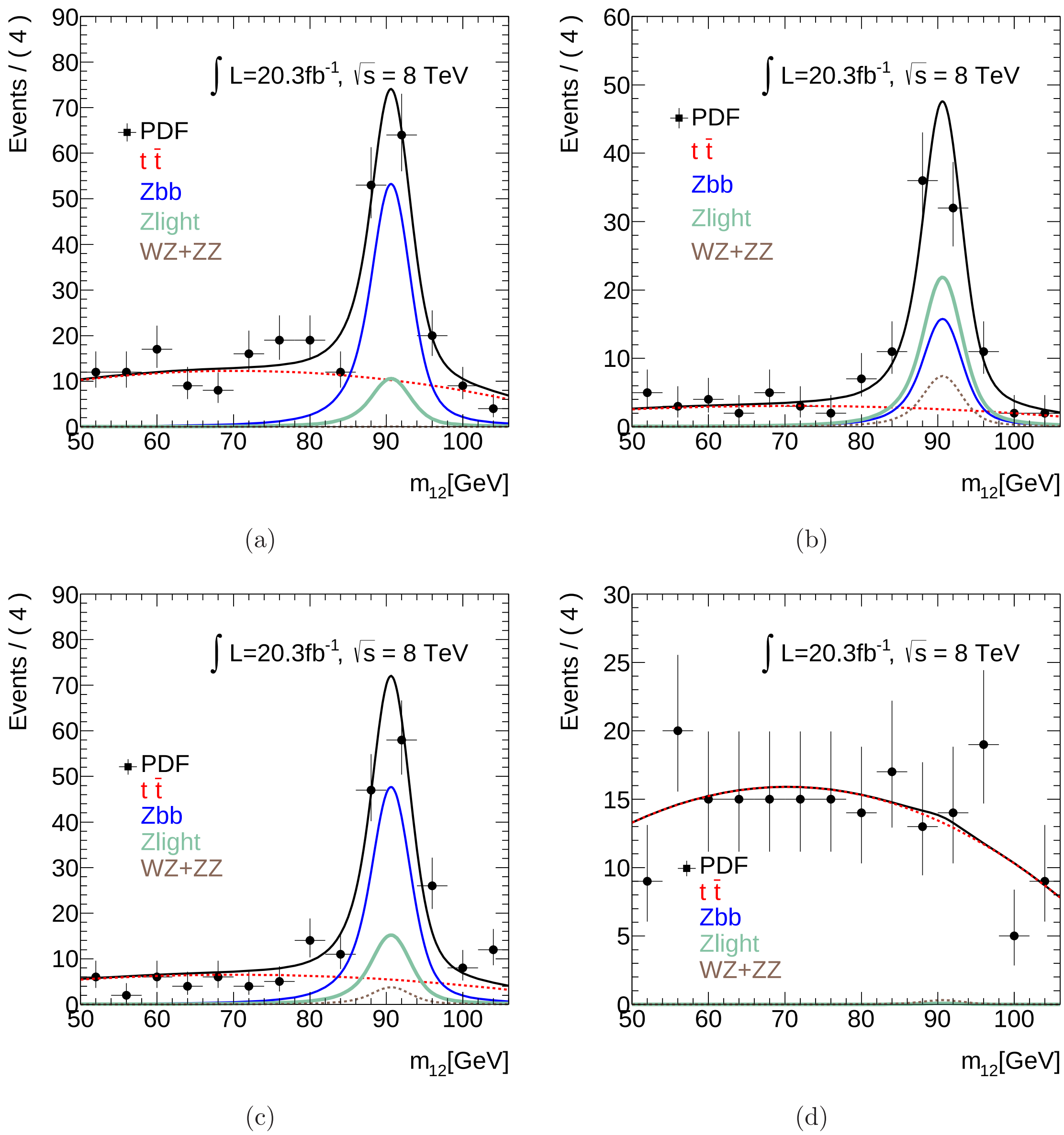

(a) (b) (c) (d)

Figure 5.12: Correlation matrix of the parameters used for the 2012 data simultaneous fit. The parameters in the matrix include the shape parameters, the fractions of each control region with respect to the reference OS CR following the naming convention "frac_(Process)_(Control Region)" and the estimated reducible backgrounds in the reference CR.

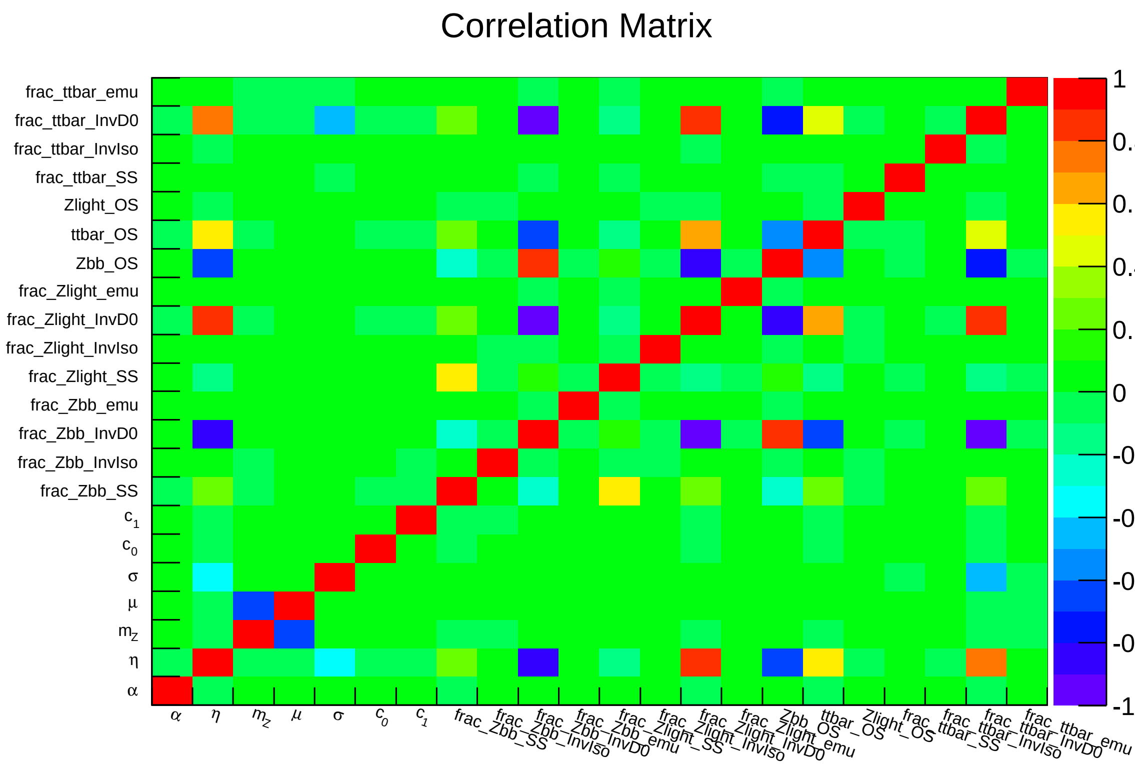

Figure 5.13: 2012 fit parameters pull distributions defined as $(p_{fit} - p_{nominal})/\delta p_{nominal}$ centering around 0.00 as expected. The "nominal" values correspond to the pre-fit values. The parameters include the shape parameters described in the text and the fractions of each control region with respect to the reference OS CR following the naming convention "Fraction_(Process)_(Control Region)". The pull error bars correspond to the ratio of the estimated fit uncertainty divided by the pre-fit assigned uncertainty.

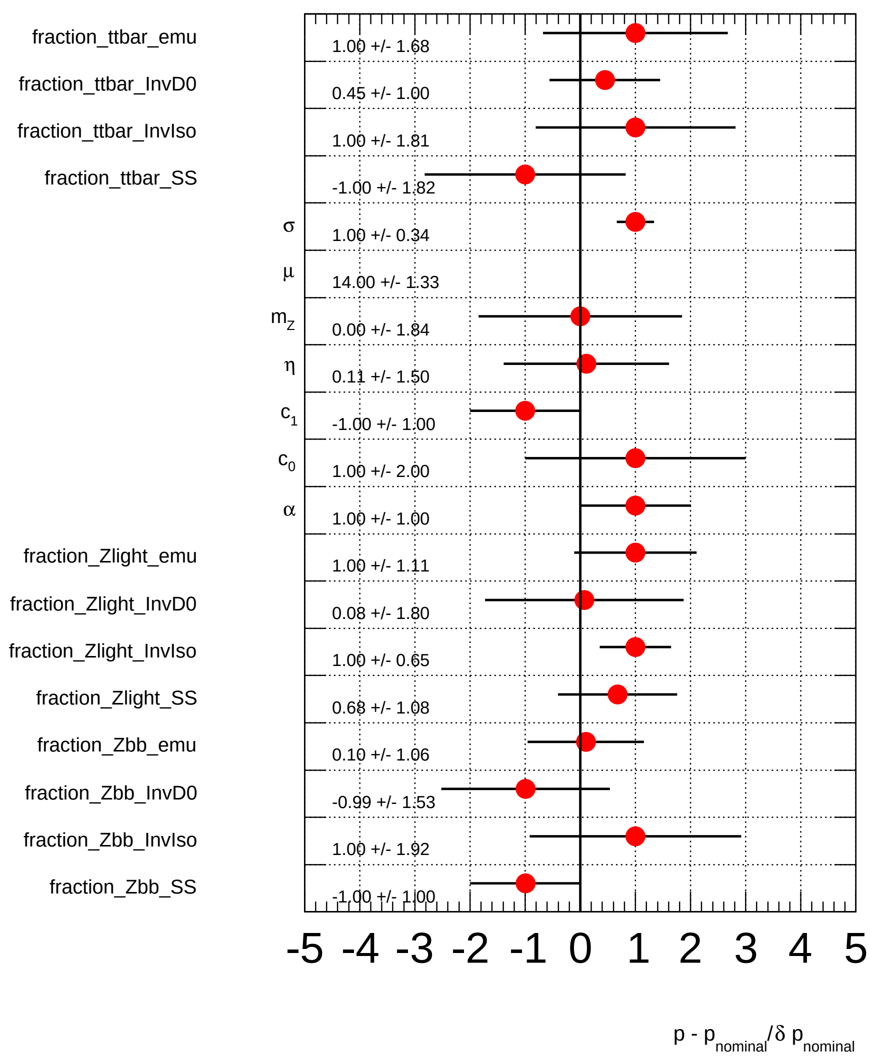

Figure 5.14: 2012 $Z + \mu^+\mu^-$ event distributions in data and the expected backgrounds. The reducible backgrounds contributions come from the fit while the ZZ and WZ are taken from the MC. The Higgs signal contamination is not shown. The m_{12} (a), m_{34} (b) and $m_{4\ell}$ (c) are presented.

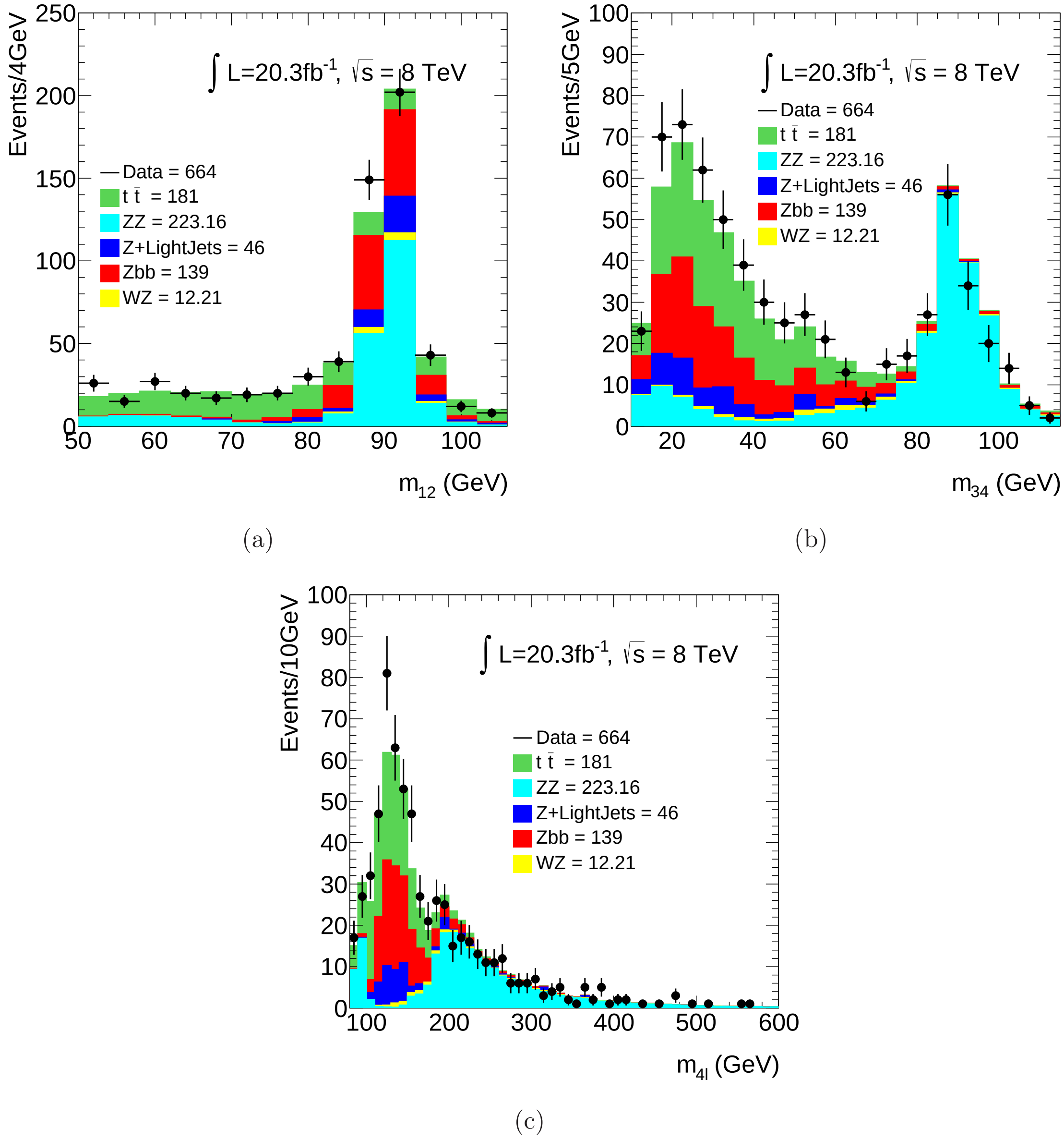

(a) (b) (c)

Table 5.19: Fit estimated results for the OS CR from the nominal fit method and by un-constraining the shape parameters for testing reasons. The test is performed on the 2012 data because of the higher statistics.

Reducible Background	Test Fit	Nominal Fit estimation
$Zb\bar{b}$	137 ± 15	139 ± 16
Zlight	46 ± 9	46 ± 9
$t\bar{t}$	183 ± 11	181 ± 11

Table 5.20: Fit estimated results for the OS CR from the nominal fit method and by reducing the fractions uncertainties to 0.1 of each value for testing reasons. The test is performed on the 2012 data because of the higher statistics.

Reducible Background	Test Fit	Nominal Fit estimation
$Zb\bar{b}$	137 ± 14	139 ± 16
Zlight	46 ± 7	46 ± 9
$t\bar{t}$	185 ± 10	181 ± 11

(for which the fitted distributions are located in the Appendix C):

(1) Shape Parameters Effect
In this check, the shape parameters are set essentially free to fluctuate rather than being constrained in the MC values. Table 5.19 shows the estimated $Zb\bar{b}$, $Zlight$ and $t\bar{t}$ contributions and for comparison the values that the nominal fit method estimates are presented. The results are compatible within the statistical uncertainties and no unexpected shape is observed in the fitted CR (Figure C.1).

(2) Fractions Uncertainties Effect
The fractions uncertainties are set to 0.1 of each value and the fit is performed without other modifications. No significant discrepancy is observed within the uncertainties as the Table 5.20 and the Figures C.2 show.

In another test the uncertainties are doubled, Table 5.21 and Figure C.3 show the results, once again no discrepancy with the nominal results is observed.

(3) $Zjets$ and $t\bar{t}$ Fit
The fit in this case is performed without trying to separate the heavy and light flavor of the $Zjets$, in all the rest the fit is similar to the nominal method. The results are reported in Table 5.22 and the fitted masses are shown in Figure C.4. No significant discrepancy from the nominal method is observed.

Table 5.21: Fit estimated results for the OS CR from the nominal fit method and by doubling the fractions uncertainties for testing reasons. The test is performed on the 2012 data because of the higher statistics.

Reducible Background	Test Fit	Nominal Fit estimation
$Zb\bar{b}$	136 ± 19	139 ± 16
Zlight	46 ± 14	46 ± 9
$t\bar{t}$	175 ± 11	181 ± 11

Table 5.22: Fit estimated results for the OS CR from the nominal fit method where the $Zb\bar{b}$ and the $Zlight$ have been merged and the fit is performed for the $Zjets$ and $t\bar{t}$ estimation for testing reasons. The test is performed on the 2012 data because of the higher statistics.

Reducible Background	Test Fit	Nominal Fit estimation
$Zjets$	189 ± 16	185 ± 18
$t\bar{t}$	180 ± 11	181 ± 11

(4) Individual CR Fits

The individual CRs are fitted for the extraction of each background component. The shape parameters are fixed to the values of the simultaneous fit, in order to avoid the tail mismodeling, and the $Zb\bar{b}$ and $Zlight$ are treated as $ZJets$ since it is impossible to distinguish their identical shapes from one CR. The results are presented in Table 5.23 and are in well agreement with the simultaneous fit estimations withing the statistical uncertainties.

(5) $t\bar{t}$ Cross Checks

The $e\mu + \mu\mu$ results can be used to estimate the 4μ and $2e2\mu$ $t\bar{t}$ results using the formulas:

$$N^{4\mu}_{t\bar{t}\ estimated} = N^{e\mu+\mu\mu}_{data} \times N^{\frac{4\mu}{e\mu+\mu\mu}}_{MC} \tag{5.11}$$

$$N^{2e2\mu}_{t\bar{t}\ estimated} = N^{e\mu+\mu\mu}_{data} \times N^{\frac{2e2\mu}{e\mu+\mu\mu}}_{MC} \tag{5.12}$$

For this estimation only $e\mu + \mu^+\mu^-$ events with OS secondary pairs are considered, given that the result of the estimation has to be the expected reference OS events. The data $e\mu + \mu^+\mu^-$ are found to be 101 ± 10. From the MC samples, the ratios of

Figure 5.15: The data m_{12} distributions are presented after the individual fit of each CR. No separation between light and heavy jets made, given that their same shape does not allow it. The CRs of the inverted $d_0/\sigma d_0$ (a), inverted isolation and nominal $d_0/\sigma d_0$ (b), SS (c) and $e\mu + \mu\mu$ (d) are presented. The test proves no significant deviation with the nominal results.

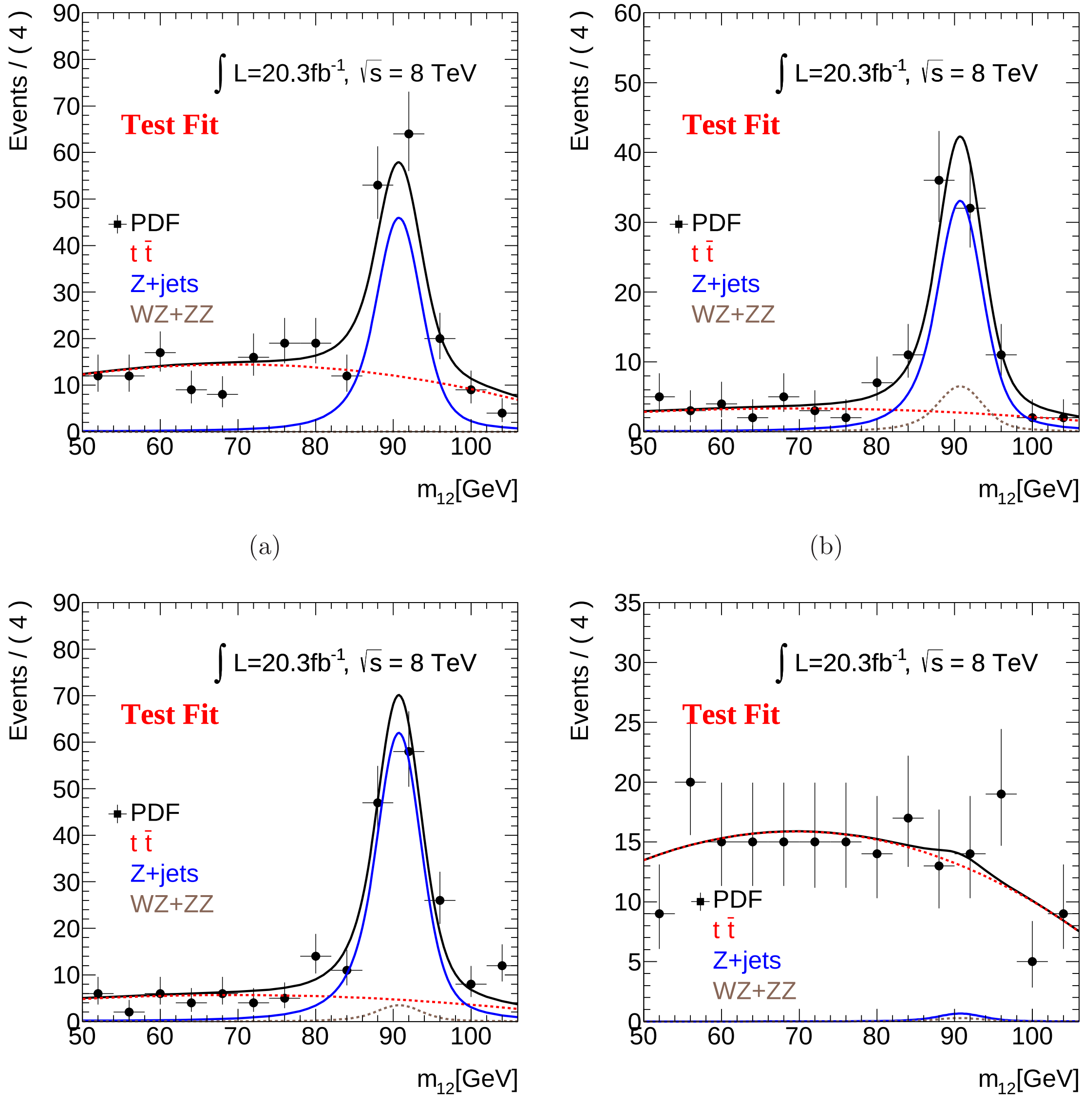

(a) (b) (c) (d)

Table 5.23: Individual CR fit results of the $ZJets$ (including heavy and light jets) and $t\bar{t}$ background is performed as a sanity check of the simultaneous fit results for the 2012. In the case of $e\mu + \mu\mu$ CR the $ZJets$ component cannot be extracted because of its small contamination.

Control Region	$Z + Jets$	$t\bar{t}$
Inverted $d_0/\sigma d_0$	186 ± 29	181 ± 18
Inverted Isolation	194 ± 24	189 ± 26
SS	198 ± 23	155 ± 25
$e\mu + \mu\mu$	meaningless	184 ± 21
Simultaneous Fit	185 ± 18	181 ± 11

Table 5.24: $t\bar{t}$ cross checks made from the $e\mu + \mu^+\mu^-$ CR and are compared to the fit results in the reference CR. No systematic uncertainties are included.

$t\bar{t}$	Individual CR	Nominal Simultaneous Fit
Estimations in the Reference CR	166 ± 6	181 ± 11

the reference over the $t\bar{t}$ enriched CR are calculated as:

$$N_{MC}^{\frac{4\mu}{e\mu+\mu\mu}} = 0.840 \pm 0.016 \tag{5.13}$$

$$N_{MC}^{\frac{2e2\mu}{e\mu+\mu\mu}} = 0.798 \pm 0.015 \tag{5.14}$$

The $t\bar{t}$ reference OS estimations are presented in Table 5.24 for both the 4μ and the $2e2\mu$ channels. In the same Table the nominal fit estimations are given for comparison.

5.10.6 2012 Signal Region (SR) Extrapolations

The results of the fit, reported in Table 5.17, can be extrapolated to the SR by multiplying with the probability of each background type to fulfill the additional selection, i.e. isolation and $d_0/\sigma d_0$ criteria. The so called "transfer factor" (T.F.) is calculated from the relevant MC samples and is presented in Table 5.25. The quoted uncertainties correspond to the statistical MC uncertainties and the systematic uncertainties which originate from the efficiency difference of the additional selection observed in the 3ℓ

Table 5.25: Efficiencies for each background type to fulfill the isolation and impact parameter criteria, calculated from $\sqrt{s} = 8$ TeV MC samples. The uncertainties correspond to the statistical MC errors and the systematic uncertainty from the efficiency difference of the additional selection observed in the 3ℓ final state (Section 5.9) between data and MC.

Reducible Background	Transfer Factor (%)
$Zb\bar{b}$	3.10 ± 0.19
Zlight	3.0 ± 1.8
$t\bar{t}$	0.55 ± 0.09

final state (Section 5.9) between data and MC (1.6%). During the fit, only the $Zb\bar{b}$ uncertainty for the case of inverted isolation was included (4%). This is considered to be the only source of systematic uncertainties during the fitting procedure, given that the final estimation is dominated by the statistical uncertainties and the transfer factor error.

The final reducible backgrounds estimations in the signal region are estimated based on the formula:

$$N_x^{SR} = N_x \times T.F._x \tag{5.15}$$

where the N_x is the $x-$background estimated from the fit events in the OS CR (Table 5.17) and the corresponding transfer factors are the $T.F._x$. The results correspond to the sum of the $Z \to e^+e^- + \mu^+\mu^-$ and $Z \to \mu^+\mu^- + \mu^+\mu^-$ final states, also denoted as $2e2\mu$ and 4μ respectively. In order to split those, a multiplication with the ratios of $2e2\mu/(2e2\mu + 4\mu)$ or $4\mu/(2e2\mu + 4\mu)$ is needed, i.e.:

$$N_x^{SR} = N_x \times T.F._x \times \frac{4\mu \; OR \; 2e2\mu}{2e2\mu + 4\mu} \tag{5.16}$$

The final estimations for the 2012 data are given in Table 5.26. The fit uncertainty is assigned as the statistical error and the transfer factor uncertainty with the channel splitting uncertainty ($2e2\mu/(2e2\mu + 4\mu)$ or $4\mu/(2e2\mu + 4\mu$ error) as the systematic uncertainty of the method.

5.10.7 2011 Reducible Background Estimations

The method followed for the 2012 $Z + \mu\mu$ background estimation at $\sqrt{s} = 8$ TeV is applied in a similar way to the 2011 data. The method is fully validated in the

Table 5.26: Reducible background estimated contamination in the SR for the 2012 data, based on the formula 5.16. The fit uncertainty is assigned as the statistical error and the transfer factor uncertainty with the channel splitting uncertainty ($2e2\mu/(2e2\mu+4\mu)$ or $4\mu/(2e2\mu+4\mu$ error) as the systematic uncertainty of the method.

	$\sqrt{s} = 8$ TeV	
Reducible Background	4μ	$2e2\mu$
$Zjets$	3.11 ± 0.46(stat) ± 0.43(syst)	2.58 ± 0.39(stat) ± 0.43(syst)
$t\bar{t}$	0.51 ± 0.03(stat) ± 0.09(syst)	0.48 ± 0.03(stat) ± 0.08(syst)
WZ MC expectation	0.42 ± 0.07	0.44 ± 0.06
	$Zjets$ decomposition	
$Zb\bar{b}$	2.30 ± 0.26(stat) ± 0.14(syst)	2.01 ± 0.23(stat) ± 0.13(syst)
$Zlight$	0.81 ± 0.38(stat) ± 0.41(syst)	0.57 ± 0.31(stat) ± 0.41(syst)

2012 data (Section 5.10.5) and no further cross check is necessary. The data are fitted simultaneously with each CR modeling taken from Equation 5.8. The fractions between the CR are extracted from the 2011 MC at $\sqrt{s} = 7$ TeV and are presented in Table 5.27.

Figure 5.16 shows the simultaneous fit results in the four CRs. The number of events in the OS CR are presented in Table 5.28 for both the expectations from MC and the fit results. Their difference is also reported.

The m_{12}, m_{34} and $m_{4\ell}$ masses in the reference OS CR are presented in Figure 5.17, where the irreducible backgrounds are scaled to the fit estimation and the ZZ and WZ are taken from the MC. The exact numbers of each background are mentioned on the legends of the Figures. The Higgs signal contribution is not included.

Table 5.27: MC estimated ratios for the reducible background of the fit CRs with respect to the OS CR at $\sqrt{s} = 7$ TeV, following the naming convention $f_x = CR_x/CR_{OS}$. The uncertainties correspond to the MC statistical errors. This fractions are used by the fit, as Equation 5.8 describes, after being promoted to nuisance parameters for better handling of the uncertainties.

Background	f_{inv-d0}	$f_{inv-iso}$	f_{SS}	$f_{e\mu+\mu\mu}$
Zbb	0.76 ± 0.10	0.231 ± 0.005	0.699 ± 0.012	0.0000 ± 0.0003
$Z + light$	0.49 ± 0.19	0.48 ± 0.16	0.89 ± 0.23	0.0000 ± 0.0029
$t\bar{t}$	0.79 ± 0.05	0.206 ± 0.022	0.89 ± 0.05	1.13 ± 0.04

Figure 5.16: The 2011 data m_{12} distributions are presented after the unbinned simultaneous fit in the control regions of inverted $d_0/\sigma d_0$ (a), inverted isolation and nominal $d_0/\sigma d_0$ (b), SS (c) and $e\mu + \mu\mu$ (d). The WZ and ZZ contamination is fixed to the MC estimations and the rest of the background results are estimated using the nominal fit.

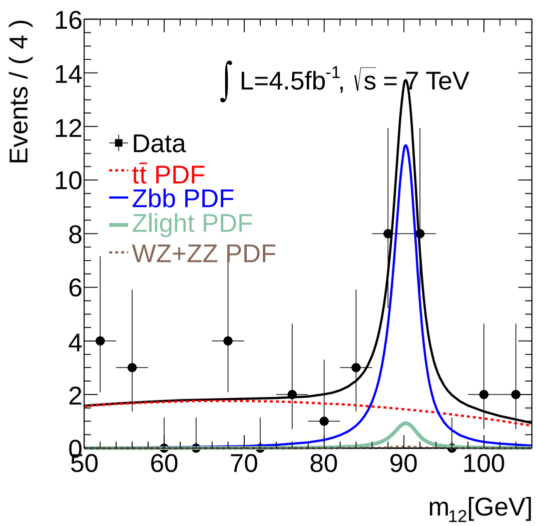

(a)

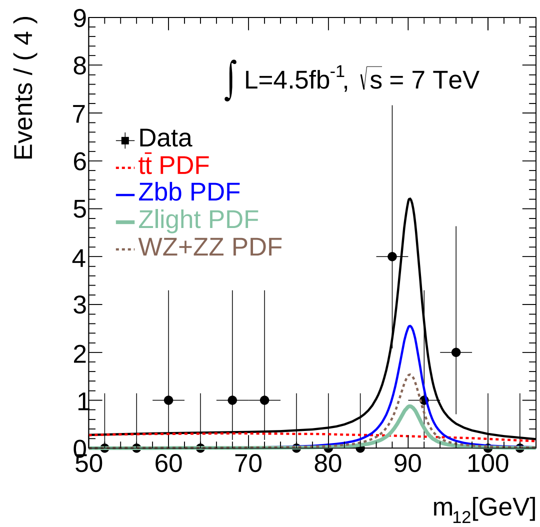

(b)

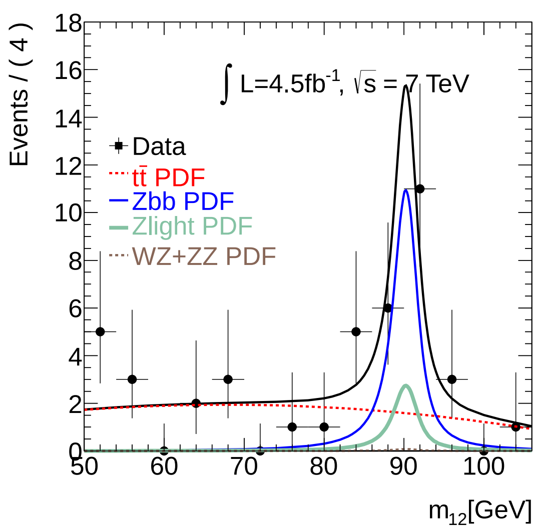

(c)

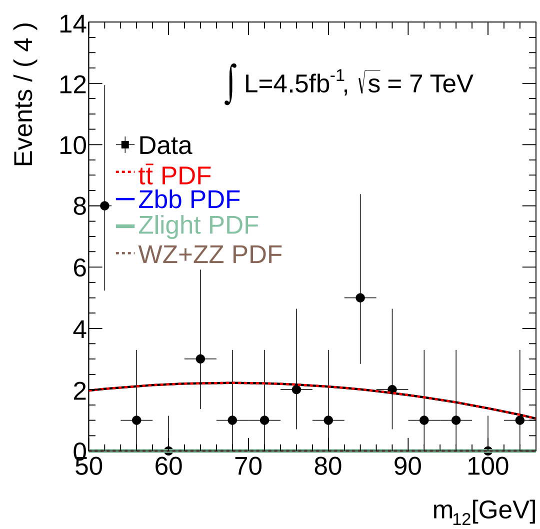

(d)

Figure 5.17: 2011 $Z + \mu^+\mu^-$ event distributions in data and the expected backgrounds in the reference CR. The reducible backgrounds contributions come using the nominal fit while the ZZ and WZ are taken from the MC. The Higgs signal contamination is not shown. The m_{12} (a), m_{34} (b) and $m_{4\ell}$ (c) are presented.

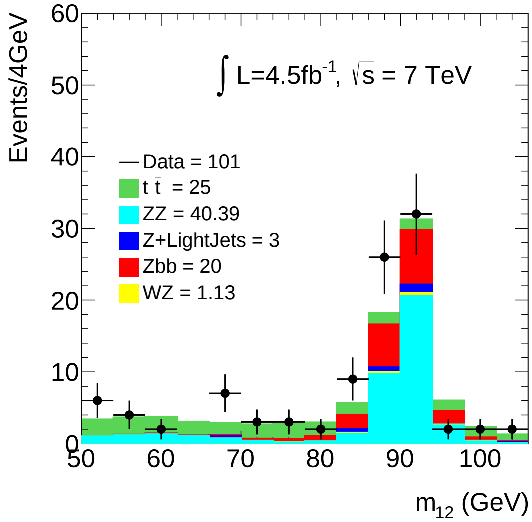

(a)

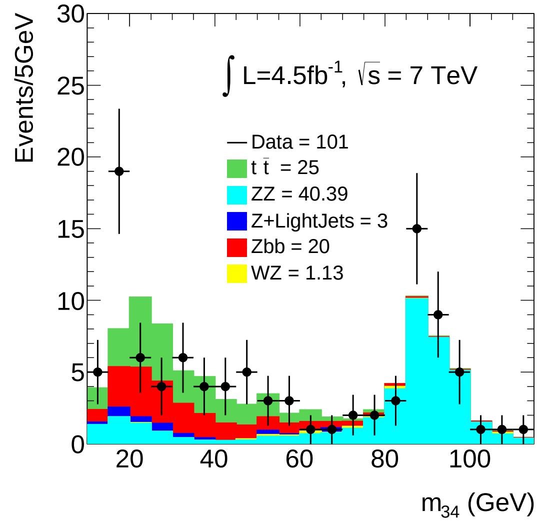

(b)

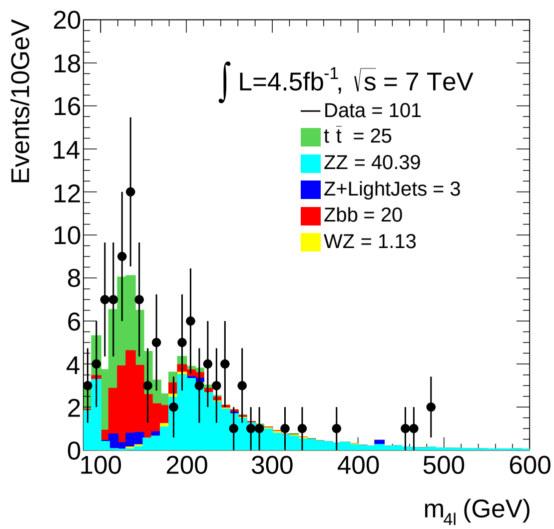

(c)

Table 5.28: Estimations of the reducible background contributions made from the 2011 data simultaneous fit in the OS CR and the relevant MC expectations. The difference between the two is quoted as "scaling". The presented uncertainties are the statistical uncertainties estimated from the fit and the MC available statistics accordingly.

Reducible Background	MC prediction	Fit estimation	Scaling
$Zb\bar{b}$	15.1 ± 0.06	20 ± 12	1.3 ± 0.8
$Zlight$	3.9 ± 0.9	3 ± 4	0.8 ± 1.0
$t\bar{t}$	22.4 ± 1.0	25 ± 5	1.14 ± 0.23

Table 5.29: Per-event efficiencies for each background type at $\sqrt{s} = 7$ TeV to fulfill the isolation and impact parameter criteria. The $t\bar{t}$ transfer factor is taken from the 2012 MC because of the inadequate statistical precision of the MC samples used in the 2011 analysis. The uncertainties correspond to the statistical MC error and the systematic efficiency difference of the additional selection observed in the 3ℓ final state (Section 5.9) between data and MC.

Reducible Background	Transfer Factor %
$Zb\bar{b}$	3.2 ± 0.3
$Zlight$	3.4 ± 1.9
$t\bar{t}$	0.55 ± 0.11

The fit results of Table 5.28 are extrapolated to the SR using formula 5.16. The transfer factors are quoted in Table 5.29 and are estimated from the $\sqrt{s} = 7$ TeV MC except from the $t\bar{t}$ transfer factor which is taken from the 2012 MC because of the inadequate statistical precision of the MC samples used in the 2011 analysis. The motivation for this is the agreement between the heavy flavor extrapolation in the $Zb\bar{b}$ sample of the 7 TeV and the 8 TeV samples using the same generator (ALPGEN HERWIG). The quoted uncertainties correspond to the statistical MC uncertainties and the systematic uncertainty comes from the squared efficiency difference of the additional selection that is observed in the 3ℓ final state (Section 5.9) between data and MC (5.0%).

The final reducible backgrounds estimations in the SR are given in Table 5.30 based on the extrapolation formula 5.16. The fit uncertainty is assigned as the statistical error and the transfer factor uncertainty with the channel splitting uncertainty, $2e2\mu/(2e2\mu+4\mu)$ or $4\mu/(2e2\mu+4\mu$ error, as the systematic uncertainty of the method.

Table 5.30: Reducible background estimated contamination in the SR for the 2011 data, based on the formula 5.16. The fit uncertainty is assigned as the statistical error and the transfer factor uncertainty with the channel splitting uncertainty ($2e2\mu/(2e2\mu+4\mu)$ or $4\mu/(2e2\mu+4\mu$ error) as the systematic uncertainty of the method.

	$\sqrt{s} = 7$ TeV	
Reducible Background	4μ	$2e2\mu$
$Zjets$	0.42 ± 0.21(stat) ± 0.08(syst)	0.29 ± 0.14(stat) ± 0.05(syst)
$t\bar{t}$	0.081 ± 0.016(stat) ± 0.021(syst)	0.056 ± 0.011(stat) ± 0.015(syst)
WZ MC expectation	0.08 ± 0.05	0.19 ± 0.10
	$Zjets$ decomposition	
$Zb\bar{b}$	0.36 ± 0.19(stat) ± 0.07(syst)	0.25 ± 0.13(stat) ± 0.05(syst)
$Zlight$	0.06 ± 0.08(stat) ± 0.04(syst)	0.04 ± 0.06(stat) ± 0.02(syst)

5.11 4ℓ Angular Distributions

When the $ZZ^{(*)}$ system decays to the four leptons, the angles of Figure 5.18 appear. These angles are the observables for the Higgs Spin and Parity analysis and therefore this background measurement was used to control the contribution of the reducible backgrounds to the distributions of these angles. The production and decay angles are defined in the following way:

- θ_1, θ_2: are the angles between negative final state leptons and the direction of flight of their respective Z-bosons. The 4-vectors of the leptons are calculated in the rest frame of the corresponding Z-bosons.
- ϕ is the angle between the decay planes of the four final state leptons expressed in the rest frame of the four-leptons system
- ϕ_1 is the angle defined between the decay plane of the first lepton pair and a plane defined by the vector of Z_1 in the rest frame of the four-leptons system and the positive direction of the collision axis.
- θ^* is the production angle of Z_1 defined in the rest frame of the four-lepton system.

The angular distributions in the reference OS CR of the 4μ and $2e2\mu$ channels are presented in Figures 5.19 and 5.20 for the 2011 and the 2012 data respectively. The reducible background is normalized to the estimations of the previously presented data

Figure 5.18: Graphical display of production and decay angles in the $X \to ZZ^{(*)} \to 4\ell$ decay. These angles are the observables used for the Spin and Parity analysis.

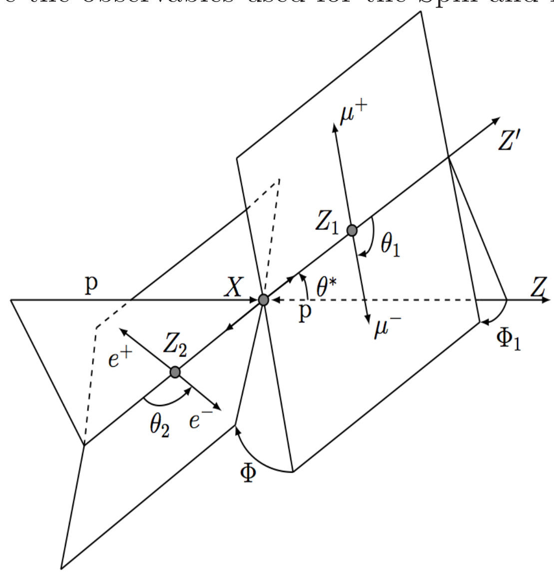

driven methods (Section 5.10), the irreducible background is taken from the MC and no signal MC is included. These estimations are the inputs for the determination of the Spin/CP of the Higgs boson.

5.12 Systematic Uncertainties

For the $H \to ZZ^{(*)} \to 4\ell$ decay modes involving electrons, the electron energy scale uncertainty which is determined from $Z \to ee$ and $J/\psi \to ee$ decays, is propagated as a function of the pseudorapidity and the transverse energy of the electrons. The precision of the energy scale is better than 0.1% for $|\eta| < 1.2$ and $1.8 < |\eta| < 2.47$, and a few per mille for $1.2 < |\eta| < 1.8$ [59]. The uncertainties on the measured Higgs boson mass due to the electron energy scale uncertainties are $\pm 0.04\%$, $\pm 0.025\%$ and $\pm 0.04\%$ for the $4e$, $2e2\mu$ and $2\mu 2e$ final states, respectively.

Similarly, for the $H \to ZZ^{(*)} \to 4\ell$ decay modes involving muons, the various components of the systematic uncertainty on the muon momentum scale are determined using large samples of $J/\psi \to \mu\mu$ and $Z \to \mu\mu$ decays and are validated using $\Upsilon \to \mu\mu$, $J/\psi \to \mu\mu$ and $Z \to \mu\mu$ decays. In the muon transverse momentum range of $6-100$ GeV, the systematic uncertainties on the scales are about $\pm 0.04\%$ in the barrel region and reach $\pm 0.2\%$ in the region $|\eta| > 2$ [61]. The uncertainties on the measured Higgs boson mass due to the muon energy scale uncertainties are estimated to be

Figure 5.19: Angular distributions for the 4μ and $2e2\mu$ reference OS CR events at $\sqrt{s} = 7$ TeV: (a) θ_1, (b) θ_2, (c) ϕ, (d) ϕ_1 and (e) θ^*. The reducible background is normalized to the estimations made using the nominal fit, the irreducible background is taken from the MC and no signal MC is included.

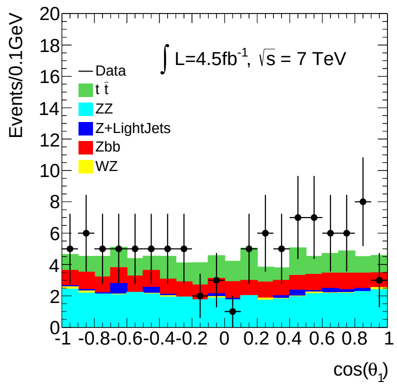

(a)

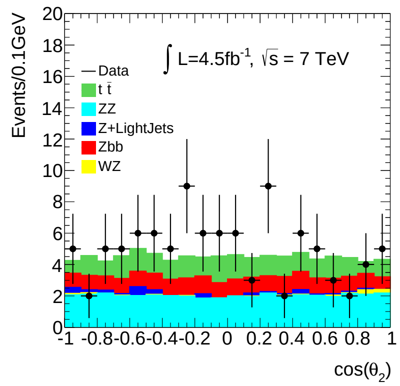

(b)

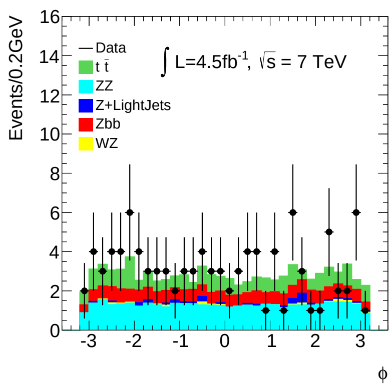

(c)

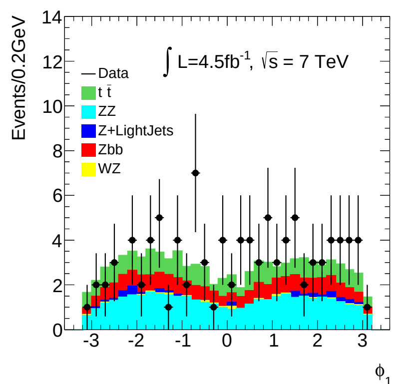

(d)

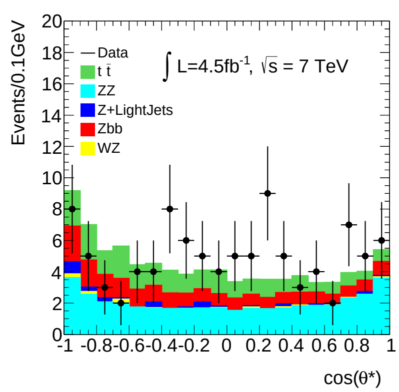

(e)

Figure 5.20: Angular distributions for the 4μ and $2e2\mu$ reference OS CR events at $\sqrt{s} = 8$ TeV: (a) θ_1, (b) θ_2, (c) ϕ, (d) ϕ_1 and (e) θ^*. The reducible background is normalized to the estimations made using the nominal fit, the irreducible background is taken from the MC and no signal MC is included.

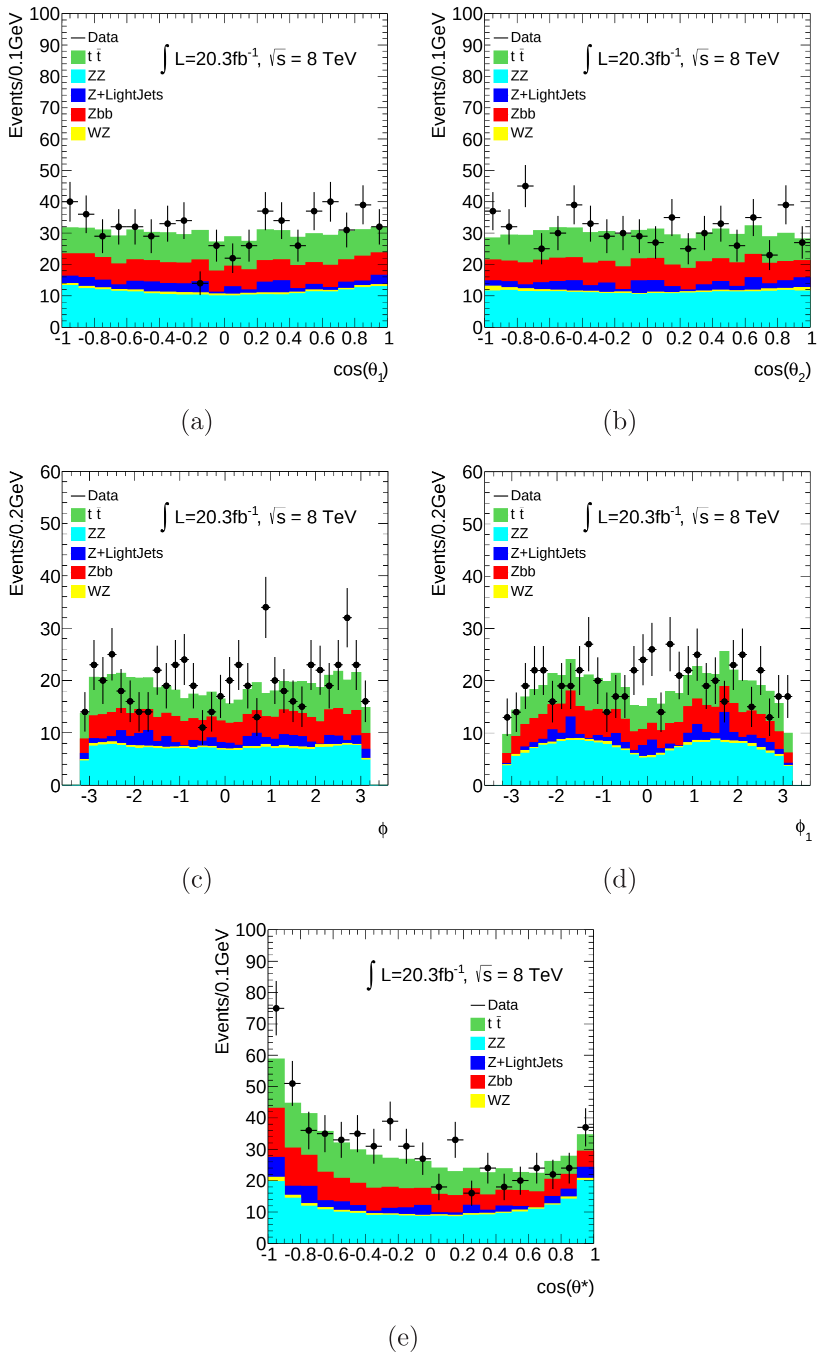

(a) (b)

(c) (d)

(e)

$\pm 0.04\%$, $\pm 0.015\%$ and $\pm 0.02\%$ for the 4μ, $2e2\mu$ and $2\mu 2e$ final states, respectively.

Uncertainties on the measured Higgs boson mass related to the background contamination and final-state QED radiation modeling are negligible compared to the other sources described above.

The weighted contributions to the uncertainty in the mass measurement, when all the final states are combined, are $\pm 0.01\%$ for the electron energy scale uncertainty and $\pm 0.03\%$ for the muon momentum scale uncertainty. The larg impact of the muon momentum scale uncertainty is due to the fact that the muons final states have more significant weight in the combined mass.

The efficiencies to trigger, reconstruct and identify electrons and muons are studied using $Z \to \ell\ell$ and $J/\psi \to \ell\ell$ decays [67, 57, 68, 61]. The expected impact from the simulation of the associated systematic uncertainties on the signal yield are presented in Table 5.31. The impact is presented for the individual final states and for all channels combined.

A small additional uncertainty on the isolation and impact parameter selection efficiency is applied for electrons with E_T below 15 GeV. The effect of the isolation and impact parameter uncertainties on the signal strength is given in Table 5.31. The corresponding uncertainty for muons is found to be negligible. The background uncertainties, as estimated from the data driven methods, are also presented in Table 5.31. Additionally the three most important theoretical uncertainties are given in the same Table. Uncertainties on the predicted Higgs boson p_T spectrum due to those on the PDFs and higher-order corrections are estimated to affect the signal strength by less than $\pm 1\%$. The systematic uncertainty of the ZZ background rate is around $\pm 4\%$ for $m_{4\ell} = 125$ GeV and increases for higher masses, averaging to around $\pm 6\%$ for the ZZ production above 110 GeV.

The overall uncertainty on the integrated luminosity for the complete 2011 data set is $\pm 1.8\%$ [69]. The uncertainty on the integrated luminosity for the 2012 data set is $\pm 2.8\%$; this uncertainty is derived following the methodology used for the 2011 data set, from a preliminary calibration of the luminosity scale with beam-separation scans performed in November 2012.

5.13 Higgs Candidates and Background

The selection described in Section 5.6 is applied for the allocation of Higgs candidates in the four possible decay channels (4μ, $2e2\mu$, $2\mu 2e$, $4e$). This analysis, along with the previously presented muons background measurement, was a major contribution in the discovery of the Higgs boson, officially announced in summer 2012. The analysis was performed on the Run-I data corresponding to 20.3 fb^{-1} at $\sqrt{s} = 8$ TeV and 4.5 fb^{-1} at $\sqrt{s} = 7$ TeV and the results are presented in the following paragraphs.

Table 5.31: The expected impact of the systematic uncertainties on the signal yield, derived from the simulation for $m_H = 125$ GeV, are summarized for each of the four final states for the combined $\sqrt{s} = 7$ TeV and $\sqrt{s} = 8$ TeV data. The missing fields of the table do not contribute significantly and therefore are omitted.

Source of uncertainty	4μ	$2e2\mu$	$2\mu2e$	$4e$	combined
Electron reconstruction and identification efficiencies	–	1.7%	3.3%	4.4%	1.6%
Electron isolation and impact parameter selection	–	0.07%	1.1%	1.2%	0.5%
Electron trigger efficiency	–	0.21%	0.05%	0.21%	<0.2%
$\ell\ell + ee$ backgrounds	–	–	3.4%	3.4%	1.3%
Muon reconstruction and identification efficiencies	1.9%	1.1%	0.8%	–	1.5%
Muon trigger efficiency	0.6%	0.03%	0.6%	–	0.2%
$\ell\ell + \mu\mu$ backgrounds	1.6%	1.6%	–	–	1.2%
QCD scale uncertainty					6.5%
PDF, α_s uncertainty					6.0%
$H \to ZZ^{(*)}$ branching ratio uncertainty					4.0%

In total 428 candidate events are selected by the analysis (with $m_{4\ell} > 100$ GeV), 137 4μ, 212 $2e2\mu$ and 79 $4e$ events, in the 2012 data and 83 candidate events, 34 4μ, 31 $2e2\mu$ and 18 $4e$ events in the 2011 data. Table 5.32 presents the results of the separate channels in the "Low" and "High" mass regions, defined as $m_{4\ell} < 160$ GeV and $m_{4\ell} \geq 160$ GeV respectively, the estimated background and the signal expectations normalized to the theoretical cross sections for $\sqrt{s} = 7$ TeV. Table 5.33 presents the similar results for the 2012 data at $\sqrt{s} = 8$ TeV. The $m_{4\ell}$ mass distributions are presented in Figure 5.21. The corresponding primary and secondary mass distributions are shown in Figure 5.22. In all these Figures, the systematic uncertainty associated to the total background contribution is represented by the hatched areas.

Especially around the region of the Higgs boson (~ 125 GeV) the observations are compared to the expected background and the theoretical signal expectations in Table 5.34. It has to be noted that in this region only 2 events were found with non-collinear FSR correction.

In the low mass region, where the reducible background contributes, the separate mass distributions for each channel, 4μ, $2e2\mu$, $2\mu2e$ and $4e$, are presented for the combined 2012 and 2011 data in Figure 5.23.

5.14 Summary

The final Run-I analysis for the study of the final state $H \to ZZ^{(*)} \to 4\ell$ is presented. The analysis is performed using pp collision data corresponding to integrated

Table 5.32: The observed number of events and the final estimate for the expected background, separated into "Low mass" ($m_{4\ell} < 160$ GeV) and "High mass" ($m_{4\ell} \geq 160$ GeV) regions, are presented for the $\sqrt{s} = 7$ TeV data. The expected signal events are also shown for a Higgs boson of 125 GeV mass hypothesis.

	4μ		$2e2\mu + 2\mu2e$		$4e$	
	Low mass	High mass	Low mass	High mass	Low mass	High mass
$ZZ(*)$	5.27±0.26	16.98±1.26	4.39±0.24	25.71±1.91	2.02±0.13	9.85±0.77
Z, $Zb\bar{b}$, and $t\bar{t}$	0.43±0.19	0.17±0.07	2.32±0.57	1.16±0.28	2.16±0.45	1.13±0.24
Total Background	5.70±0.32	17.15±1.26	6.71±0.64	26.87±1.94	4.18±0.47	10.98±0.81
Data	11	23	7	24	4	14
$m_H = 125$ GeV	1.00±0.10		1.16±0.11		0.46±0.05	

Table 5.33: The observed number of events and the final estimate for the expected background, separated into "Low mass" ($m_{4\ell} < 160$ GeV) and "High mass" ($m_{4\ell} \geq 160$ GeV) regions, are presented for the $\sqrt{s} = 8$ TeV data. The expected signal events are also shown for a Higgs boson mass hypothesis.

	4μ		$2e2\mu + 2\mu2e$		$4e$	
	Low mass	High mass	Low mass	High mass	Low mass	High mass
$ZZ(*)$	27.58±1.37	95.00±7.06	23.43±1.28	145.25±10.85	11.20±0.74	56.42±4.44
Z, $Zb\bar{b}$, and $t\bar{t}$	2.90±0.53	1.14±0.21	4.44±0.87	1.98±0.40	1.89±0.40	0.99±0.21
Total Background	30.49±1.47	96.13±7.07	27.86±1.55	147.23±10.85	13.10±0.84	57.41±4.44
Data	42.00	95.00	38.00	174.00	23.00	56.00
$m_H = 125$ GeV	5.80±0.57		6.99±0.70		2.79±0.29	

Figure 5.21: $m_{4\ell}$ distributions of the selected candidates compared to the background expectation and the theoretical Higgs signal expectation for $m_H = 125$ GeV scaled by 1.51. (a) is the low mass region at $\sqrt{s} = 7$ TeV, (b) is the full mass region at $\sqrt{s} = 7$ TeV, (c) is the low mass region at $\sqrt{s} = 8$ TeV, (d) is the full mass region at $\sqrt{s} = 8$ TeV, (e) is the high mass region of the combined dataset and (f) is the full mass region of the combined dataset.

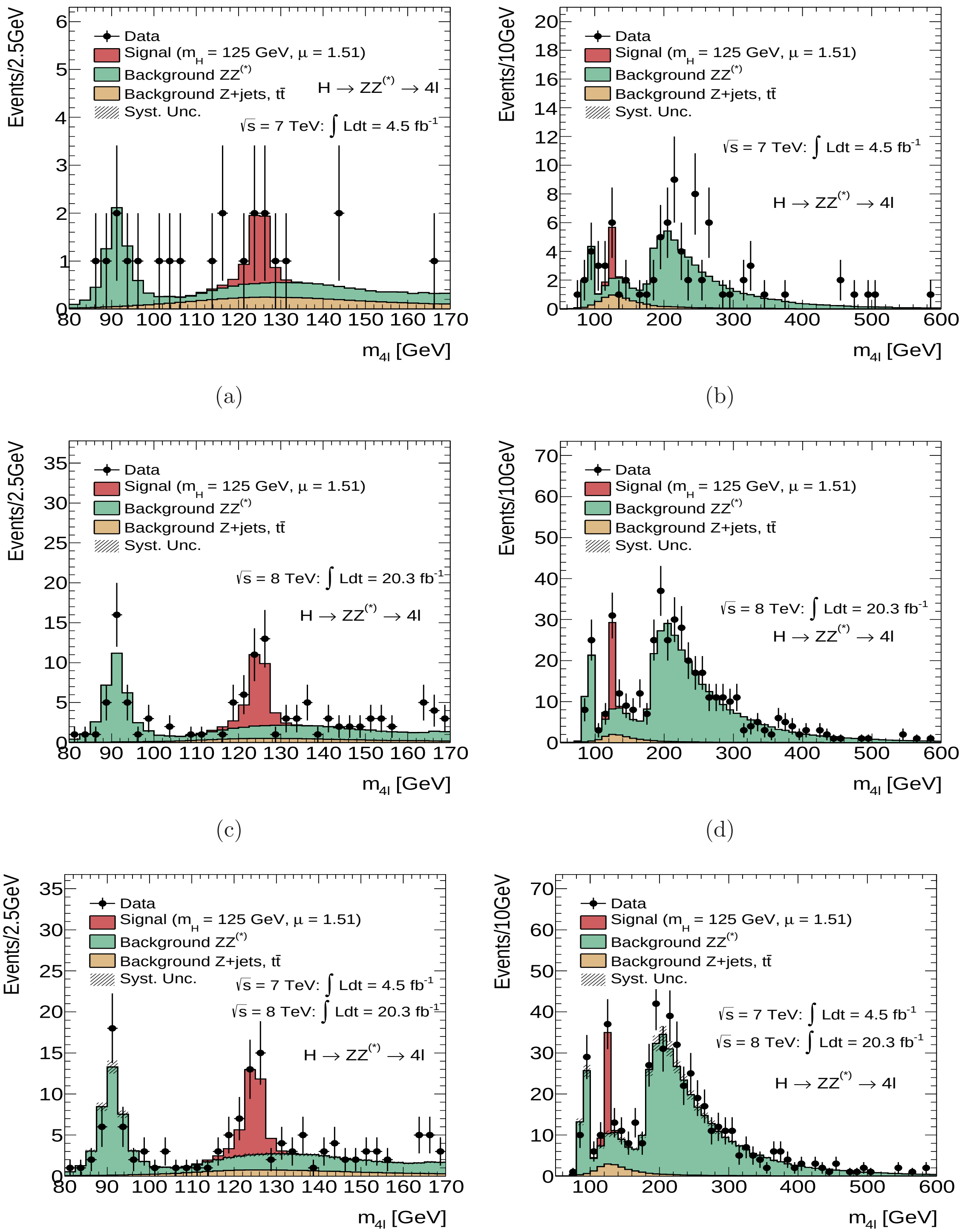

(a) (b)

(c) (d)

(e) (f)

Table 5.34: The number of events expected and observed for a m_H=125 GeV hypothesis for the four-lepton final states in a window of $120 < m_{4\ell} < 130$ GeV. The second column shows the number of expected signal events for the full mass range, without a selection on $m_{4\ell}$. The other columns show for the $120 - 130$ GeV mass range the number of expected signal events, the number of expected ZZ background and reducible background events, the signal-to-background ratio (S/B), together with the number of observed events, for 4.5 fb^{-1} at $\sqrt{s} = 7$ TeV and 20.3 fb^{-1} at $\sqrt{s} = 8$ TeV as well as for the combined data sample.

Final state	Signal full mass range	Signal	ZZ	$Zjets,\ t\bar{t}$	S/B	Expected	Observed
			$\sqrt{s} = 7$ TeV				
4μ	1.00 ± 0.10	0.91 ± 0.09	0.46 ± 0.02	0.10 ± 0.04	1.7	1.47 ± 0.10	2
$2e2\mu$	0.66 ± 0.06	0.58 ± 0.06	0.32 ± 0.02	0.09 ± 0.03	1.5	0.99 ± 0.07	2
$2\mu 2e$	0.50 ± 0.05	0.44 ± 0.04	0.21 ± 0.01	0.36 ± 0.08	0.8	1.01 ± 0.09	1
$4e$	0.46 ± 0.05	0.39 ± 0.04	0.19 ± 0.01	0.40 ± 0.09	0.7	0.98 ± 0.10	1
Total	2.62 ± 0.26	2.32 ± 0.23	1.17 ± 0.06	0.96 ± 0.18	1.1	4.45 ± 0.30	6
			$\sqrt{s} = 8$ TeV				
4μ	5.80 ± 0.57	5.28 ± 0.52	2.36 ± 0.12	0.69 ± 0.13	1.7	8.33 ± 0.6	12
$2e2\mu$	3.92 ± 0.39	3.45 ± 0.34	1.67 ± 0.08	0.60 ± 0.10	1.5	5.72 ± 0.37	7
$2\mu 2e$	3.06 ± 0.31	2.71 ± 0.28	1.17 ± 0.07	0.36 ± 0.08	1.8	4.23 ± 0.30	5
$4e$	2.79 ± 0.29	2.38 ± 0.25	1.03 ± 0.07	0.35 ± 0.07	1.7	3.77 ± 0.27	7
Total	15.6 ± 1.6	13.8 ± 1.4	6.24 ± 0.34	2.00 ± 0.28	1.7	22.1 ± 1.5	31
			$\sqrt{s} = 7$ TeV and $\sqrt{s} = 8$ TeV				
4μ	6.80 ± 0.67	6.20 ± 0.61	2.82 ± 0.14	0.79 ± 0.13	1.7	9.81 ± 0.64	14
$2e2\mu$	4.58 ± 0.45	4.04 ± 0.40	1.99 ± 0.10	0.69 ± 0.11	1.5	6.72 ± 0.42	9
$2\mu 2e$	3.56 ± 0.36	3.15 ± 0.32	1.38 ± 0.08	0.72 ± 0.12	1.5	5.24 ± 0.35	6
$4e$	3.25 ± 0.34	2.77 ± 0.29	1.22 ± 0.08	0.76 ± 0.11	1.4	4.75 ± 0.32	8
Total	18.2 ± 1.8	16.2 ± 1.6	7.41 ± 0.40	2.95 ± 0.33	1.6	26.5 ± 1.7	37

Figure 5.22: Distributions of $\sqrt{s} = 8$ TeV and 7 TeV data and the expected signal and backgrounds events. The m_{12} (a) and m_{34} (b) are shown for $m_{4\ell}$ in the range of $110 - 140$ GeV.

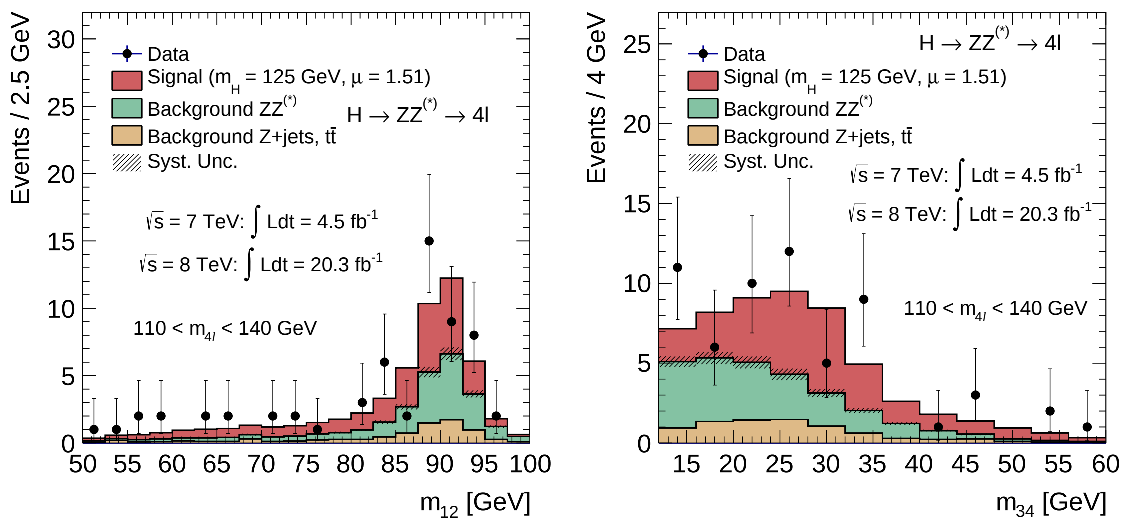

(a) (b)

luminosities of 4.5 and 20.3 fb^{-1} at $\sqrt{s} = 7$ TeV and $\sqrt{s} = 8$ TeV respectively recorded with the ATLAS detector at the LHC. The signal and background simulation, the electron and muon reconstruction and identification, the event selection and in particular the method which were developed to measure the reducible background in the case where the secondary dilepton is a muon pair are discussed in detail. The analysis is performed inclusively at this Chapter and in the next Chapter the events are separated into categories for VBF, VH and ggF production modes.

For the inclusive analysis, in the m_H range of $120 - 130$ GeV, 37 events are observed while 26.5 ± 1.7 events are expected, decomposed as 16.2 ± 1.6 events for a SM Higgs signal with $m_H = 125$ GeV, 7.4 ± 0.4 $ZZ^{(*)}$ background events and 2.9 ± 0.3 reducible background events. This excess corresponds to a $H \rightarrow ZZ^{(*)} \rightarrow 4\ell$ signal observed with a significance of 8.1 standard deviations[3] at the combined ATLAS measurement of the Higgs boson mass [70].

One 4μ candidate event display is shown in Figure 5.24. All the muons of this events pass through one EndCap of the detector and two of the muons pass through the CSC detector. The quadruplet mass of this events is 123.2 GeV.

[3]Standard deviation measures the distribution of data points around a mean or average.

Figure 5.23: $m_{4\ell}$ distributions of the selected candidates for $\sqrt{s} = 7$ and 8 TeV for the different subchannels of the analysis, compared to the background expectation in the mass range of $80 - 170$ GeV: (a) 4μ, (b) $2\mu 2e$, (c) $2e2\mu$, (d) $4e$. The $2e2\mu$ and $2\mu 2e$ channels are differentiated by the pair with a mass closest to the Z boson mass which is listed first. The contribution of the reducible background is also shown separately. The signal expectation for $m_H = 125$ GeV is also shown scaled to 1.51 times the SM prediction.

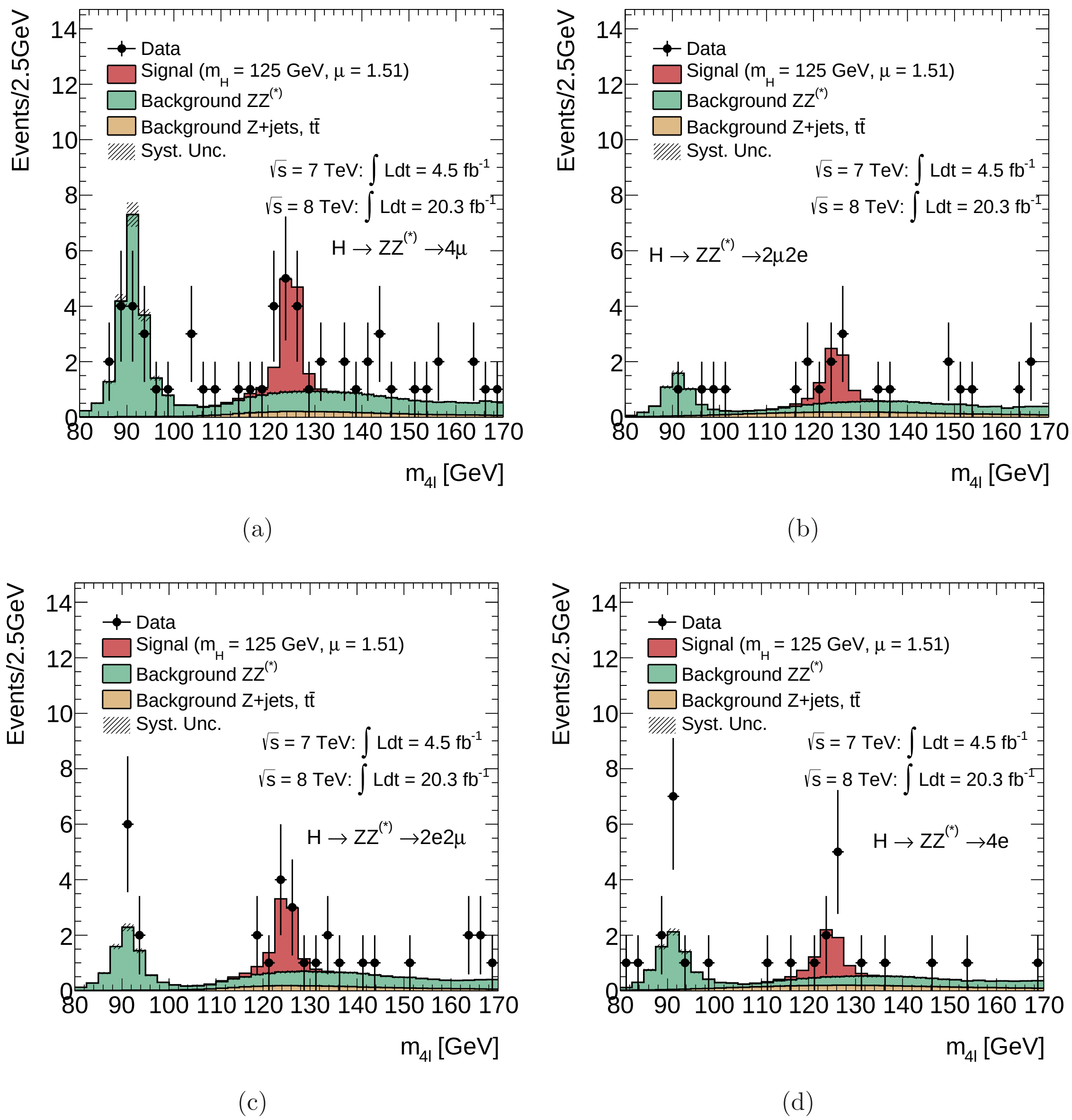

Figure 5.24: Display of a 4μ candidate with mass $m_{4\ell} = 123.2$ GeV. All the muons of this events pass through one EndCap of the detector and two of the muons pass through the CSC detector.

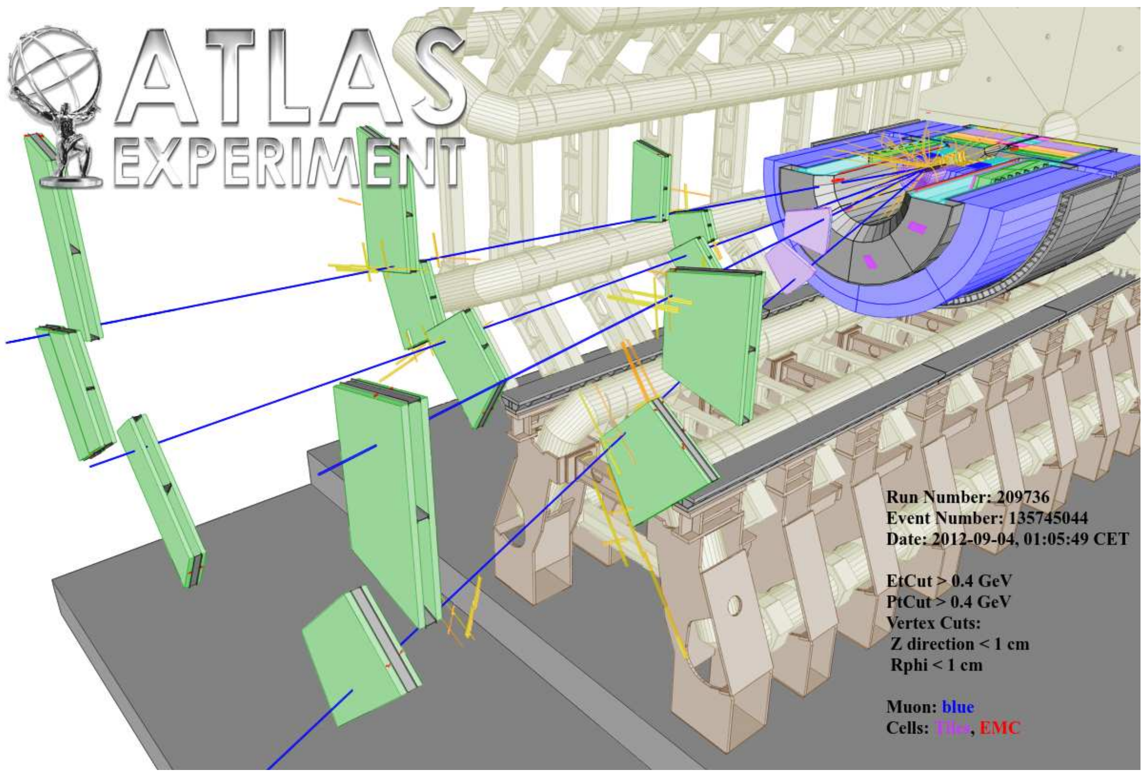

Chapter Bibliography

[1] LEP Working Group for Higgs boson searches, ALEPH, DELPHI, L3 and OPAL Collaborations, Search for the standard model Higgs boson at LEP, *Phys. Lett.*, B 565:61–75, 2003, hep-ex/0306033.

[2] The T.E.V.N.P.H..Working Group, Combined CDF and D0 Upper Limits on Standard Model Higgs-Boson Production with up to 6.7 fb^{-1} of Data, 2010, 1007.4587.

[3] ATLAS Collaboration, Limits on the production of the Standard Model Higgs Boson in pp collisions at $\sqrt{s} = 7TeV$ with the ATLAS detector, *Eur. Phys. J.*, C 71:1728, 2011, 1106.2748.

[4] ATLAS Collaboration, ATLAS luminosity public results, https://twiki.cern.ch/twiki/bin/view/AtlasPublic/LuminosityPublicResults.

[5] ATLAS Collaboration, Data quality information public results, https://twiki.cern.ch/twiki/bin/view/AtlasPublic/RunStatsPublicResults2010.

[6] Simone Alioli, Paolo Nason, Carlo Oleari, and Emanuele Re, NLO Higgs boson production via gluon fusion matched with shower in POWHEG, *JHEP*, 04:002, 2009, 0812.0578.

[7] Paolo Nason and Carlo Oleari, NLO Higgs boson production via vector-boson fusion matched with shower in POWHEG, *JHEP*, 02:037, 2010, 0911.5299.

[8] Daniel de Florian and Massimiliano Grazzini, Higgs production at the LHC: updated cross sections at $\sqrt{s} = 8$ TeV, *Phys.Lett.*, B718:117–120, 2012, 1206.4133.

[9] Torbjorn Sjostrand, Stephen Mrenna, and Peter Z. Skands, PYTHIA 6.4 Physics and Manual, *JHEP*, 05:026, 2006, hep-ph/0603175.

[10] Piotr Golonka and Zbigniew Was, PHOTOS Monte Carlo: A Precision tool for QED corrections in Z and W decays, *Eur. Phys. J.*, C 45:97–107, 2006, hep-ph/0506026.

[11] S. Dittmaier et al., Handbook of LHC Higgs Cross Sections: 1. Inclusive Observables, 2011, 1101.0593.

[12] S. Dittmaier, S. Dittmaier, C. Mariotti, G. Passarino, R. Tanaka, et al., Handbook of LHC Higgs Cross Sections: 2. Differential Distributions, 2012, 1201.3084.

[13] A. Djouadi, M. Spira, and P. M. Zerwas, Production of Higgs bosons in proton colliders: QCD corrections, *Phys. Lett.*, B 264:440–446, 1991.

[14] S. Dawson, Radiative corrections to Higgs boson production, *Nucl. Phys.*, B 359:283–300, 1991.

[15] M. Spira, A. Djouadi, D. Graudenz, and P. M. Zerwas, Higgs boson production at the LHC, *Nucl. Phys.*, B 453:17–82, 1995, hep-ph/9504378.

[16] Robert V. Harlander and William B. Kilgore, Next-to-next-to-leading order Higgs production at hadron colliders, *Phys. Rev. Lett.*, 88:201801, 2002, hep-ph/0201206.

[17] Charalampos Anastasiou and Kirill Melnikov, Higgs boson production at hadron colliders in NNLO QCD, *Nucl. Phys.*, B 646:220–256, 2002, hep-ph/0207004.

[18] V. Ravindran, J. Smith, and W. L. van Neerven, NNLO corrections to the total cross-section for Higgs boson production in hadron hadron collisions, *Nucl.Phys.*, B665:325–366, 2003, hep-ph/0302135.

[19] Stefano Catani, Daniel de Florian, Massimiliano Grazzini, and Paolo Nason, Soft gluon resummation for Higgs boson production at hadron colliders, *JHEP*, 0307:028, 2003, hep-ph/0306211.

[20] U. Aglietti, R. Bonciani, G. Degrassi, and A. Vicini, Two loop light fermion contribution to Higgs production and decays, *Phys.Lett.*, B595:432–441, 2004, hep-ph/0404071.

[21] Stefano Actis, Giampiero Passarino, Christian Sturm, and Sandro Uccirati, NLO Electroweak Corrections to Higgs Boson Production at Hadron Colliders, *Phys.Lett.*, B670:12–17, 2008, 0809.1301.

[22] D. de Florian and M. Grazzini, Higgs production at the LHC: updated cross sections at $\sqrt{s} = 8\ TeV$, 2012, 1206.4133.

[23] Charalampos Anastasiou, Stephan Buehler, Franz Herzog, and Achilleas Lazopoulos, Inclusive Higgs boson cross-section for the LHC at 8 TeV, *JHEP*, 1204:004, 2012, 1202.3638.

[24] Julien Baglio and Abdelhak Djouadi, Higgs production at the lHC, *JHEP*, 1103:055, 2011, 1012.0530.

[25] M. Ciccolini, Ansgar Denner, and S. Dittmaier, Strong and electroweak corrections to the production of Higgs + 2jets via weak interactions at the LHC, *Phys.Rev.Lett.*, 99:161803, 2007, 0707.0381.

[26] Mariano Ciccolini, Ansgar Denner, and Stefan Dittmaier, Electroweak and QCD corrections to Higgs production via vector-boson fusion at the LHC, *Phys.Rev.*, D77:013002, 2008, 0710.4749.

[27] K. Arnold, M. Bahr, Giuseppe Bozzi, F. Campanario, C. Englert, et al., VBFNLO: A Parton level Monte Carlo for processes with electroweak bosons, *Comput.Phys.Commun.*, 180:1661–1670, 2009, 0811.4559.

[28] Paolo Bolzoni, Fabio Maltoni, Sven-Olaf Moch, and Marco Zaro, Higgs production via vector-boson fusion at NNLO in QCD, *Phys.Rev.Lett.*, 105:011801, 2010, 1003.4451.

[29] Tao Han and S. Willenbrock, QCD correction to the $pp \rightarrow WH$ and Z H total cross-sections, *Phys.Lett.*, B273:167–172, 1991.

[30] Oliver Brein, Abdelhak Djouadi, and Robert Harlander, NNLO QCD corrections to the Higgs-strahlung processes at hadron colliders, *Phys.Lett.*, B579:149–156, 2004, hep-ph/0307206.

[31] M.L. Ciccolini, S. Dittmaier, and M. Kramer, Electroweak radiative corrections to associated WH and ZH production at hadron colliders, *Phys.Rev.*, D68:073003, 2003, hep-ph/0306234.

[32] Z. Kunszt, Associated Production of Heavy Higgs Boson with Top Quarks, *Nucl.Phys.*, B247:339, 1984.

[33] W. Beenakker, S. Dittmaier, M. Kramer, B. Plumper, M. Spira, et al., Higgs radiation off top quarks at the Tevatron and the LHC, *Phys.Rev.Lett.*, 87:201805, 2001, hep-ph/0107081.

[34] W. Beenakker, S. Dittmaier, M. Kramer, B. Plumper, M. Spira, et al., NLO QCD corrections to t anti-t H production in hadron collisions, *Nucl.Phys.*, B653:151–203, 2003, hep-ph/0211352.

[35] S. Dawson, L.H. Orr, L. Reina, and D. Wackeroth, Associated top quark Higgs boson production at the LHC, *Phys.Rev.*, D67:071503, 2003, hep-ph/0211438.

[36] S. Dawson, C. Jackson, L.H. Orr, L. Reina, and D. Wackeroth, Associated Higgs production with top quarks at the large hadron collider: NLO QCD corrections, *Phys.Rev.*, D68:034022, 2003, hep-ph/0305087.

[37] A. Djouadi, J. Kalinowski, and M. Spira, HDECAY: A Program for Higgs boson decays in the standard model and its supersymmetric extension, *Comput.Phys.Commun.*, 108:56–74, 1998, hep-ph/9704448.

[38] A. Bredenstein, Ansgar Denner, S. Dittmaier, and M.M. Weber, Precise predictions for the Higgs-boson decay $H \rightarrow WW/ZZ \rightarrow to4$ leptons, *Phys.Rev.*, D74:013004, 2006, hep-ph/0604011.

[39] A. Bredenstein, Ansgar Denner, S. Dittmaier, and M.M. Weber, Radiative corrections to the semileptonic and hadronic Higgs-boson decays $H \to WW/ZZ \to 4$ fermions, *JHEP*, 0702:080, 2007, hep-ph/0611234.

[40] Michiel Botje, Jon Butterworth, Amanda Cooper-Sarkar, Albert de Roeck, Joel Feltesse, et al., The PDF4LHC Working Group Interim Recommendations, 2011, 1101.0538.

[41] Hung-Liang Lai, Marco Guzzi, Joey Huston, Zhao Li, Pavel M. Nadolsky, et al., New parton distributions for collider physics, *Phys.Rev.*, D82:074024, 2010, 1007.2241.

[42] A.D. Martin, W.J. Stirling, R.S. Thorne, and G. Watt, Parton distributions for the LHC, *Eur.Phys.J.*, C63:189–285, 2009, 0901.0002.

[43] Richard D. Ball, Valerio Bertone, Francesco Cerutti, Luigi Del Debbio, Stefano Forte, et al., Impact of Heavy Quark Masses on Parton Distributions and LHC Phenomenology, *Nucl.Phys.*, B849:296–363, 2011, 1101.1300.

[44] Sergey Alekhin, Simone Alioli, Richard D. Ball, Valerio Bertone, Johannes Blumlein, et al., The PDF4LHC Working Group Interim Report, 2011, 1101.0536.

[45] Tom Melia, Paolo Nason, Raoul Rontsch, and Giulia Zanderighi, W+W-, WZ and ZZ production in the POWHEG BOX, *JHEP*, 1111:078, 2011, 1107.5051.

[46] T. Binoth, N. Kauer, and P. Mertsch, Gluon-induced QCD corrections to pp$\to$ $ZZ \to$ l anti-l l-prime anti-l-prime, page 142, 2008, 0807.0024.

[47] Michelangelo L. Mangano, Mauro Moretti, Fulvio Piccinini, Roberto Pittau, and Antonio D. Polosa, ALPGEN, a generator for hard multiparton processes in hadronic collisions, *JHEP*, 0307:001, 2003, hep-ph/0206293.

[48] Michelangelo L. Mangano, Mauro Moretti, Fulvio Piccinini, and Michele Treccani, Matching matrix elements and shower evolution for top-quark production in hadronic collisions, *JHEP*, 0701:013, 2007, hep-ph/0611129.

[49] Kirill Melnikov and Frank Petriello, Electroweak gauge boson production at hadron colliders through O(alpha(s)**2), *Phys.Rev.*, D74:114017, 2006, hep-ph/0609070.

[50] Charalampos Anastasiou, Lance J. Dixon, Kirill Melnikov, and Frank Petriello, High precision QCD at hadron colliders: Electroweak gauge boson rapidity distributions at NNLO, *Phys.Rev.*, D69:094008, 2004, hep-ph/0312266.

[51] John M. Campbell and R.K. Ellis, MCFM for the Tevatron and the LHC, *Nucl.Phys.Proc.Suppl.*, 205-206:10–15, 2010, 1007.3492.

[52] S. Jadach, Z. Was, R. Decker, and Johann H. Kuhn, The tau decay library TAUOLA: Version 2.4, *Comput.Phys.Commun.*, 76:361–380, 1993.

[53] P. Golonka, B. Kersevan, T. Pierzchala, E. Richter-Was, Z. Was, et al., The Tauola photos F environment for the TAUOLA and PHOTOS packages: Release. 2., *Comput.Phys.Commun.*, 174:818–835, 2006, hep-ph/0312240.

[54] T. Gleisberg, Stefan. Hoeche, F. Krauss, M. Schonherr, S. Schumann, et al., Event generation with SHERPA 1.1, *JHEP*, 0902:007, 2009, 0811.4622.

[55] G. Aad et al., The ATLAS Simulation Infrastructure, *Eur.Phys.J.*, C70:823–874, 2010, 1005.4568.

[56] S. Agostinelli et al., GEANT4: A Simulation toolkit, *Nucl.Instrum.Meth.*, A506:250–303, 2003.

[57] Georges Aad et al., Electron reconstruction and identification efficiency measurements with the ATLAS detector using the 2011 LHC proton-proton collision data, *Eur.Phys.J.*, C74(7):2941, 2014, 1404.2240.

[58] Improved electron reconstruction in ATLAS using the Gaussian Sum Filter-based model for bremsstrahlung, 2012, ATLAS-CONF-2012-047, ATLAS-COM-CONF-2012-068.

[59] Georges Aad et al., Electron and photon energy calibration with the ATLAS detector using LHC Run 1 data, *Eur.Phys.J.*, C74(10):3071, 2014, 1407.5063.

[60] P. Speckmayer, A. Hocker, J. Stelzer, and H. Voss, The toolkit for multivariate data analysis, TMVA 4, *J.Phys.Conf.Ser.*, 219:032057, 2010.

[61] Georges Aad et al., Measurement of the muon reconstruction performance of the ATLAS detector using 2011 and 2012 LHC proton-proton collision data, *Eur.Phys.J.*, C74(11):3130, 2014, 1407.3935.

[62] G. Aad et al., Expected Performance of the ATLAS Experiment - Detector, Trigger and Physics, 2009, 0901.0512.

[63] Muon Reconstruction Performance, 2010, ATLAS-CONF-2010-064, ATLAS-COM-CONF-2010-065.

[64] A measurement of the ATLAS muon reconstruction and trigger efficiency using J/psi decays, 2011, ATLAS-CONF-2011-021, ATLAS-COM-CONF-2011-002.

[65] Reconstruction of collinear final-state-radiation photons in Z decays to muons in sqrts=7 TeV proton-proton collisions., Technical Report ATLAS-CONF-2012-143, CERN, Geneva, Nov 2012.

[66] Wouter Verkerke and David P. Kirkby, The RooFit toolkit for data modeling, *eConf*, C0303241:MOLT007, 2003, physics/0306116.

[67] The ATLAS collaboration, Electron efficiency measurements with the ATLAS detector using the 2012 LHC proton-proton collision data, 2014, ATLAS-CONF-2014-032, ATLAS-COM-CONF-2014-030.

[68] The ATLAS collaboration, Preliminary results on the muon reconstruction efficiency, momentum resolution, and momentum scale in ATLAS 2012 pp collision data, 2013, ATLAS-CONF-2013-088, ATLAS-COM-CONF-2013-096.

[69] Georges Aad et al., Improved luminosity determination in pp collisions at $\sqrt{s} =$ 7 TeV using the ATLAS detector at the LHC, *Eur.Phys.J.*, C73(8):2518, 2013, 1302.4393.

[70] Georges Aad et al., Measurement of the Higgs boson mass from the $H \to \gamma\gamma$ and $H \to ZZ^* \to 4\ell$ channels with the ATLAS detector using 25 fb^{-1} of pp collision data, *Phys.Rev.*, D90:052004, 2014, 1406.3827.

[71] ATLAS Collaboration, Luminosity public results - 2011 pp collisions, https://twiki.cern.ch/twiki/bin/view/AtlasPublic/LuminosityPublicResults.

[72] Muon Momentum Resolution in First Pass Reconstruction of pp Collision Data Recorded by ATLAS in 2010, 2011, ATLAS-CONF-2011-046, ATLAS-COM-CONF-2011-003.

[73] Muon reconstruction efficiency in reprocessed 2010 LHC proton-proton collision data recorded with the ATLAS detector, 2011, ATLAS-CONF-2011-063, ATLAS-COM-CONF-2011-068.

[74] R. Fruhwirth, Track fitting with nonGaussian noise, *Comput.Phys.Commun.*, 100:1–16, 1997.

6

Study of the $H \rightarrow ZZ^{(*)} \rightarrow 4\ell$ Production Mechanisms

6.1 Introduction

The Higgs signal candidates identified in the previous Chapter 5 are studied to reveal the mechanism that generates them. At the LHC, the dominant production mechanism for a Standard Model Higgs boson is the gluons fusion (denoted as ggF for simplicity) with an expected cross section of (19.27 ± 2.9) pb for a Higgs boson with mass $m_H = 125$ GeV at $\sqrt{s} = 8$ TeV. The second biggest contribution to the total cross section is given by the vector boson fusion (VBF) process, where the Higgs boson is produced together with two energetic jets with large rapidity gap. The third production mechanism of interest is the associated production with a vector boson (VH) and the lowest cross section contributions are the associated production with a $b\bar{b}$ pair (bbH) and a $t\bar{t}$ pair (ttH). In Table 6.1 the cross sections for the various production mechanisms of a Higgs boson with mass $m_H = 125$ GeV are reported at both $\sqrt{s} = 7$ TeV and $\sqrt{s} = 8$ TeV [1]. Measuring the production cross section for each of these processes is an important test of the Standard Model of the Higgs boson (introduced in Chapter 1).

The events selected as Higgs candidates (Chapter 5) are classified in four different categories: *VBF-like*, *hadronic VH-like*, *leptonic VH-like* and *ggF-like*. For the Run-I, the $b\bar{b}H$ and $t\bar{t}H$ productions are not studied because of their small cross section. The background is measured with data driven techniques in the different categories, with

Table 6.1: Higgs boson ($m_H = 125$ GeV) production cross sections for ggF, VBF, VH, $b\bar{b}H$ and $t\bar{t}H$ processes, for both $\sqrt{s} = 7$ TeV and $\sqrt{s} = 8$ TeV [1].

	$\sqrt{s} = 7$ TeV		$\sqrt{s} = 8$ TeV	
Production mechanism	cross section [pb]	fraction of total [%]	cross section [pb]	fraction of total [%]
$gg \to H$	15.1	86.4	19.3	86.4
$qq' \to Hqq'$	1.22	7.0	1.58	7.1
$q\bar{q} \to WH$	0.579	3.3	0.705	3.2
$q\bar{q} \to ZH$	0.335	1.9	0.415	1.9
$q\bar{q}/gg \to t\bar{t}H$	0.086	0.5	0.13	0.6

focus on the muon background. The data driven method is based on the simultaneous fit used for the inclusive analysis. The measured candidates in each category are compared to the Standard Model expectations stemming from the different production mechanisms.

Important role of this study play the jets selection and their uncertainties. Jets selection and the corresponding uncertainties are crucial for this study. Therefore, this chapter starts with a summary of the jets reconstruction and identification.

6.2 Jet Identification and Reconstruction

Jets are reconstructed from topological clusters [2] using an anti-k_T algorithm [3] with a distance parameter $R = 0.4$. The topological clusters are then corrected from the electromagnetic scale to the hadronic energy scale using a p_T- and η-dependent jet energy scale (JES) determined from Monte Carlo simulation (2011) and from data (2012). The latter significantly decreases the associated uncertainty.

Dedicated correction methods addressing contributions from in-time and out-of-time pile-up to jets in the calorimeters have been developed using a MC simulation-based approach to measure the change of the jet signal as function of the characteristic variables measuring the pile-up activity, which are the number of reconstructed primary vertexes NPV (in-time pile-up) and the average number of pile-up interactions per bunch crossing μ (out-of-time pile-up).

The pile-up correction was also improved for the full 2012 dataset, based on the jet area and event p_T density, which results in reduced pile-up uncertainties, improves jet energy resolution at low p_T, and provides higher suppression of fake pile-up jets. Jets originating from pile-up are removed by requiring that at least 50% (75% for 2011) of

Table 6.2: Summary of jets selection for 7 TeV and 8 TeV data and Monte Carlo.

Selection criteria	Data 2011	Data 2012
Identification	Anti-k_T $R = 0.4$ topological jets	Anti-k_T $R = 0.4$ topological jets
Kinematic cuts	$p_T > 25$ GeV (30 GeV) $\lvert\eta\rvert < 2.5$ (> 2.5)	$p_T > 25$ GeV (30 GeV) $\lvert\eta\rvert < 2.5$ (> 2.5)
Quality	Looser quality cuts	Looser quality cuts
pile-up	$\lvert JVF\rvert > 0.5$	$\lvert JVF\rvert > 0.75$

the tracks associated to the jet (within $\Delta R = 0.4$ around the jet axis) must originate from the primary vertex. This is implemented as a cut on the absolute value of the "jet vertex fraction", respectively $|JVF| > 0.75$ for 7 TeV and $|JVF| > 0.5$ for 8 TeV data and Monte Carlo.

As a pre-selection cut, the jets are required to have $p_T > 25$ GeV for $|\eta| < 2.5$ and $p_T > 30$ GeV for $2.5 < |\eta| < 4.5$. To avoid double-counting objects in the event, a jet is removed if an electron, satisfying the criteria of the Section 5.4, is found within $\Delta R < 0.2$ around the jet axis. The jet selection is summarized in Table 6.2 for the 2011 and 2012 dataset.

6.3 Definition of Categories

6.3.1 VBF-like Section

The classification process starts by testing the event for VBF-like properties. VBF-like events are selected by requiring the Higgs candidate to be accompanied by at least two energetic jets passing the pre-selection criteria listed in Section 6.2. If more than two jets fulfill these requirements, the two highest p_T jets are tagged as VBF jets. In order to increase the purity of this category, the di-jet mass is required to be greater than 130 GeV. The efficiency of the simple requirement of two jets in the event is 62% for the VBF production mechanism while the efficiency of the VBF-specific cuts is $\sim 55\%$. This category has also a considerable contamination from ggF events, specifically 58% of the ggF events pass the VBF selection. To cope with this, a multi-variate discriminant is developed to improve the sensitivity of the couplings fit.

The boosted decision tree (BDT)with gradient boost is used to discriminate VBF against other production mechanisms, specifically the $ZZ^{(*)}$ background and the ggF production. The training is performed using POWHEG+PYTHIA8 ggF and VBF samples and the $ZZ^{(*)}$ samples used for the inclusive analysis. The following variables are used to build the multi-variate discriminant:

- Invariant mass of the di-jet system (after applying $m_{JJ} > 130$ GeV pre-selection)
- pseudo-rapidity separation between the two jets
- transverse momentum of both jets
- pseudo-rapidity of the leading (i.e. the highest p_T) jet.

The separation provided by the variable x, is calculated via the integral:

$$\frac{1}{2}\int \frac{(\hat{x}_S(x) - \hat{x}_B(x))^2}{\hat{x}_S(x) + \hat{x}_B(x)} \tag{6.1}$$

where $\hat{x}_S(x)$ and $\hat{x}_B(x)$ are the signal and background PDFs. Table 6.3 shows the separation strength of this variables, together with their importance which is calculated by counting how many times this variable has been used in the splitting of a node. Each of these counts is then weighted with the number of events belonging to the specific node and the separation gain-squared provided by the node. This is a method that takes into account correlations between the inputs which are not accounted for by the simple ranking based on the separation.

Table 6.3: Results of the variables ranking performed by the VBF BDT for its discrimination against the ggF and the $ZZ^{(*)}$. For each input variable, both the separation and the importance are specified together with their ranking.

Variable	Separation (Rank)	Importance (Rank)
m_{JJ}	0.220 (1)	0.1937 (4)
$\Delta\eta_{JJ}$	0.155 (2)	0.2092 (2)
Leading jet p_T	0.033 (3)	0.1906 (5)
Sub-leading jet p_T	0.032 (4)	0.1955 (3)
Leading jet η	0.027 (5)	0.2110 (1)

The variables used represent the minimal set of variables providing discrimination between VBF and the other production mechanisms. They are presented in Figure 6.1 and their correlations are shown in Figures 6.2, 6.3, 6.4 for the VBF, the ggF and the $ZZ^{(*)}$ respectively for the $\sqrt{s} = 8$ TeV data.

Figure 6.1: Distributions of VBF (red), ggF (blue) and $ZZ^{(*)}$ (magenta) events used in the training of the VBF boosted decision tree. The dijet invariant mass (a), the dijet η distance (b), the leading jet p_T (c), the subleading jet p_T (d) and the leading jet η (e) are presented. Histograms are normalized to the same area.

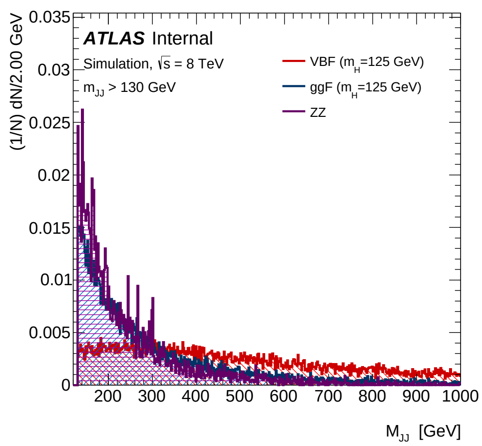

(a)

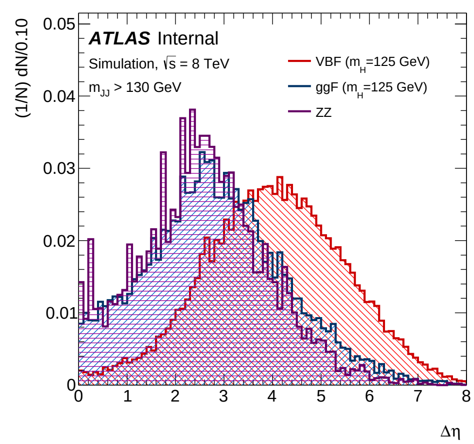

(b)

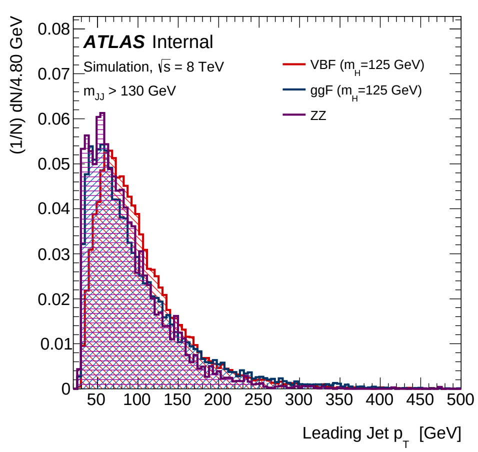

(c)

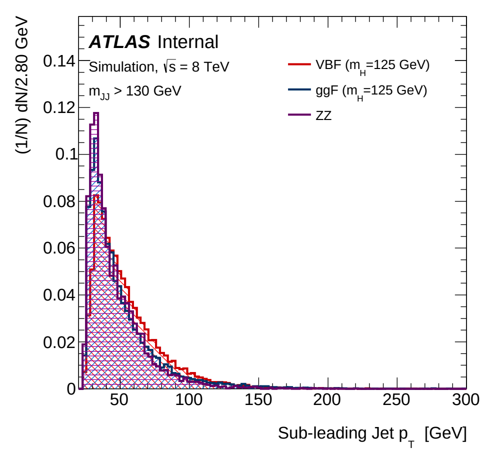

(d)

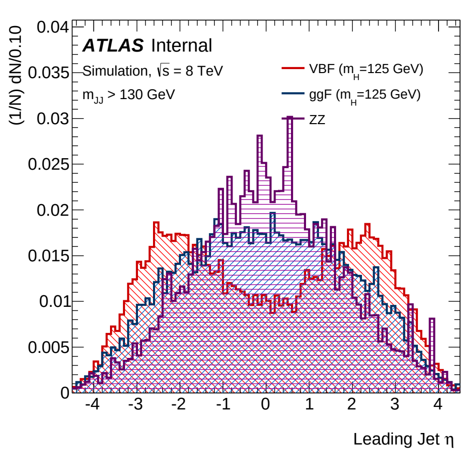

(e)

Figure 6.2: Correlations among the input variables used in the BDT for the VBF-like category, for VBF events.

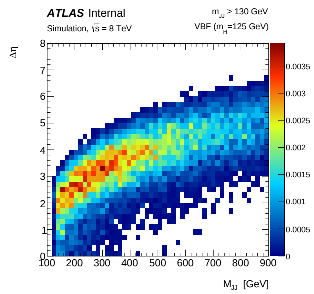

(a) m_{JJ} vs $\Delta\eta_{JJ}$

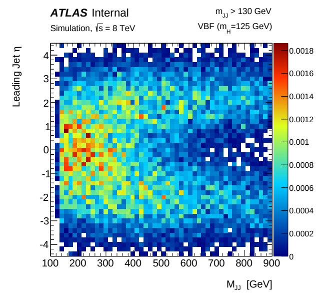

(b) m_{JJ} vs η_{lead}

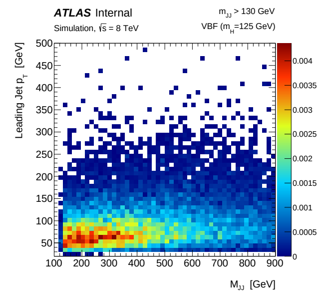

(c) m_{JJ} vs $p_{T\,lead}$

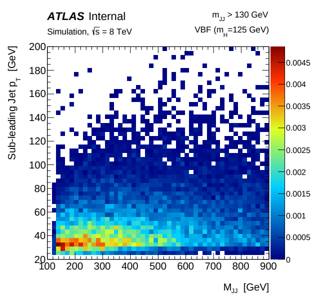

(d) m_{JJ} vs $p_{T\,sub}$

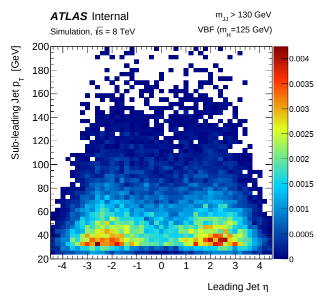

(e) η_{lead} vs $p_{T\,sub}$

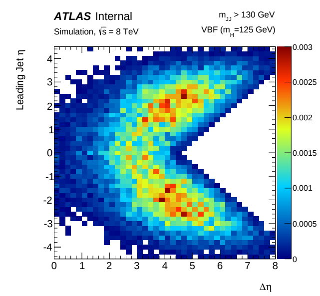

(f) $\Delta\eta_{JJ}$ vs η_{lead}

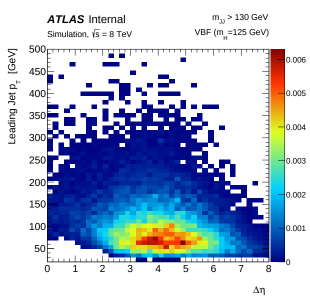

(g) $\Delta\eta_{JJ}$ vs $p_{T\,lead}$

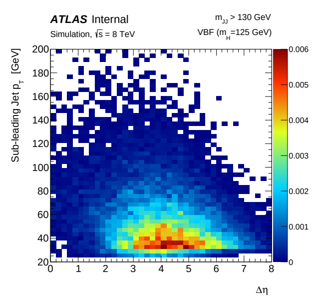

(h) $\Delta\eta_{JJ}$ vs $p_{T\,lead}$

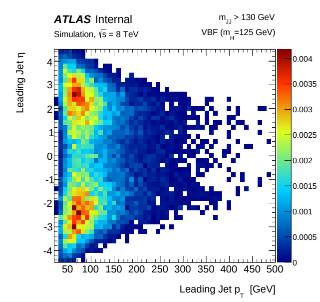

(i) $p_{T\,lead}$ vs η_{lead}

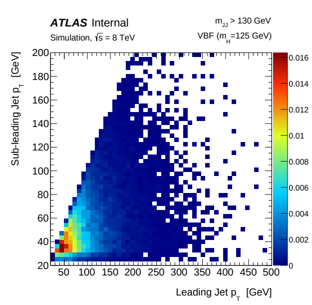

(j) $p_{T\,lead}$ vs $p_{T\,sub}$

Figure 6.3: Correlations among the input variables used in the BDT for the VBF-like category, for ggF events.

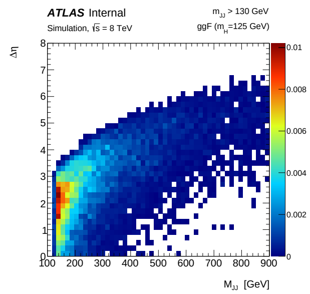

(a) m_{JJ} vs $\Delta\eta_{JJ}$

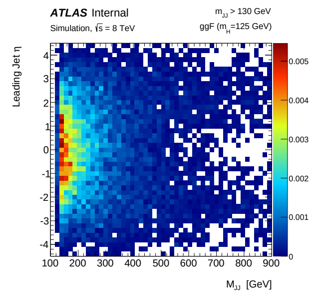

(b) m_{JJ} vs η_{lead}

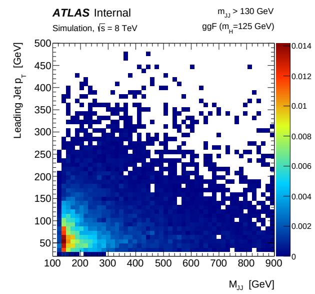

(c) m_{JJ} vs $p_{T\,lead}$

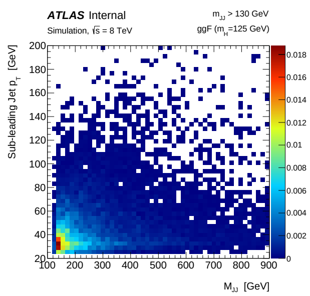

(d) m_{JJ} vs $p_{T\,sub}$

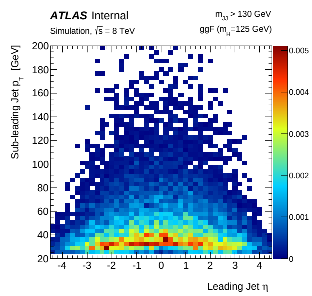

(e) η_{lead} vs $p_{T\,sub}$

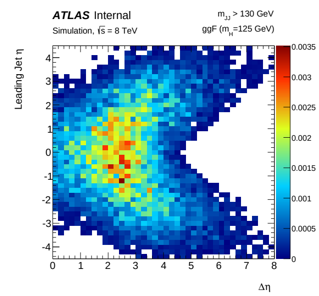

(f) $\Delta\eta_{JJ}$ vs η_{lead}

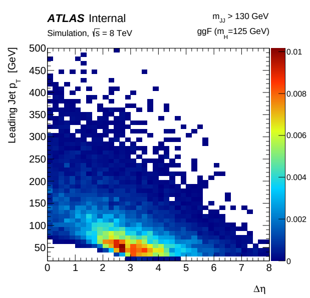

(g) $\Delta\eta_{JJ}$ vs $p_{T\,lead}$

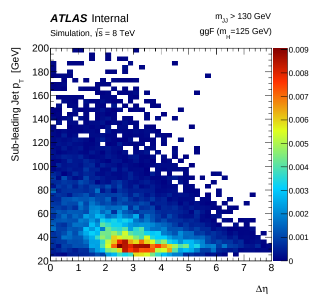

(h) $\Delta\eta_{JJ}$ vs $p_{T\,lead}$

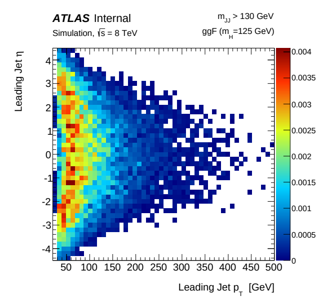

(i) $p_{T\,lead}$ vs η_{lead}

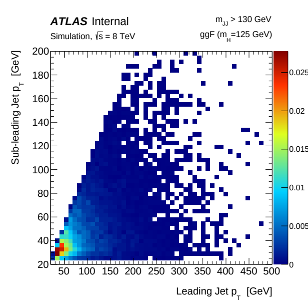

(j) $p_{T\,lead}$ vs $p_{T\,sub}$

Figure 6.4: Correlations among the input variables used in the BDT for the VBF-like category, for $ZZ^{(*)}$ events.

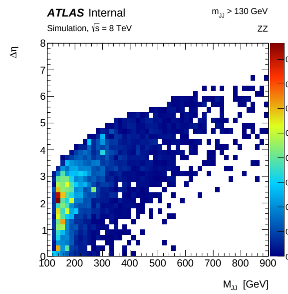

(a) m_{JJ} vs $\Delta\eta_{JJ}$

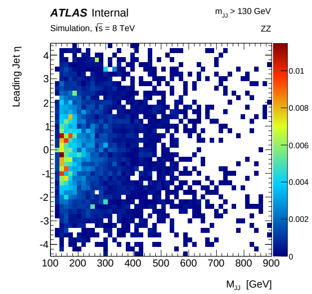

(b) m_{JJ} vs η_{lead}

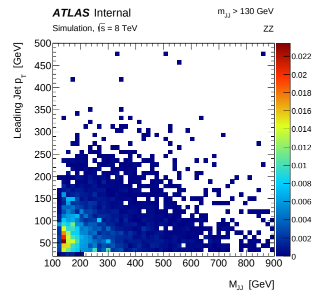

(c) m_{JJ} vs $p_{T lead}$

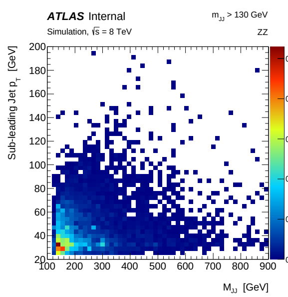

(d) m_{JJ} vs $p_{T sub}$

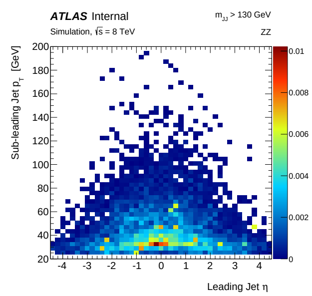

(e) η_{lead} vs $p_{T sub}$

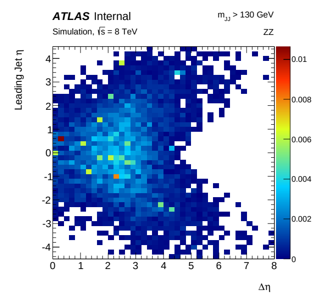

(f) $\Delta\eta_{JJ}$ vs η_{lead}

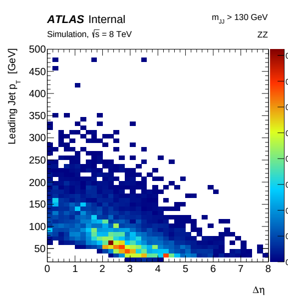

(g) $\Delta\eta_{JJ}$ vs $p_{T lead}$

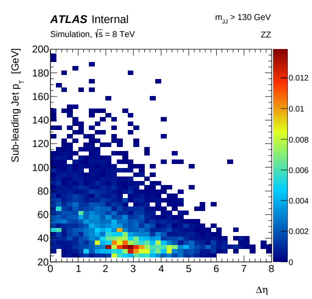

(h) $\Delta\eta_{JJ}$ vs $p_{T lead}$

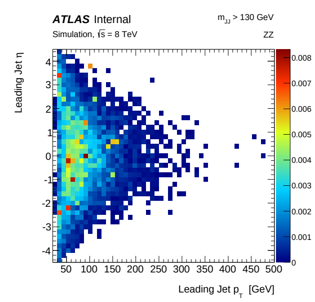

(i) $p_{T lead}$ vs η_{lead}

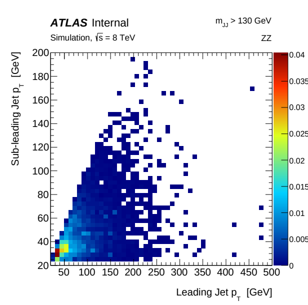

(j) $p_{T lead}$ vs $p_{T sub}$

In these plots the expected features of the vector-boson fusion production of a Higgs boson are visible. The di-jet system has a high invariant mass and the two jets are emitted in the forward region with a considerable $\Delta\eta$ separation between them. The ggF events, on the other hand, are more centrally produced with a smaller invariant mass and $\Delta\eta$ separation. The output of the BDT is shown in Figure 6.5 using different mass hypotheses, on the left for the vector boson fusion produced Higgs and on the right for the gluon fusion produced Higgs. The Figure also shows clearly that the output of the BDT discriminant has little dependence on the generated mass of the Higgs boson. This is exploited by using in the training all the samples with a Higgs boson generated mass between 123 and 127 GeV for the VBF and ggF processes. The direct VBF BDT output compared to the ggF and $ZZ^{(*)}$ backgrounds is shown in Figure 6.6.

Figure 6.5: BDT output for Higgs masses between 123 and 127 GeV for the vector boson fusion production mechanism on the left and for the gluon fusion production mechanism on the right.

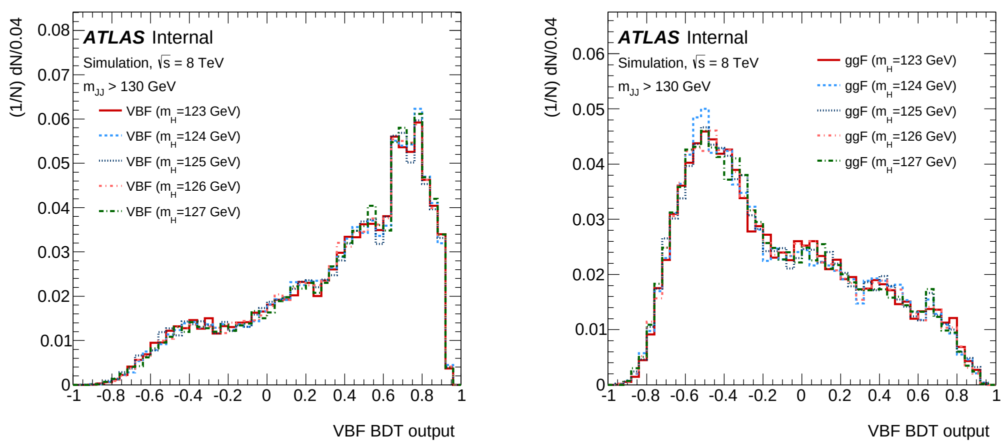

The BDT output is used as an observable together with the quadruplet mass ($m_{4\ell}$) in a maximum likelihood fit dedicated for the VBF category. Therefore, no BDT cut is chosen and no significance as a function of the BDT is shown.

6.3.2 Hadronic VH-like Selection

If the event does not fulfill the VBF criteria, then is tested for hadronic VH-like properties. Hadronic VH events are those where an electroweak boson is produced together with a Higgs boson and decays in hadrons. Experimentally, this results to the presence of two jets whose invariant mass peaks at either $m_{W^\pm} = 80.4$ GeV or

Figure 6.6: VBF BDT output distributions for the VBF compared to the $ZZ^{(*)}$ irreducible background and the ggF production. Histograms are normalized to the same area.

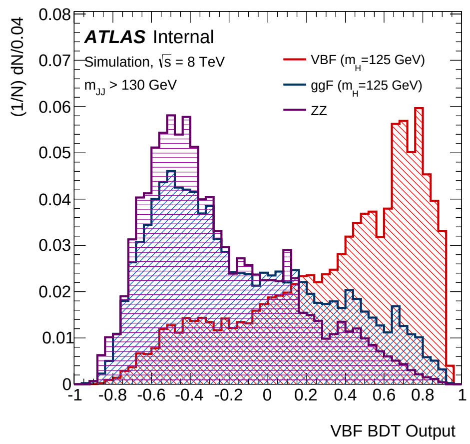

$m_Z = 91.2$ GeV (as Figure 6.7 shows). For this reason, a preliminary cut is applied on the invariant mass of the di-jet system and specifically it is required to be in the range of $40 - 130$ GeV. Events surviving the mass cuts are then passed through a multi-variate analysis (MVA) [4] to discriminate those coming from the associated production with an electroweak boson. The discriminant is built using a boosted decision tree with gradient boost, trained with the same variables as the VBF BDT tree.

These variables are presented in Figure 6.8 for the VH and the dominant ggF background. The ranking of these variables is shown in Table 6.4, for a training that is performed using merged samples with different generated Higgs masses of $m_H = 123, 124, 126, 127$ GeV. The correlations of the variables can be seen in Figures 6.9, 6.10 for the signal VH and the ggF background respectively. The BDT response and the efficiencies are shown in Figure 6.11. The cut used for the BDT is -0.432 for 2011 and -0.393 for 2012, in order for the ggF contamination to be the same. The VH efficiency after this selection is estimated to be $\sim 25\%$.

Figure 6.7: Invariant mass distribution of the dijet system for the hadronic WH (red) and ZH (blue) processes.

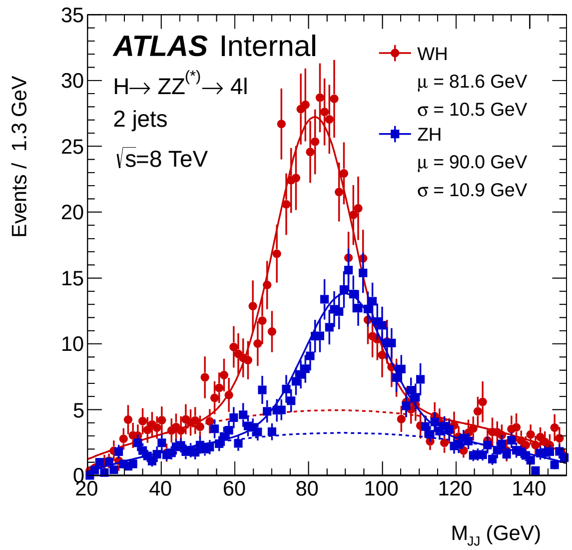

Table 6.4: Results of the variables ranking performed by the MVA for the hadronic VH category. For each input variable both the separation and the importance are specified, together with their ranking.

Variable	Separation (Rank)	Importance (Rank)
m_{JJ}	0.085 (1)	0.235 (1)
Sub-leading jet p_T	0.083 (2)	0.190 (4)
Leading jet p_T	0.055 (3)	0.204 (2)
$\Delta\eta_{JJ}$	0.047 (4)	0.191 (3)
Leading jet η	0.033 (5)	0.180 (5)

Figure 6.8: Distribution of the VH signal, i.e. WH and ZH, and the dominant ggF background at $\sqrt{s} = 8$ TeV used for the BDT discriminant. The figures show the di-jet mass (a), the η separation between the jets (b), the leading jet p_T (c), the subleading jet p_T (d) and the leading jet η (e).

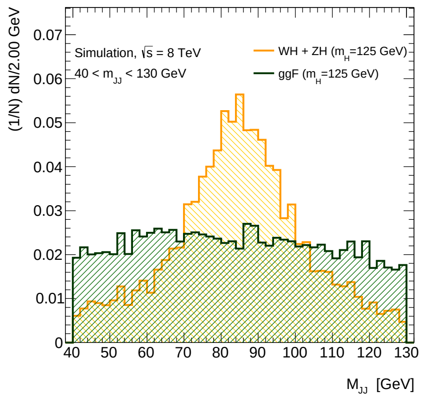

(a)

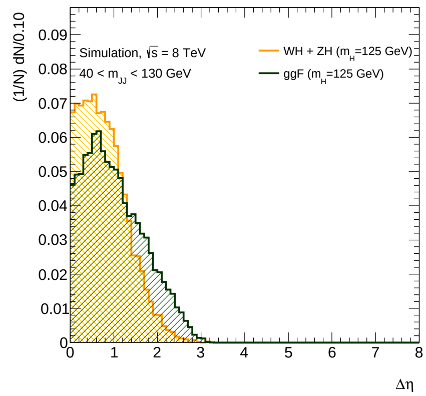

(b)

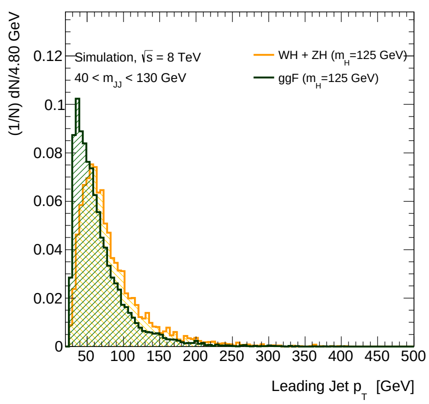

(c)

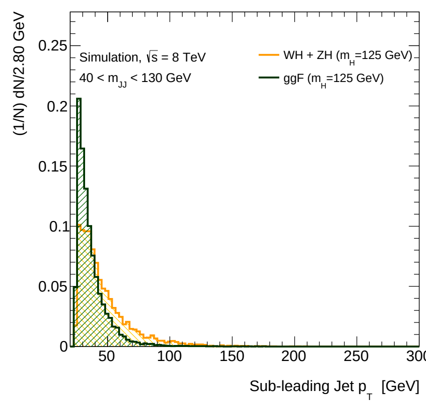

(d)

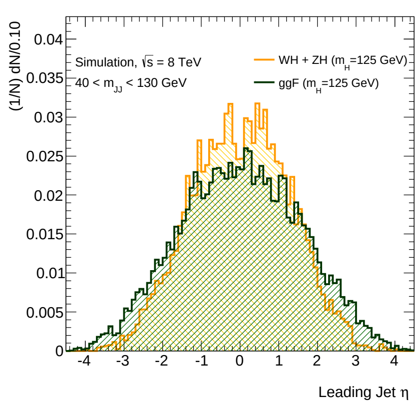

(e)

Figure 6.9: Correlations among the input variables used in the BDT for the hadronic-VH-like category, for VH events.

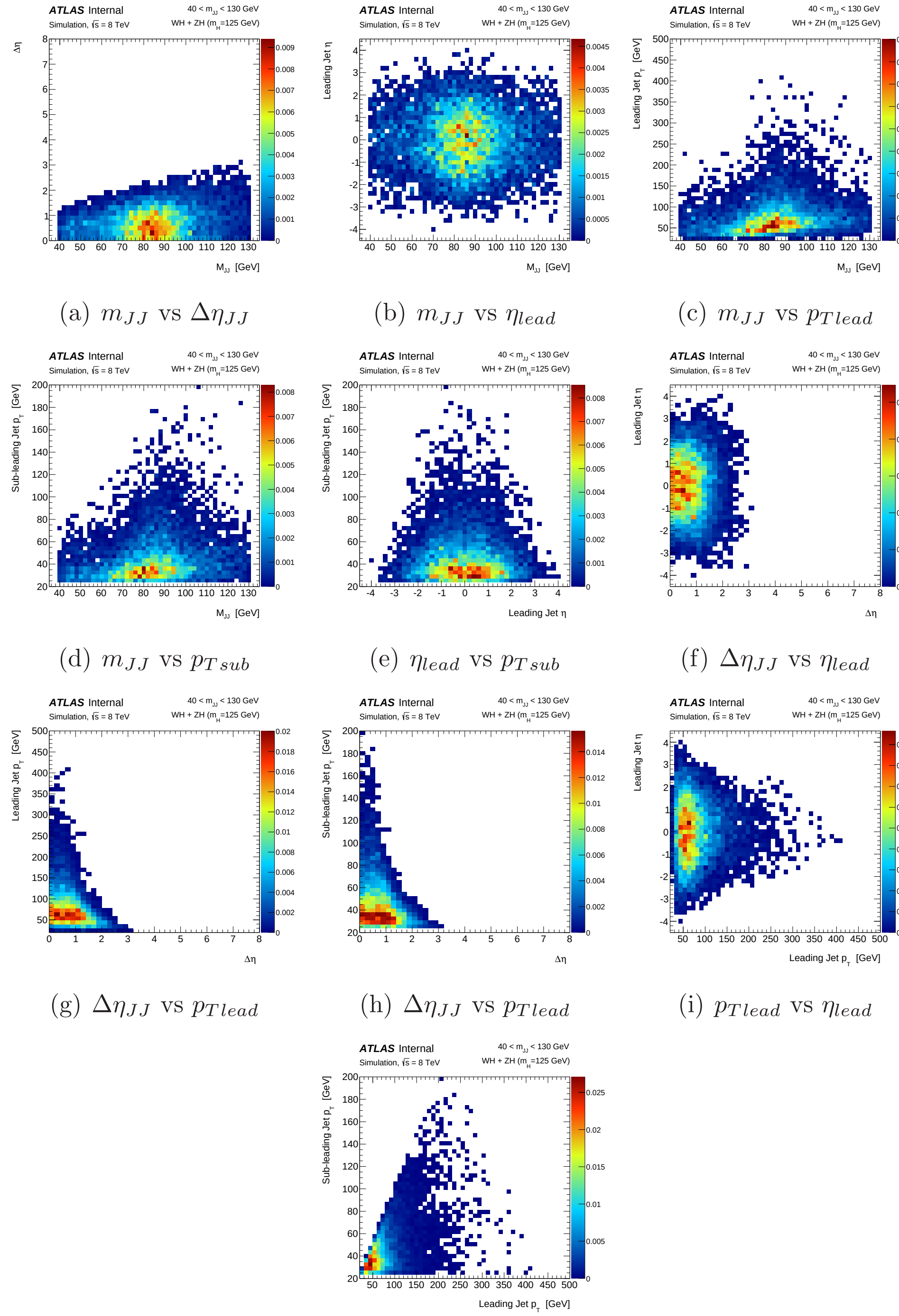

(a) m_{JJ} vs $\Delta\eta_{JJ}$

(b) m_{JJ} vs η_{lead}

(c) m_{JJ} vs $p_{T\,lead}$

(d) m_{JJ} vs $p_{T\,sub}$

(e) η_{lead} vs $p_{T\,sub}$

(f) $\Delta\eta_{JJ}$ vs η_{lead}

(g) $\Delta\eta_{JJ}$ vs $p_{T\,lead}$

(h) $\Delta\eta_{JJ}$ vs $p_{T\,lead}$

(i) $p_{T\,lead}$ vs η_{lead}

(j) $p_{T\,lead}$ vs $p_{T\,sub}$

Figure 6.10: Correlations among the input variables used in the BDT for the hadronic-VH-like category, for ggF events.

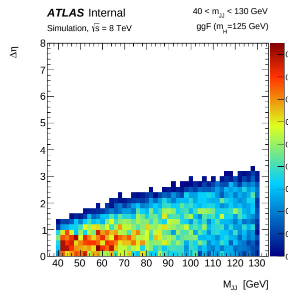

(a) m_{JJ} vs $\Delta\eta_{JJ}$

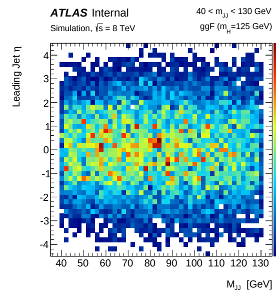

(b) m_{JJ} vs η_{lead}

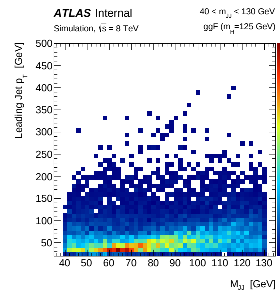

(c) m_{JJ} vs $p_{T lead}$

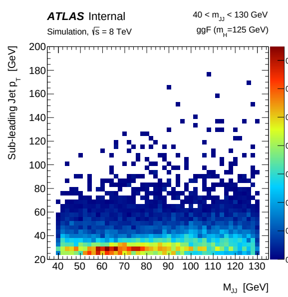

(d) m_{JJ} vs $p_{T sub}$

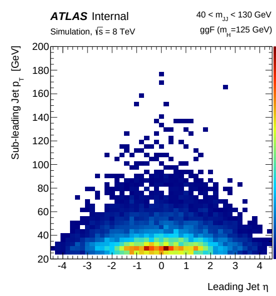

(e) η_{lead} vs $p_{T sub}$

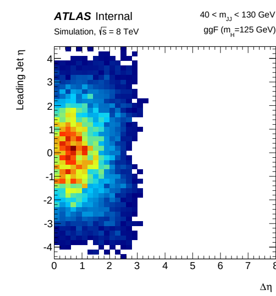

(f) $\Delta\eta_{JJ}$ vs η_{lead}

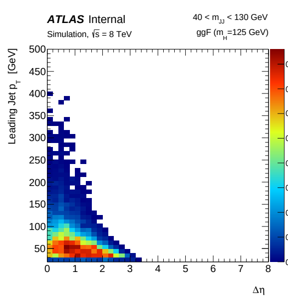

(g) $\Delta\eta_{JJ}$ vs $p_{T lead}$

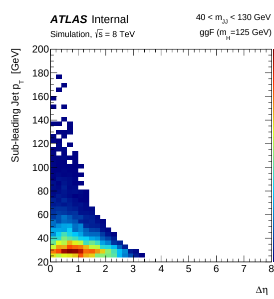

(h) $\Delta\eta_{JJ}$ vs $p_{T lead}$

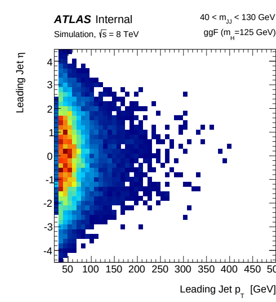

(i) $p_{T lead}$ vs η_{lead}

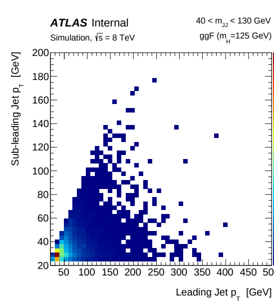

(j) $p_{T lead}$ vs $p_{T sub}$

6.3.3 Leptonic VH-like Selection

Events that are neither VBF nor VH-hadronic like are tested for the leptonic VH categorization. The presence of at least one extra lepton (e or μ) in addition to the four used to reconstruct the Higgs decay is required. To suppress backgrounds, this additional lepton should pass the standard lepton identification, has $p_T > 8$ GeV and satisfy the same isolation, impact parameter significance and ΔR requirements as the leptons from the Higgs decay (presented in Section 5.6). The efficiency of that for VH signal events at $m_H = 125$ GeV is $\sim 15\%$.

6.3.4 ggF-like Selection

If the event does not comply any of the previous selections then it is considered to be a ggF-like event.

6.4 Expected Yields and Signal MC

The efficiency of each selection used in the VBF-like and hadronic VH-like categories are presented in Table 6.5. The expected yields, after following the previously defined categorization, is presented in Table 6.6, in the range of $110 < m_H < 140$ GeV, assuming a Higgs mass of $m_H = 125$ GeV.

Table 6.5: The efficiency table for VBF-like and Hadronic VH-like specific cuts.

Production Mode	> 1 jet	$m_{jj} \in [40, 130]$ GeV	$m_{jj} > 130$ GeV	hadronic VH-like cuts
ggF	16%	6%	8%	2%
VBF	62%	5%	55%	2%
WH	48%	34%	12%	25%
ZH	48%	34%	11%	25%

The irreducible $ZZ^{(*)}$ background also contributes to the production mechanisms. The $ZZ^{(*)}$ continuum is modeled using POWHEG [5] for quark-antiquark annihilation and gg2ZZ [6] for gluon fusion. The mass-dependent PDF and α_s scale uncertainties are parametrized as recommended in Reference [7]. The QCD scale uncertainty has a $\pm 5\%$ effect on the expected $ZZ^{(*)}$ background at 125 GeV, and the effect due to the PDF and α_s uncertainties is $\pm 4\%$ ($\pm 8\%$) at 125 GeV for quark-initiated (gluon-initiated) processes. The EW production of the $ZZ^{(*)}$ with two jets down to $O(\alpha_W^6)$ is generated

Figure 6.11: The VH hadronic BDT response is presented for the $\sqrt{s} = 7$ TeV MC (a) and the 8 TeV (b). The cut values on the output are selected to be the points which give the same significance. The corresponding efficiencies are shown in Figures (c).

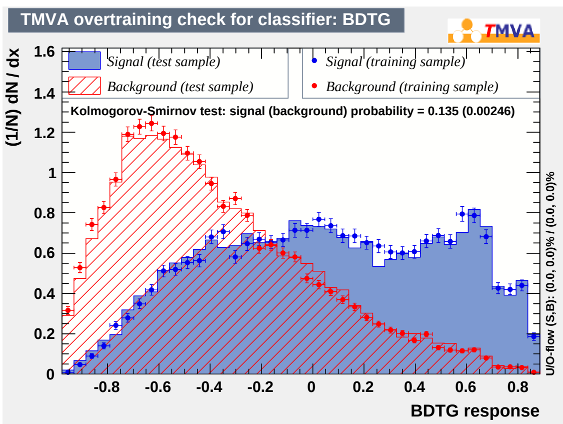

(a)

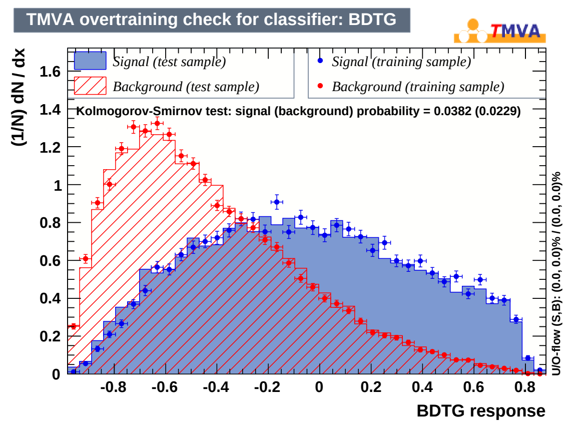

(b)

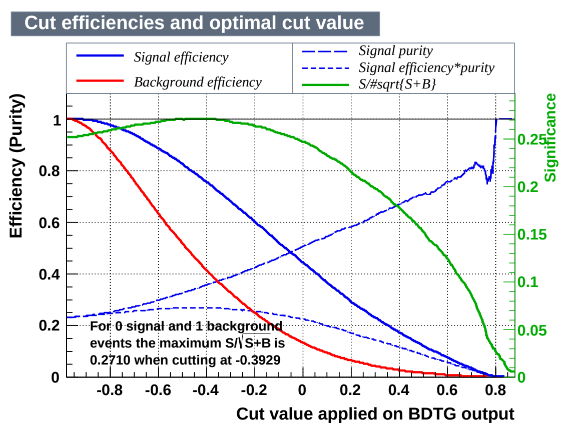

(c)

Table 6.6: Expected events in each category (ggF-like,VBF-like, hadronic VH-like, leptonic VH-like) assuming $m_H = 125$ GeV for the 2011 and 2012 data in the range of $110 < m_{4\ell} < 140$ GeV.

True Origin	**Category**			
	ggF-like	VBF-like	hadronic VH-like	leptonic VH-like
			$\sqrt{s} = 7$ TeV	
ggF	2.035	0.107	0.046	0.004
VBF	0.114	0.135	0.007	0.000
WH	0.034	0.009	0.023	0.011
ZH	0.026	0.005	0.014	0.002
$t\bar{t}H$	0.000	0.007	0.002	0.000
			$\sqrt{s} = 8$ TeV	
ggF	11.846	1.084	0.367	0.009
VBF	0.508	0.679	0.030	0.001
WH	0.195	0.059	0.124	0.062
ZH	0.148	0.035	0.080	0.010
$t\bar{t}$H	0.002	0.051	0.012	0.002

using SHERPA [8], in which the process $ZZZ \to 4\ell qq$ is also taken into account. The scale uncertainty is obtained by varying the factorization scale and renormalization scale by a factor of 4.0. The largest deviation from the nominal value, 6.5%, is considered as the corresponding uncertainty. Another source of theoretical uncertainty comes from the multi-jet criteria, specified by CKKW parameter, that defines which phase-space regions are populated by matrix elements and which ones by parton showers. Changing the CKKW from $\sqrt{20/E_{CMS}}$ to $\sqrt{30/E_{CMS}}$ and $\sqrt{10/E_{CMS}}$, leads to a largest deviation of $\sim 0.8\%$. Therefore the total uncertainties of ZZqq cross section is about 7.3%, which is treated as the theoretical uncertainty in the VBF-like category for the ZZ background.

The expected $ZZ^{(*)}$ background in the categories and in the range of $110 < m_H < 135$ GeV is presented in Table 6.7.

6.5 Reducible Background

The reducible background is estimated using the same methods as for the inclusive analysis, described in Section 5.10.2. Specifically the muons background is estimated by multiplying the estimated background in the inclusive analysis with the probability of

Table 6.7: Expected $ZZ^{(*)}$ background events in the range $110 < m_{4\ell} < 140$ GeV for the inclusive case (before any categorization selection), the VBF-like category, the VH-like categories and the ggF category for the 2011 data and 2012 data.

Category	**2012 Dataset**			**2011 Dataset**		
	$qq \to ZZ$	$gg \to ZZ$	SHERPA $ZZqq'$	$qq \to ZZ$	$gg \to ZZ$	SHERPA $ZZqq'$
Inclusive	16.51	0.27	0.07	3.169	0.082	0.011
VBF-like	0.398	0.0219	0.043	0.057	0.003	0.007
Hadronic VH-like	0.219	0.004	0.007	0.040	0.000	0.002
Leptonic VH-like	0.037	0.001	0.000	0.017	0.000	0.000
ggF-like	16.001	0.242	0.019	3.055	0.079	0.003

each background type to pass the selection of each category (estimated from the MC):

$$N^{SR}_{Category} = N^{SR} \times \frac{Inclusive\ MC\ Events\ Passing\ the\ Category\ Selection}{Inclusive\ MC\ Events}. \quad (6.2)$$

This fractions are presented in Table 6.8 for the $Zjets$ and $t\bar{t}$ backgrounds. The $Zb\bar{b}$ and $Zlight$ are treated together because of the limited statistics. The uncertainties correspond to the statistical MC uncertainties.

If the statistics allowed, a simultaneous fit could be performed on the reference OS CR which passes the category selection (separately for each category) without the application of the additional selection (isolation and impact parameter criteria). Then the fit estimations could be extrapolated to the SR events by the application of the transfer factors used in Chapter 5.

The estimated reducible background in the 4μ and $2e2\mu$ channels is presented in Table 6.9 for the 2012 and in Table 6.10 for the 2011 data. In summary, the total irreducible backgrounds is given in Table 6.11.

6.6 Systematic Uncertainties

The systematic uncertainties on the expected yields from the different processes contributing to the VBF, hadronic VH, leptonic VH and ggF categories are reported in Table 6.12, expressed as the fractional uncertainties on the yields. The uncertainties on the theoretical predictions for the cross sections for the different processes arise mainly from the requirement on the jet multiplicity used in the event categorization [9, 1]. Because of event migrations, this also affects the leptonic VH and the ggF categories, where no explicit requirement on jets is applied. The uncertainty accounting for a potential mismodeling of the underlying event is conservatively estimated with $Z \to \mu\mu$

Table 6.8: The expected yield and relative fractions, from the MC, of $Zjets$ and $t\bar{t}$ 4μ and $2e2\mu$ backgrounds.

Category	Z+jets	
	4μ (fraction)	2e2μ (fraction)
ggF-like	2.18 ± 0.09 (96.42%)	1.87 ± 0.17 (95.36%)
VBF-like	0.07 ± 0.13 (3.10%)	0.07 ± 0.13 (3.57%)
VH-hadronic-like	0.01 ± 0.12 (.44%)	0.02 ± 0.12 (1.02%)
VH-leptonic-like	0.001 ± 0.12 (.04%)	0.001 ± 0.12 (.05%))
Category	$t\bar{t}$	
	4μ (fraction)	2e2μ (fraction)
ggF-like	0.13 ± 0.05 (41.94%)	0.35 ± 0.07 (78.65%)
VBF-like	0.14 ± 0.05 (45.16%)	0.031 ± 0.015 (6.97%)
VH-hadronic-like	0.039 ± 0.027 (12.58%)	0.063 ± 0.025 (14.16%)
VH-leptonic-like	0.001 ± 0.014 (.32%)	0.001 ± 0.014 (.22%)

Table 6.9: Reducible background estimates in the signal region after the categories selection, for the 4μ and $2e2\mu$ channels in the 2012 data.

4μ		
Category	$Z + jets$	$t\bar{t}$
ggF-like	2.98 ± 0.67	0.33 ± 0.06
VBF-like	0.10 ± 0.02	0.14 ± 0.03
VH-hadronic-like	0.02 ± 0.005	0.05 ± 0.01
VH-leptonic-like	0.001 ± 0.001	0.001 ± 0.001
$2e2\mu$		
Category	$Z + jets$	$t\bar{t}$
ggF-like	2.47 ± 0.55	0.31 ± 0.06
VBF-like	0.09 ± 0.02	0.13 ± 0.02
VH-hadronic-like	0.02 ± 0.004	0.05 ± 0.01
VH-leptonic-like	0.001 ± 0.001	0.001 ± 0.001

Table 6.10: Reducible background estimates in the signal region after the categories selection, for the 4μ and $2e2\mu$ channels in the 2011 data.

	4μ	
Category	$Z + jets$	$t\bar{t}$
ggF-like	0.422 ± 0.243	0.051 ± 0.017
VBF-like	0.015 ± 0.008	0.022 ± 0.007
VH-hadronic-like	0.003 ± 0.002	0.007 ± 0.002
VH-leptonic-like	0.0002 ± 0.0001	~ 0
	$2e2\mu$	
ggF-like	0.288 ± 0.170	0.036 ± 0.017
VBF-like	0.010 ± 0.006	0.015 ± 0.005
VH-hadronic-like	0.002 ± 0.001	0.005 ± 0.002
VH-leptonic-like	0.0001 ± 0.0001	~ 0

Table 6.11: Summary of the background estimates in both the 4μ and $2e2\mu$ channels for the 2011 and 2012 years. The uncertainty quoted includes both statistical and systematic errors.

Year	ggF-like	VBF-like	VH-hadronic-like	VH-leptonic-like
2012	0.98 ± 0.32	0.12 ± 0.08	0.04 ± 0.02	0.004 ± 0.004
2011	6.71 ± 1.44	0.63 ± 0.59	0.21 ± 0.13	0.003 ± 0.003

simulated events by applying the selection for the VBF (or hadronic VH) category and taking the difference of the efficiencies with and without multiparton interactions.

The main experimental uncertainty is related to the jet energy scale determination, including the uncertainties associated with the modeling of the absolute and relative *in situ* jet calibrations, as well as the flavor composition of the jet sample. The impact on the yields of the various categories is anti-correlated because a variation of the jet energy scale results primarily in the migration of events among the categories. The impact of the jet energy scale uncertainty results in an uncertainty of about $\pm 10\%$ for the VBF category, $\pm 8\%$ for the hadronic VH category, $\pm 1.5\%$ for the leptonic VH category and $\pm 1.5\%$ for the ggF category.

The uncertainty on the jet energy resolution is also taken into account, even though its impact is small compared to that of the jet energy scale uncertainty, as reported in Table 6.12. Finally, the uncertainties associated with the additional leptons in the leptonic VH category are the same as already described in Chapter 5 for the four leptons of the Higgs boson decay.

6.7 Higgs Categorized Candidates

The numbers of expected and observed events in each of the categories previously described are summarized in Table 6.13. The expected yield in each enriched category is given for each of the production modes, where the ggF, $b\bar{b}H$ and $t\bar{t}H$ yields are combined. The expected and observed numbers of events are given for two $m_{4\ell}$ mass ranges: $120 - 130$ GeV and above 110 GeV. Three of the VBF candidates are found in the mass region $120 - 130$ GeV with invariant masses of 123.2 GeV, 123.4 GeV and 125.7 GeV.

Only one VBF candidate ($m_{4\ell} = 123.4$ GeV) has a BDT output value of 0.7. In this mass window, the expected number of VBF candidates with BDT output above zero is 1.26 ± 0.15, where half of this is expected to be from a true VBF signal, about 35% from ggF production and the rest is mostly from $ZZ^{(*)}$ and reducible backgrounds. The distributions of $m_{4\ell}$ and the BDT output for the VBF category in the full mass range and in the fit range of $110 - 140$ GeV are shown in Figure 6.12.

There is no VH candidate in the $120 - 130$ GeV mass range for either the hadronic or leptonic categories. For the full mass range above 110 GeV all categories are dominated by the $ZZ^{(*)}$ background as can be seen in Table 6.13.

Table 6.12: Systematic uncertainties on the yields expected from various processes contributing to the VBF, hadronic VH, leptonic VH and ggF categories expressed as percentages of the yield. The various uncertainties are added in quadrature. Uncertainties that are negligible are omitted in the table.

Process	$gg \rightarrow H, q\bar{q}/gg \rightarrow b\bar{b}H/t\bar{t}H$	$qq' \rightarrow Hqq'$	$q\bar{q} \rightarrow W/ZH$	$ZZ^{(*)}$
	VBF category			
Theoretical cross section	20.4%	4%	4%	8%
Underlying event	6.6%	1.4%	–	–
Jet energy scale	9.6%	4.8%	7.8%	9.6%
Jet energy resolution	0.9%	0.2%	1.0%	1.4%
Total	23.5%	6.4%	8.8%	12.6%
	Hadronic VH category			
Theoretical cross section	20.4%	4%	4%	2%
Underlying event	7.5%	3.1%	–	–
Jet energy scale	9.4%	9.3%	3.7%	12.6%
Jet energy resolution	1.0%	1.7%	0.6%	1.8%
Total	23.7%	10.7%	5.5%	12.9%
	Leptonic VH category			
Theoretical cross section	12%	4%	4%	5%
Leptonic VH-specific cuts	1%	1%	5%	–
Jet energy scale	8.8%	9.9%	1.7%	3.2%
Total	14.9%	10.7%	6.6%	5.9%
	ggF category			
Theoretical cross section	12%	4%	4%	4%
Jet energy scale	2.2%	6.6%	4.0%	1.0%
Total	12.2%	7.7%	5.7%	4.1%

Figure 6.12: Distributions of the selected events and expected signal and background yields for the VBF enriched category: $m_{4\ell}$ (a) and the BDT output (b) in the full mass range, the $m_{4\ell}$ (c) and the BDT output (d) in the signal mass of range $110 < m_{4\ell} < 140$ GeV. The expected Higgs signal contributions, assuming $m_H = 125$ GeV, from the ggF, VBF and VH production modes are included. The expected background contributions, $ZZ^{(*)}$ and $Zjets$ plus $t\bar{t}$, are also shown; the systematic uncertainty associated to the total background contribution is represented by the hatched areas. In every case, the combination of 7 TeV and 8 TeV results is shown.

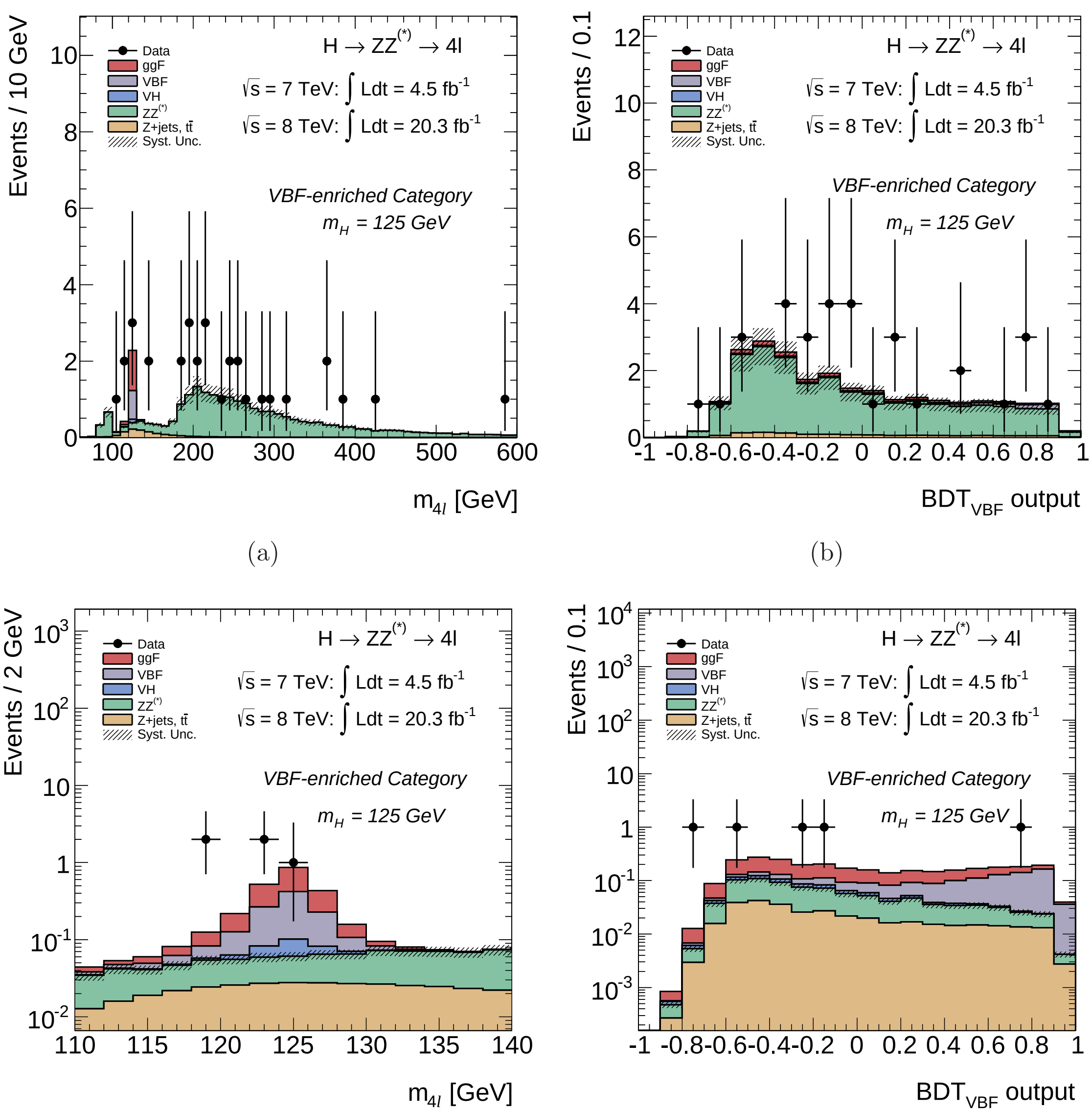

(a) (b)

(c) (d)

Table 6.13: Expected and observed yields in the VBF-enriched, hadronic VH-enriched, leptonic VH-enriched and ggF-enriched categories. Yields are given for the different production modes and the $ZZ^{(*)}$ and reducible background for 4.5 fb^{-1} at $\sqrt{s} = 7$ TeV and 20.3 fb^{-1} at $\sqrt{s} = 8$ TeV. The estimates are given for the both the $m_{4\ell}$ mass range of $120 - 130$ GeV and the full mass range above 110 GeV.

Enriched	Signal				Background		Total	Observed
category	$ggF + b\bar{b}H + t\bar{t}H$	VBF	VH-hadronic	VH-leptonic	$ZZ^{(*)}$	$Z +$ jets, $t\bar{t}$	expected	
				$120 < m_{4\ell} < 130$ GeV				
VBF	1.18 ± 0.37	0.75 ± 0.04	0.083 ± 0.006	0.013 ± 0.001	0.17 ± 0.03	0.25 ± 0.14	2.4 ± 0.4	3
VH-hadronic	0.40 ± 0.12	0.034 ± 0.004	0.20 ± 0.01	0.009 ± 0.001	0.09 ± 0.01	0.09 ± 0.04	0.80 ± 0.12	0
VH-leptonic	0.013 ± 0.002	< 0.001	< 0.001	0.069 ± 0.004	0.015 ± 0.002	0.016 ± 0.019	0.11 ± 0.02	0
ggF	12.8 ± 1.3	0.57 ± 0.02	0.24 ± 0.01	0.11 ± 0.01	7.1 ± 0.2	2.7 ± 0.4	23.5 ± 1.4	34
				$110 < m_{4\ell}$ GeV				
VBF	1.4 ± 0.4	0.82 ± 0.05	0.092 ± 0.007	0.022 ± 0.002	$20. \pm 4.$	1.6 ± 0.9	$24. \pm 4.$	32
VH-hadronic	0.46 ± 0.14	0.038 ± 0.004	0.23 ± 0.01	0.015 ± 0.001	9.0 ± 1.2	0.6 ± 0.2	10.3 ± 1.2	13
VH-leptonic	0.026 ± 0.004	< 0.002	< 0.002	0.15 ± 0.01	0.63 ± 0.04	0.11 ± 0.14	0.92 ± 0.16	1
ggF	14.1 ± 1.5	0.63 ± 0.02	0.27 ± 0.01	0.17 ± 0.01	$351. \pm 12.$	16.6 ± 2.2	$383. \pm 12.$	420

6.8 Summary

The inclusive events identified in Chapter 5 undergo further selection to unveil their production mechanism. The categories explored are the VBF, VH hadronic and leptonic and the dominant ggF production. Due to small cross sections, the ttH and bbH categories are ignored for the $\sqrt{s} = 7$ and 8 TeV analysis. The selection of each one is described and alternative methods are also studied. The background method of the inclusive analysis is extended in order to measure the reducible background in the categories.

For the VBF category, one event is seen with a high multivariate discriminant value and a mass of 123.4 GeV, the event display of this event is presented in Figure 6.13. No VH candidate is found in the m_H range $120 - 130$ GeV with the W or Z decaying either hadronically or leptonically. The observed yields for VBF and especially ggF are higher than the expected values. This fact leads to a higher production rate than the one expected from the Standard Model. Thus, one of the most interesting measurements of Run-II would be to verify if this excess persists or it can be classified as a statistical fluctuation.

Figure 6.13: Display of a $2e2\mu$ candidate with $m_{4\ell} = 123.4$ GeV. This is the only VBF candidate with $BDT_{VBF} > 0$, specifically the BDT_{VBF} value is 0.7. There are six jets in total, the two leading jets have $p_T = 180$ and 150 GeV and $\Delta\eta_{jj} = 3.4$, the missing of the event is $E_T = 40$ GeV.

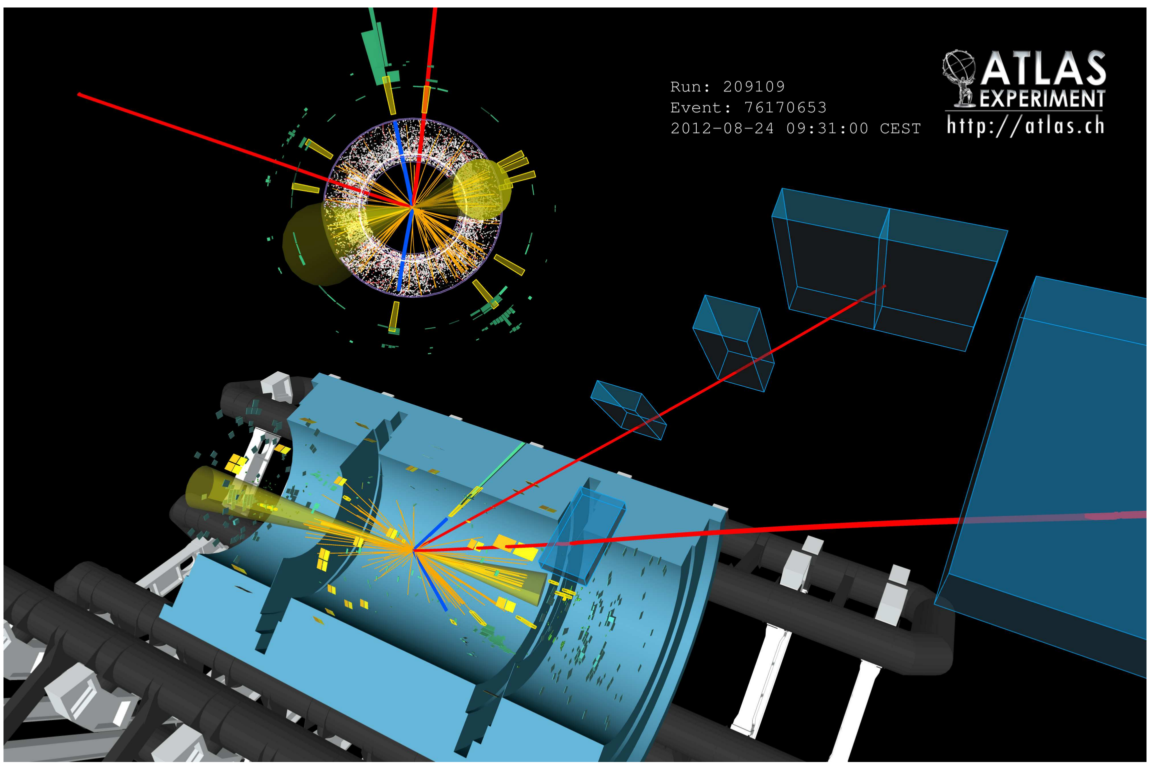

Chapter Bibliography

[1] S. Heinemeyer et al., Handbook of LHC Higgs Cross Sections: 3. Higgs Properties, 2013, arXiv:1307.1347.

[2] W. Lampl, S. Laplace, D. Lelas, P. Loch, H. Ma, et al., Calorimeter clustering algorithms: Description and performance, 2008.

[3] Matteo Cacciari, Gavin P. Salam, and Gregory Soyez, The Anti-k(t) jet clustering algorithm, *JHEP*, 0804:063, 2008, 0802.1189.

[4] P. Speckmayer, A. Hocker, J. Stelzer, and H. Voss, The toolkit for multivariate data analysis, TMVA 4, *J.Phys.Conf.Ser.*, 219:032057, 2010.

[5] Tom Melia, Paolo Nason, Raoul Rontsch, and Giulia Zanderighi, W^+W^-, WZ and ZZ production in the POWHEG BOX, *JHEP*, 1111:078, 2011, 1107.5051.

[6] T. Binoth, N. Kauer, and P. Mertsch, Gluon-induced QCD corrections to $pp \rightarrow ZZ \rightarrow$ l anti-l l-prime anti-l-prime, page 142, 2008, 0807.0024.

[7] S. Dittmaier, S. Dittmaier, C. Mariotti, G. Passarino, R. Tanaka, et al., Handbook of LHC Higgs Cross Sections: 2. Differential Distributions, 2012, 1201.3084.

[8] T. Gleisberg, Stefan. Hoeche, F. Krauss, M. Schonherr, S. Schumann, et al., Event generation with SHERPA 1.1, *JHEP*, 0902:007, 2009, 0811.4622.

[9] Iain W. Stewart and Frank J. Tackmann, Theory Uncertainties for Higgs and Other Searches Using Jet Bins, *Phys.Rev.*, D85:034011, 2012, 1107.2117.

[10] Georges Aad et al., Light-quark and gluon jet discrimination in pp collisions at $\sqrt{s} = 7$ TeV with the ATLAS detector, 2014, 1405.6583.

7

$H \rightarrow ZZ^{(*)} \rightarrow 4\ell$ Prospect Studies

7.1 Introduction

One of the main motivations for an upgrade of the LHC to deliver high luminosity, HL-LHC, is to enable precise measurements of the Higgs boson properties. In the Standard Model, all the properties of the Higgs boson are defined once its mass is known. However, this model leaves many open questions such as the hierarchy problem or the nature of dark matter. Many alternative theories addressing these issues make different predictions for the properties of one or more Higgs bosons. Precise measurements in the Higgs sector are therefore a priority in the future program of particle physics [1].

The present LHC program is expected to deliver a total integrated luminosity of about 300 fb^{-1} by the year 2022. The peak instantaneous luminosity will be in the range $2-3\times10^{34}\ cm^{-2}s^{-1}$. The luminosity will decrease from the peak value during a fill, though a typical average number of pile-up events per bunch crossing is estimated to be $\mu = 50-60$. The HL-LHC would deliver a total luminosity of about 3000 fb^{-1}, at a peak leveled luminosity of $5\times10^{34}\ cm^{-2}s^{-1}$, with a value of $\mu = 140$.

The detector design for the high luminosity phase is not yet completely defined and it will take years to adapt and optimize the event reconstruction software to the high-pile-up conditions. The goal is that the performance of the new detector in the harsh conditions of the high luminosity phase will not be worse than the performance of the current detector with $\mu = 20$.

A study is performed based on efficiency and resolution (smearing) functions to physics objects [2], which were derived from samples using the Run-I ATLAS detector with various values of μ, up to a maximum average of $\mu = 69$. Many of these functions were updated with the results of full the simulation of the Phase-I detector [2] with μ values up to 80, and the Phase-II detector with μ values of 80, 140 and 200.

The rates of tagging b, c and *light* flavor jets have been parametrized using one of the more robust tagging algorithms at a 70% efficiency working point for $b-$jets produced in $t\bar{t}$ events. It is expected that more sophisticated algorithms will give even better light jet rejection for the same efficiency, but they are not yet optimized for the Phase-II detector. A higher efficiency working point would also be preferred for some of the statistics limited channels presented here, since the light-jet rejection rate is better than with the Run-I detector, despite the high pile-up.

Functions to describe the detector resolution, reconstruction efficiency and trigger efficiency were defined by extrapolations from the existing data sample and Monte Carlo simulations in the same bunch crossing (in-time pile-up) and in preceding bunch crossings (out-of-time pile-up). In defining these parametrizations, it is also considered that the Phase-II detector would be designed to retain the performance of the present detector for many aspects.

In this chapter, the $H \rightarrow ZZ^{(*)} \rightarrow \ell^+\ell^-\ell^+\ell^-$ channel study is presented for 300 fb^{-1} and 3000 fb^{-1}. This channel offers a very clean final state signature with excellent signal to background ratio at the LHC environment. The large number of events expected in a 3000 fb^{-1} sample, allows the study of all the Higgs production modes separately using this final state, adding important sensitivity to the measurement of the Higgs coupling parameters.

The 4ℓ analysis is based on the same selection criteria applied for the Run-I analysis (Chapter 5). Track confirmation is required for all candidate jets falling inside the ID acceptance and their p_T thresholds are tuned to allow 1% jet fake rate, thus making the contribution from pile-up jets marginal. An alternative scenario, allowing 10% fake rate is also presented. The main background is the Standard Model is $q\bar{q} \rightarrow ZZ^{(*)}$ di-boson production. The relevant reducible background processes which are Z+jets, Z$b\bar{b}$ and $t\bar{t}$, are added conservatively as a 50% proportion of the main irreducible background.

Investigation of possible gain from an increased muon acceptance is explored. Specifically, it is considered that both the inner detector and the muon spectrometer could be extended with sectors covering the region of $2.7 < \eta < 4.0$. Expected yields and important Higgs properties are reported.

At the end of this chapter, the Run-II expectations are explored through projections made from the Run-I (Chapter 6) due to the lack of fully simulated events for the Run-II conditions. In Run-II, the expected center of mass collision energy is expected to be $\sqrt{s} = 13$ TeV and the delivered luminosity will not exceed the 100 fb^{-1}. The pile up conditions will lie between the Run-I and the Phase-II conditions of 300 fb^{-1}, but the allowed fake rate will be closer to the Run-I. For the Run-II yields prediction, the previously estimated yields are extrapolated to the $\sqrt{s} = 13$ TeV and the 100 fb^{-1}, using the theoretical cross sections from Reference [3], already summarized in Chapter 1.

The production theoretical cross sections used for this study have been presented in Chapter 1 and the MC samples used are mentioned in the Appendix B.

7.2 Categories Event Selection

After the $H \to ZZ^{(*)} \to \ell^+\ell^-\ell^+\ell^-$ candidates identification, using the selection presented in Chapter 5, the production mechanisms categorization follows. The selection of the events in the different categories is chosen in a way to allow the minimal cross talk between the production mechanisms and hence is different from Chapter 6. Namely, the order followed aims to tag $t\bar{t}$H, ZH, WH and VBF respectively. The remaining events are assumed to fall in the gluon-gluon fusion category.

A lepton quadruplet is formed from two pairs of same flavor and opposite sign leptons. The dilepton pair, with mass closest to the Z nominal mass, is required to have a mass between 50 and 115 GeV. The mass of the remaining dilepton is required to be between 12 and 115 GeV. Quadruplets with same flavor opposite sign lepton pairs with mass less that 5 GeV are excluded to avoid J/ψ contamination. p_T thresholds of 20, 15, 10 and 6 (7 for electrons) GeV are applied to the leptons. At this level, the agreement between the analysis based on smeared truth quantities and the one obtained from full simulation is very good.

The last requirement in the full analysis is the lepton isolation, which can not be applied with truth level information. The lepton isolation, however, is very important for the suppression of the reducible backgrounds. In particular for leptons with $p_T \leq$ 10 GeV, for which the pile-up can induce some loss of efficiency with respect to Run-I (95% at $p_T \simeq 20$ GeV, 90% at $p_T \simeq 10$ GeV). Therefore, in order to maintain similar suppression of the reducible backgrounds at peak level luminosities of $5 \times 10^{34}\ cm^{-2}s^{-1}$ compared to the 2012 analysis, a conservative 20% inefficiency, for leptons with $p_T <$ 20 GeV, is assumed.

7.2.1 $t\bar{t}H$, $H \to ZZ^{(*)}$

The selection of the $t\bar{t}H$ events exploits the existence of two b-jets stemming from the decays of the top quarks. Therefore, the presence of at least one b-tagged jet is required. To account for the leptonic W decays, one additional lepton with $p_T > 8$ GeV is also required. If the event does not pass this selection, at least four additional jets are required in order to account for hadronic decays of both Ws and classify the event in the ttH category. Figure 7.1 shows the distribution of the number of b-tagged jets, as well as the distribution of the number of the additional leptons (excluding the ones coming from the Higgs decay) in the events where at least one b-tagged jet is present, for the different Higgs production mechanisms and the background. It is clear that on top of the initial four lepton requirement, the criteria imposed in this analysis are sufficient to produce a very clean $t\bar{t}H$ sample. To reduce the ZH contamination in this category, events with two additional opposite sign same flavor leptons within ± 15 GeV of the nominal Z mass are vetoed. The mispairing effect, between the additional leptons and the quadruplet, is also taken into account for the category decision.

Figure 7.1: The distribution of the number of b-tagged jets (a) and the number of additional leptons in events with at least one b-tagged jet (b), for different Higgs production mechanisms and the background.

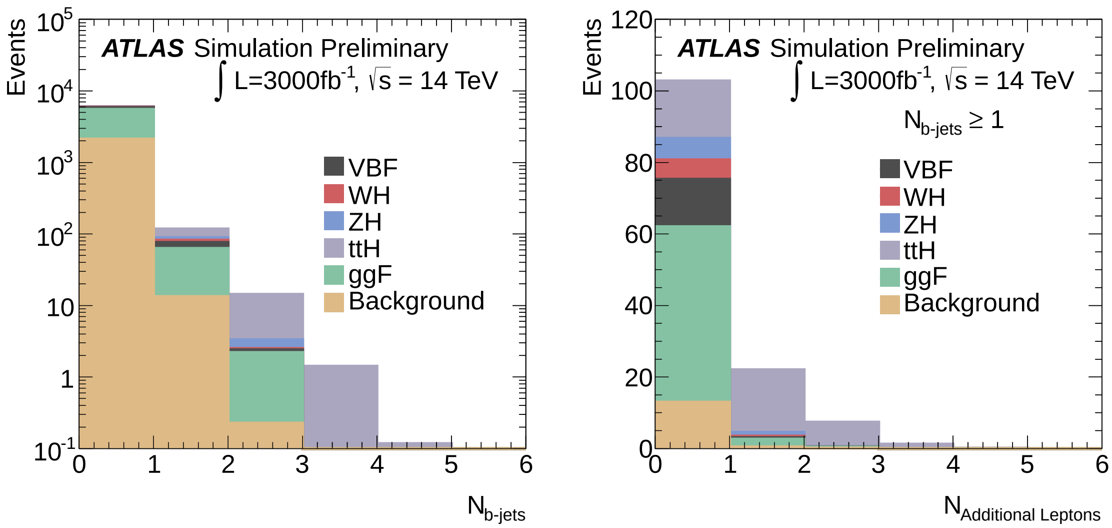

(a) (b)

7.2.2 VH, $V = Z$ or W, $H \to ZZ^{(*)}$

Events that contain two additional same flavor opposite sign leptons and do not fall in the previous category are classified as ZH, $H \to ZZ^{(*)}$, candidates. In order to reduce that $t\bar{t}$H events, that failed b-tagging and would populate this category, the additional lepton pair mass is required to be within 15 GeV to the nominal Z boson mass. Events which are not yet selected and contain one additional lepton are classified in the WH category.

7.2.3 $VBF,\ H \rightarrow ZZ^{(*)}$

Events that are not selected in the above categories are supposed to fall either in the VBF category or the gluon-gluon fusion category. A search for at least two additional jets is then performed in these events. A jet pair is accepted if it has an η difference above $\Delta\eta > 3$. The invariant mass of the two higher p_T jets is then used as discriminant for the VBF category. In this analysis, the event is accepted in the VBF category if this mass is $m_{jj} > 350$ GeV.

Figure 7.2 shows the distribution of $\Delta\eta$ (a) and the mass m_{jj} (b) of the selected di-jet pair, for different Higgs production mechanisms and the background.

Figure 7.2: The distribution of $\Delta\eta$ (a) and the mass m_{jj} (b) of the selected di-jet pair, for different Higgs production mechanisms and the background.

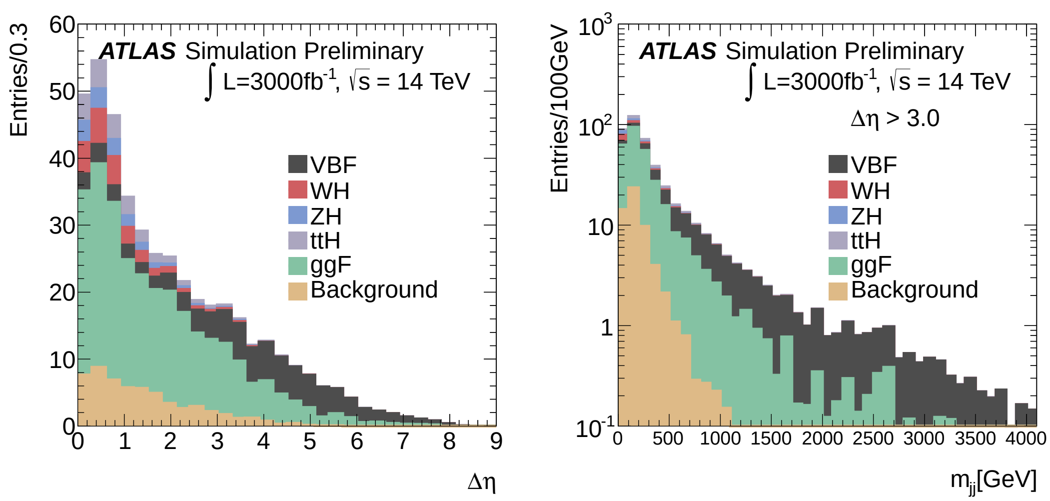

(a) (b)

7.2.4 $ggF,\ H \rightarrow ZZ^{(*)}$

The gluon-gluon fusion category consists of all the events that are not tagged with the above requirements.

7.3 Simulation Procedure

The code for the selection of the 4ℓ final state performs also the reweighting of the event accounting for trigger and lepton reconstruction efficiency, as well as the smearing of the lepton momenta and energies. At this level of the analysis, the overall efficiencies of the $H \rightarrow ZZ^{(*)} \rightarrow \ell^+\ell^-\ell^+\ell^-$ signature are found to vary between 63% ($4e$) and 74% (4μ), for the final states containing only electrons and muons. Lepton isolation is expected to be less effective in suppressing the reducible backgrounds with instantaneous luminosities of $5 \times 10^{34}\ cm^{-2}s^{-1}$ compared to the Run-I analysis. Due to the lack of precise full simulation studies to measure this effect, a conservative approach has been adopted, decreasing the lepton efficiency, for leptons with $p_T < 20$ GeV, by 20%. As a result of this assumption the signal efficiency is decreased by approximately 27%.

The subsequent categorization of events is performed using additional leptons and jets. For the additional leptons the same treatment as the ones produced by the Higgs boson decay is followed. Figure 7.3 shows the p_T distribution of the additional leptons and the dilepton mass in the case where two additional leptons exist. Track confirmation is required for all jets in the relevant acceptance in order to be considered as jet candidates. The jets are then smeared according to the recommendation. Furthermore a p_T threshold allowing for a fake jet rate below 1% is required. Jet truth origin is established by ΔR requirement between the jet candidates and truth partons. Then b-tagging is applied. The efficiency of the b-tagging in the $t\bar{t}H$ sample is found to be $\sim 70\%$, and the rejection of light quark jets close to 100%. The track confirmation efficiency is found to be $\sim 90\%$. Figure 7.4 shows the p_T distribution of the b-tagged jets in the ttH category and the tagged jets in the VBF category, following this procedure.

7.4 Systematic Uncertainties

The theoretical uncertainties on the signal yields assumed in this analysis for the different production mechanisms of the Higgs boson, follow Reference [4]. The irreducible background will be evaluated using the side-band regions around the Higgs boson mass peak. Reducible backgrounds are also expected to be evaluated using data driven methods similarly to the Run-I (Chapter 5). In the cases where it is not possible to constrain it with data driven methods, a 7% (35% for the VBF case) uncertainty on the background is introduced.

The detector uncertainties concerning lepton reconstruction and selection, are affecting all channels in a similar way and are assumed to be equal to the ones measured in the Run-I [5]. The uncertainty on the muon identification and reconstruction efficiency results in an uncertainty on the yields for the signal and the dominant $ZZ^{(*)}$ back-

Figure 7.3: Distribution of the p_T of additional leptons (a) and the dilepton mass (b) in case there are two additional leptons.

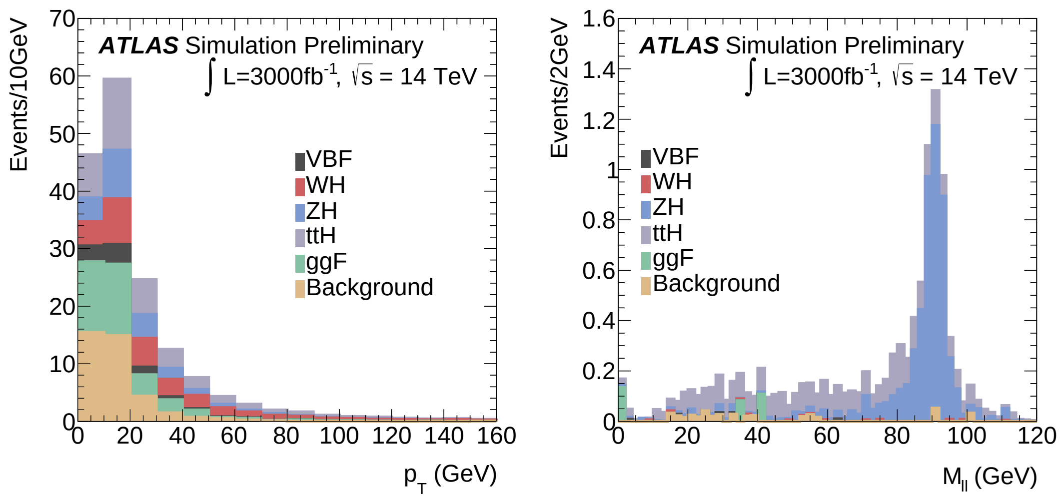

(a) (b)

Figure 7.4: Distribution of the p_T of b-tagged jets (a) and tagged jets in VBF analysis (b).

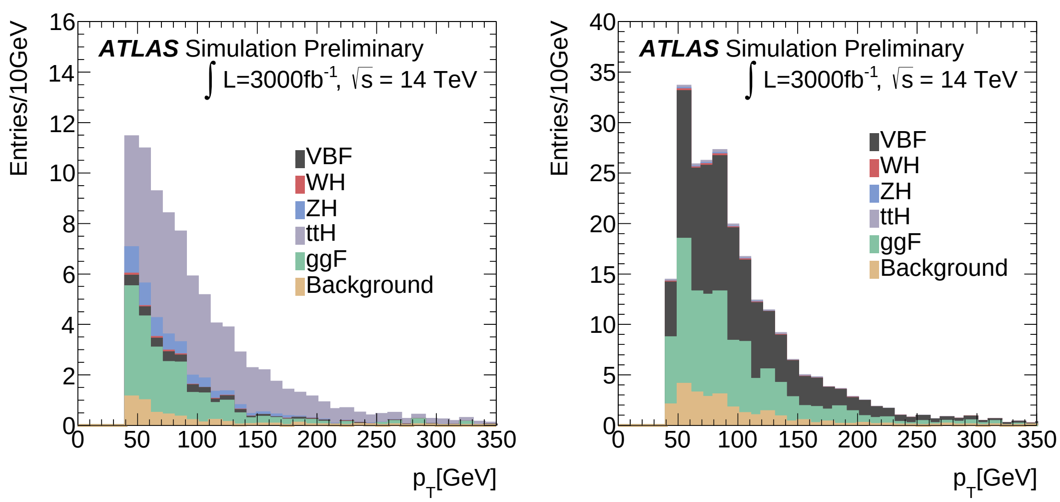

(a) (b)

ground which is uniform over the low mass range of interest, and amounts to $\pm 0.8\%$ ($\pm 0.4\% / \pm 0.4\%$) for the 4μ ($2\mu 2e/2e2\mu$) channel. The uncertainty on the electron identification and reconstruction efficiency results in an uncertainty on the yields for the signal of $\pm 2.4\%$ ($\pm 1.8\%/\pm 1.6\%$) for the $4e$ ($2\mu 2e/2e2\mu$) channel at $m_{4\ell} = 1$ TeV and $\pm 9.4\%$ ($\pm 8.7\%/\pm 2.4\%$) at $m_{4\ell} = 125$ GeV.

The selection efficiency of the isolation and impact parameter requirements, studied using data from Z decays in Run-I and were found with good accuracy to be in good agreement between data and simulation. Similarly in this study, the systematic uncertainty from this source is estimated to be small with respect to other systematic uncertainties.

The jet energy scale, the jet track confirmation and the b-tagging performance are the main jet related uncertainties that affect mostly the ttH and VBF categories. The main systematic uncertainty for the ttH category is due to b-tagging and the track confirmation is required for the jets. However these uncertainties are quite small, compared to the theory uncertainties. A 5% uncertainty on b-tagging efficiency or the track confirmation inefficiency corresponds to 2% uncertainty on the ttH efficiency. The other Higgs boson production contributions as well as the background are also affected by the jet energy scale and resolution below the level of 10%. The dominant sources of detector related uncertainties, in the VBF category, are due to the jet energy scale and resolution together with uncertainties concerning the underlying events. It is assumed that their contribution is similar to the Run-I, i.e. amounts $\sim 10\%$ for the VBF-like category, 0.7% for the VH-like category and 0.7% for the ggF-like category.

Finally, a 3% uncertainty on the luminosity is assumed [2].

7.5 3000 fb^{-1} Results

Following the event selection defined above, the yields of expected events in each category from the signal and background events are reported in Table 7.1 for 3000 fb^{-1}. The yields are reported in the lepton quadruplet mass interval between 115 and 130 GeV. The total uncertainties on the corresponding estimates are given. Figure 7.5 shows the invariant mass distributions of the lepton quadruplets coming from Higgs production mechanisms and background for the different category selections.

7.6 Comparison with the Full Analysis at 8 TeV

In order to verify the validity of the smearing used in this analysis, a comparison is made using the full analysis results at 8 TeV normalized to the cross section and integrated luminosity of the current analysis. After the application of the trigger and lepton efficiencies and resolutions at the truth level, the yields of the events are expected to be 5080 from gluon-gluon fusion production and 470 from VBF production compared

Table 7.1: Expected events in each category (ggF-like,VBF-like, WH-like, ZH-like, ttH-like) assuming $m_H = 125$ GeV and 3000 fb^{-1} of data. For each category, the expected events from the various Higgs production mechanisms are specified. Estimates are given in the lepton quadruplet mass interval between 115 and 130 GeV, along with their total uncertainties.

Category	**Truth Origin**					
	ggF	VBF	WH	ZH	ttH	Background
ttH-like	3.1 ±1.0	0.6 ±0.1	0.6 ±0.1	1.1 ±0.2	30 ±6	0.6 ±0.2
ZH-like	0.0	0.0	0.01 ±0.02	4.4 ±0.3	1.3 ±0.3	0.06 ±0.06
WH-like	22 ±7	6.6 ±0.4	25 ±2	4.4 ±0.3	8.8 ±1.8	13 ±0.8
VBF-like	41 ±14	54 ±6	0.7 ±0.1	0.4 ±0.1	1.0 ±0.2	4.2 ±1.5
ggF-like	3380 ±650	274 ±17	77 ±5	53 ±3	25 ±4	2110 ± 50

to 5000 and 460 respectively, from the extrapolation of the 8 TeV results. At the VBF category, using the same criteria, 106 events are expected from gluon-gluon fusion and 167 events from VBF, while the corresponding expectations from 8 TeV are 100 and 165 respectively. The agreement between the extrapolation of the 8 TeV analysis and the current one is, therefore, considered to be very satisfactory.

Despite the good agreement of the parametrized analysis and the full simulation analysis at 8 TeV, the pile-up conditions in the current study, require certain changes. The most important is the 20% decrease of the efficiency of the leptons with $p_T <$ 20 GeV. Furthermore, to reduce the fake jets due to pile-up harder jet p_T thresholds have to be used. In this analysis, a working point of jet fake rate of 1% is used together with the requirement of track confirmation for the jets falling in the acceptance of the Inner Detector. This reduced the efficiency in identifying the true VBF events to $\sim 50\%$. Furthermore, the jet energy resolution allowed the migration of a substantial number of gluon-gluon fusion events, as well as ZZ background events in the VBF category. In general the treatment of the VBF category in the current analysis is conservative.

7.7 Study of the VBF Category with Higher Jet Fake Rate

As an attempt to have higher efficiency in the VBF category, jet thresholds corresponding to 10% fake rate were used. To emulate the effect of pile-up at 14 TeV, extra jets were inserted according to an extrapolation done from Run-I data. The amount of these jets corresponds to the fake rate chosen according to the jet p_T thresholds, as

Figure 7.5: Quadruplet mass for the $t\bar{t}H$-like (a), VH-like (b), VBF-like (c) and ggF-like (d) categories.

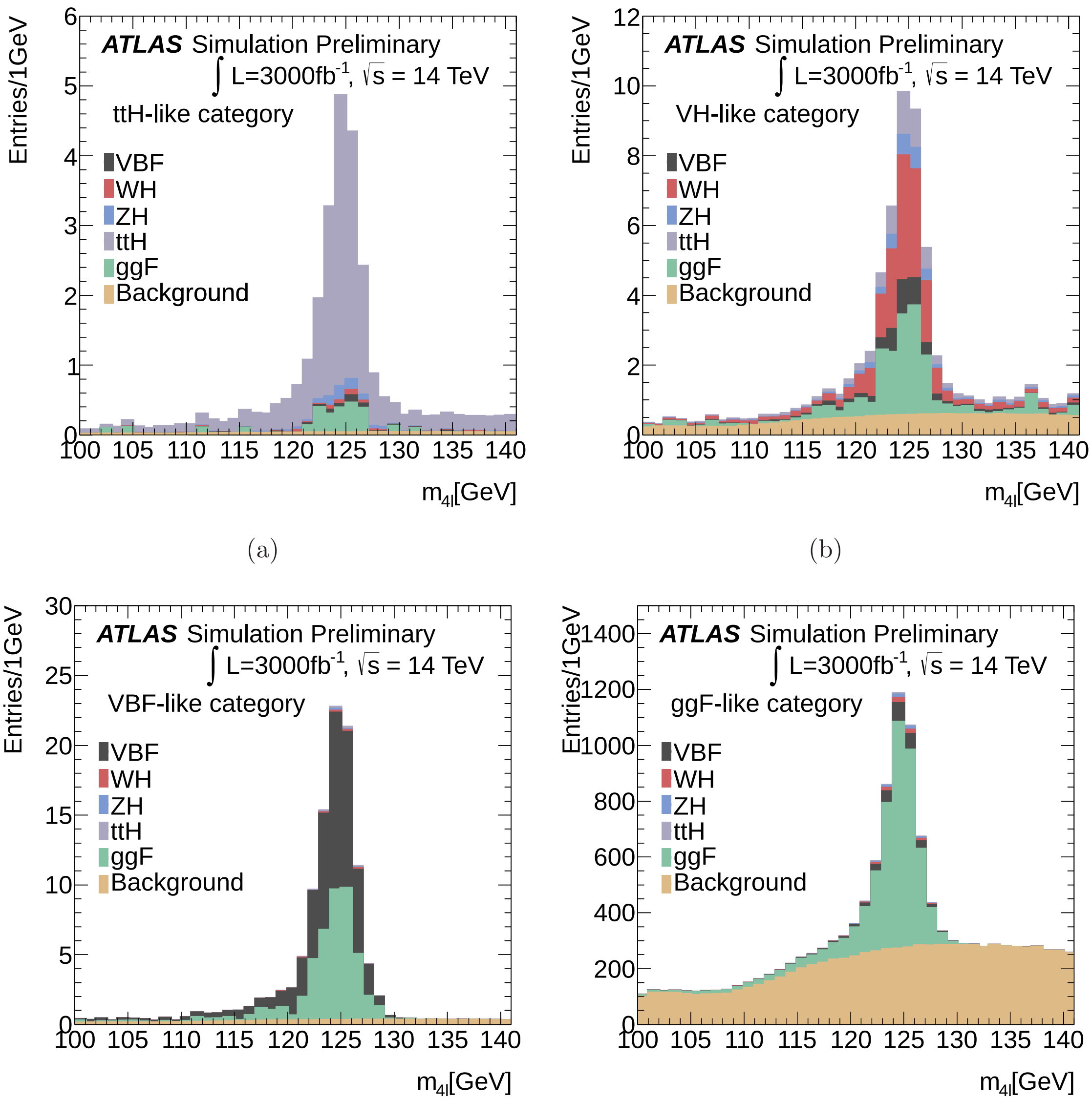

(a) (b) (c) (d)

described in Reference [2]. These jets follow the rest of the analysis steps as the original jets of the event. Using the working point of 10% jet fake rate for the case of $\mu = 140$, an increase of 8% of the gluon-gluon fusion contribution in the VBF category is observed. For $\mu = 50$, the increase is estimated at the 3% level. Since this effect should be studied in detail with fully simulated samples, an equal amount of uncertainty is introduced in the background of this category. In the case of 1% jet fake rate the effect contributes below the 1% level and is considered negligible. The analysis based on the 10% jet fake rates, results in a statistical accuracy which is better than the one using 1% fake rates thresholds by $\sim$ 30%. Nevertheless, the systematic error in this case is increased by $\sim$ 20%. Therefore, the gain in accuracy is estimated to be less than 10%.

Results obtained with p_T thresholds corresponding to 10% fake rate are reported in Table 7.2.

Table 7.2: Expected events in each category (ggF-like,VBF-like, WH-like, ZH-like, ttH-like) assuming m_H = 125 GeV and 3000 fb^{-1} of data. The p_T thresholds used for the jets correspond to 10% fake rate. For each category, the expected events from the various Higgs production mechanisms are specified. Estimates are given in the lepton quadruplet mass interval between 115 and 130 GeV, along with their total uncertainties.

Category	**Truth Origin**					
	ggF	VBF	WH	ZH	ttH	Background
ttH-like	5.8 ±1.5	0.9 ±0.2	0.9 ±0.1	1.6 ±0.2	36 ±7	1.0 ±0.2
ZH-like	0.0	0.0	0.01 ±0.01	4.4 ±0.3	1.2 ±0.3	0.06 ±0.06
WH-like	21 ±7	6.3 ±0.4	25 ±2	4.4 ±0.3	7.3 ±1.7	12 ±0.8
VBF-like	102 ±34	101 ±11	1.2 ±0.2	0.9 ±0.1	1.0 ±0.2	12.8 ±4.5
ggF-like	3310 ±650	227 ±14	77 ±5	53 ±3	20 ±4	2110 ±150

7.8 300 fb^{-1} Results

This study is performed similarly to the one of the 3000 fb^{-1}. Concerning lepton reconstruction different parametrizations are used to account for the status of the detector. Furthermore, isolation criteria are expected to behave more similarly to the full simulation analysis of 8 TeV and therefore the 20% inefficiency introduced for leptons with p_T below 20 GeV is changed to 10%. The yields of expected events in each category from signal and background events are reported in Table 7.3. The yields are reported in the lepton quadruplet mass interval between 115 and 130 GeV. The total uncertainties on the corresponding estimates are also provided.

Table 7.3: Expected events in each category (ggF-like,VBF-like, WH-like, ZH-like, ttH-like) assuming $m_H = 125$ GeV and 300 fb^{-1} of data. For each category, the expected events from the various Higgs production mechanisms are specified. Estimates are given in the lepton quadruplet mass interval between 115 and 130 GeV, along with their total uncertainties.

Category	**Truth Origin**					
	ggF	VBF	WH	ZH	ttH	Background
ttH-like	0.47 ±0.12	0.07 ±0.02	0.07 ±0.01	0.15 ±0.02	3.9 ±0.7	0.15 ±0.04
ZH-like	0.0	0.0	0.0	0.51 ±0.03	0.15±0.03	0.01 ±0.01
WH-like	2.8 ±0.7	0.85 ±0.06	3.3 ±0.3	0.6 ±0.1	1.0 ±0.2	1.7 ±0.1
VBF-like	5.0 ±1.7	6.7 ±0.7	0.08 ±0.02	0.05 ±0.01	0.12±0.04	0.41±0.14
ggF-like	457 ±41	36 ±3	10 ±0.6	7.1 ±0.4	3.1 ±0.6	296 ±20

7.9 Large-η Acceptance Scenario

The possibility of extending the coverage of the muon acceptance for the Phase-II upgrade of the ATLAS detector and its impact on the $H \to ZZ^{(*)} \to 4\ell$ channel is investigated in this section.

The muon identification requires tracking, which is more precise if it combines information from the inner detector and the muon chambers, as well as a magnetic field for the charge identification and momentum measurement. In the most optimistic scenario, the tracker is considered to extend up to $\eta = 4.0$ with additional Pixel sensors and the current beam pipe layout, the muon spectrometer is considered to have additional stations covering the region of $2.7 < \eta < 4.5$ and an enhanced magnetic field in this region is assumed. No change in the electrons identification is foreseen in this scenario.

In order to study the effect on the $H \to ZZ^{(*)} \to 4\ell$ sensitivity, a study similar to the one conducted in the previous sections of this chapter is performed based on the truth information. The channel that is expected to be affected the most by the extended detector layout is the $H \to ZZ^{(*)} \to 4\mu$. The yields of the expected events in this final state are reported in Table 7.4 and for comparison reasons the yields for the current layout ($\eta < 2.7$) are given. Based on these, the gain in the truth and smeared level is calculated. It has to be noted that no production mechanisms categorization applied to extract these yields.

The mass distributions of the 4μ candidates are presented in Figure 7.6 and the muons p_T and η distributions are presented in Figure 7.7. The η as a function of the p_T distributions for the muons that form the quadruplets are shown in Figure 7.8 for the different signals and the background. The formed Higgs candidates p_T and η spectrum appear in Figure 7.9.

Table 7.4: Expected events in the $H \rightarrow ZZ^{(*)} \rightarrow 4\mu$ final state from different Higgs signals and the SM background. It has to be noted that no production mechanisms categorization is applied. For comparison, the yields for the current detector layout are given ($\eta < 2.7$) and the gains are extracted from both the truth level and after the application of the smearing functions.

	Signal Samples					
	ggF	VBF	WH	ZH	ttH	Background
$\eta < 2.7$	1030	101	31	19	19	651
$\eta < 4.0$	1244	117	39	24	20	911
Smeared Gain	20.78%	16.50%	26.69%	25.26%	8.13%	40.00%
Truth Gain	29.66%	23.31%	39.37%	37.98%	9.87%	70.73%

The other channels which include muons, the $2e2\mu$ and $2\mu2e$, are affected less with respect to the 4μ final state. Table 7.5 presents the $H \rightarrow ZZ^{(*)} \rightarrow 4\ell$ results for the high eta region, where the electrons acceptance is unchanged (hence the $4e$ channel is not affected) and the muons acceptance is increased. The gains in the truth and smeared levels are also reported.

The observed gain is non-negligible, however the background increase is significant. Thus further studies should be made to reach a final decision.

Table 7.5: Expected events in the $H \rightarrow ZZ^{(*)} \rightarrow 4\ell$ final state from different Higgs signals and the SM background. It has to be noted that no production mechanisms categorization is applied. The electrons acceptance is unchanged (therefore the $4e$ channel is not affected) and the muons acceptance is increased. For comparison, the yields for the current detector layout are given ($\eta < 2.7$) and the gains are extracted from both the truth level and after the application of the smearing.

	Signal Samples					
	ggF	VBF	WH	ZH	ttH	Background
$\eta < 2.7$	3439	335	104	64	66	2126
$\eta < 4.0$	3765	361	116	72	68	2493
Smeared Gain	9.49%	7.88%	11.92%	11.88%	3.81%	17.30%
Truth Gain	12.04%	9.85%	15.97%	15.46%	4.31%	26.86%

Figure 7.6: The m_{12} (a), m_{34} (b) and $m_{4\ell}$ (c) of the $H \rightarrow ZZ^{(*)} \rightarrow 4\mu$ candidates with η up to 4.0.

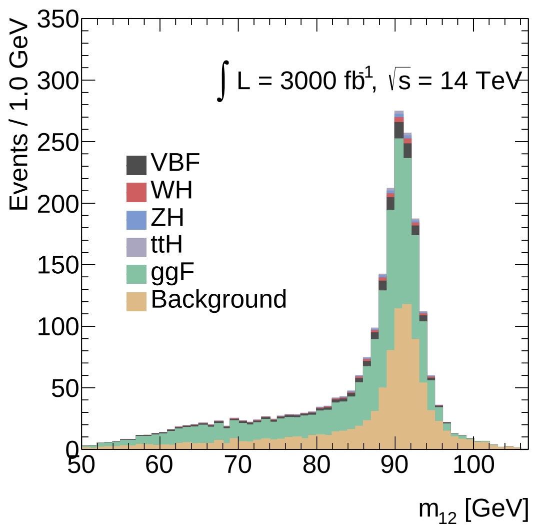

(a)

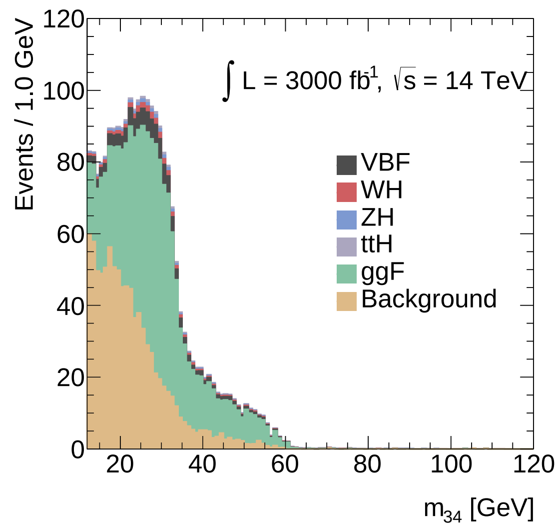

(b)

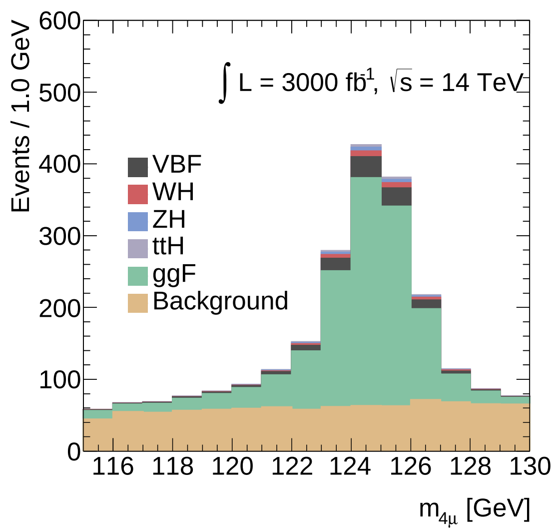

(c)

7.10 Run-II Projections

In this section projections are made from the Run-I results presented in Chapter 6. The summary expectations for the $ggF-like$, $VBF-like$, $VH-leptonic-like$ and $VH-hadronic-like$ categories are in Table 7.6. The yields are reported in the mass

Figure 7.7: The p_T (a) and η (b) distributions of the muons forming the $H \rightarrow ZZ^{(*)} \rightarrow 4\mu$ candidates. The maximum allowed η is the 4.0.

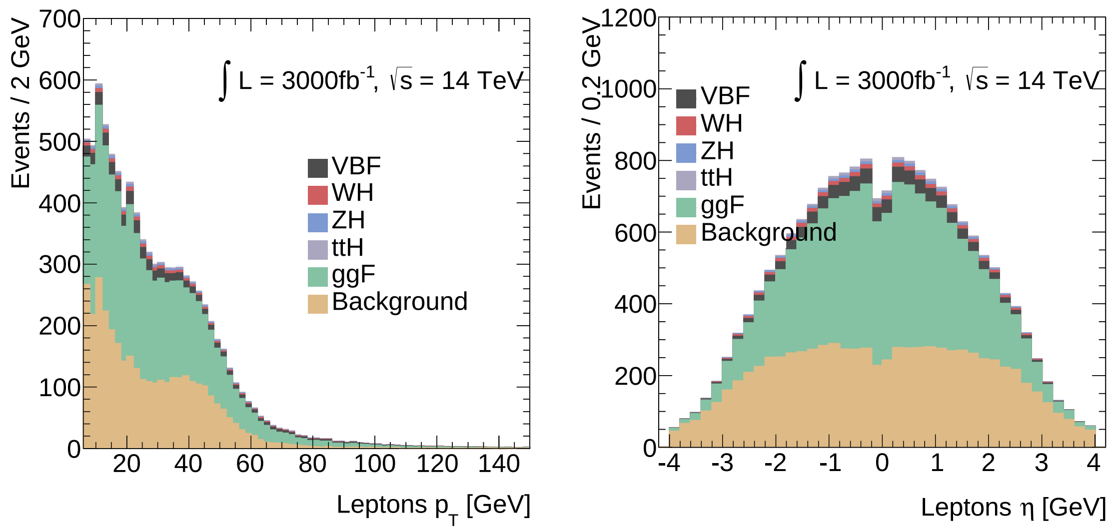

(a) (b)

range of 110 − 140 GeV and the $ttH - like$ and $bbH - like$ categories are ignored due to marginal cross sections in the Run-I. These numbers are considered to be optimistic given that the pile-up conditions are expected to be harsher.

Table 7.6: Projections are made from the Run-I results (Chapter 6) for the Run-II at $\sqrt{s} = 13$ TeV and 100 fb^{-1} considered luminosity. The cross section scaling is taken into account according to the Reference [3]. The reported events are in the mass range of 110 − 140 GeV and the $ttH - like$ and $bbH - like$ categories are missing due to marginal cross sections in the Run-I. The "Background" corresponds to the ZZ and 50% of the ZZ to account for the reducible background.

Origin	$ggF - like$	$VBF - like$	$VH - hadronic - like$	$VH - leptonic - like$
ggF	134.4	12.4	4.2	0.2
VBF	6.0	8.0	0.4	0.012
WH	1.2	0.6	1.2	0.9
ZH	1.7	0.4	0.9	0.4
ttH	0.04	1.3	0.3	0.06
Background	131.6	3.3	1.8	0.3

Figure 7.8: The distributions of the p_T vs η for the muons forming $H \to ZZ^{(*)} \to 4\mu$ candidates for the ggF (a), VBF (b), WH (c), ZH (d), ttH (e) and $ZZ^{(*)}$ background (f) samples. The muons in the high η region tend to populate in low p_T region.

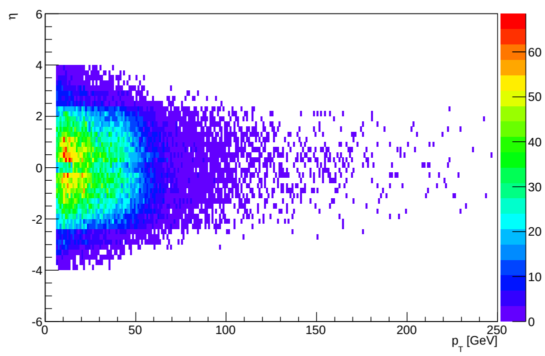

(a)

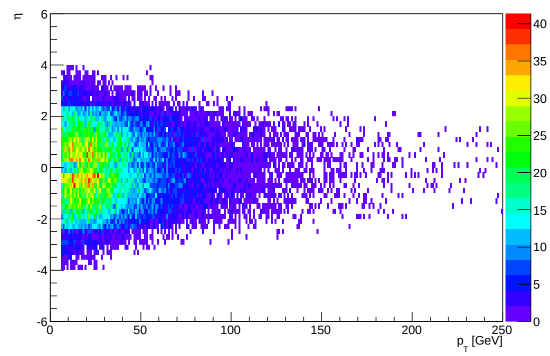

(b)

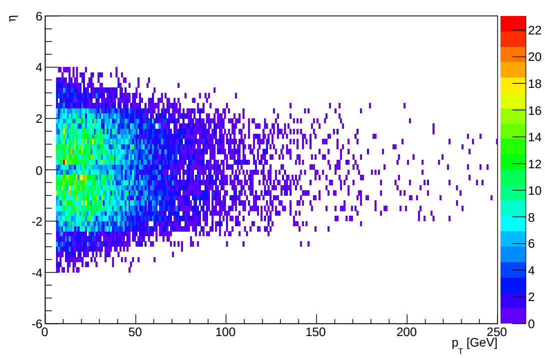

(c)

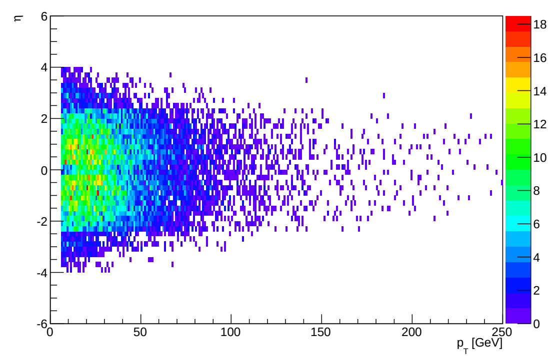

(d)

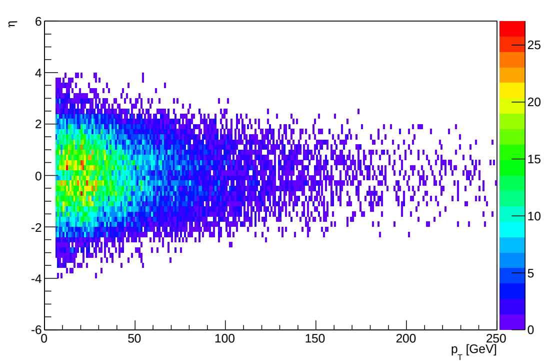

(e)

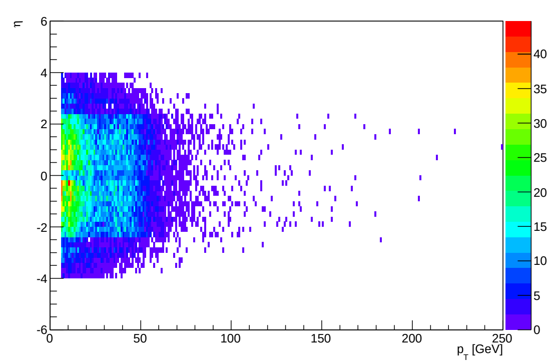

(f)

Figure 7.9: The p_T (a) and η (b) distributions of the $H \rightarrow ZZ^{(*)} \rightarrow 4\mu$ candidates. The maximum allowed muons η is the 4.0.

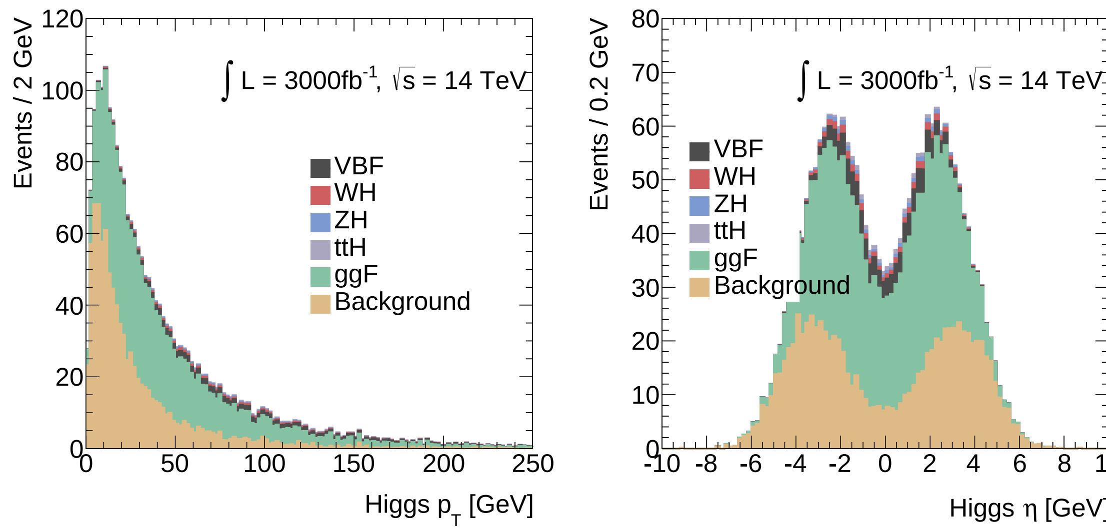

(a) (b)

7.11 Summary

The $H \rightarrow ZZ^{(*)} \rightarrow 4\ell$ decay mode presented for the 3000 fb^{-1} at the HL-LHC and for a sample of 300 fb^{-1} that would be accumulated before the Phase-II upgrades at $\sqrt{s} = 14$ TeV. The result is compared to the Run-I projections, to verify the validity of the parametrizations, and is found to be in agreement given the different pile-up conditions. At high luminosities, the precision of the channels can be improved and the couplings accuracy will be significant as Tables 7.7 and 7.8 report for 3000 and 300 fb^{-1} respectively. Even rare production such as the ttH will be possible to be measured.

The scenario of the extended muons acceptance coverage with new inner detector sectors, muon spectrometer chambers and magnets in the η region between 2.7 and 4.0 is explored. The 4μ final state is affected the most and the estimated gain is not negligible. However, the study of the properties of the Higgs boson may not benefit because of the background increase.

Projections are made for Run-II based on the Run-I due to lack of fully simulated events. The pile up is expected to be higher compared to the Run-I and lower compared to the Run-II, however the allowed fake rate will be closer to the Run-I. The projections do not include estimations of the bbH and ttH productions because of their negligible production in the Run-I [3].

Table 7.7: Expected uncertainties on the signal strength, with 3000 fb^{-1} of data at peak instantaneous luminosity $5\times10^{34}\ cm^{-2}s^{-1}$, for the various Higgs production mechanisms and their combination.

Production Mode	μ (over all error)	μ (stat error)	μ (exp syst error)	μ (theory error)
ggF	0.128	0.025	0.027	0.124
VBF	0.370	0.187	0.223	0.226
WH	0.389	0.375	0.053	0.085
ZH	0.531	0.526	0.024	0.073
$t\bar{t}$H	0.222	0.184	0.016	0.120
Combined	0.095	0.016	0.019	0.093

Table 7.8: Expected uncertainties on the signal strength, with 300 fb^{-1} of data at peak instantaneous luminosity $2\times10^{34}\ cm^{-2}s^{-1}$, for the various Higgs production mechanisms and their combination.

Production Mode	μ (over all error)	μ (stats error)	μ (syst error)	μ (theory error)
ggF	0.149	0.066	0.044	0.124
VBF	0.624	0.545	0.231	0.226
WH	1.074	1.064	0.053	0.085
$t\bar{t}$H	0.534	0.516	0.023	0.120
Combined	0.121	0.042	0.032	0.108

Chapter Bibliography

[1] Projections for measurements of Higgs boson cross sections, branching ratios and coupling parameters with the ATLAS detector at a HL-LHC, Technical Report ATL-PHYS-PUB-2013-014, CERN, Geneva, Oct 2013.

[2] Performance assumptions based on full simulation for an upgraded ATLAS detector at a High-Luminosity LHC, Technical Report ATL-PHYS-PUB-2013-009, CERN, Geneva, Sep 2013.

[3] S. Dittmaier, S. Dittmaier, C. Mariotti, G. Passarino, R. Tanaka, et al., Handbook of LHC Higgs Cross Sections: 2. Differential Distributions, 2012, 1201.3084.

[4] S. Dittmaier, S. Dittmaier, C. Mariotti, G. Passarino, R. Tanaka, et al., Handbook of LHC Higgs Cross Sections: 2. Differential Distributions, 2012, 1201.3084.

[5] Measurements of the properties of the Higgs-like boson in the four lepton decay channel with the ATLAS detector using 25 fb.1 of proton-proton collision data, 2013.

Appendices

A

RunI MC Samples List

The MC samples used for the $H \rightarrow ZZ^{(*)} \rightarrow 4\ell$ RunI analysis are summarized below.

A.0.1 Signal Samples

A.0.1.1 ggF with No tau Decays

These samples are used for the m4l models.

e.g. mc12_8TeV.167895.PowhegPythia8_AU2CT10_ggH120_ZZ4lep_noTau.merge.NTUP_HSG2.e2220_s1771_s1741_r4829_r4540_p1344/

Generators	PDFs	Generator tune
Powheg+Pythia8+Photospp	CT10	AUET2 CT10

Table A.1: Signal MC ggF with no tau decays.

MC ID	Mass (GeV)	Tags
167895	120	e2220_s1771_s1741_r4829_r4540_p1344
181330	121	e2113_s1771_s1741_r4829_r4540_p1344
181331	122	e2113_s1771_s1741_r4829_r4540_p1344
167890	123	e1622_s1771_s1741_r4829_r4540_p1344
181332	123.5	e2099_s1771_s1741_r4829_r4540_p1344
167891	124	e1622_s1771_s1741_r4829_r4540_p1344
181333	124.5	e2099_s1771_s1741_r4829_r4540_p1344
167892	125	e1622_s1771_s1741_r4829_r4540_p1344
181334	125.5	e2099_s1771_s1741_r4829_r4540_p1344
167893	126	e1622_s1771_s1741_r4829_r4540_p1344
167894	127	e1622_s1771_s1741_r4829_r4540_p1344
181335	128	e2113_s1771_s1741_r4829_r4540_p1344
181336	129	e2113_s1771_s1741_r4829_r4540_p1344
167896	130	e2220_s1771_s1741_r4829_r4540_p1344

A.0.1.2 ggF with tau decays

e.g. mc12_8TeV.160152.PowhegPythia8_AU2CT10_ggH110_ZZ4lep.merge.NTUP_HSG2.e1191_s1771_s1741_r4829_r4540_p1344/

Generators	PDFs	Generator tune
Powheg+Pythia8+Photospp	CT10	AUET2 CT10

Table A.2: Signal MC ggF with tau decays.

MC ID	Mass (GeV)	Tags
160152	110	e1191_s1771_s1741_r4829_r4540_p1344
160153	115	e1191_s1771_s1741_r4829_r4540_p1344
160154	120	e1191_s1771_s1741_r4829_r4540_p1344
167220	123	e1437_s1771_s1741_r4829_r4540_p1344
167222	124	e1437_s1771_s1741_r4829_r4540_p1344
160155	125	e1191_s1771_s1741_r4829_r4540_p1344
167225	126	e1437_s1771_s1741_r4829_r4540_p1344
167227	127	e1437_s1771_s1741_r4829_r4540_p1344
160156	130	e1191_s1771_s1741_r4829_r4540_p1344
160157	135	e1191_s1771_s1741_r4829_r4540_p1344
160158	140	e1191_s1771_s1741_r4829_r4540_p1344
160159	145	e1191_s1771_s1741_r4829_r4540_p1344
160160	150	e1191_s1771_s1741_r4829_r4540_p1344
160161	155	e1191_s1771_s1741_r4829_r4540_p1344
160162	160	e1191_s1771_s1741_r4829_r4540_p1344
160163	165	e1191_s1771_s1741_r4829_r4540_p1344
160164	170	e1191_s1771_s1741_r4829_r4540_p1344
160165	175	e1191_s1771_s1741_r4829_r4540_p1344
160166	180	e1191_s1771_s1741_r4829_r4540_p1344
160167	185	e1191_s1771_s1741_r4829_r4540_p1344
160168	190	e1191_s1771_s1741_r4829_r4540_p1344
160169	195	e1191_s1771_s1741_r4829_r4540_p1344
160170	200	e1191_s1771_s1741_r4829_r4540_p1344
160171	220	e1191_s1771_s1741_r4829_r4540_p1344
160172	240	e1191_s1771_s1741_r4829_r4540_p1344
160173	260	e1191_s1771_s1741_r4829_r4540_p1344
160174	280	e1191_s1771_s1741_r4829_r4540_p1344
160175	300	e1191_s1771_s1741_r4829_r4540_p1344
160176	320	e1191_s1771_s1741_r4829_r4540_p1344
160177	340	e1191_s1771_s1741_r4829_r4540_p1344
160178	360	e1191_s1771_s1741_r4829_r4540_p1344
160179	380	e1191_s1771_s1741_r4829_r4540_p1344

A.0.1.3 VBF with no tau decays

These samples are not merged with the including-tau ones. They are used for the m4l models. e.g. mc12_8TeV.167995.PowhegPythia8_AU2CT10_VBFH120_ZZ4lep_noTau.merge.NTUP_HSG2.e2464_s1831_s1741_r4829_r4540_

Generators	PDFs	Generator tune
Powheg+Pythia8+Photospp	CT10	AUET2 CT10

Table A.3: Signal MC VBF with no tau decays.

MC ID	Mass (GeV)	Tags
167995	120	e2464_s1831_s1741_r4829_r4540_p1344
181337	121	e2113_s1831_s1741_r4829_r4540_p1344
181338	122	e2113_s1831_s1741_r4829_r4540_p1344
167990	123	e1890_s1771_s1741_r4829_r4540_p1344
181339	123.5	e2099_s1771_s1741_r4829_r4540_p1344
167991	124	e1890_s1771_s1741_r4829_r4540_p1344
181340	124.5	e2099_s1771_s1741_r4829_r4540_p1344
167992	125	e1890_s1771_s1741_r4829_r4540_p1344
181341	125.5	e2099_s1771_s1741_r4829_r4540_p1344
167993	126	e1890_s1771_s1741_r4829_r4540_p1344
167994	127	e1890_s1771_s1741_r4829_r4540_p1344
181342	128	e2113_s1831_s1741_r4829_r4540_p1344
181343	129	e2113_s1771_s1741_r4829_r4540_p1344
167996	130	e2464_s1831_s1741_r4829_r4540_p1344

A.0.1.4 VBF with tau decays

e.g. mc12_8TeV.160202.PowhegPythia8_AU2CT10_VBFH110_ZZ4lep.merge.NTUP_HSG2.e1195_s1771_s1741_r4829_r4540_p1344/

Generators	PDFs	Generator tune
Powheg+Pythia8+Photospp	CT10	AUET2 CT10

Table A.4: Signal MC VBF with tau decays.

MC ID	Mass (GeV)	Tags
160202	110	e1195_s1771_s1741_r4829_r4540_p1344
160203	115	e1195_s1771_s1741_r4829_r4540_p1344
160204	120	e1195_s1771_s1741_r4829_r4540_p1344
167230	123	e1437_s1771_s1741_r4829_r4540_p1344
167232	124	e1437_s1771_s1741_r4829_r4540_p1344
160205	125	e1195_s1771_s1741_r4829_r4540_p1344
167235	126	e1437_s1771_s1741_r4829_r4540_p1344
167237	127	e1437_s1771_s1741_r4829_r4540_p1344
160206	130	e1195_s1771_s1741_r4829_r4540_p1344
160207	135	e1195_s1771_s1741_r4829_r4540_p1344
160208	140	e1195_s1771_s1741_r4829_r4540_p1344
160209	145	e1195_s1771_s1741_r4829_r4540_p1344
160210	150	e1195_s1771_s1741_r4829_r4540_p1344
160211	155	e1195_s1771_s1741_r4829_r4540_p1344
160212	160	e1195_s1771_s1741_r4829_r4540_p1344
160213	165	e1195_s1771_s1741_r4829_r4540_p1344
160214	170	e1195_s1771_s1741_r4829_r4540_p1344
160215	175	e1195_s1771_s1741_r4829_r4540_p1344
160216	180	e1195_s1771_s1741_r4829_r4540_p1344
160217	185	e1195_s1771_s1741_r4829_r4540_p1344
160218	190	e1195_s1771_s1741_r4829_r4540_p1344
160219	195	e1195_s1771_s1741_r4829_r4540_p1344
160220	200	e1195_s1771_s1741_r4829_r4540_p1344
160221	220	e1195_s1771_s1741_r4829_r4540_p1344
160222	240	e1195_s1771_s1741_r4829_r4540_p1344
160223	260	e1195_s1771_s1741_r4829_r4540_p1344
160224	280	e1195_s1771_s1741_r4829_r4540_p1344
160225	300	e1195_s1771_s1741_r4829_r4540_p1344
160226	320	e1195_s1771_s1741_r4829_r4540_p1344
160227	340	e1195_s1771_s1741_r4829_r4540_p1344
160228	360	e1195_s1771_s1741_r4829_r4540_p1344
160229	380	e1195_s1771_s1741_r4829_r4540_p1344

A.0.1.5 WH

e.g. mc12_8TeV.160250.Pythia8_AU2CTEQ6L1_WH100_ZZ4lep.merge.NTUP_HSG2.e1419_s1771_s1741_r4829_r4540_p1344/

Generators	PDFs	Generator tune
Pythia8+Photospp	CTEQ6L1 LO, LO a_s	AUET2 CTEQ6L1

MC ID	Mass (GeV)	Tags
160250	100	e1419_s1771_s1741_r4829_r4540_p1344
160251	105	e1419_s1771_s1741_r4829_r4540_p1344
160252	110	e1419_s1771_s1741_r4829_r4540_p1344
160253	115	e1419_s1771_s1741_r4829_r4540_p1344
160254	120	e1419_s1771_s1741_r4829_r4540_p1344
167240	123	e1436_s1771_s1741_r4829_r4540_p1344
167242	124	e1436_s1771_s1741_r4829_r4540_p1344
160255	125	e1419_s1771_s1741_r4829_r4540_p1344
167245	126	e1436_s1771_s1741_r4829_r4540_p1344
167247	127	e1436_s1771_s1741_r4829_r4540_p1344
160256	130	e1419_s1771_s1741_r4829_r4540_p1344
160257	135	e1419_s1771_s1741_r4829_r4540_p1344
160258	140	e1419_s1771_s1741_r4829_r4540_p1344
160259	145	e1419_s1771_s1741_r4829_r4540_p1344
160260	150	e1419_s1771_s1741_r4829_r4540_p1344
160261	155	e1419_s1771_s1741_r4829_r4540_p1344
160262	160	e1419_s1771_s1741_r4829_r4540_p1344
160263	165	e1419_s1771_s1741_r4829_r4540_p1344
160264	170	e1419_s1771_s1741_r4829_r4540_p1344
160265	175	e1419_s1771_s1741_r4829_r4540_p1344
160266	180	e1419_s1771_s1741_r4829_r4540_p1344
160267	185	e1419_s1771_s1741_r4829_r4540_p1344
160268	190	e1419_s1771_s1741_r4829_r4540_p1344
160269	195	e1419_s1771_s1741_r4829_r4540_p1344
160270	200	e1419_s1771_s1741_r4829_r4540_p1344
160271	220	e1419_s1771_s1741_r4829_r4540_p1344
160272	240	e1419_s1771_s1741_r4829_r4540_p1344
160273	260	e1419_s1771_s1741_r4829_r4540_p1344
160274	280	e1419_s1771_s1741_r4829_r4540_p1344
160275	300	e1419_s1771_s1741_r4829_r4540_p1344
160276	320	e1419_s1771_s1741_r4829_r4540_p1344
160277	340	e1419_s1771_s1741_r4829_r4540_p1344
160278	360	e1419_s1771_s1741_r4829_r4540_p1344
160279	380	e1419_s1771_s1741_r4829_r4540_p1344
160280	400	e1191_s1771_s1741_r4829_r4540_p1344

A.0.1.6 ZH

e.g. mc12_8TeV.160300.Pythia8_AU2CTEQ6L1_ZH100_ZZ4lep.merge.NTUP_HSG2.e1217_s1771_s1741_r4829_r4540_p1344/

Generators	PDFs	Generator tune
Pythia8+Photospp	CTEQ6L1 LO, LO a_s	AUET2 CTEQ6L1

MC ID	Mass (GeV)	Tags
160300	100	e1217_s1771_s1741_r4829_r4540_p1344
160301	105	e1217_s1771_s1741_r4829_r4540_p1344
160302	110	e1217_s1771_s1741_r4829_r4540_p1344
160303	115	e1217_s1771_s1741_r4829_r4540_p1344
160304	120	e1217_s1771_s1741_r4829_r4540_p1344
167250	123	e1436_s1771_s1741_r4829_r4540_p1344
167252	124	e1436_s1771_s1741_r4829_r4540_p1344
160305	125	e1217_s1771_s1741_r4829_r4540_p1344
167255	126	e1436_s1771_s1741_r4829_r4540_p1344
167257	127	e1436_s1771_s1741_r4829_r4540_p1344
160306	130	e1217_s1771_s1741_r4829_r4540_p1344
160307	135	e1217_s1771_s1741_r4829_r4540_p1344
160308	140	e1217_s1771_s1741_r4829_r4540_p1344
160309	145	e1217_s1771_s1741_r4829_r4540_p1344
160310	150	e1217_s1771_s1741_r4829_r4540_p1344
160311	155	e1217_s1771_s1741_r4829_r4540_p1344
160312	160	e1217_s1771_s1741_r4829_r4540_p1344
160313	165	e1217_s1771_s1741_r4829_r4540_p1344
160314	170	e1217_s1771_s1741_r4829_r4540_p1344
160315	175	e1217_s1771_s1741_r4829_r4540_p1344
160316	180	e1217_s1771_s1741_r4829_r4540_p1344
160317	185	e1217_s1771_s1741_r4829_r4540_p1344
160318	190	e1217_s1771_s1741_r4829_r4540_p1344
160319	195	e1217_s1771_s1741_r4829_r4540_p1344
160320	200	e1217_s1771_s1741_r4829_r4540_p1344
160321	220	e1217_s1771_s1741_r4829_r4540_p1344
160322	240	e1217_s1771_s1741_r4829_r4540_p1344
160323	260	e1217_s1771_s1741_r4829_r4540_p1344
160324	280	e1217_s1771_s1741_r4829_r4540_p1344
160325	300	e1217_s1771_s1741_r4829_r4540_p1344
160326	320	e1217_s1771_s1741_r4829_r4540_p1344
160327	340	e1217_s1771_s1741_r4829_r4540_p1344
160328	360	e1217_s1771_s1741_r4829_r4540_p1344
160329	380	e1217_s1771_s1741_r4829_r4540_p1344
160330	400	e1217_s1771_s1741_r4829_r4540_p1344

A.0.2 ZZ background samples

A.0.2.1 ZZ Full Mass

e.g. mc12_8TeV.126937.PowhegPythia8_AU2CT10_ZZ_4e_mll4_2pt5.merge.NTUP_HSG2.e1280_s1771_s1741_r4829_r4540_p1344/

Generators	PDFs	Generator tune
Powheg+Pythia8+Photospp	CT10	AUET2 CT10

Table A.5: ZZ Full Mass.

MC ID	final state	Tags
126937	$4e$	e1280_s1771_s1741_r4829_r4540_p1344
126938	$2e2\mu$	e1280_s1771_s1741_r4829_r4540_p1344
126939	$2e2\tau$	e2372_s1771_s1741_r4829_r4540_p1344
126940	4μ	e1280_s1771_s1741_r4829_r4540_p1344
126941	$2\mu2\tau$	e2372_s1771_s1741_r4829_r4540_p1344
126942	4τ	e2372_s1771_s1741_r4829_r4540_p1344

A.0.2.2 ZZ Filter 100-150 GeV

e.g. mc12_8TeV.167162.PowhegPythia8_AU2CT10_ZZ_4e_m4l100_150_mll4_4pt3.merge.NTUP_HSG2.e1486_s1771_s1741_r4829_r4540_p1344/

Generators	PDFs	Generator tune
Powheg+Pythia8+Photospp	CT10	AUET2 CT10

A.0.2.3 ZZ Filter 500-50000 GeV

e.g. mc12_8TeV.169690.PowhegPythia8_AU2CT10_ZZ_4e_m4l500_50000_mll4_4pt3.merge.NTUP_HSG2.e1776_s1771_s1741_r4829_r4540_p1344/

A.0.2.4 gg2ZZ

e.g. mc12_8TeV.116601.gg2ZZJimmy_AUET2CT10_ZZ4e.merge.NTUP_HSG2.e1525_s1771_s1741_r4829_r4540_p1344/

A.0.2.5 qq2ZZ Inclusive

e.g. mc12_8TeV.161988.Sherpa_CT10_llll_ZZ_EW6_noHiggs.merge.NTUP_HSG2.e1434_s1771_s1741_r4829_r4540_p1344/

Table A.6: ZZ Filter 100 − 150 GeV.

MC ID	final state	Tags
167162	$4e$	e1486_s1771_s1741_r4829_r4540_p1344
167163	$2e2\mu$	e1486_s1771_s1741_r4829_r4540_p1344
167164	$2e2\tau$	e2372_s1771_s1741_r4829_r4540_p1344
167165	4μ	e1486_s1771_s1741_r4829_r4540_p1344
167166	$2\mu2\tau$	e2372_s1771_s1741_r4829_r4540_p1344
167167	4τ	e2372_s1771_s1741_r4829_r4540_p1344

Generators	PDFs	Generator tune
Powheg+Pythia8+Photospp	CT10	AUET2 CT10

Table A.7: ZZ Filter 500 − 50000 GeV.

MC ID	final state	Tags
169690	$4e$	e1776_s1771_s1741_r4829_r4540_p1344
169691	$2e2\mu$	e1776_s1771_s1741_r4829_r4540_p1344
169692	4μ	e1776_s1771_s1741_r4829_r4540_p1344

Generators	PDFs	Generator tune
McAtNlo+Herwig+Photos+Tauola	CT10	AUET2 CT10

MC ID	final state	Tags
116601	$4e$	e1525_s1771_s1741_r4829_r4540_p1344
116602	4μ	e1525_s1771_s1741_r4829_r4540_p1344
116603	$2e2\mu$	e1525_s1771_s1741_r4829_r4540_p1344

Generators	PDFs	Generator tune
Sherpa	CT10	CT10

A.0.2.6 Single Z

e.g. mc12_8TeV.147563.PowhegPythia8_AU2CT10_ZZ_4e_mll1_4lpt3_m4l40.merge.NTUP_HSG2.e2111_s1831_s1741_r4829_r4540_p1344/

Generators	PDFs	Generator tune
Powheg+Pythia8+Photospp	CT10	AUET2 CT10

MC ID	final state	Tags
147563	4e	e2111_s1831_s1741_r4829_r4540_p1344
147565	4mu	e2111_s1831_s1741_r4829_r4540_p1344
147564	2e2mu	e2111_s1831_s1741_r4829_r4540_p1344

A.0.3 Reducible Background Samples

A.0.3.1 $t\bar{t}$

mc12_8TeV.181087.PowhegPythia_P2011C_ttbar_dilepton.merge.NTUP_HSG2.e2091_a188_a205_r4540_p1344/

Generators	PDFs	Generator tune
Powheg+Pythia+Photos+Tauola	CTEQ6L1 LO, LO a_s	Perugia2011C

A.0.3.2 Z+jets (light jets), $m_{\ell\ell} > 60\,GeV$

e.g. mc12_8TeV.117650.AlpgenPythia_P2011C_ZeeNp0.merge.NTUP_HSG2.e1477_s1499_s1504_r3658_r3549_p1344/

Generators	PDFs	Generator tune
Alpgen+Pythia+Photos	CTEQ6L1 LO, LO a_s	Perugia2011C

MC ID	Process	Tags
117650	Zee, Np0	e1477_s1499_s1504_r3658_r3549_p1344
117651	Zee, Np1	e1477_s1499_s1504_r3658_r3549_p1344
117652	Zee, Np2	e1477_s1499_s1504_r3658_r3549_p1344
117653	Zee, Np3	e1477_s1499_s1504_r3658_r3549_p1344
117654	Zee, Np4	e1477_s1499_s1504_r3658_r3549_p1344
117655	Zee, Np5	e1477_s1499_s1504_r3658_r3549_p1344
117660	$Z\mu\mu$, Np0	e1477_s1499_s1504_r3658_r3549_p1344
117661	$Z\mu\mu$, Np1	e1477_s1499_s1504_r3658_r3549_p1344
117662	$Z\mu\mu$, Np2	e1477_s1499_s1504_r3658_r3549_p1344
117663	$Z\mu\mu$, Np3	e1477_s1499_s1504_r3658_r3549_p1344
117664	$Z\mu\mu$, Np4	e1477_s1499_s1504_r3658_r3549_p1344
117665	$Z\mu\mu$, Np5	e1477_s1499_s1504_r3658_r3549_p1344
117670	$Z\tau\tau$, Np0	e1711_s1581_s1586_r3658_r3549_p1344
117671	$Z\tau\tau$, Np1	e1711_s1581_s1586_r3658_r3549_p1344
117672	$Z\tau\tau$, Np2	e1711_s1581_s1586_r3658_r3549_p1344
117673	$Z\tau\tau$, Np3	e1711_s1581_s1586_r3658_r3549_p1344
117674	$Z\tau\tau$, Np4	e1711_s1581_s1586_r3658_r3549_p1344
117675	$Z\tau\tau$, Np5	e1711_s1581_s1586_r3658_r3549_p1344
147105	Zee, Np0	e1879_s1581_s1586_r3658_r3549_p1344
147106	Zee, Np1	e1879_s1581_s1586_r3658_r3549_p1344
147107	Zee, Np2	e1879_s1581_s1586_r3658_r3549_p1344
147108	Zee, Np3	e1879_s1581_s1586_r3658_r3549_p1344
147109	Zee, Np4	e1879_s1581_s1586_r3658_r3549_p1344
147110	Zee, Np5incl	e1879_s1581_s1586_r3658_r3549_p1344
147113	$Z\mu\mu$, Np0	e1880_s1581_s1586_r3658_r3549_p1344
147114	$Z\mu\mu$, Np1	e1880_s1581_s1586_r3658_r3549_p1344
147115	$Z\mu\mu$, Np2	e1880_s1581_s1586_r3658_r3549_p1344
147116	$Z\mu\mu$, Np3	e1880_s1581_s1586_r3658_r3549_p1344
147117	$Z\mu\mu$, Np4	e1880_s1581_s1586_r3658_r3549_p1344
147118	$Z\mu\mu$, Np5incl	e1880_s1581_s1586_r3658_r3549_p1344
147121	$Z\tau\tau$, Np0	e1881_s1581_s1586_r3658_r3549_p1344
147122	$Z\tau\tau$, Np1	e1881_s1581_s1586_r3658_r3549_p1344
147123	$Z\tau\tau$, Np2	e1881_s1581_s1586_r3658_r3549_p1344
147124	$Z\tau\tau$, Np3	e1881_s1581_s1586_r3658_r3549_p1344
147125	$Z\tau\tau$, Np4	e1881_s1581_s1586_r3658_r3549_p1344
147126	$Z\tau\tau$, Np5incl	e1881_s1581_s1586_r3658_r3549_p1344

A.0.3.3 Z+jets, $10\,GeV < m_{\ell\ell} < 40\,GeV$

e.g. mc12_8TeV.178354.AlpgenPythia_P2011C_ZeeNp0Excl_Mll10to40_2LeptonFilter5.merge.NTUP_HSG2.e2373_s1581_s1586_r4485_r4540_p1344/

Generators	PDFs	Generator tune
Alpgen+Pythia+Photos+Tauola	CTEQ6L1 LO, LO a_s	Perugia2011C

Table A.8: Z+jets samples, 10 $GeV < m_{\ell\ell} <$ 40 GeV.

MC ID	Process	Tags
178354	Zee, Np0	e2373_s1581_s1586_r4485_r4540_p1344
178355	Zee, Np1	e2371_s1581_s1586_r4485_r4540_p1344
178356	Zee, Np2	e2371_s1581_s1586_r4485_r4540_p1344
178357	Zee, Np3	e2371_s1581_s1586_r4485_r4540_p1344
178358	Zee, Np4	e2371_s1581_s1586_r4485_r4540_p1344
178359	$Z\mu\mu$, Np0	e2373_s1581_s1586_r4485_r4540_p1344
178360	$Z\mu\mu$, Np1	e2371_s1581_s1586_r4485_r4540_p1344
178361	$Z\mu\mu$, Np2	e2371_s1581_s1586_r4485_r4540_p1344
178362	$Z\mu\mu$, Np3	e2371_s1581_s1586_r4485_r4540_p1344
178363	$Z\mu\mu$, Np4	e2371_s1581_s1586_r4485_r4540_p1344
178364	$Z\tau\tau$, Np0	e2373_s1581_s1586_r4485_r4540_p1344
178365	$Z\tau\tau$, Np1	e2371_s1581_s1586_r4485_r4540_p1344
178366	$Z\tau\tau$, Np2	e2371_s1581_s1586_r4485_r4540_p1344
178367	$Z\tau\tau$, Np3	e2371_s1581_s1586_r4485_r4540_p1344
178368	$Z\tau\tau$, Np4	e2371_s1581_s1586_r4485_r4540_p1344

A.0.3.4 Z+jets, $40\,GeV < m_{\ell\ell} < 60\,GeV$

e.g. mc12_8TeV.178369.AlpgenPythia_P2011C_ZeeNp0Excl_Mll40to60_2LeptonFilter5.merge.NTUP_HSG2.e2373_s1581_s1586_r4485_r454

Generators	PDFs	Generator tune
Alpgen+Pythia+Photos+Tauola	CTEQ6L1 LO, LO a_s	Perugia2011C

Table A.9: Z+jets samples, 40 $GeV < m_{\ell\ell} < 60$ GeV.

MC ID	Process	Tags
178369	Zee, Np0	e2373_s1581_s1586_r4485_r4540_p1344
178370	Zee, Np1	e2371_s1581_s1586_r4485_r4540_p1344
178371	Zee, Np2	e2371_s1581_s1586_r4485_r4540_p1344
178372	Zee, Np3	e2371_s1581_s1586_r4485_r4540_p1344
178373	Zee, Np4	e2371_s1581_s1586_r4485_r4540_p1344
178374	$Z\mu\mu$, Np0	e2373_s1581_s1586_r4485_r4540_p1344
178375	$Z\mu\mu$, Np1	e2371_s1581_s1586_r4485_r4540_p1344
178376	$Z\mu\mu$, Np2	e2371_s1581_s1586_r4485_r4540_p1344
178377	$Z\mu\mu$, Np3	e2371_s1581_s1586_r4485_r4540_p1344
178378	$Z\mu\mu$, Np4	e2371_s1581_s1586_r4485_r4540_p1344
178379	$Z\tau\tau$, Np0	e2373_s1581_s1586_r4485_r4540_p1344
178380	$Z\tau\tau$, Np1	e2371_s1581_s1586_r4485_r4540_p1344
178381	$Z\tau\tau$, Np2	e2371_s1581_s1586_r4485_r4540_p1344
178382	$Z\tau\tau$, Np3	e2371_s1581_s1586_r4485_r4540_p1344
178383	$Z\tau\tau$, Np4	e2371_s1581_s1586_r4485_r4540_p1344

A.0.3.5 $Z + bb$

e.g. mc12_8TeV.181435.AlpgenPythia_Auto_P2011C_3lFilter_4lVeto_ZbbmumuNp0.merge.NTUP_HSG2.e2314_s1581_s1586_r4485_r4540_p1344/

Generators	PDFs	Generator tune
Alpgen+Pythia+Photos+Tauola	CTEQ6L1 LO, LO a_s	Perugia2011C

MC ID	Filter	Process	Tags
181435	3ℓ	$Zbb\mu\mu$, Np0	e2314_s1581_s1586_r4485_r4540_p1344
181436	3ℓ	$Zbb\mu\mu$, Np1	e2314_s1581_s1586_r4485_r4540_p1344
181437	3ℓ	$Zbb\mu\mu$, Np2	e2314_s1581_s1586_r4485_r4540_p1344
181430	3ℓ	$Zbbee$, Np0	e2314_s1581_s1586_r4485_r4540_p1344
181431	3ℓ	$Zbbee$, Np1	e2314_s1581_s1586_r4485_r4540_p1344
181432	3ℓ	$Zbbee$, Np2	e2314_s1581_s1586_r4485_r4540_p1344
181425	3ℓ	$Zbb\mu\mu$, Np0	e2314_s1581_s1586_r4485_r4540_p1344
181426	3ℓ	$Zbb\mu\mu$, Np1	e2314_s1581_s1586_r4485_r4540_p1344
181427	3ℓ	$Zbb\mu\mu$, Np2	e2314_s1581_s1586_r4485_r4540_p1344
181420	3ℓ	$Zbbee$, Np0	e2314_s1581_s1586_r4485_r4540_p1344
181421	3ℓ	$Zbbee$, Np1	e2314_s1581_s1586_r4485_r4540_p1344
181422	3ℓ	$Zbbee$, Np2	e2314_s1581_s1586_r4485_r4540_p1344

A.0.3.6 WZ

e.g. mc12_8TeV.147194.Sherpa_CT10_lllnjj_WZjj_EW6.merge.NTUP_HSG2.e1613_s1499_s1504_r3658_r3549_p1344/

Generators	PDFs	Generator tune
Sherpa	CT10	CT10

MC ID	Process	Tags
147194	$\ell\ell\ell\nu jj$	e1613_s1499_s1504_r3658_r3549_p1344
147197	$\ell\ell\ell\nu$	e1614_s1499_s1504_r3658_r3549_p1344

B

HL-LHC MC Samples List

The following Monte Carlo samples are used for the Higgs signal:

```
mc12-14TeV.160155.PowhegPythia8-AU2CT10-ggH125-ZZ4lep.evgen.EVNT.e1337
mc12-14TeV.160205.PowhegPythia8-AU2CT10-VBFH125-ZZ4lep.evgen.EVNT.e1337
mc12-14TeV.160255.Pythia8-AU2CTEQ6L1-WH125-ZZ4lep.evgen.EVNT.e2286
mc12-14TeV.160305.Pythia8-AU2CTEQ6L1-ZH125-ZZ4lep.evgen.EVNT.e1413
mc12-14TeV.167562.Pythia8-AU2CTEQ6L1-ttH125-ZZ4lep.evgen.EVNT.e2211
```

For the ZZ background a million Monte Carlo events were generated with MadGraph5 V1.5 showered with Pythia 8, in the mass range $100 - 150$ GeV with 4l-filter with $\eta < 2.8$ and lepton p_T thresholds of $20,\ 15,\ 10$ and 6 GeV.

C
Test Fit Distributions

The fitted CR of the fits presented in Chapter 5 are available in this appendix.

Figure C.1: The data m_{12} distributions are presented after the test fit, where the shape parameters set free to fluctuate, applied for consistency reasons. The CRs of the inverted $d_0/\sigma d_0$ (a), inverted isolation and nominal $d_0/\sigma d_0$ (b), SS (c) and $e\mu + \mu\mu$ (d) are presented. The test proves no significant deviation with the nominal results.

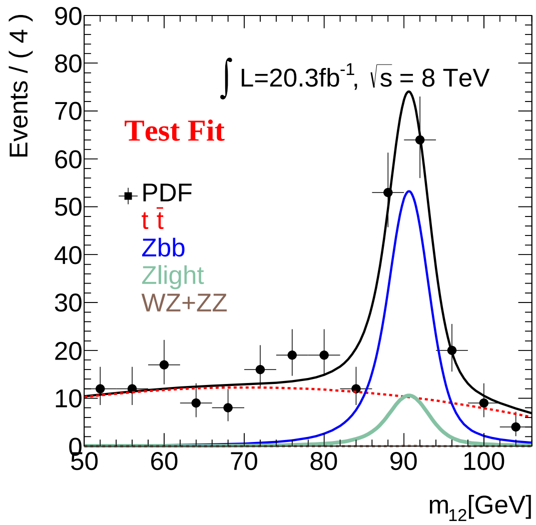

(a)

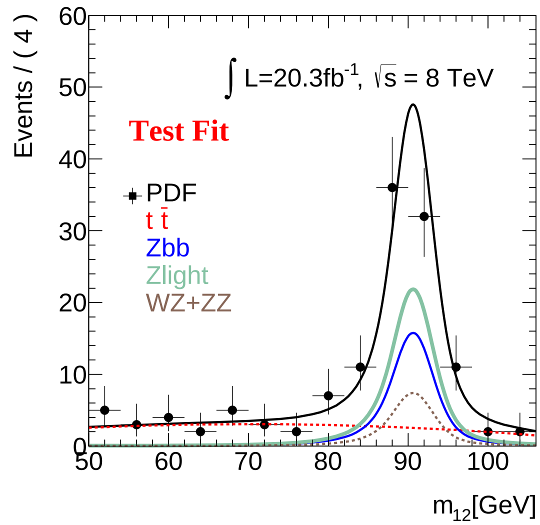

(b)

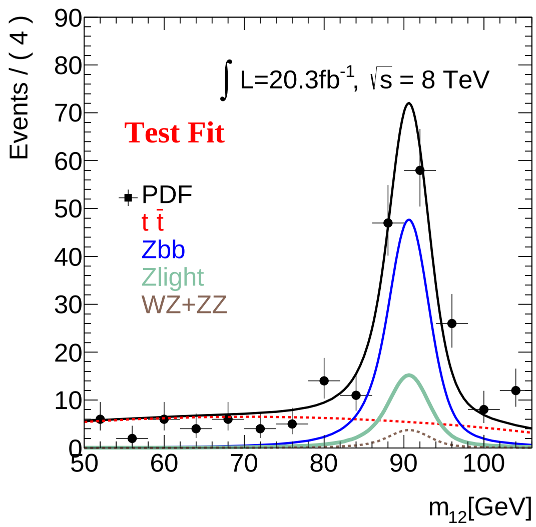

(c)

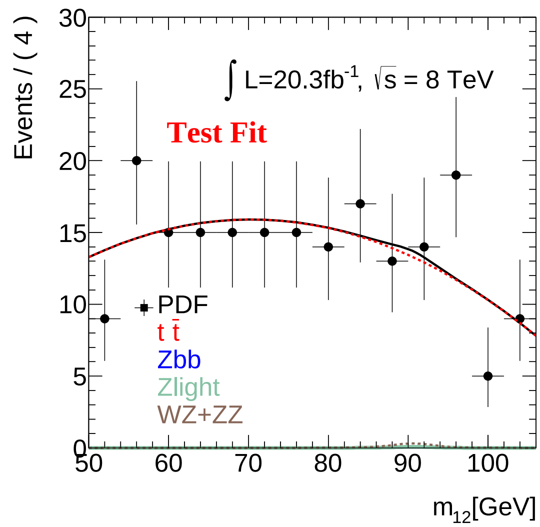

(d)

Figure C.2: The data m_{12} distributions are presented after the test fit, where the fractions uncertainties reduced to 0.1 of each value, applied for consistency reasons. The CRs of the inverted $d_0/\sigma d_0$ (a), inverted isolation and nominal $d_0/\sigma d_0$ (b), SS (c) and $e\mu+\mu\mu$ (d) are presented. The test proves no significant deviation with the nominal results.

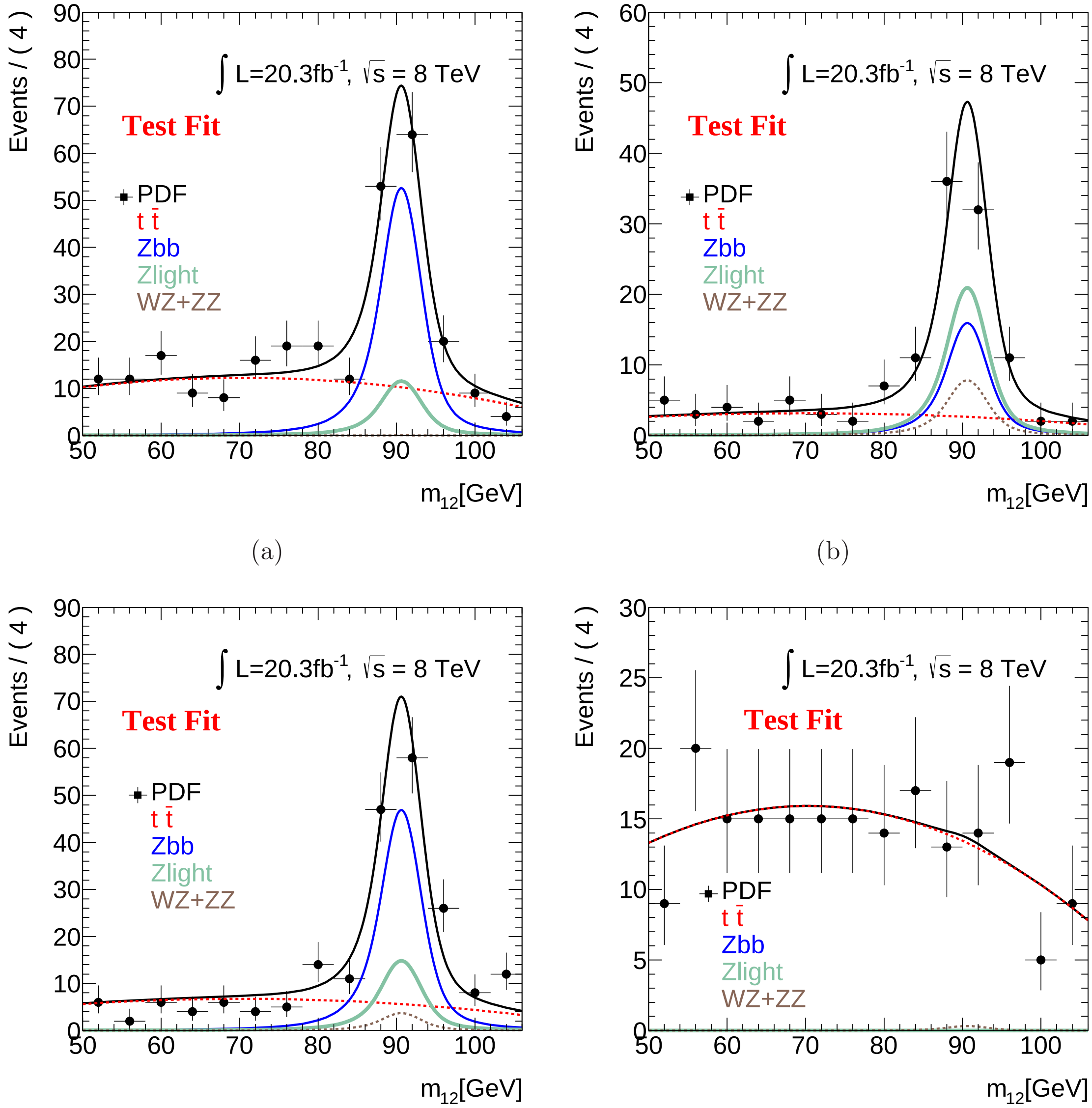

(a) (b) (c) (d)

Figure C.3: The data m_{12} distributions are presented after the test fit, where the fractions uncertainties doubled, applied for consistency reasons. The CRs of the inverted $d_0/\sigma d_0$ (a), inverted isolation and nominal $d_0/\sigma d_0$ (b), SS (c) and $e\mu + \mu\mu$ (d) are presented. The test proves no significant deviation with the nominal results.

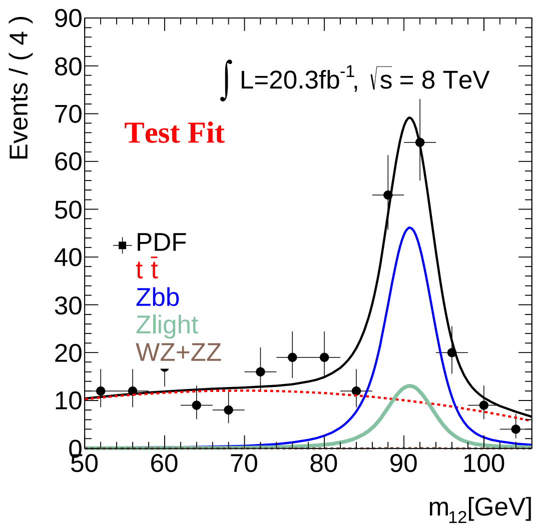

(a)

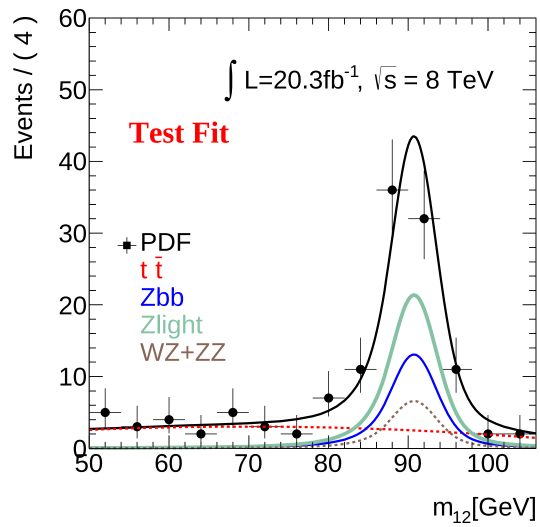

(b)

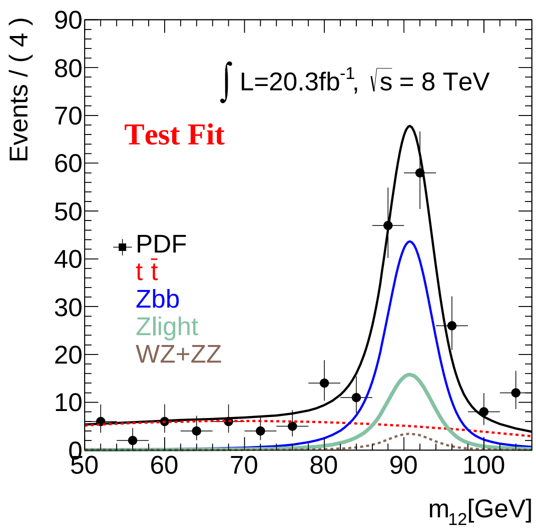

(c)

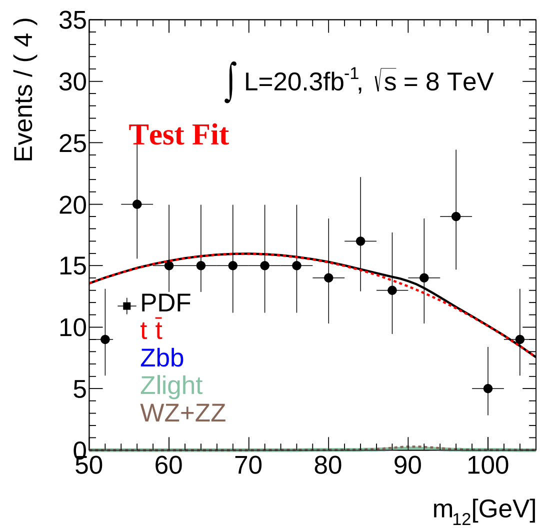

(d)

Figure C.4: The data m_{12} distributions are presented after the test fit, where the $Zb\bar{b}$ and $Zlight$ are treated as one background, the $Zjets$, for testing reasons. The CRs of the inverted $d_0/\sigma d_0$ (a), inverted isolation and nominal $d_0/\sigma d_0$ (b), SS (c) and $e\mu + \mu\mu$ (d) are presented. The test proves no significant deviation with the nominal results.

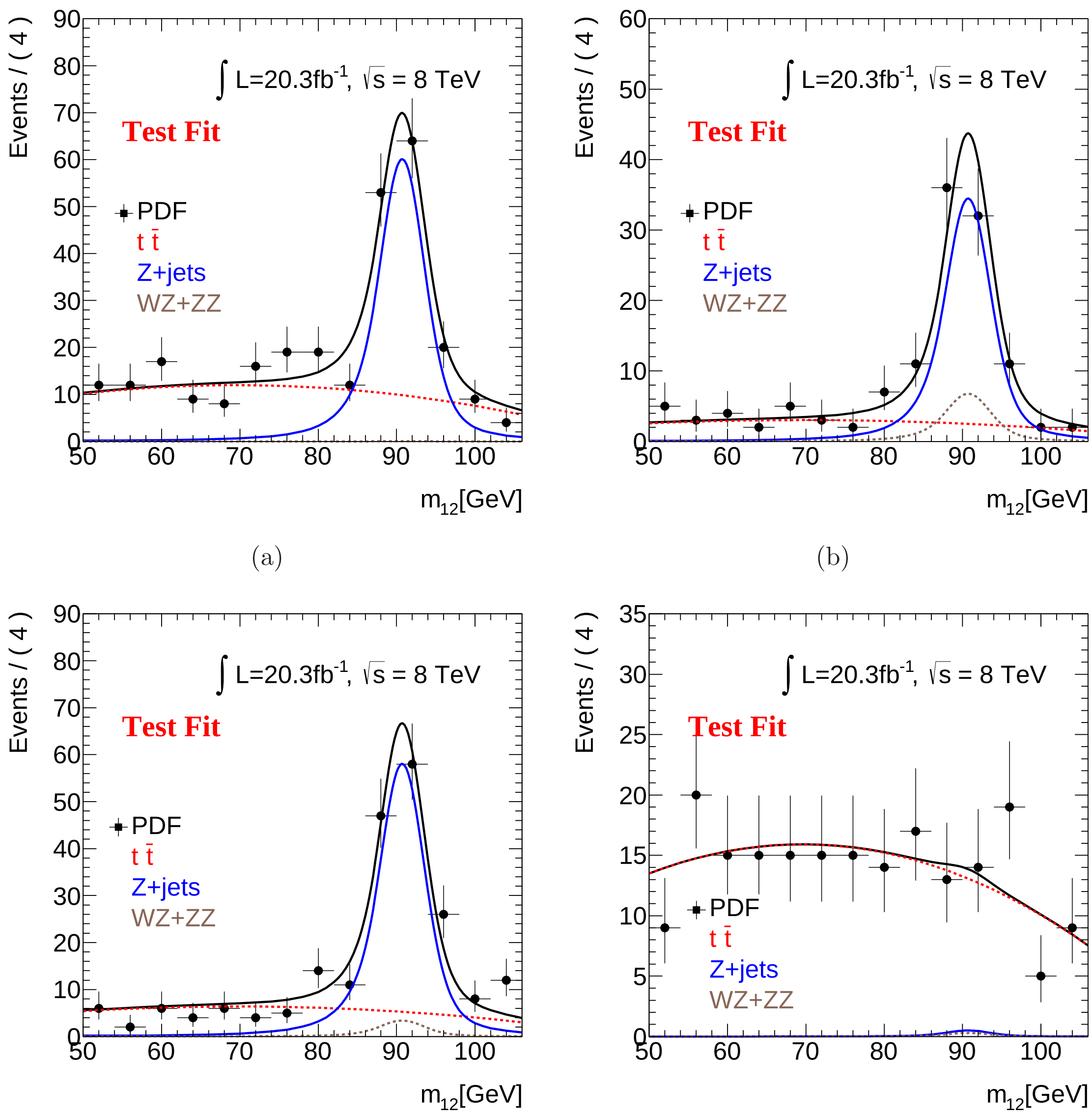

(a) (b)

(c) (d)

List of Figures

List of Tables